Statistical mechanics and thermodynamics of adhesion, phase transformations, and fracture in micro- and nano-systems

Andrea Cannizzo

Centrale Lille

Thése

Présentée en vue
d'obtenir le grade de

Docteur

dans la spécialité

« Micro et nano technologies, acoustique et télécommunications »

Par

Andrea Cannizzo

DOCTORAT délivré conjointement par CENTRALE LILLE et POLITECNICO DI BARI

Titre de la thèse :

Mécanique statistique et thermodynamique de l'adhésion, des transformations de phase et de la rupture dans les micro et nanosystèmes

Statistical mechanics and thermodynamics of adhesion, phase transformations, and fracture in micro- and nano-systems

Soutenue le 19/12/2023 devant le jury d'examen :

Président	M. Matteo, Ciccotti,	Prof. ESPCI Paris
Rapporteur	M. Loïc, Vanel,	Prof. ILM CNRS, Univ. Lyon 1
Rapporteure	Mme Anne, Tanguy,	Prof. INSA Univ. Lyon
Examinateur	M. Stéphane, Santucci,	DR CNRS, ENS de Lyon
Examinatrice	Mme Delphine, Brancherie,	Prof. UTC Compiègne
Codirecteur	M. Stefano, Giordano,	DR CNRS, IEMN CNRS, Univ. Lille
Codirecteur	M. Giuseppe, Puglisi,	Prof. DICATECh Bari, Italie
Invité	M. Giuseppe, Florio,	Prof. DICATECh Bari, Italie

Thèse préparée dans les laboratoires IEMN et DMMM
Ecole Doctorale ENGSYS; SCUDO (Bari)

Acknowledgments

Few words allotted in the acknowledgments section of a thesis will never be able to express how sincerly and deeply grateful I am to my PhD supervisor, Stefano Giordano. I have been extremely fortunate to know him as my thesis supervisor and, more importantly, as a person in general. His great example transcends the boundaries of science and will forever accompany my future journey. Along with Stefano, I also thank my italian side supervisors, Giuseppe Puglisi and Giuseppe Florio, for their invaluable insights and contributions from a scientific perspective, which greatly enriched the quality of this work.

Besides my supervisors, I am very much obliged to Delphine Brancherie, Matteo Ciccotti and Stéphane Santucci for their participation as members of my thesis committee, and to Anne Tanguy and Loïc Vanel for kindly accepting to review this manuscript.

I thank all the members of the AIMAN-FILMS group that have made me feel integrated and welcomed from the very first day of my PhD and, particularly, Nicolas Tiercelin for his kindness and endless help throughout the entirety of my PhD. More broadly, I want to thank every person that works at *iemn* laboratories for creating such an amazing workplace everyday with their kindness and professionality.

I would also thank my Master's thesis supervisors, Flavio Seno and Armando Bazzani, as their support and endorsement have been instrumental in my academic and professional pursuits.

I express my sincere gratitude to Centrale Lille and Hauts-de-France Region for their generous financial contributions, which made this research possible and, more gerenally, to France and french people for welcoming me in their great Community as one of theirs.

I want to extend a heartfelt thank you to my dear friend Alberto Da Re, who played a pivotal role in helping me choose this incredible PhD journey, along with the new friends I've made over the course of these three years, and my family for their unwavering support.

Publications

Some ideas and figures have appeared previously in the following publications:

1. Andrea Cannizzo, Giuseppe Florio, Giuseppe Puglisi, and Stefano Giordano. "Temperature controlled decohesion regimes of an elastic chain adhering to a fixed substrate by softening and breakable bonds". In: *Journal of Physics A: Mathematical and Theoretical* 54.44 (2021), p. 445001. DOI: 10.1088/1751-8121/ac2a07 [1]

2. Andrea Cannizzo, Luca Bellino, Giuseppe Florio, Giuseppe Puglisi, and Stefano Giordano. "Thermal control of nucleation and propagation transition stresses in discrete lattices with non-local interactions and non-convex energy". In: *The European Physical Journal Plus* 137.5 (2022), p. 569. DOI: 10.1140/epjp/s13360-022-02790-9 [2]

3. Andrea Cannizzo and Stefano Giordano. "Thermal effects on fracture and the brittle-to-ductile transition". In: *Phys. Rev. E* 107 (3 Mar. 2023), p. 035001. DOI: 10.1103/PhysRevE.107.035001 [3]

Résumé en français

Les micro-instabilités jouent un rôle clé dans divers systèmes mécaniques, tant artificiels que biologiques. Dans le cas des systèmes artificiels, les exemples de ces instabilités peuvent inclure le décollement d'un film d'un substrat [4–10], la propagation d'ondes dans des réseaux bistables [11–15], la récolte d'énergie à travers des chaînes multistables [16–18], la plasticité et l'hystérésis dans les transitions de phase et les transformations martensitiques des solides [19–29], ainsi que la nucléation et la propagation des fissures et des dislocations dans les matériaux et les alliages [30–38], et le frottement à l'échelle nanométrique [39–48]. D'autre part, dans le cas des systèmes biologiques, les micro-instabilités se manifestent sous la forme de transitions conformationnelles dans les chaînes polymères et biopolymères [49–58], le passage entre les états attachés et détachés des fibrilles dans l'adhésion cellulaire [59–64], l'ouverture des épingles à cheveux macromoléculaires [65–69], le comportement des sarcomères dans les muscles squelettiques [70–76], la dégradation ou la dénaturation des acides nucléiques, des chaînes polypeptidiques et d'autres polymères [77–86], ainsi que le frottement des macromolécules ou de la matière molle [87–90].

Dans toutes ces situations physiques, le système présente toujours un paysage énergétique complexe caractérisé par une multitude de bassins et, selon le bassin particulier dans lequel il se trouve d'un point de vue énergétique, le système peut se trouver dans une configuration stable ou méta-stable. Nous soulignons que ces systèmes sont constitués d'un grand nombre d'unités qui, prises individuellement, présentent des états physiques bien définis, mais qui, considérées dans leur ensemble, présentent un comportement plutôt non linéaire et chaotique difficile à décrire au premier abord. Les transitions entre ces états ou, de manière équivalente, les explorations du paysage énergétique complexe, régissent le comportement macroscopique de l'ensemble du système et, en particulier, ses caractéristiques statiques et dynamiques. Les micro-instabilités peuvent être divisées en deux catégories principales. Dans un premier type, les micro-instabilités intrinsèques peuvent décrire des unités bistables (ou multi-stables) avec des transitions entre un état fondamental et un (ou plusieurs) état(s) métastable(s) (par exemple, pour les transitions conformationnelles plié-déplié dans les macromolécules ou les changements de phase martensitique dans les alliages métalliques, ou encore la friction). Ces états représentent des conformations différentes, mais mécaniquement résistantes. Ce cas peut être représenté dans un cadre unidimensionnel en introduisant une énergie potentielle effective à double puits $U(x)$ fonction d'un paramètre $x \in \mathrm{R}$ qui, dans ce cas, représente parfaitement un paramètre d'ordre effectif utile pour décrire la transition entre les différents puits de potentiel. Dans la deuxième classe, les micro-instabilités peuvent décrire les transitions entre les états non rompus et rompus des unités cassables du système (par exemple, dans l'ouverture des épingles à cheveux, la dénaturation des macromolécules, l'adhésion biologique fibrillaire, le décollement des films, la propagation des fissures, et ainsi de suite). Ce processus peut être réversible, partiellement réversible ou irréversible en fonction du phénomène physique spécifique. Là encore, le paysage énergétique unidimensionnel considéré dans ce second cas peut être modélisé par une fonction potentielle unidimensionnelle où la configuration non rompue correspond à un puits de potentiel

et la configuration rompue correspond à une énergie constante et à une force nulle.

Il est intéressant de noter qu'il existe un parallèle entre tous les problèmes de la biophysique et de la science des matériaux. Cette similitude est à la base du développement de modèles mathématiques applicables indistinctement aux deux domaines de recherche, comme nous le verrons plus loin. En fait, le but principal de cette thèse est de développer des modèles entre la physique et la mécanique qui sont capables d'étudier les transitions d'état (micro-instabilités) dans tous ces systèmes biologiques et artificiels afin de mieux comprendre les effets de la température et des actions mécaniques externes sur leur comportement.

Comme la longueur caractéristique qui sépare deux états différents Δx est de l'ordre d'unités de nanomètres et que les énergies impliquées dans les liaisons chimiques sont de l'ordre de dizaines de $K_B T$, il est crucial d'observer que les effets de la température sur ces systèmes sont non-négligeables. En effet, les transitions entre les états dans tous les systèmes précédents sont fortement influencées par les fluctuations thermiques, qui peuvent modifier la probabilité d'être dans un état donné ou le taux de passage entre les puits d'énergie voisins. C'est la raison pour laquelle le cadre correct dans lequel nous pouvons développer la modélisation théorique de ces phénomènes est celui de la mécanique statistique classique. En particulier, les systèmes présentant des mécanismes de commutation entre différents bassins d'énergie peuvent être étudiés au moyen de l'approche des variables de spin, qui est basée sur l'introduction d'une série de variables discrètes (similaires aux spins utilisés pour traiter les systèmes magnétiques), capables d'identifier l'état associé à une unité de système donnée. Par exemple, dans le cas d'un potentiel bistable, l'énergie décrivant le passage d'un élément de chaîne d'une conformation pliée à une conformation dépliée peut être approximée par une fonction bi-parabolique, le passage d'un puits à l'autre étant décrit par la variable de spin. Cela signifie que, selon la valeur de ces variables discrètes, la fonction d'énergie peut changer de forme et, en particulier, de position et de profondeur de ses puits. L'introduction des variables de spin simplifie fréquemment le calcul de la fonction de partition et, par conséquent, l'analyse des quantités thermodynamiques moyennées correspondantes. Ce dispositif théorique permet d'obtenir des résultats mathématiques en forme fermée, très utiles pour faire progresser la compréhension de la mécanique et de la physique sous-jacentes.

Dans ce manuscrit, nous considérons deux protocoles expérimentaux différents [91–93] pour la perturbation mécanique de petits systèmes. En particulier, les expériences réalisées à des forces appliquées constantes (réalisées à l'aide de dispositifs extrêmement mous) correspondent à l'ensemble statistique de Gibbs, et les expériences réalisées à des déplacements prescrits (menées à l'aide de dispositifs extrêmement durs) sont une réalisation de l'ensemble statistique de Helmholtz. En général, ces deux conditions limites conduisent à des réponses force-extension différentes puisque, dans chacun des deux cas, nous explorons un espace de phase différent. En fait, en fonction de la rigidité équivalente du dispositif, l'expérience d'étirement correspond à une situation située entre les ensembles de Gibbs et de Helmholtz de la mécanique statistique [94, 95].

Dans le deuxième chapitre de ce manuscrit, nous introduisons et analysons un modèle simple pour mettre en évidence les différences fondamentales entre les ensembles de Gibbs et de Helmholtz tout en les étudiant à travers les principes de la mécanique statistique à l'équilibre. La simplicité intrinsèque du modèle représente le terrain de départ idéal dans lequel nous sommes en mesure d'appliquer une approximation de spin et de comprendre sa véritable signification et sa faisabilité. Grâce à l'approche de la mécanique statistique, nous obtenons des résultats à première vue en désaccord avec ce que nous attendrions d'un point de vue purement pratique mais, heureusement, ces incongruités apparentes sont ensuite entièrement expliquées et résolues à l'aide d'une approche purement axée sur le bilan énergétique.

Dans les chapitres suivants, nous appliquons ces techniques à trois cas différents. Dans le premier, nous avons élaboré un modèle pour décrire le processus de cohésion/décohésion lié à un film déposé sur un substrat, en nous concentrant sur les effets des fluctuations thermiques. Nous

avons analysé ce processus sous une action mécanique supplémentaire, représentée soit par une force externe, soit par une extension prescrite appliquée à l'extrémité de la chaîne correspondant aux ensembles de Gibbs et de Helmholtz, respectivement, introduits précédemment. Pour aborder le problème, nous avons combiné la méthode basée sur les variables de spin [91, 92] avec une analyse raffinée des propriétés de certaines matrices tridiagonales [96, 97], caractérisant le système à l'étude. Nous avons tout d'abord développé la théorie pour l'ensemble de Helmholtz, puis nous avons obtenu les résultats pour l'ensemble de Gibbs par le biais de la transformation de Laplace décrivant la relation entre les fonctions de partition des deux ensembles [98]. Finalement, pour les deux ensembles statistiques, nous avons obtenu des résultats explicites donnant la relation force-extension, le nombre moyen d'unités brisées et l'extension moyenne de tous les éléments de la chaîne en tant que fonctions de la température et de l'action mécanique externe (une force pour l'ensemble de Gibbs et une extension pour l'ensemble de Helmholtz). Ces résultats, obtenus pour un nombre arbitraire N d'éléments de la chaîne, sont utiles pour bien comprendre le comportement du système, pour comparer avec les résultats existants concernant le pliage/dépliage des chaînes bistables macromoléculaires, et, enfin, pour effectuer l'analyse de la limite thermodynamique. En effet, lorsque $N \to \infty$, certains des calculs précédemment effectués pour le nombre fini d'éléments N, peuvent être remplacés par des intégrales appropriées en introduisant une transformation discrète à continue. Une telle analyse prouve que, dans la limite thermodynamique, le décollement du film du substrat a lieu à une force critique donnée, qui dépend de la température. Dans le processus de cohésion/décohésion, l'origine de la force de décollement dépendante de la température est expliquée par l'observation d'une transition de phase se produisant à une température critique donnée, capable de détacher complètement le film du substrat. Dans le régime sous-critique, les fluctuations thermiques favorisent le détachement du film et, par conséquent, une force de décollement plus faible est nécessaire pour des températures plus élevées. La tendance à la baisse de la force de décollement avec la température est la même pour les deux ensembles statistiques. Cependant, ces derniers ne sont pas équivalents dans la limite thermodynamique puisqu'ils présentent une courbe force-extension différente. La relation obtenue pour la force de dénaturation dépendant de la température a été testée par rapport à des données expérimentales concernant la décomposition d'épingles à cheveux d'ARN et d'ADN, ce qui a finalement permis d'obtenir un bon accord entre la théorie et les mesures. Bien que le modèle présenté soit intéressant car il conduit à une approche entièrement analytique capable d'expliquer l'émergence de la transition de phase et la non-équivalence des ensembles, il pourrait être généralisé pour prendre en considération des situations plus complexes. Par exemple, la méthodologie des variables de spin employée pour calculer les fonctions de partition est limitée à l'étude de la thermodynamique à l'équilibre. Il pourrait être intéressant de la généraliser au régime dynamique, où la fonction d'énergie réelle décrivant les unités du système joue un rôle important [99–101]. De plus, notre approche pourrait être appliquée à différentes configurations de systèmes, y compris les faisceaux de fibres avec des brins cassables, le flambage des films déposés sur des substrats, la propagation des fissures dans les solides fragiles ou plastiques, et les phénomènes de rupture dans les réseaux de polymères.

Dans le quatrième chapitre, nous analysons un modèle similaire à celui présenté dans le chapitre précédent, avec la différence importante que, maintenant, les liens de liaison des unités de la chaîne peuvent se trouver dans un troisième état de ramollissement possible avant d'atteindre le point de rupture complet. Plus précisément, ces éléments sont décrits par un mécanisme de ramollissement, c'est-à-dire par trois régions de fonctionnement comme suit : la première région linéaire correspond aux éléments intacts (petite déformation), la deuxième région correspond aux éléments ramollis avec une rigidité réduite (déformation intermédiaire), et enfin, la troisième région correspond aux éléments cassés (grande déformation). Ce système paradigmatique a été étudié en supposant qu'il est noyé dans un bain thermique à une température donnée et qu'il

est soumis à une action mécanique externe. Cette dernière peut être soit une extension prescrite (dispositif dur), soit une force appliquée (dispositif mou) au dernier élément de la chaîne, ce qui correspond, là encore, à l'ensemble de Helmholtz (condition isométrique) et à l'ensemble de Gibbs (condition isotensionnelle) de la mécanique statistique à l'équilibre, respectivement. Afin de procéder à l'analyse mathématique du problème, nous avons à nouveau adopté l'approche des variables de spin pour définir l'état de tout élément cassable [91, 92, 94, 95, 102, 103], nous avons introduit l'hypothèse du modèle de fermeture éclair avec deux parois de domaine pour décrire les trois régions de fonctionnement de la chaîne de liens [104–107], et nous avons finalement exploité certaines propriétés analytiques des matrices tridiagonales [96, 97] pour obtenir des résultats sous forme fermée dans des conditions isométriques et isotensionnelles. Dans les deux cas, nous avons obtenu la solution générale du problème pour une chaîne composée d'un nombre N d'éléments. Ces solutions, dans les deux cas, conduisent à une force de décohésion constante, qui représente la force du système. Il est important de noter que cette force dépend de la température et que sa valeur diminue avec l'augmentation de la température. L'interprétation physique de ce comportement peut être faite en observant que les fluctuations thermiques favorisent l'endommagement des éléments cassables, réduisant ainsi la force du système. En outre, le nombre d'éléments cassés et ramollis a été déterminé en fonction de la température et de l'action mécanique externe pour les deux ensembles statistiques. Il est intéressant de noter que nous avons prouvé que le nombre d'éléments ramollis ne dépend que de la température et qu'il est indépendant de l'action mécanique externe. Cette analyse fournit une image complète du comportement du système avec un nombre fini N d'éléments. Pour mieux comprendre la signification de ces résultats, nous avons analysé le comportement du système sous l'hypothèse de la limite thermodynamique, c'est-à-dire pour $N \to \infty$. Dans ce cas, les sommes apparaissant dans les fonctions de partition des deux ensembles et dans les moyennes macroscopiques des variables thermodynamiques pertinentes peuvent être remplacées par des intégrales, ce qui conduit finalement à des expressions utiles de forme fermée. L'analyse de ces résultats fournit une explication claire de la force dépendant de la température en termes de transitions de phase. En effet, une première température critique existe pour le système et correspond à la rupture partielle de tous les éléments de la chaîne. Ensuite, une deuxième température critique décrit la rupture complète de toutes les liaisons. Ce scénario critique complexe permet de donner une explication rigoureuse de la relation entre résistance et température dans les systèmes où se produit une transition dans le mécanisme de rupture (ici représentée par le ramollissement des liaisons). Dans plusieurs mesures expérimentales, une courbe à deux branches pour la relation résistance-température a effectivement été observée [33, 35, 38]. Un autre résultat intéressant concerne la non-équivalence des ensembles dans la limite thermodynamique. Cela signifie que les courbes force-extension sont différentes pour les ensembles de Helmholtz et de Gibbs, y compris pour $N \to \infty$. Il est bien connu que l'équivalence des ensembles statistiques de Gibbs et de Helmholtz a été prouvée pour une grande classe de systèmes physiques comprenant, par exemple, des chaînes de polymères flexibles simples sans effets de confinement et avec un potentiel d'interaction d'appariement continu entre les monomères voisins [56, 108–112]. Cependant, il est difficile de prouver l'équivalence de l'ensemble pour des systèmes ou des structures plus généraux. Par exemple, d'autres problèmes, concernant par exemple l'échappement d'un polymère confiné entre deux plans ou la désorption d'un polymère attaché à une surface, conduisent à la non-équivalence entre les ensembles statistiques définis [113–118]. Il est intéressant de noter que ces recherches sont cohérentes avec nos résultats et prouvent définitivement la possibilité d'une non-équivalence des ensembles entre différents ensembles statistiques dans des systèmes physiques pertinents. En outre, les généralisations possibles de cette théorie peuvent inclure le comportement dynamique des processus de cohésion/décohésion (où les barrières entre les puits du paysage énergétique jouent un rôle important [99–101]), ou l'adoucissement multi-états, c'est-à-dire composé de plusieurs étapes avec une rigidité différente

(décrite par plusieurs parois de domaine dans la chaîne).

Au chapitre 5, nous avons élaboré deux modèles distincts, avec différents niveaux de complexité, pour décrire le comportement en fonction de la température de systèmes non convexes unidimensionnels et non locaux. Le système paradigmatique étudié est composé d'une séquence d'unités, présentant un comportement bistable décrit par une énergie potentielle à deux états, en interaction les unes avec les autres. D'une part, ce système est capable de représenter les caractéristiques spécifiques de plusieurs macromolécules d'origine biologique (principalement des protéines). Dans ce cas, la non-convexité (bistabilité) décrit la commutation possible de chaque domaine de la macromolécule entre ses états plié et déplié. En outre, la non-localité, introduite au moyen du schéma d'Ising, décrit la coopérativité observée dans la plupart des structures biologiques. D'autre part, le modèle proposé est également capable de représenter les transformations de phase dans les matériaux. Les deux états du comportement bistable représentent dans ce cas deux microstructures du matériau solide, correspondant *e.g.* à deux structures cristallines ou à des phases austénitiques et martensitiques. Cela permet d'étudier la pseudo-élasticité et les effets de mémoire de forme dans les systèmes solides tels que les trichites, les nanofils ou les nanocomposites. Pour ces systèmes, le schéma d'interaction d'Ising reproduit le coût énergétique de la création d'une interface entre les deux états différents de la matière en raison de l'absence de compatibilité cinématique. Notre modèle décrit alors de manière prototypique l'origine des phénomènes de nucléation, de propagation et, éventuellement, de coalescence, ainsi que leur éventuelle dépendance à la température lorsque de petites dimensions sont considérées, comme dans le cas des nanofils, de sorte que les contributions entropiques peuvent rivaliser avec les termes d'énergie élastique globale. En effet, dans l'approche proposée, les effets thermiques sont soigneusement pris en compte en introduisant l'analyse de la mécanique statistique du problème, basée sur la méthode des variables de spin. Cela nous permet de développer un cadre thermodynamique complet des processus de transformation dans les systèmes avec non-localité et non-convexité. La première approche proposée est la plus raffinée et met en œuvre la complexité du système dans toute sa généralité, sans hypothèses simplificatrices. Le système est constitué d'une chaîne d'éléments bistables interagissant à travers un schéma d'Ising. Nous pouvons étudier les ensembles de Gibbs (isotensionnels) et de Helmholtz (isométriques) de la mécanique statistique en évaluant les fonctions de partition pertinentes sous forme fermée. Ces résultats sont valables pour les cas ferromagnétiques (interaction d'Ising positive) et antiferromagnétiques (interaction d'Ising négative). Cependant, dans ce chapitre, nous nous concentrons principalement sur le comportement ferromagnétique. Dans ce modèle, chaque unité peut librement prendre l'un des deux états admis, en fonction de la température du système et des actions mécaniques appliquées au système. Le nombre d'interfaces entre les régions pliées et dépliées est donc libre de varier et représente une mesure des effets entropiques sur le système. Ainsi, on peut observer une augmentation du nombre d'interfaces avec l'augmentation de la température pour un système ferromagnétique. Le point important est que pour les systèmes fortement ferromagnétiques (avec un coût énergétique élevé de la génération d'interfaces), qui sont les plus courants dans les applications pratiques, une seule interface est observée entre les deux états différents et elle se propage le long de la chaîne lorsque la traction ou l'allongement sont appliqués au système. Outre le phénomène de propagation de l'interface, dans le cas isométrique de Helmholtz, nous pouvons également observer un pic initial de force vers le haut, représentant la nucléation de la nouvelle phase dépliée, et un pic final de force vers le bas, représentant la coalescence de la phase pliée dans la phase dépliée. Une caractéristique importante de ce système est que le plateau de force, décrivant la propagation de l'interface à l'intérieur de la chaîne, dépend en général de la température pour les conditions limites isotensionnelles et isométriques. L'origine de cette dépendance réside dans la différence entre les constantes élastiques des phases dépliée et repliée. En fait, lorsque ces constantes élastiques sont égales, le plateau de force devient

indépendant de la température, et les résultats connus de la littérature sont retrouvés. Comme l'analyse de la limite thermodynamique est extrêmement complexe pour le modèle d'Ising exact (en particulier, pour le cas isométrique), et comme le cas important pour les applications est le cas fortement ferromagnétique, nous avons introduit le modèle de fermeture éclair dans lequel nous considérons une seule interface se propageant le long du système. Cette hypothèse rend le calcul de la fonction de partition beaucoup plus simple dans les ensembles de Gibbs et de Helmholtz. La limite thermodynamique pour l'ensemble de Gibbs peut être analysée directement et les résultats sont parfaitement cohérents avec le modèle d'Ising exact étudié précédemment. En particulier, le comportement du plateau de force en fonction de la température est également confirmé par cette approche de fermeture éclair. L'étude de la limite thermodynamique concernant le modèle de fermeture éclair en condition isométrique, *i.e* dans l'ensemble de Helmholtz, représente la troisième approche de ce travail. Cette analyse est basée sur la méthode de la phase stationnaire et permet d'obtenir trois résultats importants : (i) une expression simplifiée de la relation force-extension dans des conditions isométriques, valable pour des chaînes très longues et fortement ferromagnétiques (qui décrit parfaitement les phénomènes de nucléation, de propagation et de coalescence), (ii) une expression explicite de l'amplitude du premier pic de force (basée sur la fonction de Lambert), représentant la nucléation des unités dépliées, et (iii) une démonstration rigoureuse de l'équivalence des ensembles de Gibbs et de Helmholtz pour le modèle de la fermeture éclair (les pics de nucléation et de coalescence disparaissent à mesure que la longueur augmente). Ces résultats, basés sur l'approximation de la phase stationnaire, décrivent correctement les processus de transformation dans des objets unidimensionnels (macromolécules ou nanofils solides) en termes de fluctuations thermiques et d'actions mécaniques appliquées au système. Quelques exemples de comparaisons quantitatives sont présentés pour l'évolution microstructurale des nanofils métalliques et semi-conducteurs. Bien que ce travail puisse être généralisé et étendu de nombreuses façons, nous ne mentionnons ici que deux perspectives d'avenir d'un certain intérêt. Le premier aspect négligé représente la microstructure réelle des états métastables considérés. Ce point peut être amélioré en introduisant les principales propriétés des structures moléculaires réelles des deux phases du système. Le deuxième aspect concerne le fait que nous avons mené toute la discussion à l'équilibre thermodynamique et donc dans des conditions statiques ou quasi-statiques. La dynamique pourrait être introduite en tenant compte de la mécanique statistique hors équilibre et, en particulier, des méthodologies de Langevin et/ou de Fokker-Planck. Ces deux questions seront abordées dans les développements futurs.

Dans le dernier chapitre, nous avons finalement proposé et étudié deux modèles prototypiques capables de décrire les effets de la température dans les processus de rupture. Le premier vise à expliquer le comportement des systèmes fragiles en fonction de la température, et le second vise à montrer les processus d'endommagement complexes qui se produisent en présence de liens ductiles cassables avec une possibilité de transition fragile-ductile régulée par les effets thermiques. Les deux modèles sont basés sur une structure en treillis simple constituée de ressorts incassables et cassables. Le système est confiné entre deux couches, l'une fixe et l'autre mobile, et est conçu de telle sorte que le soulèvement de la couche supérieure entraîne une force subie par le système, capable de générer une propagation de la fracture. Cette structure est censée être intégrée dans un bain thermique à température fixe. Les modèles sont donc développés dans le cadre du formalisme de la mécanique statistique à l'équilibre. La différence entre les deux modèles réside dans le comportement à la rupture des ressorts cassants. Dans le premier modèle de rupture fragile, chaque ressort cassant peut se trouver dans deux états, à savoir élastique ou cassé, en fonction de l'extension appliquée à l'élément lui-même. La transition d'état se produit par l'absorption d'une quantité d'énergie qui correspond à l'énergie de surface typique du critère de Griffith [119]. Dans le second modèle, chaque ressort cassant peut se trouver dans trois états différents représentant les régimes élastique, ramolli et cassé. L'état intermédiaire ramolli est introduit pour reproduire

l'éventuel régime ductile du processus de rupture. Dans ce cas, nous avons un point de "résistance" entre les régimes élastique et ductile, suivi d'un point de défaillance final correspondant à la rupture. La transition entre l'état intact et l'état ramolli se produit après l'absorption de l'énergie de déformation, et la transition entre l'état ramolli et l'état rompu se produit par l'absorption d'une autre quantité d'énergie correspondant à la rupture. Ainsi, dans les deux modèles, le bilan énergétique est similaire à ce qui est généralement supposé dans la mécanique linéaire des fractures élastiques depuis les travaux pionniers de Griffith et Irwin [119–121], le phénomène de fracture étant régi par l'énergie élastique, l'énergie d'endommagement et l'énergie de fracture (surface). Cependant, l'inclusion des fluctuations thermiques modifie sensiblement les résultats et ajoute des caractéristiques importantes à la description du système. En ce qui concerne le modèle de rupture fragile, nous obtenons une contrainte de rupture dépendant de la température et une déformation de rupture correspondante, représentant une transition de phase "authentique". Nous obtenons ainsi une température critique à laquelle la contrainte et la déformation de rupture sont toutes deux nulles et, par conséquent, le matériau est toujours cassé pour les températures supercritiques. Il est intéressant de noter que la résistance obtenue en fonction de la température est en bon accord avec plusieurs expériences et simulations de dynamique moléculaire, comme cela a été démontré précédemment. Il est intéressant de noter que, bien que les ressorts cassables aient un comportement de rupture indépendant de la température, le système global présente un point de rupture qui dépend fortement de la température. Il s'agit d'un cas typique de système complexe avec un comportement collectif, donnant lieu à un phénomène critique. Nous soutenons que cet effet est pertinent dans le cas de liens faibles, tels que les liaisons hydrogène dans les matériaux biologiques, ou dans le caoutchouc, où l'élasticité a un caractère entropique, ou dans les systèmes métalliques ou semi-conducteurs de petite taille, tels que les nanofils considérés [122–133]. Le modèle avec des éléments cassables ductiles présente un comportement encore plus riche. Dans ce cas, c'est la réponse complète du système qui dépend de la température. En effet, nous avons démontré l'existence d'une température de transition fragile-ductile T^* (dont l'expression est obtenue en forme fermée) qui régule le comportement du processus de rupture. D'une part, pour des températures inférieures à T^*, on observe un comportement fragile caractérisé par une transition directe des ressorts de l'état élastique à l'état cassé, sans passer par l'état ramolli intermédiaire. En revanche, pour des températures supérieures à T^*, nous constatons que, lorsque l'extension appliquée au système augmente, les ressorts s'assouplissent d'abord (limite d'élasticité), puis passent de l'état assoupli à l'état cassé (limite de rupture). La région intermédiaire ramollie reproduit dans ce contexte discret la zone cohésive du modèle classique de Dugdale-Barenblatt de la fracture ductile [134, 135]. Bien entendu, les points de rupture et d'affaiblissement dépendent tous deux de la température et sont à nouveau caractérisés par des transitions de phase. En fait, nous sommes non seulement capables de calculer la température de transition fragile-ductile, mais aussi de prédire le comportement critique des limites d'élasticité supérieure et inférieure, ainsi que les propriétés thermiques de la résistance à la rupture. Notre modèle est également capable de prédire l'existence d'un régime de rupture particulier, appelé ici sur-ductile, dans lequel la température est suffisamment élevée pour endommager tous les éléments sans action mécanique. Dans cette situation, lorsque l'extension du système augmente, nous observons la seule transition entre le régime ramolli et le régime rompu. D'un point de vue méthodologique, pour élaborer l'expression en forme fermée de la fonction de partition dans les deux modèles proposés, nous avons adopté des techniques spécifiques particulièrement adaptées au calcul du déterminant et de l'inverse des matrices tridiagonales [96, 97]. Nous soulignons que même si les modèles présentés ici clarifient les aspects fondamentaux des phénomènes de rupture thermiquement activés, ils doivent être généralisés pour prendre en compte la réalité complexe de ces processus. Nous souhaitons mentionner ici au moins quatre points qui limitent partiellement l'applicabilité de ces modèles aux situations réelles. Le premier point concerne l'homogénéité spatiale des modèles

adoptés. Nous avons toujours considéré que tous les ressorts des systèmes discrets avaient le même comportement mécanique (en termes de constantes élastiques, de seuils de rupture, etc.) En réalité, ceci n'est vrai que pour des structures monocristallines parfaites qui sont assez rares. Il serait intéressant d'étudier ces phénomènes dans des systèmes désordonnés qui, d'une part, sont plus proches de plusieurs structures réelles, et d'autre part, peuvent générer des comportements critiques encore plus intéressants, typiques des systèmes complexes avec un désordre atténué [136–147]. Le deuxième point à explorer est la cinétique des processus de rupture. Nous n'avons considéré ici que des phénomènes quasi-statiques étudiés au moyen de la mécanique statistique de l'équilibre. Dans les expériences réelles, la traction peut être appliquée à différentes vitesses de traction, et la réponse dépend évidemment de ces taux de traction [148, 149]. Pour modéliser ces phénomènes, il faudrait adopter la mécanique statistique hors équilibre, puis baser l'analyse sur les méthodologies de Langevin ou de Fokker-Planck [100, 101, 150, 151]. En conclusion, le troisième point à améliorer concerne le fait que le processus d'adoucissement se limite à une seule étape de réduction de la constante élastique des ressorts cassants. Afin de mieux coller à la réalité physique du processus d'assouplissement, il faudrait imaginer une série d'étapes où plusieurs réductions de la constante élastique ont lieu progressivement. En ce sens, la limite d'élasticité serait mise en œuvre par le biais d'un processus de ramollissement multiple, plus proche de ce qui se passe dans les matériaux non linéaires réels. Le quatrième et dernier point concerne la géométrie trop simple de notre modèle, qui devrait être améliorée (avec des treillis 2D ou 3D) afin de pouvoir représenter des champs élastiques réels à comparer avec les modèles de la mécanique des milieux continus.

Table of contents

Chapter 1

Introduction

Micro-instabilities play a key role in various mechanical systems, both artificial and biological. In the case of artificial systems, examples of these instabilities can include the peeling of a film from a substrate [4–10], the wave propagation in bistable lattices [11–15], the energy harvesting through multistable chains [16–18], the plasticity and the hysteresis in phase transitions and martensitic transformations of solids [19–29], as well as the nucleation and propagation of cracks and dislocations in materials and alloys [30–38], and the friction at the nanoscale [39–48]. On the other hand, in the case of biological systems, micro-instabilities manifest in the form of conformational transitions in polymeric and biopolymeric chains [49–58], the switch between the attached and detached states of fibrils in cell adhesion [59–64], the unzipping of macromolecular hairpins [65–69], the sarcomeres behavior in skeletal muscles [70–76], the degradation or denaturation of nucleic acids, polypeptide chains, and other polymers [77–86], as well as the friction of macromolecules or soft matter [87–90]. Furthermore, it is also noteworthy to mention that friction is also essential for the understanding of the evolution of geophysical systems [152–155] and plastic phenomena in solid materials since it can regulate the nucleation of dislocations and fractures and control the shear transformations and the ductile-to-brittle failure transition [156–161].

In all these physical situations, the system always presents a complex energy landscape characterized by a multitude of basins, and, depending on which particular basin it lies in from an energetic point of view, the system can be either in a stable or meta-stable configuration. We point out that these systems are constituted of a large number of units that, taken individually, present well-defined physical states, but, considered as a whole, present a rather non-linear and chaotic behavior difficult to describe at first. The transitions between these states or, equivalently, the explorations of the complex energy landscape, govern the macroscopic behavior of the whole system and, in particular, its static and dynamic features. Microinstabilities can be divided into two main classes. In one type, the intrinsic micro-instabilities may describe bistable (or multi-stable) units with transitions between one ground state and one (or more) metastable state(s) (*e.g.* for the conformational folded-to-unfolded transitions in macromolecules or martensitic phase changes in metallic alloys or also friction). These states represent different, yet mechanically resistant conformations. This case can be represented in a one-dimensional setting by introducing an effective double-well potential energy U, as shown in Fig.1.1 (top-left panel). We observe that the choice of a simple one-dimensional system is aimed at a simple presentation of the idea. In other words, in this case, x is a variable that perfectly represents an effective order parameter adopted to describe the transition between the different wells, whereas all other variables can be considered to be minimized. In the second class, the micro-instabilities can describe transitions

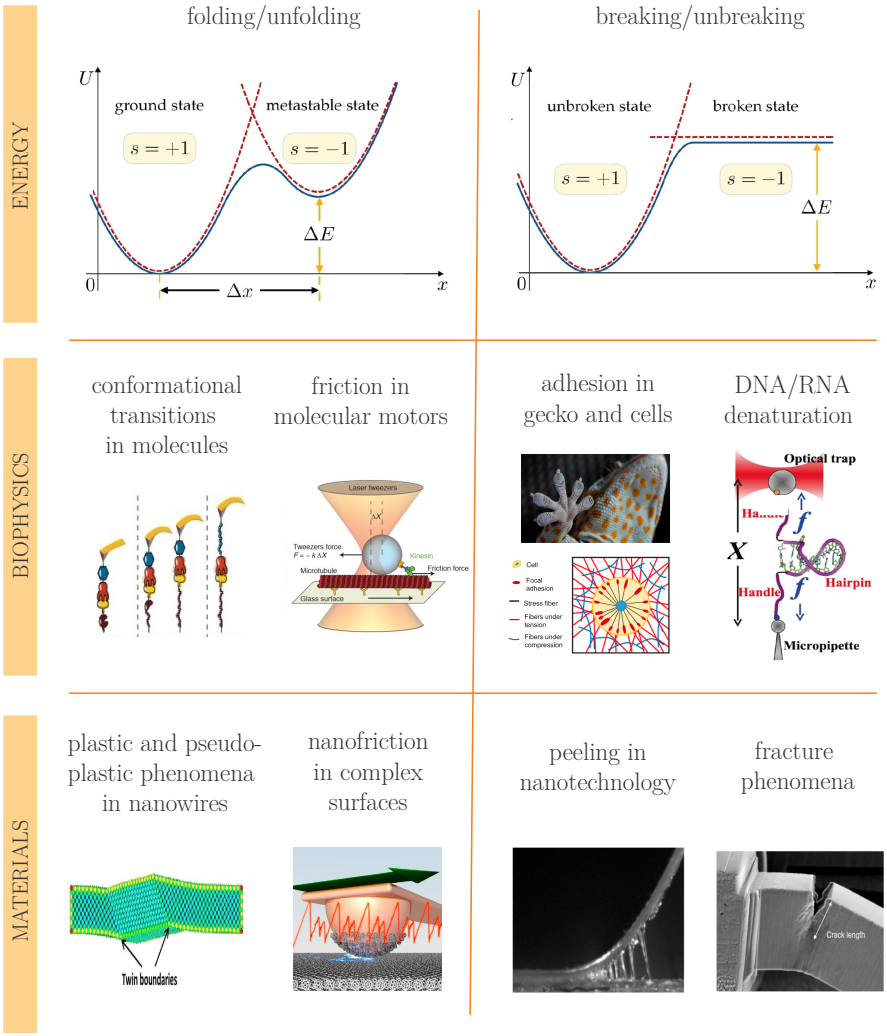

Figure 1.1: In the first row one can find two different energy landscapes representing two classes of micro-instabilities: bistability between a folded (ground) state and an unfolded (metastable) state in the left panel, and transition between attached (unbroken) and detached (broken) states in the right panel. In the second and third rows, one finds some examples of microinstabilities in biophysics and materials science, corresponding to conformational transitions (bistability or multistability) in the first column, or rupture phenomena (deadhesion and decohesion) in the second one.

between unbroken and broken states of the breakable units of the system (*e.g.* in the unzipping of hairpins, denaturation of macromolecules, fibrillar biological adhesion, peeling of films, cracks propagation, and so on). This process can be reversible, partly reversible, or irreversible according to the specific physical phenomenon. The one-dimensional energy landscape considered in this second case is shown in Fig.1.1 (top-right panel). Here, the unbroken configuration corresponds to a potential well and the broken configuration corresponds to constant energy and zero force.

In the second and third rows of Fig.1.1, one can find the most of previously mentioned examples following the classification between folding/unfolding or breaking/unbreaking energies (see the first row of the image). The different situations have been further subdivided between biophysics (second row) and materials science (third row), for the sake of clarity. It is interesting to note that there is a parallel between all the problems in biophysics and materials science. This similarity is at the basis of the development of mathematical models that are applicable indistinctly to both areas of research, as discussed in the following. In fact, the main goal of this thesis is to develop models between physics and mechanics that are able to study state transitions (micro-instabilities) in all these biological and artificial systems in order to better understand the effects of temperature and external mechanical actions on their behavior.

Since the characteristic length that separates two different states Δx is of the order of units of nanometers and the energies involved in chemical bonds are of the order of tens of $K_B T$, it is crucial to observe that the effects of the temperature on these systems is non-negligible. As a matter of fact, the transitions between the states in all previous systems are strongly influenced by thermal fluctuations, which can modify the probability of being in a given state or the passage rate between the neighboring energy wells. This is the reason why the correct framework in which we can develop the theoretical modeling of these phenomena is within classical statistical mechanics. In particular, the systems exhibiting switching mechanisms between different energy basins can be studied by means of the spin variables approach which will be described more in detail in the following discussion. For now, we just mention that the spin approach is based on the introduction of a series of discrete variables (similar to the spins used to deal with magnetic systems), which are able to identify the state associated with a given system unit (see the variable S in Fig.1.1, first row). For example, the bistable potential energy of Fig.1.1 (first panel) (continuous line) can be approximated by a bi-parabolic function (dashed lines) with the switching among the wells described by the spin variable. It means that, depending on the value of these discrete variables, the energy function may change its shape and, in particular, the position and the depth of its wells.

The first theoretical approaches based on this method have been developed to model the biomechanical response of skeletal muscles [70, 71]. Since these pioneering investigations, this technique has been generalized to study different multi-stable systems including the folding of macromolecules [91, 92, 94, 95, 102, 103, 162–164], the adhesion/deadhesion processes [1, 93], the phase transformations in solids [2, 165] and the stick-slip on rigid substrate [166]. The introduction of the spin variables frequently simplifies the calculation of the partition function and, consequently, the analysis of the corresponding averaged thermodynamic quantities. This theoretical device is able to give mathematical results in closed form, very useful to advance the understanding of the underlying mechanics and physics. It is important to remark that, as discussed in detail in Ref.[91], the evaluation of the partition function based on the spin approach assumes that for both configurations all possible deformations (values of x in Fig.1.1, first row) can be attained by the system. This corresponds to the assumption of a multivalued energy function (see the superposition of dashed lines in Fig.1.1, first row). As shown numerically in Ref.[91], with typical experimental temperatures, the effect of this approximation can be considered (statistically) negligible since these artificial configurations (superposition of dashed curves) have an energy sensibly higher than real configurations (continuous lines). This technique

has been largely exploited to investigate bistable systems from biophysics and materials science, as mentioned above.

The stretching of macromolecular chain or, more in general, the mechanical perturbation of small systems, can be typically performed following two different experimental protocols [91–93]. In particular, experiments performed at constant applied forces (realized through extremely soft devices) correspond to the Gibbs statistical ensemble, and experiments performed at prescribed displacements (conducted with extremely hard devices) are a realization of the Helmholtz statistical ensemble. In general, these two boundary conditions lead to different force-extension responses since, in each of the two cases we explore a different phase space. Actually, depending on the equivalent stiffness of the device, the stretching experiment corresponds to a situation placed in between the Gibbs and Helmholtz ensembles of the statistical mechanics [94, 95].

The introduction of different boundary conditions leads to the notion of thermodynamic limit. In particular, it is possible to prove under precise hypotheses that the two different experimental strategies give the same results in terms of the force-extension curve when the number of units is large enough (thermodynamic limit) [56, 98, 108–112, 167]. Therefore, it is important to remark that the differences between the force–extension curves measured under Gibbs or Helmholtz conditions can be noticed only for a moderately small number of domains of the chain under consideration (small systems thermodynamics). Indeed, for a large number of domains, *i.e.* in the thermodynamic limits, the different Gibbs and Helmholtz statistical ensembles are equivalent and they are described by the same constitutive force–extension response [56, 98, 108–112, 167]. However, it is important to mention the fact that in some cases the ensemble equivalence is not verified and we can have different macroscopic responses of the system in the thermodynamic limit too [113–118].

1.1 Force-spectroscopy methods and micromechanical testing

Since their development and introduction in research, micro and nano force-spectroscopy methods and micromechanical testing devices have revolutionized our understanding and manipulation of matter at the smallest scales and enabled us to probe and characterize the mechanical properties and interactions between materials and objects on the micro and nanoscale. By applying controlled forces and measuring the corresponding responses, in fact, it is possible to obtain valuable insights into the behavior of materials, investigate surface interactions, and explore the fundamental forces governing the micro and nano physical world. These methods leverage advances in nanotechnology, scanning probe microscopy, and precision instrumentation to achieve exceptional resolution and sensitivity in force measurements in order to investigate mechanical properties at the nano and microscale for a vast variety of physical phenomena such as adhesion/decohesion processes, phase transformation, fracture, and crack propagation.

Usually, for biological systems, the different three-dimensional conformations of various macromolecules, such as nucleic acids, polysaccharides, and proteins, can strongly affect their biological functions, and, therefore, it is essential to study the possible rearrangements induced by external factors, such as the entropic, the purely mechanical, or the chemical ones. For example, the correlation between proteins' structure and function is entirely determined by their tertiary structure. Depending on the particular action applied to the proteins, their configuration can be modified, leading to drastic changes in their chemical and/or physical properties, ultimately resulting in the loss of their biological purpose. For instance, the capacity of these macromolecules to keep their spatial configuration stable against mechanical factors must be tested to evaluate their ability to preserve their original biological behavior. Indeed, if a macromolecule is pulled with a large force, it can lose or change its biological function since the force reduces the structural

stability and induces rearrangements. Examples of these phenomena can be the loss of catalytic capacity for an enzyme or the inability of an antibody to bind to an antigen. Thus, mechanical actions on biological macromolecules can cause changes in their functions, with significant physiological consequences. Studying the link between the three-dimensional conformation of a macromolecule and its function can be directly done by using force spectroscopy methods, which for example can be applied to unfold, through mechanical stretching, the native folded structure of a macromolecule. The controlled unfolding leads to the estimate of the involved forces (it is indeed possible to measure the force-extension relation), the energy landscape, and many other dynamic properties of the system under investigation. We remark that the energy landscape of most biological macromolecules shows a multi-stable shape, characterized by several metastable states corresponding to different conformations. Therefore, the paths the system follows to switch among these local minimums are specified by characteristic times that depend on the energy barriers between the states and the external actions applied to the system. The mechanical experiments on single-molecule are extremely useful to study intra- and inter-molecular forces and to obtain information about the thermodynamics and kinetics of several molecular processes. Different force spectroscopy techniques allow the investigation of these macromolecular features. Single-molecule experiments are indeed based on laser optical tweezers (LOT), magnetic tweezers (MT), atomic force microscopes (AFM), and micro-electro-mechanical systems (MEMS) [168–173].

On the other hand, different force spectroscopy techniques such as the micropipette aspiration and the tensile test are employed to study macromolecules' attachment/detachment behavior on a substrate or the fracture or crack propagation and nucleation in nanowires and other various artificial micro and nanosystems. The need for a different type of experimental methodology, in the latter cases, arises from the fact that the forces needed to start, for instance, the detachment of a macromolecule or a cell from a substrate or the nucleation of a crack in a nanowire, are much higher and, therefore, cannot be studied with the same single-molecule force-spectroscopy techniques described for the biological case. In any case, all these approaches are important not only for probing the response of a single macromolecule but also for testing the validity of thermodynamics and statistical mechanics at the scale of atoms and molecules. In the following discussion, we describe briefly some of the most useful techniques used to investigate micro and nanoscale systems.

1.1.1 Optical tweezers

Optical tweezers are devices able to exploit one or more focused laser beams to hold and move micro- or nano-particles or beads (Fig.1.2.a). The first detection of forces on micro-particles was performed by Arthur Ashkin in 1970, paving the way for the use of this new technology [176, 177]. Several years later, Ashkin and colleagues developed real single-beam gradient force traps, able to control the position of microscopic particles in the three-dimensional space [178]. In 2018, Ashkin was awarded the Nobel Prize in Physics for introducing these devices, which were eventually used to manipulate atoms, molecules, and biological structures. This technique is able to generate an actual energy well in the three-dimensional space inducing a force applied to the particle proportional to the displacement from the equilibrium position pinpointed by the well. Hence, the optical tweezers act like a linear spring [174]. These devices are able to apply forces in the range 0.1-100 pN with an intrinsic stiffness of 0.01-1 pN/nm and to measure the particle position with sub-nanometer resolution. Because of the rather limited force range, they have been mainly used in experiments on DNA and RNA but also with proteins or other molecules. However, the high-intensity laser used for this optical trapping generates local heating, causing degradation or denaturation of biological structures and an alteration of the viscosity of the solution. A comprehensive tutorial on laser optical tweezers can be found in the literature [179].

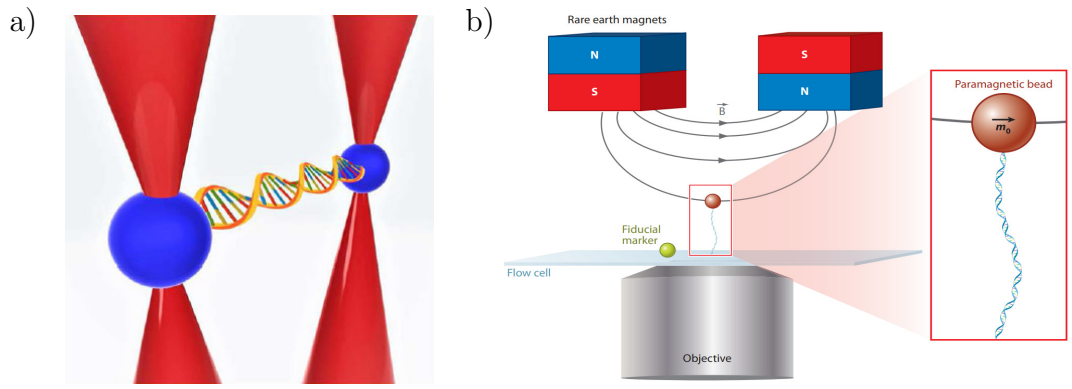

Figure 1.2: Panel a) scheme of a dual-trap optical tweezers configuration. Two focused laser beams are used to create two independent optical traps, which actuate two beads trapped at the focal points. The distance between the beads can be varied arbitrarily, thus exerting a mechanical force on the molecule tethered between them. The figure is reproduced from Ref.[174]. Panel b) basic setup of magnetic tweezers. A molecule is anchored between the surface of a container and a tiny, paramagnetic bead. When a pair of magnets generate a magnetic field, the bead becomes magnetized and develops a magnetic moment $\vec{\boldsymbol{m}}_{\mathbf{0}}$. As a result, the bead experiences a force proportional to the field gradient. By rotating the external magnet, the molecule can be coiled or twisted in various ways. The figure is reproduced from Ref.[175].

1.1.2 Magnetic tweezers

The second force-spectroscopy technique we mention is based on magnetic tweezers, which use magnets or electromagnets to create a magnetic field gradient able to generate a force acting on a paramagnetic bead (Fig.1.2.b). The force is applied in the direction of the field gradient. Typically, the investigated macromolecule is attached to the bead and it is therefore stretched. The second end-terminal of the molecule is tethered to the base or substrate, where the experiment is performed. The position of the magnets and their velocity are controlled in order to apply the desired molecular unfolding. The real-time detection of the bead position is realized with an optical system and a CCD camera. From the historical point of view, Francis Crick and Arthur Hughes first introduced a method based on magnetic particles to measure the physical properties of the cytoplasm in 1955 [180]. This technique was later improved with the idea of studying the rheology of the cell [181, 182]. Only in the 90s, this methodology has been applied to single molecules and, in particular, to study the elasticity of DNA [183, 184]. In modern magnetic devices, the force applied can reach the value of 200 pN and the magnetic trap stiffness is very low (around 10^{-4} pN/nm). The damage by heating and photodamage in biological structures is considerably reduced with magnetic tweezers based on permanent magnets. However, in some setups with electromagnets, high electric current may generate a large amount of heat, which requires the use of cooling systems. Importantly, magnetic tweezers, in addition to applying a longitudinal pull on the macromolecule, can be used to generate a chain twist. This is useful for studying conformational transitions induced by twist mechanisms. In addition, magnetic tweezers have the advantage of being able to really exert a constant force while in atomic force microscopes and optical tweezers, the constant-force mode can be achieved only by feedback-control systems, which are quite complex.

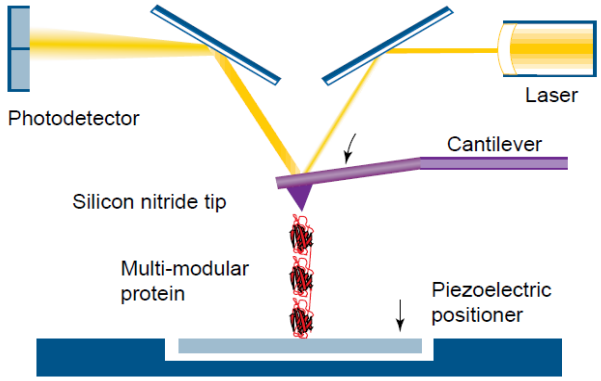

Figure 1.3: Schematic diagram of an atomic force microscope (AFM). When pressed against a layer of protein attached to a substrate, the silicon nitride tip can adsorb a single protein molecule. The extension of a molecule by retraction of the piezoelectric positioner results in the deflection of the ARM cantilever. This deflection changes the angle of reflection of a laser beam striking the cantilever, which is measured as the change in output from a photodetector. Image edited from [185].

1.1.3 Atomic force microscope

The force-spectroscopy based on the atomic force microscope is a well-established technique for studying strong covalent bonds and stiff intermolecular and intramolecular interactions. The original AFM is a device useful to investigate the morphological features of a material surface, capable of reaching an atomic resolution. This is typically done by monitoring the force between the surface under study and the tip of a silicon (or silicon nitride) cantilever. The position of the tip is measured by observing the deflection of the cantilever through a standard optical method (see Fig.1.3). A piezoelectric system allows the scanning of the whole surface, eventually producing an image corresponding to the topographical structure of the surface. This classical atomic force microscope has been invented in 1985 by Gerd Binnig, Calvin Quate and Christoph Gerber and commercialized for the first time in 1989 [186]. The AFM technique has been further generalized in order to apply force on a single molecule and to measure force-extension curves of macromolecules. In this application, the chain is stretched between the tip of the cantilever and the substrate with forces ranging in the interval 10-20 nN, with stiffness values of 10-10000 pN/nm. The spatial resolution is around 0.2 nm. These data allow us to state that this method is useful for large macromolecules such as proteins. While the classical pulling speeds used in single-molecule experiments vary in the range of a few nm/s to about 10 μm/s, the recently introduced high-speed AFM (HS-AFM) allowed to reach pulling speeds of the order of 4000 μm/s [187–190]. This is a significant development since it permits to compare results of experiments with those obtained by molecular dynamics simulations, which offer atomic-level descriptions of the forced unfolding within the out-of-equilibrium statistical mechanics [191, 192].

1.1.4 MEMS devices

The last class of devices used to perform single-molecule experiments is represented by the micro-electro-mechanical systems or MEMS devices. The development of MEMS devices started in

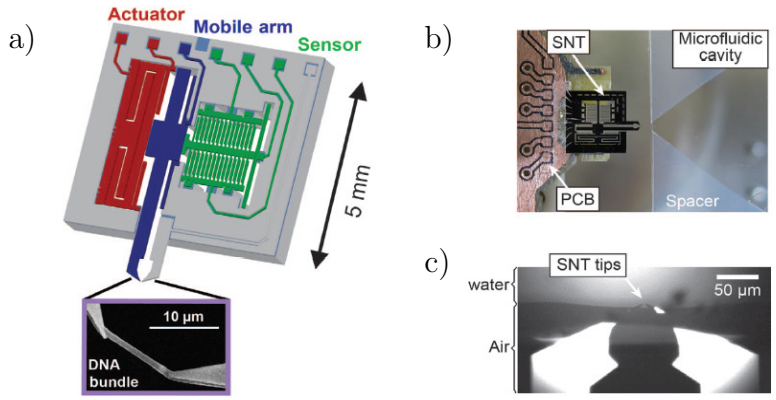

Figure 1.4: Example of a MEMS device. a) Scheme of silicon nanotweezers (SNT) for the DNA mechanical characterization in liquid where the displacement is provided by comb-drive actuators and measured by a differential capacity sensor. Opposing tips are used for handling biomolecules, for example, DNA molecules as shown in the inset picture. b) Top view of the SNT aligned to insert the tips into the cavity where DNA molecules are floating in a liquid medium. c) Tips of the SNT inside the liquid. Image edited from Ref.[84].

the 60s by means of the same technologies used for microelectronics. In fact, they are often based on silicon substrates suitably adapted and enriched with various components [193]. In general, they are based on the combination of microelectronic systems with partially mobile mechanical systems. The moving components can be plates useful to change the capacitance of the structure or electrostatically controlled cantilevers. Typically, these systems are used to obtain sensors and captors of several physical quantities. MEMS for biological or biomedical applications are named Bio-MEMS and may integrate micro-fluidic chambers, biosensors, microarrays, microelectrodes, or microreactors [194]. As mentioned before, force spectroscopy techniques, based on optical or magnetic tweezers and AFM are able to make precise measurements at the single-molecule level, however, their implementation and use are quite complex and therefore they cannot be adopted for intensive and systematic biosensing. In this context, the application of MEMS devices is more suitable. For instance, a micromachined DNA manipulation MEMS platform has been developed to stretch and rotate a single DNA molecule [195]. This device exploits the combination of micromachined magnetic tweezers and microfluidic channels. Another example concerns a new hybrid field microfluidics approach, employing both hydrodynamic forces and an electric field to regulate the DNA initial conformations [196]. Moreover, micro-electro-mechanical systems have been developed for monitoring bio/chemical interactions of biomacromolecules, by controlling their mechanical properties [197]. To conclude, a specific MEMS device shown in Fig.1.4, referred to as silicon nanotweezers (SNT), has been introduced to mechanically characterize a DNA bundle exposed to ionizing radiations, delivered by a therapeutic linear particle accelerator (LINAC) [84, 85, 198]. The radiation induces a mechanical degradation *i.e.* a population of breaks in a DNA bundle, which can be quantified by measuring the elastic properties of the bundle itself [199, 200]. Hence, one could provide a direct relationship between radiation dose and its damaging effects. The real-time observation of DNA degradation under ionizing radiation is useful for developing better techniques for the treatment of tumors.

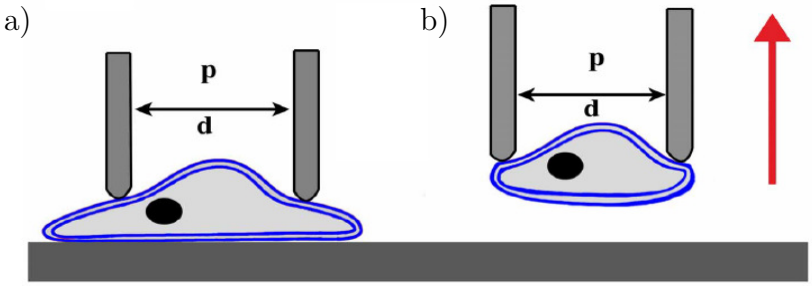

Figure 1.5: Scheme of an adhesion force measurement on an individual cell. It consists in placing the tip of a micropipette (usually with a diameter of a few micrometers) over the cell attached to a treated substrate and applying a suction pressure p corresponding to forces of the order of units of μN. The force is applied for a few instants and, if the cell remains attached to the substrate, this process is repeated increasing the applied suction force until the cell is eventually detached. Image edited from Ref.[201].

1.1.5 Micropipette

The micropipette technique relies on the suction/aspiration of a cell by the application of precise and sensitive negative pressure from a pressure-based controller. In this process, the cell is first immobilized on the tip of a micropipette and suction is applied to draw the cell inside the micropipette chamber. Usually, to quantify the distance traveled by the pipetted portion of a cell through the micropipette tube, the cell's position can be tracked using a microscope. This behavior is predicted by a lumped parameter model which represents the cell as a combination of springs and dashpots (thereby modeling stiffness and viscosity, respectively) [202]. The deformation displayed by cells undergoing micropipette aspiration shows a linearly elastic response as a result of its stiffness, and a creep response due to its viscous behavior. This response, in biological systems, for example, is unique to different types of cells (*e.g.* white blood cells measure lower stiffness than chondrocytes). This difference in cell stiffness affects the way in which cells interact with one another and the way they are affected by their immediate environment. Micropipette aspiration, then, is a very versatile technique that allows stiffness to be quantified across many different cell types. Being able to quantify the mechanical properties of cells is a useful tool for the study and diagnosis of different pathologies. Micropipette manipulation is often preferred over traditional techniques because of the fragile and very small nature of the individual cells under investigation. Furthermore, non-invasive micropipette aspiration allows repetitive measurements on the same sample so that variations in cell tension of individual cells within a tissue can be monitored over time. This method is also a powerful tool to trace the spatiotemporal map of tensions inducing morphogenesis [203]. Some of the many interesting aspects of adopting this technique are the cost accessibility, the easiness of usage, and the ease with which one can design experiments involving micropipettes especially because of their compact dimensions (that can usually fit into different microscopes) and the possibility to be employed in automated tasks thanks to modern control software. This technique is also widely used to study nuclear mechanics and provide important information on the viscoelastic behavior of the nucleus over different time scales and that is why it is a tool that has been widely used to study many biophysic phenomena, including the mechanical properties of the nucleus, the exclusion of nucleoplasm from chromatin, chromatin stretching, and to study the detachment/attachment forces found in the cell-substrate adhesion [202].

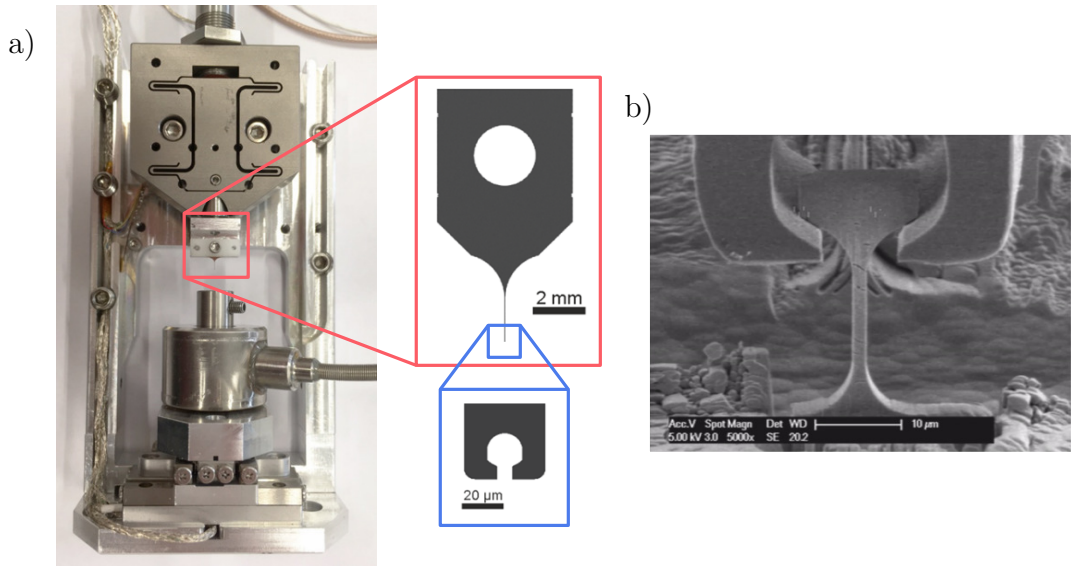

Figure 1.6: a) Detail of the tensile gripper design. b) Example of nanocrystalline Ni tensile dog-bone sample. Image edited from Ref. [204].

1.1.6 Small scale tensile testing

Tensile testing is a fundamental mechanical testing technique capable of evaluating the behavior of materials under tension. It involves subjecting a sample to an applied load along its axis, resulting in the elongation of the material until its failure point threshold. While tensile testing is commonly performed on macroscopic samples, its recent microscopic application opened new possibilities for exploring the mechanical properties of microstructures, including nanowires. This technique provides valuable insights into the mechanical behavior of materials at the smallest scale, enabling the understanding of the unique properties exhibited by microstructures. The first step in conducting tensile testing on microscopic samples is the preparation of the specimen, and, in the case of nanowires, this typically involves the fabrication of individual wires using techniques such as chemical vapor deposition, electrochemical deposition, or lithography. Furthermore, special care must be taken to ensure the nanowires are free from contaminants and defects that, at a such small scale, could easily affect their mechanical behavior. Once the nanowire specimen is crafted, it is attached to a suitable apparatus for testing. Manipulating and securing such small samples requires specialized techniques and tools such as nanomanipulation systems equipped with nanoscale grippers that allow for the accurate handling and alignment of the nanowire within the testing apparatus. One common approach involves using a microscale probe or an atomic force microscope (AFM) tip to exert a controlled force on the nanowire. This allows measuring the force and displacement simultaneously, providing real-time data on the mechanical response of the nanowire. During the tensile testing process, the nanowire is gradually stretched until it reaches failure and its deformation behavior can be captured using high-resolution imaging techniques, such as electron microscopy, which enable the observation of the nanowire's structure and any deformation mechanisms occurring during the test. The data can then be confronted with molecular dynamics simulations or finite element analysis, thus providing detailed information about stress distribution, strain localization, and atomistic-level interactions occurring within the nanowire.

1.2 Applications

The study of micro-instabilities can span many different fields of research that, at first glance, may not appear related to each other. Micro-instabilities, in fact, are a type of phenomena that occur at the micro and nanoscale in a multitude of cases: we can observe them in phase transformation processes that can affect macromolecules, in biology, or nanowires, in material science, in the adhesion and deadhesion of cells from an organic substrate as well as in the attachment of gecko's paws on a flat artificial surface to cite few. In fracture mechanics, furthermore, microinstabilities play a crucial role in the mechanical behavior of crack propagation both in biological and artificial systems. Of course, the behavior and nature of these systems are very different while being considered from a macroscopic point of view but, as soon as we zoom in at the nano and microscale, we can observe many similarities, especially from an energetic point of view. At the microscopic scale, in fact, the macroscopic system can be subdivided modularly into microsystems that present a more simple energy landscape that dictates the overall behavior of the specific phenomena considered. Because of the particular scale of the systems considered in these examples, the temperature must be taken into consideration. This is why statistical mechanics is the perfect framework to address these problems.

In the following, we briefly describe some examples of microinstabilities in different domains of research.

1.2.1 Phase transformations in macromolecules

Phase transformations occur when a system undergoes a structural change, resulting in a distinct arrangement of atoms and a corresponding alteration in its properties. Usually, these transformations can be driven by factors such as temperature, pressure, or composition variations. Understanding phase transformations is of essential importance in both material science as well as in biology, as they often lead to the emergence of unique properties and functionalities. One of the main examples in biology, where a phase transformation may occur, is the DNA structure. DNA in fact, like many other macromolecules, is susceptible to phase transformation that can occur depending on the force applied, chemical reactions, or simply the thermal agitation of the nearby ambient. Before understanding how these phenomena impact the functionality of these macromolecules, we briefly describe here some of the main models still used in research to understand the behavior of these microscopic systems.

While the structure of DNA was first elucidated in 1953 by Watson and Crick [205], who obtained the Nobel Prize in Physiology or Medicine 1962, its mechanical behavior has been tested by magnetic tweezers force spectroscopy only in 1992 [183], eventually obtaining the force-extension relation. These results, for individual DNA molecules, were obtained at three different salt concentrations and with forces in the range from 10^{-14} to 10^{-11} N [183]. These experimental achievements have been completely understood from the theoretical point of view by means of the statistical mechanic thanks to the works of Marko and Siggia [206, 207]. They proved that the DNA mechanics is well reproduced by the worm-like chain (WLC) model rather than by the freely-jointed chain (FJC) model. The ideal FJC model schematizes the macromolecule as a sequence of N non-deformable segments of length b (referred to as Kuhn length). The contour length L_C is the total length of the macromolecule at the maximum physically possible extension and then we have $L_C = Nb$ for a chain with N units. The FJC model does not take physical interactions among segments into account. Hence, there is no preferred angle between two adjacent segments. This model is useful to describe simple polymer chains but is not adapted for the DNA. Differently, the WLC model perfectly mimics double-stranded DNA, in the first entropic region of the force-extension curve [206, 207]. In the ideal FJC model, no forces are

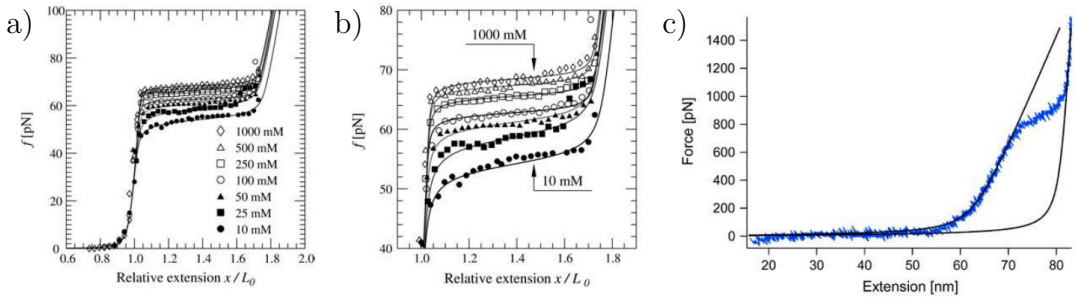

Figure 1.7: Panel (a): room temperature force-extension curves for a single dsDNA molecule in different salt concentrations. The solid lines correspond to theoretical curves calculated using the global coupling theory developed by [208]. Experimental data are taken from [209]. Panel (b): zoom in on the overstretching portion of panel (a). Panels (a) and (b) are reproduced with permission from [208]. Panel (c): force-extension curve (blue) from one dextran molecule obtained through AFM force spectroscopy and its fit in the low-force (before the transition) and high-force (after the transition) regime obtained by the extensible FJC model (reproduced with permission from [210]).

necessary to fold or bend the chain. On the contrary, in the WLC model, a cost in energy, depending on the angles between adjacent segments, is introduced. More precisely, the energy is set to zero if all segments are aligned and therefore a force can be applied to fold or bend the chain. This property is taken into consideration by means of a new parameter called persistence length p, which is defined by the ratio between the mechanical flexibility or bending stiffness and the energy of thermal fluctuations. Hence, it takes into account the balance between enthalpic and entropic contributions [206]. From the physical point of view, the persistence length p can be defined as the length over which correlations in the direction of the tangent are lost. The DNA used in the first force spectroscopy experiment corresponds to a contour length $L_C = 32.8$ μm and a persistence length $p = 53.4$ nm [206, 207].

Refined experiments have been realized on DNA with magnetic torque tweezers in order to measure the effective torsional stiffness as a function of the applied force [211, 212]. More recently, an alternative, more refined, WLC model was proposed to correctly take account of both bending and torsional stiffness by adding a coupling term between twist and bend deformations [213, 214]. In further investigations, the DNA molecule has been pulled with larger forces and an intriguing overstretching phenomenon has been observed [215]. In particular, a force plateau at around 65 pN has been measured in the force-extension curve [215]. In Fig.1.7.a) and b), we show recent results proving the dependence of the plateau on the salt concentration. Here, the theoretical results are taken from [208] whereas the experimental ones from [209]. The overstretching behavior can be interpreted by means of a bistability of the DNA chain structure. However, the real molecular origin of this transition has been largely investigated and a debate exists on the DNA conformation after the overstretching: many researchers think that there is a simple mechanical denaturation leading to a transformation of the double-stranded DNA into two single-stranded DNA [216, 217]. However, other researchers have proposed the existence of a new DNA conformation (called S-DNA or stretched DNA), which is an intermediate structure between the double-stranded DNA and its denatured structure [218]. Finally, other researchers thought that melting or S-DNA was depending on the composition of amino acids of the chain [219]. Furthermore, in recent results, a discrete worm-like chain model has been implemented to describe the DNA stretching under force and to investigate dsDNA to ssDNA and dsDNA to

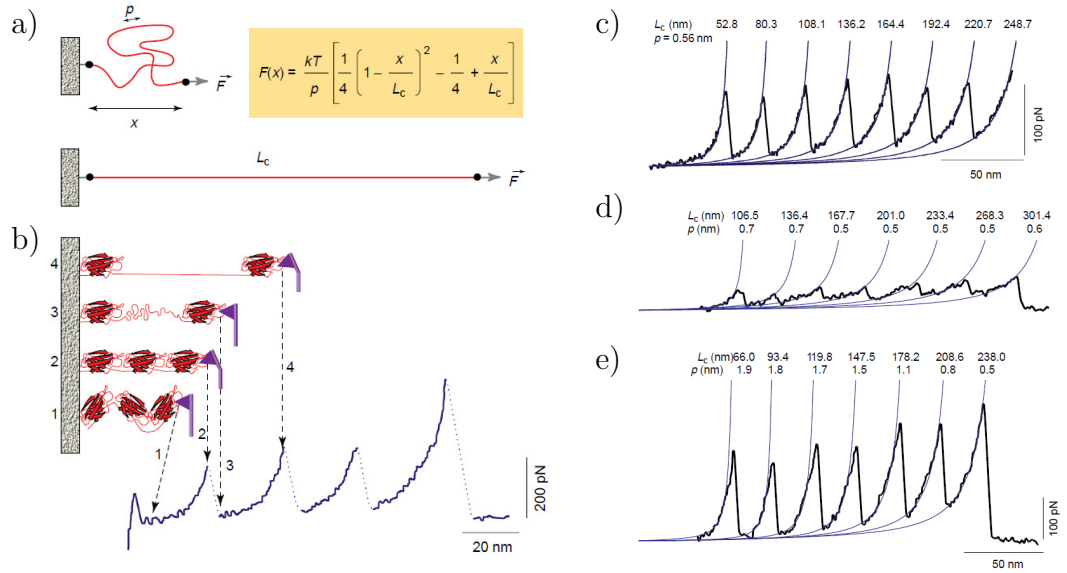

Figure 1.8: Force spectroscopy measurements on proteins based on the AFM device. Panel (a): worm-like chain (WLC) model for a semi-flexible chain used to interpret the unfolding on each protein domain. Here, L_c is the contour length of the chain and p is the persistent length. Panel (b): sawtooth force-extension curve describing the sequential unfolding of the protein domains. Panel (c): force-extension curve for the recombinant human tenascin-C. Panel (d): force-extension curve for the cytoskeletal protein spectrin showing a heterogeneous persistence length. Panel (e): force-extension curve for a recombinant fragment of titin consisting of titin Ig domains 27-34. The figure is reproduced with permission from [185]

S-DNA transitions [220].

The force-extension curve exhibiting a force plateau, corresponding to a conformational transition of the molecule, has been observed also for other macromolecules. An interesting example concerns a polysaccharide called dextran. A dextran filament has been tethered to a gold surface and probed with the atomic force microscope tip by means of a vertical stretching [221]. At low forces, the deformation of dextran is dominated by entropic forces and can be described by the FJC model with a Kuhn length of around 6 Å. At more elevated forces the dextran filament exhibits a reversible conformational transition characterized by a force plateau [221]. This transition has been explained in terms of a two-state model implemented through Monte Carlo simulations [222]. In Fig.1.7.c we show the force-extension curve for dextran recently obtained with AFM force spectroscopy [210]. These measurements have been realized with a refined AFM variance analysis able to detect conformational changes at the sub-angstrom scale [210]. Also, artificial polymers can show conformational transitions characterized by a force plateau. The study of these structures is referred to as covalent polymer mechanochemistry. In this context, chemical transformations are activated by external mechanical forces applied to the polymer chain. An example of interesting molecular architecture is given by the cyclobutane mechanophore operating as a gate to regulate the mechanical activation of a second mechanophore, thus resulting in a mechanochemical cascade reaction [223]. Single-molecule force spectroscopy shows a force-extension curve characterized by a force plateau in correspondence to the opening/closing transition of the gate [223]. Also, in this case, the underlying bistability is able to generate the conformational transition of the molecular

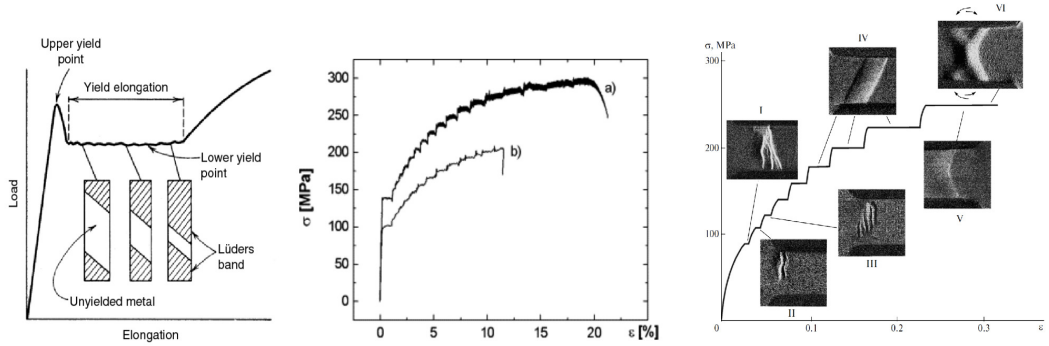

Figure 1.9: Three examples of stress-strain curves of materials showing the Lüders bands in the first case, the Portevin–Le Chatelier effect in the second case, and the Savart–Masson effect in the third one. In all these phenomena, we observe a series of microinstabilities generating plastic behavior. These images are respectively taken from Ref.[227], Ref.[228], and Ref.[229]

structure.

We have introduced a first class of mechanical responses characterized by a force plateau corresponding to the transition of the units of the chain between two configurational states. This force plateau corresponds to a synchronized transition of all the units, which is induced by the external force applied to stretch the chain. A second class of responses has been observed in different single-molecule experiments, typically concerning multi-domain proteins. The folding and unfolding of these protein systems have been widely observed through AFM force spectroscopy. Many proteins with important biological mechanical functions are composed of many units having the same chemical composition, *i.e.* the same amino acid sequence. Moreover, each unit can have one or more stable configurations and the transition between these states can be induced by applied forces. The typical force-extension response observed for these systems is represented by a sawtooth curve, where each force peak represents the unfolding of one unit. Therefore, in this case, the overall unfolding process is sequential and not synchronized as discussed above for other structures (nucleic acids and polysaccharides). The characteristic sawtooth pattern, with the number of peaks equal to the number of domains, has been first observed with titin [224] and later with tenascin [225] and spectrin [226]. The sequential character of the force-extension curve can be found in Fig.1.8, where we show the WLC model for the unfolding of one unit, the overall chain unfolding under AFM stretching and some examples of proteins [185].

1.2.2 Phase transformations in materials science

In the plastic behavior of materials, each single plastic event can be explained through the instabilities, which are able to switch the system from a ground state to a permanently deformed or metastable state. These forms of microinstabilities can be seen in different shapes of the force-extension (or stress-strain) response of plastic materials. A first example of these instabilities can be found in the so called Lüders bands (first panel of Fig.1.9) that are localized bands of plastic deformation observed in metals experiencing tensile stresses, which usually start at one end of the specimen and propagate toward the other one [227]. During the band propagation, the stress-strain curve is quite flat with some fluctuations due to the internal microinstabilities. Another example is given by the Portevin-Le Chatelier effect, which can be observed as an unstable plastic flow during tensile tests of some dilute alloys (under certain regimes of strain

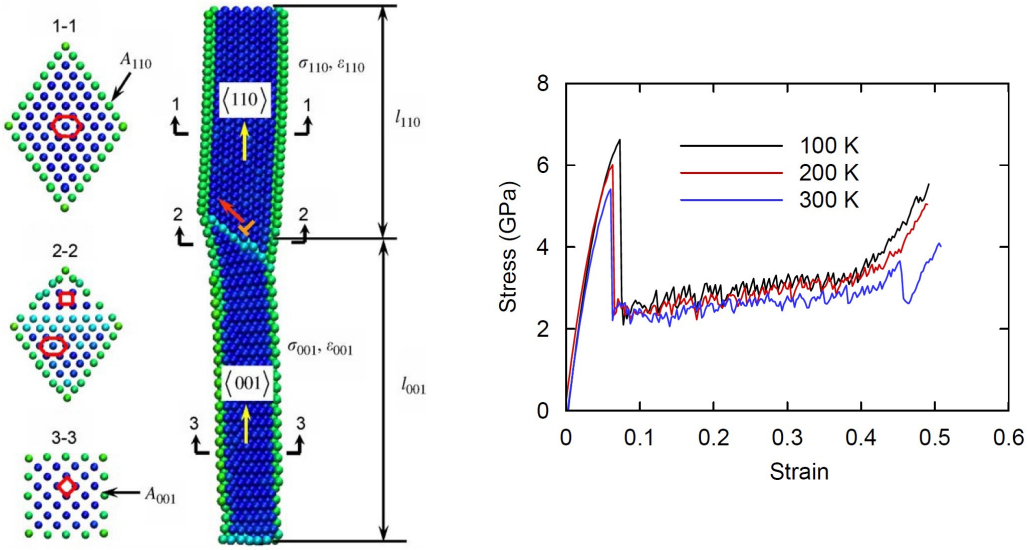

Figure 1.10: Left panel: cross-sections of a Cu nanowire. Two different crystalline structures can be identified and they are separated by a domain wall, which is moving in response to the applied strain. Right panel: temperature effect on the stress-strain curves of the Cu nanowire obtained from MD simulations. Both figures are reproduced with permission from [230].

rate and temperature) [228]. In this case, a series of peaks can be seen in a region with a positive slope of the stress-strain curve. These peaks represent the sequence of instabilities of the plastic phenomenon (center panel of Fig.1.9). Other manifestations of discontinuous deformation are staircase creep and the Savart–Masson effect. They imply the formation of steps on loading curves with a constant stress rate in a soft testing machine (right panel of Fig.1.9). There are relatively few studies on the Savart–Masson effect [229], although it was discovered long before the Portevin-Le Chatelier effect. Recent studies show how the plastic behavior of materials is strongly affected by their state of disorder. In particular, amorphous solids exhibit plastic flow which has been analysed and reproduced by means of molecular dynamic simulations [144–147]. Also failure phenomena are largely influenced by disordered geometries [136–143]. However, the study of this topic is boyond the scope of the present thesis.

For the nanoscopic cases instead, nanowires, with diameters on the order of nanometers, exhibit exceptional properties due to their high aspect ratios and quantum confinement effects. Various phase transformation processes play a significant role in determining the behavior of nanowires. For instance, the solid-to-solid phase transition from one crystal structure to another can drastically alter the electronic and mechanical properties of nanowires. Recent research revealed that single-crystalline metal nanowires with nanometric cross-section can exhibit a pseudo-elastic behavior characterized by very large elongations (up to 50% of the original length) [230–233]. This behavior, which is exceptional compared to all other shape memory alloys, can be explained by a reversible lattice reorientation process. It means that the deformation mechanism is characterized by a twin boundary propagation between two differently oriented face-centered cubic (FCC) crystalline structures. This behavior is typical of Cu and Ni, where we can identify the two following configurations: the original one named $\langle 110 \rangle / \{111\}$ with axis $\langle 110 \rangle$ and surfaces $\{111\}$, and the deformed one named $\langle 001 \rangle / \{100\}$ with axis $\langle 001 \rangle$ and surfaces $\{100\}$, as shown by [230] (see left panel of Fig.1.10). Because of the nanometric dimensions of the cross-section

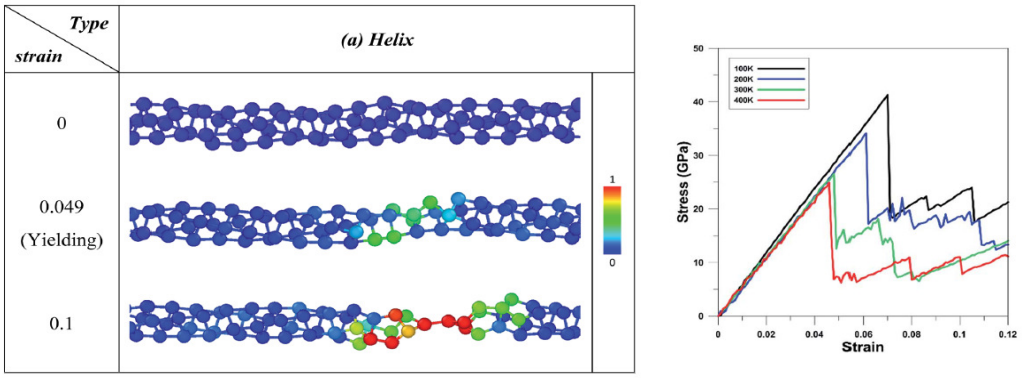

Figure 1.11: Left panel: MD simulation for the nucleation of a new phase in a helix-structure germanium nanowire. Right panel: temperature effect on the stress-strain curves of the Ge nanowire obtained from MD simulations. Both figures are reproduced with permission from [234].

geometry, the surface-to-volume ratio is very large, and surface energies dominate the strain energy difference between the two different nanowire configurations. In this study, a series of molecular dynamics simulations have been performed to numerically obtain the stress–strain behavior of Cu nanowires at different temperatures and under quasi-static tensile deformation (see right panel of Fig.1.10). The simulations are based on the embedded-atom-method interatomic potential for Cu, and the uniaxial displacement-controlled loading strategy is comparable to the Helmholtz fixed-displacement approach.

Semiconductor nanowires have been recently studied since their properties are sometimes more interesting than those of the bulk counterpart [234]. For this reason, the thermo-mechanical properties of ultrathin germanium nanowires have been investigated by means of molecular dynamics simulations [234]. We consider here the results concerning the helix Ge nanowire with a radius of 1.8 Å, for which the stress-strain curve has been obtained for temperatures of 100, 200, 300, and 400 K [234] (see right panel of Figure 1.11). The simulations for germanium were based on the Stillinger-Weber potential, coupled with the Nosé-Hoover thermostat to impose the system temperature. The helical structure is perfectly ordered initially, as shown for null strains in the left panel of Figure 1.11 from [234], and exhibits a transition to an amorphous structure, following a plastic process that begins with a peak of stress, namely the nucleation stress. After the yielding strain, the unfolded region evolves into the one-atom chain structure. In the two examples of nanowires discussed, we considered systems where two possible states or configurations are present. In the first example, they correspond to two different crystal structures, and in the second example to a regular helical structure and an irregular amorphous structure.

1.2.3 Adhesion and deadhesion processes

Adhesion and deadhesion processes play pivotal roles in various research fields such as material science, biophysics, and engineering. Understanding these phenomena, especially on the micro and nanoscale, is crucial for the development of advanced materials, new effective drugs, or elucidating biological processes. In biology, cell adhesion refers to the process where different cells start creating bonds between each other (in the case of cell-cell adhesion) or with a substrate in their surroundings usually called the extracellular matrix adhesions (cell-ECM). This linkage process usually is made possible through special protein complexes. In these cases, the adhesion

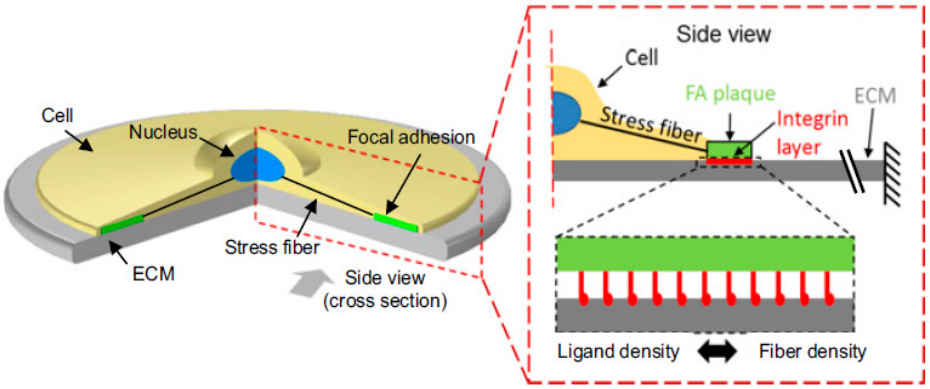

Figure 1.12: Schematic of a cell adhered to a fibrous extracellular matrix (ECM). Stress fibers connect the focal adhesion band/plaque and the nucleus. Image edited from [235].

phenomenon involves both the recognition and binding of structural proteins as well as the transmission of mechanical forces throughout the adhesion process [236]. More specifically, in nature, multicellular organisms usually require a 3-dimensional structure in order to both provide structural integrity to the organism itself and to denote functional tissue boundaries and delineate specific microenvironments [237, 238]. Even the slightest alteration in cell adhesions can strongly influence cellular mechanotransduction and mechanosensing in a cytoskeleton-dependent manner, thereby linking to tissue development, immune activation, and tumorigenesis [239]. Therefore, pinpointing the key molecules and quantifying the adhesion forces involved can reveal essential information on the dynamic process of cell adhesions. As an example, in Fig.1.12 we show a schematic of a coarse-grained model for the adhesion process of a biological cell on the extracellular matrix. In this model, the stress fibers connect the focal adhesion (FA) band/plaque and the nucleus. The FA band/plaquem then, is connected to ECM through an integrin layer whose density is positively correlated with the fiber density underneath the cell. Furthermore, in this case, the ECM is treated as an elastic material.

Deahdesion, on the other hand, is the process opposite to adhesion and involves the separation or breaking of the intermolecular forces between two surfaces. Understanding deadhesion processes, then, is essential for developing strategies to weaken or break adhesive bonds in different applications. In material science and engineering, the study of deahdesion mechanisms is crucial for analyzing the failure of adhesive bonds. For example, in aerospace applications, understanding the deadhesion processes at the interface between composite materials and adhesives is essential for ensuring structural integrity. By investigating failure modes and stress distributions, it is possible to develop improved adhesive formulations and bonding techniques. Deadhesion is also relevant in biophysics, particularly when studying cell-cell dissociation. During processes like metastasis, in fact, cells detach from the primary tumor and invade surrounding tissues. Understanding the deahdesion mechanisms involved can provide insights into cancer progression and potential therapeutic targets. Furthermore, investigating the weakening of cell-cell adhesion forces and the signaling pathways involved in cell dissociation can contribute to the development of novel anti-cancer therapies.

A crucial aspect of the adhesion/deadhesion processes occurring at the micro and nanoscale is that it is strongly affected by temperature. It has been observed in many instances, in fact, that the increase in the temperature can be one of the main driving factors in the partial or

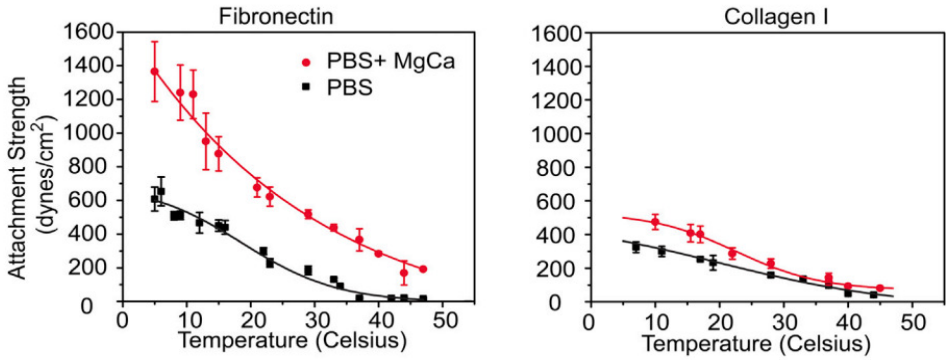

Figure 1.13: Attachment strengths of HT1080 cells (with and without cations, red and black curves respectively) monotonically increase with the decreasing temperature independently if the substrate is fibronectin (left panel) or Collagen type 1 (right panel). Image edited from [240].

complete detachment of a cell from a substrate. In this regard, figure 1.13 from Ref.[240] shows that the attachment strength of an HT1080 cell decreases with the increase of the temperature. Observing the graphs from the figure, in fact, we can notice that the force necessary to detach the cell decreases to a null force at a critical temperature meaning that the high temperatures can be the only factor needed for the complete detachment of a cell. This is why, as mentioned before, the investigation of how temperature affects the adhesion/deadhesion behavior process can be of crucial importance for the study of cancer cell metastasis where the cancerous cells break away from the original (primary) tumor, travel through the blood or lymph system, and form a new tumor in other organs or tissues of the body. In this case, the cancer region temperature can increase due to the body's inflammation response leading to a detachment of these cells that can, unfortunately, trigger a metastasis.

These phenomena are also commonly observed in most of the activities concerning DNA. Although the DNA structure is robust in order to preserve the genetic information of life, it is sufficiently loose to allow the opening of the double helix through the controlled detachment and attachment of the base pairs. These phenomena are called hybridization and de-hybridization and are fundamental processes in molecular and cell biology. Spontaneous opening of the DNA is rare at physiological temperatures but is promoted by particular enzymes whenever the genetic code stored in the DNA has to be accessed by molecular machinery. This can occur during transcription (DNA translation into messenger RNA), replication (DNA copy), recombination (DNA "cut-and-paste"), repair, or some enzyme binding on single strands. At high enough temperatures, thermal energy promotes partial or even complete base-pairs dissociation, a phenomenon called DNA denaturation or melting. This property is fully exploited, *e.g.*, in Polymerase Chain Reaction (PCR) where the DNA is denatured before short sequences are hybridized which are then extended, this occurring during several dozen cycles controlled by the temperature. DNA hybridization kinetics is also of importance for fast-developing nanotechnology designs. A specific example of these denaturation processes is presented by DNA or RNA hairpins that are closed loops composed of nucleobases of DNA or RNA (as shown in panel a of Fig.1.14). In this case, the force spectroscopy techniques are applied to measure the force necessary to open the hairpin's structures by going through what can be easily modelized as an adhesion problem.

The study of the adhesion and deadhesion processes has been of course of interest to the

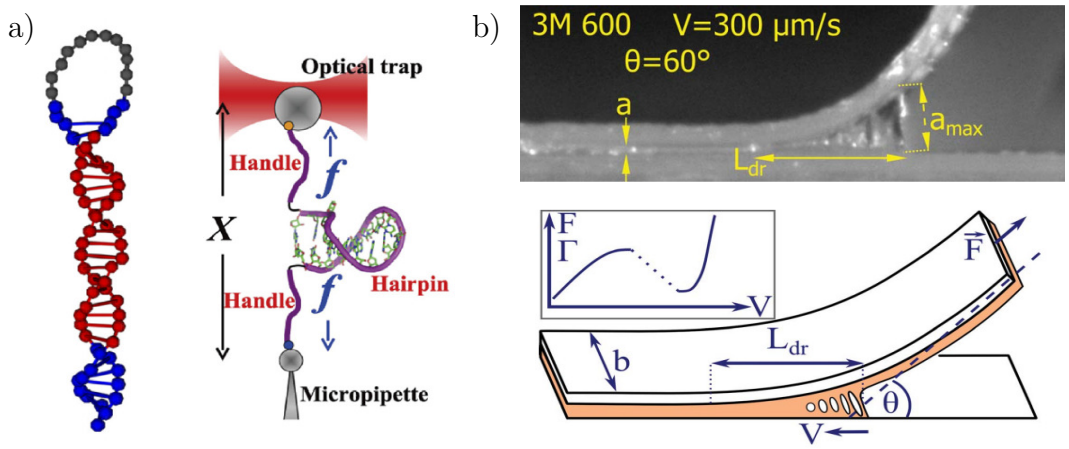

Figure 1.14: Panel a) Principle of hairpin unfolding experiments. A force f is applied to the strands of a short DNA hairpin. For a force of about 15 pN, two states are equally accessible to the hairpin, which is either open or closed. Image edited from [241]. Panel b) Picture of a peeling experiment of a Pressure Sensitive Adhesive (PSA). L_{dr} is the characteristic extension of the debonding region, where the adhesive is significantly strained. $a_{\max}$ is the maximum elongation after which the PSA linking bonds are considered completely detached from the surface. [242].

industrial sector as well. The modeling of the adherence energy during the peeling of Pressure Sensitive Adhesives (PSA) (see panel b of Fig.1.14) has been the focus of many research and development projects in the industry of adhesive products since the 50s, uncovering several factors that aim at explaining their high adherence on most substrates, such as the softness and strong viscoelastic behavior of the adhesive, the low thickness of the adhesive layer and its confinement by a rigid backing. The more recent studies of adhesives by probe-tack methods also revealed the importance of cavitation and stringing mechanisms during debonding, underlining the influence of large deformations and of the related non-linear response of the material, which also intervenes during the peeling process. The peeling of a substrate from another occurs in fact through the inside failure of the adhesive layer ("cohesive failure") or through the debonding of the adhesive from the substrate ("interfacial" or "adhesive" failure). In all of these cases the temperature, once again, plays an important role in the decohesion process by modifying the force necessary to nucleate and propagate the peeling process through the whole specimen.

1.2.4 Fracture and crack propagation

Fracture and crack propagation are critical phenomena in material science and biophysics, influencing the mechanical integrity and failure behavior of various materials. More specifically, fracture mechanics is a branch of materials science that investigates the behavior of cracks and their propagation within materials and/or biological systems. Understanding fracture and crack propagation mechanisms is essential for predicting and preventing failure in structural materials, as well as exploring biological systems' resilience. We are particularly interested here in micro and nanoscale systems, where thermal fluctuation plays a crucial role in fracture behavior and crack propagation phenomena. It has been observed that, under specific conditions, the temperature can be at times the main physical cause of crack propagation. The motivation behind this is that, when it comes to the micro and nanoscale, the thermal fluctuations can significantly help the molecular structure of the surrounding area of the crack tip to overcome the energetic threshold

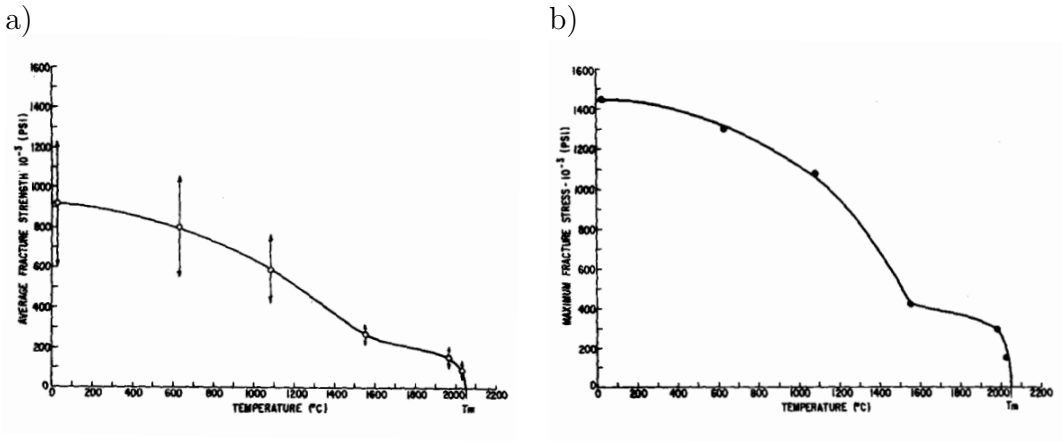

Figure 1.15: Mechanical behavior of sapphire whiskers at elevated temperatures. The experimental average fracture strength (panel a) and the experimental maximum fracture stress (panel b), as a function of the temperature, are reproduced from [33].

holding them from propagating the crack front. This phenomenon is particularly important when we investigate micro and nanoscopic systems such as nanowires or biological macromolecules. These systems often present unique size-dependent mechanical properties and therefore offer an intriguing platform to study such temperature-driven crack propagations. The effects of the thermal fluctuation on the fracture and crack propagation phenomena have been first investigated by Brenner in 1962 who used sapphire whiskers (Al_2O_3) with a diameter between 8 and 40 μm to lead his investigation of the matter. In such structures, the damage induced by the fracture can be viewed as a sequence of ruptures, representing the breaking of the chemical bonds along the direction of the crystal structure. As shown in Fig.1.15, Brenner was able to measure the temperature dependence of the stresses necessary to completely break the specimens. From the figure, furthermore, we can observe that the transition around $T = 1550$ C in the stress decrease suggests a change in the mechanism of failure leading to complete failure.

The presence of nanoscale defects and the high surface-to-volume ratio influence the fracture mechanics of nanowires. In addition to the temperature, crack propagation in nanowires can be influenced by other factors such as the specific crystal structure, material composition, and external loading conditions. For example, it has been observed that the presence of twin boundaries in nanowires can impede or facilitate crack propagation, depending on their orientation and interaction with the crack front. Understanding these processes is crucial for designing nanowires with enhanced mechanical properties and reliability. An interesting example of the dependence of the fracture phenomena on the temperature can be found in a recent study performed on a [110]-oriented silicon nanowires [125]. In this study, the silicon nanowire behavior has been investigated through molecular dynamic simulations that eventually highlighted the dependence of the tensile strength, the stress in which the nanowire breaks, on the temperature. If we observe the right panel of Figure 1.16, in fact, we can see that the tensile strength necessary to break nanowires of different diameters decreases as the temperature increases. We emphasize that statistical mechanics is, once again, the best frame to study these phenomena due to the particularly small-scale system in which they occur and the fact that the thermal fluctuations play an important role.

Similar analysis methodologies were used in a different study to investigate the case of GaN nanowire [124] (see figure 1.17). In this case, the nanowire under investigation presented a

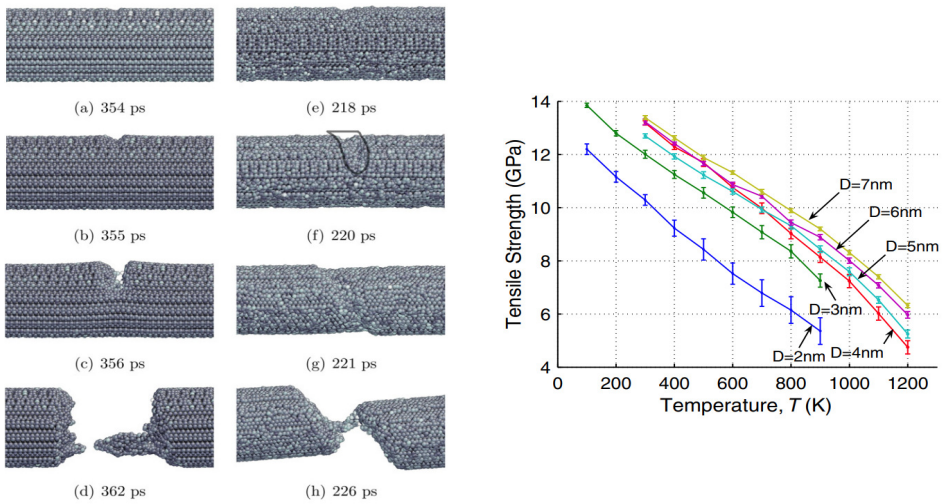

Figure 1.16: Left panel: snapshots of a [110] Si nanowire with a diameter $D = 7$ nm during fracutre under tensile loading with temperature $T = 300$ K (first columnm) and $T = 1000$ K (second column). Under each figure, there is the time elapsed since the beginning of the tensile loading. We can notice that the same nanowire breaks earlier when the temperature is higher since the tensile loading increases with time at the same pace for both. Right panel: tensile strength of Si nanowire as a function of temperature for different diameters. [125].

diameter of 1.92 nm and a length of 6.12 nm as reported in Figure 2(d) of Ref.[124]. Through the molecular dynamic simulation of the stretching of the nanowires, it has been possible to observe the brittle-to-ductile transition. Observing the right panel of Figure 1.17, in fact, we can notice that the force-extension curve relative to lower temperatures (from the 300 K case up to the 1500 K one) presents a brittle behavior, meaning that the force applied to the nanowire increases until reaching a final elongation point after which the nanowire completely breaks resulting in a null applied force. On the other hand, in the 1800 K case, we can notice that exists an elongation point (around 9% of the strain parameter) where the force drastically drops to a lower value only to continue increasing at a slightly slower pace than before. This middle critical point represents the ductility of the material that, contrary to the previous brittle ones, shows a plasticity behavior when reaching a critical precise threshold. In this case, we can notice that the effect of the temperature is not only that of lowering the fracture force threshold responsible for the complete breaking of the examined nanowire but also that of changing the behavior of the material itself that, as we have seen, switches from brittle to ductile.

The discovery of new characteristics at the nanoscale has prompted the advancement and creation of nanoelectromechanical systems (NEMS) for diverse applications. Extensive research has focused on investigating the mechanical, electrical, thermal, and optical properties at the nanoscale of one-dimensional nanostructures such as the nanowires we showed here. Understanding the mechanical properties, particularly the stiffness, and strength, of these nanostructures is crucial, as they play a vital role in determining the stability and lifespan of numerous potential applications. Recently, extensive experimental and numerical simulations have been performed to understand the mechanical properties of carbon-based nanostructures such as graphene. Since the initial investigations of graphene, numerous studies have provided evidence demonstrating that graphene possesses a stable two-dimensional structure exhibiting remarkable electronic and optical

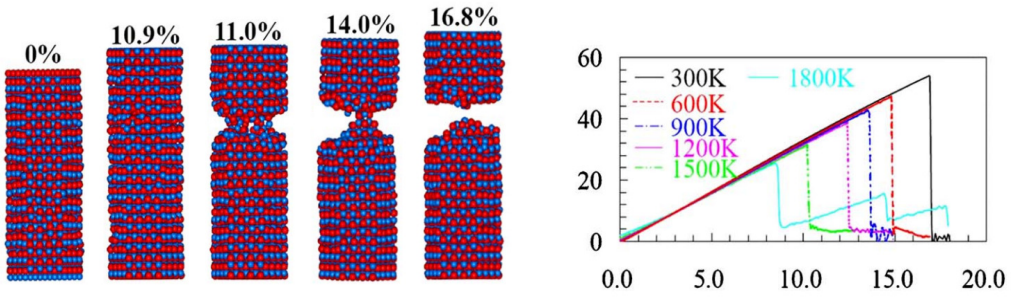

Figure 1.17: Left panel: Atomic configurations of selected stages for the [0001]-oriented nanowire with $[10\bar{1}0]$-oriented lateral facets at 1500 K, the number over each snapshot represent the strain. Right panel: Tensile stress-strain curves of the [001]-oriented nanowires with a diameter of 1.92 nm. The lateral facets of the investigated nanowire are $[11\bar{2}0]$. Images edited from [124].

properties. In a recent study Ref.[124], the mechanical properties of graphene have been studied under various temperatures and stress conditions. To do so, molecular dynamics simulations were performed using adaptive intermolecular reactive empirical bond potential which has been shown to accurately capture the Young's modulus of graphene as well as bond breaking and bond reforming between carbon atoms. More precisely, the study focused on the uniaxial tensile test of graphene along the armchair direction. To study the mechanical properties, the simulations were performed on a sample large enough to represent the mechanical properties of an infinitely large graphene monolayer where a deformation-controlled uniaxial tensile test has been applied. The stress-strain relations for various temperatures ranging between 300 K and 2400 K are shown in figure 1.18.c. As we can see from these results, the fracture strength decreases significantly with the increase in temperature. As a matter of fact, as shown by this study, the fracture strength decreases as much as 60% less from a temperature of 2400 K to a room temperature of 300 K.

Since it is very probable that during the fabrication of graphene some defects can arise at the nanoscale, it has been deemed interesting to investigate the effects of such defects, especially slits in the nano scale, on the strenth and stiffness of graphene. To perform this investigation a 5 nm $\times$ 5 nm squarelike graphene sheet with a slit has been considered in which a strain rate was applied along the armchair direction to perform the uniaxial tensile test (see panel a of figure 1.18). In this fracuture simulation, the bonds between carbon atoms break continuously in the direction identifide by the slit opening, until the graphene structure complete failure. In the panel b of figure 1.18, instead, we display the variation in the fracture strenth as a function of the slit semilength for two different temperature, namely at $T = 300$ K and $T = 1200$ K. Again, we can observe that the effect of the increasing temperature is that of descreasing the fracture strenght of the graphene specimen considered in the simulation. Another important aspect we can notice from the graph is that the fracture strenght, for both temperatures, decreases with the increase of the slit semi-length L in perfect agreement with Griffith's crack propagation theory [119].

Along with solid materials, it is interesting to investigate the nucleation and propagation of cracks in soft and rubbery materials also. Many new soft materials and applications such as stretchable electrodes, flexible prosthetics, or soft robotics continuously emerge yet an appropriate multiscale quantitative theory of crack propagation and fracture of these materials hasn't been already settled.

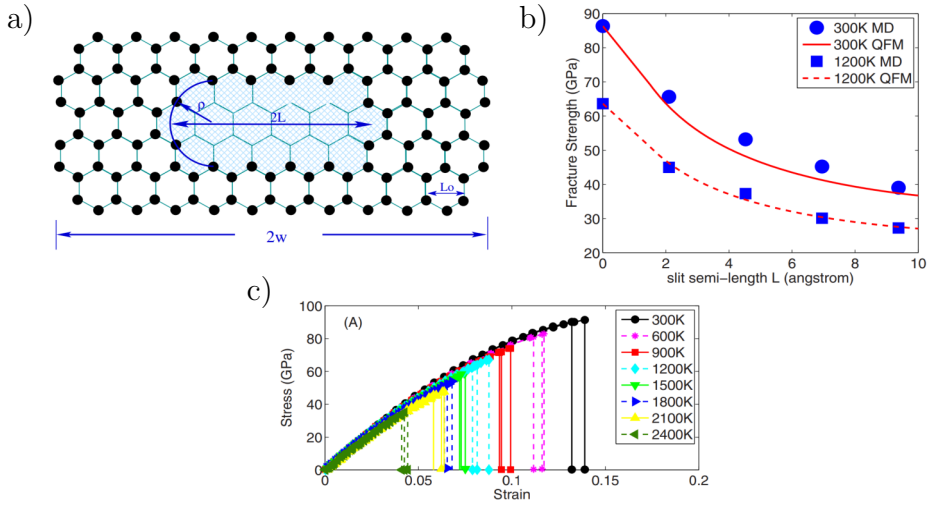

Figure 1.18: Panel a) atomic-scale slit structure of graphene for mode I loading, L here is the semi-length of the slit. Panel b) fracture strength as a function of the slit semilength L for a damaged graphene monolayer uniaxially loaded along the armchair direction. Panel c) Nominal strain vs stress of graphene under uniaxial tensile test along the armchair direction at various temperatures. Images edited from [243].

1.3 Motivations

The behavior of many natural and artificial systems of considerable biological and technological importance, as discussed in previous introductory Sections, is characterized by micro-instabilities, which generate a variety of complex responses with strongly nonlinear features. The study of micro-instabilities in molecules of biological origin is of central importance to developing biological applications, which can lead to a better understanding of the disease mechanisms and improvements in some disease treatments. This is especially true in cancer research, where the mechanical properties of macromolecules and the adhesion of cells are crucial to determine the evolution of cancer invasion and metastasis. On the other hand, in the mechanics of materials, and more generally in material science, similar microinstabilities have been observed in different situations. For example, an important situation where the microinstabilities play a central role is the adhesion of films and their peeling from a substrate. In this context, one idea to improve and tailor the adhesion properties of artificial materials is to use bioinspired geometries and mechanisms. Several industrial processes require indeed the peeling of layers of different kinds and with different velocities. Additionally, it is crucial to better understanding the physics of adhesion within a large temperature range. The combination of thermal fluctuations and microinstabilities is also at the origin of fracture phenomena in materials. If we think of a crystalline material, the propagation of a crack front must be identified by the gradual breaking of the atomic bonds along a line of the crystal structure. Therefore, each single crack propagation step is a form of instability, which can be defined by assuming a maximum length of the interatomic distance before rupture. Of course, the thermal fluctuations influence the crack propagation, fostering the breaking of the interatomic bonds, and for such reason they need to be take in into accuount.

There are several experimental observations showing the effect of thermal fluctuations on system with microinstabilities, and in particular based on adhesion/cohesion processes. This

effect is particularly pronounced in nanomaterials and nanostructures, where thermal energy can rival mechanical energy, facilitating spontaneous de-adhesion. Indeed, in most experimental cases, the force needed to separate a film from its substrate diminishes with rising temperature. This reduction in adhesion strength is primarily attributed to thermal fluctuations, which facilitate the exploration of phase space. Even when external forces alone would not lead to detachment, thermal fluctuations can drive the system into phase space regions where rupture occurs. Sometimes, the force required for de-adhesion reaches zero for large temperature values, marking a phase transition characterized by a specific critical temperature. Beyond this critical temperature, the system consistently remains in a de-bonded state, regardless of the applied mechanical conditions. This behavior has been experimentally shown for several systems where adhesion and cohesion phenomena occur. Concerning cell adhesion, it has been observed that the attachment strength monotonically decreases with increasing temperature independent of substrate properties, and a possible phase transition can be inferred from experimental data. Moreover, researchers have conducted experimental investigations into the mechanical unfolding of nucleic acid hairpins, aiming to establish a phase diagram within the force-temperature plane. For both RNA and DNA, it has been observed that the force required to separate the two polynucleotide strands decreases as temperature rises, exhibiting indications of a phase transition at a critical temperature known as the denaturation temperature. In materials science, similar phenomena have also been observed. A historical example can be found in the study of sapphire whisker fractures at various temperatures. Once again, there is a discernible trend of decreasing fracture strength with increasing temperature, culminating in a well-defined phase transition at elevated temperatures. More recent studies have further validated these observations, extending their validity to materials engineered to withstand high-temperature environments, including high-entropy and medium-entropy alloys. These observed behaviors are quite similar for rather different physical systems (cells, nucleic acids, micro- and nano-wires and so on) and need therefore to be explained by means of a unifying theory that has not been yet completely developed and disclosed in the scientific literture. The aim of the present manuscript is that of trying to fill this gap by proposing a mathematical and physical approach to deal with these problems by combining the effect of thermal fluctuations (by statistical mechanics) with the effect of mechanicam actions (by micro- and nano-mechanics) on complex systems.

The observed similarities between the problems concerning microinstabilities in biophysics and material science are of great importance, not only from the cultural point of view but also for the possibility to adopt the same techniques to approach very different systems. Indeed, the common denominator in all these examples, from both biophysics and materials science, is that some units of the system under investigation exhibit a two-state or multi-state character. It means that such units are allowed to be in only one of two (or more) distinct physical states, and can therefore experience a transition between these states, characterized by specific static and dynamic features. The large number of units in these systems generates a collective behavior of the transitions and an interaction between the transition mechanisms. Consistently, to address the problem of describing the behavior of systems with microinstabilities, we apply the method of the so-called "spin variables". It is based on the introduction of a series of discrete or spin variables to identify the state of the system units. In a two-state instability case, for example, they can assume the values +1 and -1, similar to a magnetic spin. As we will show in the following discussion, this approach strongly facilitates the calculations performed to determine the behavior of the system. In particular, this simplification allows for an easy calculation of the partition function, typically adopted in statistical mechanics, useful to describe the system behavior and all the relevant thermodynamic quantities. As we will see, the introduction of this technique not only helps by lowering the degree of complexity in the evaluation of some of the most interesting quantities but also allow us to perform closed-form analytical calculations. This was not always the case in past

studies where often these particular equations were solved numerically. Being able to analytically calculate the results gives us a better insight into the physics of the system studied and the model adopted. Altough our approach proves to be useful to better understand the previously discussed experimental situations, it shows several limitations that should be considered in further studies. For examle, we did not consider out-of-equilibrium phenomena in our models, and we never introduced disorder or heterogeneous structure. Also, all our models are discrete and they should be generalized to continuous systems in ordere to foster the development of a new and more comprhensive continuum mechanics theory.

The complexity presented by the study of such micro-instabilities has already generated a great impulse to scientific development, in particular concerning the synergy between the force-spectroscopy techniques (experimental investigation) and the small-systems statistical mechanics (theoretical investigation). Importantly, when force-spectroscopy techniques are applied to a microscopic system that presents a bi- or multi-stable behavior, they allow us to directly observe the switching process between the states and quantify its static and dynamic features. Another important reason to delve into the study of microinstabilities is the possibility to test and validate the adoption of the statistical mechanics approach in the study of these phenomena. Historically speaking, in fact, these natural and artificial systems have been mostly investigated using continuous mechanical techniques that usually do not consider or, at best, strongly approximate the crystalline structure of the systems. Considering these systems with a statistical mechanics lens does not mean that we reject the extensive and sophisticated studies that have been employed in this field in the past but, rather, we intend to give a different and integrative explanation to better understand some features and phenomena for the instabilities. Of course, since we are dealing with small systems, temperature plays an essential role in the dynamic evolution of all physical and chemical quantities. Hence, the direct quantification of the mechanical response of single molecules (force-spectroscopy) has allowed for the first time the comparison of experimental results with those of the thermodynamics and the statistical mechanics of small systems. This synergy between experimental and theoretical activities has delivered important outcomes and applications. For instance, force spectroscopy is used to investigate the enzymatic activity of proteins involved in DNA processes (replication, transcription, organization, and repair). Another important innovation that we propose here is the extensive investigation of how the thermal effect influences the particular systems studied. We will show that temperature plays a crucial role in the behavior and development of the instabilities sometimes triggering phase transition that changes the very same crystalline structure of the system.

The resulting structure of this manuscript is the following. In Chapter 2, we introduce the spin varibale method through two simple example of application. We also discuss the statistical mechanics based on the Gibbs and the Helmholtz statitical ensembles. In Chapter 3, we briefly describe the simple model of adhesion processes already elaborated in our research group before the beginning of this PhD thesis. It represents the starting point for the following generalizations and developments. In Chapter 4, we discuss a generalization of this approach, able to take into consideration an intermediate softened condition between the intact and the broken standard states of the adhesion process. This is useful to take account of plastic phenomena in this context. In Chapter 5, we elaborate a model for studying the effect of temperature on phase transformations in one-dimensional structures. This approach considers the interaction among the units by means of an Ising scheme, and can be applied both to proteins conformational changes, and to pseudo-elasticity in nanowires. In Chapter 6, we finally investigate the thermal fluctuations effect on the crack propagation. We firstly develop a model for the brittle fracture and we are able to explain the temperature dependent fracture strength of nanomaterials. Then, we also elaborate an approach for studying the brittle-to-ductile fracture behavior by identifying the transition temperature betwenn the brittle and ductile regimes. To develop this second model,

we adopt the same strategy introduced in Chaper 4, based on an intermediate softened state between intact and broken bonds.

Chapter 2

Statistical ensembles and spins

We describe here a single-unit discrete model in order to highlight the fundamental differences between the Gibbs and the Helmholtz ensembles studied through the principles of statistical mechanics at equilibrium. The intrinsic simplicity of the model represents the perfect starting ground in which we can apply the spin approximation and understand its true meaning and feasibility limits. Thanks to the statistical mechanic's approach, we will obtain results at first glance in disagreement with what we would expect from a merely practical point of view but, fortunately, these apparent incongruities will be fully explained and solved later in the discussion using a purely energetic balance approach.

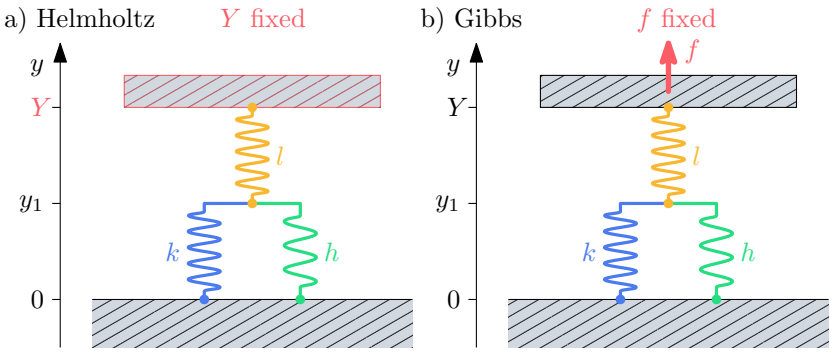

Figure 2.1: Scheme of the two-rigidity model in the isometric Helmholtz ensemble (left) and in the isotensional Gibbs one (right). In both ensembles, the model consists of three springs linking together a bottom fixed layer located at $y = 0$ to an upper layer located at $y = Y$. In the Helmholtz case, the upper substrate is fixed at $y = Y$ while in the Gibbs case, it is pulled with a fixed force f.

The structure of the model studied (shown in Fig.2.1) is the same both while considering the isometric Helmholtz ensemble (left panel in the figure) and while considering the isotensional Gibbs ensemble (right panel) and it consists of three springs of different elastic constants k, l, and h arranged in order to link two separate substrates. Springs k and h (in the figure in blue and green respectively) are connected in parallel and link together the bottom substrate, fixed at $y = 0$, to the lower end of spring l (in yellow), located at $y = y_1$, with which they are connected in series. Spring l, in turn, connects the latter parallel springs to an upper layer located at $y = Y$.

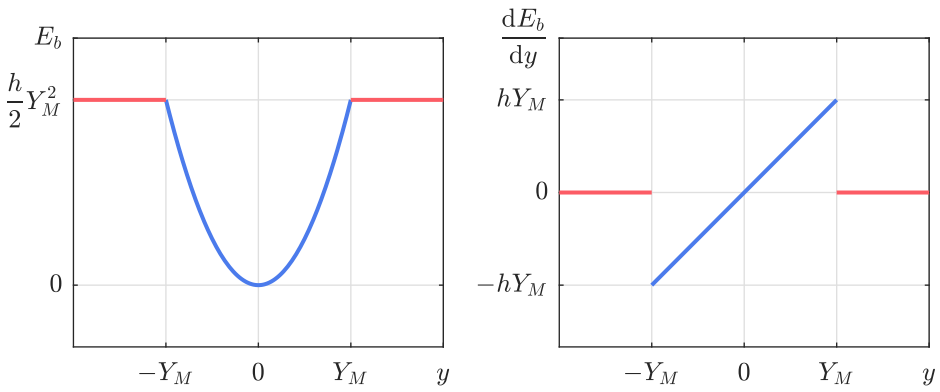

Figure 2.2: Potential energy of a breakable spring of elastic constant h (left) and resulting force (right). The quantity Y_M is the elongation after which the spring breaks resulting in an exerted force equal to zero.

Since y_1 will be the only variable of the system, from now on we refer to it simply by y. The important aspect of this model is that, while springs l and k behave like normal linear springs, spring h is a breakable one, meaning that it exists a threshold elongation Y_M after which the h spring "breaks" or, more precisely, its potential energy E_b is constant resulting in a null force for elongation $|y| > Y_M$. The behavior of this breakable spring h is better described through its potential energy landscape in the left panel of Fig.2.2. Here, we observe that the breakable spring behavior is described by a standard parabolic potential when its elongation $|y| < Y_M$ does not exceed the threshold (blue curve), meaning that in this region the spring behaves like a standard one, and by a constant potential $\frac{1}{2}hY_M^2$ when its elongation overcome the threshold $|y| > Y_M$ (red curves), meaning that the resulting force, in this case, is null (see right panel of Fig.2.2).

The main difference between the two statistical ensembles is that in the Helmholtz ensemble, the system is studied at equilibrium while the position of the upper layer is fixed at $y = Y$ instead, in the Gibbs ensemble, this upper layer is free to move and a fixed force f is applied. In the following sections, we will analyze this system in both ensembles adopting three different approaches: firstly, we study the model considering the exact Hamiltonian of the system, secondly, we approximate the total energy by introducing the spin variable approach, and lastly, we perform an analysis based on the energy balances of the system.

2.1 Exact Helmholtz ensemble

In this Section, we adopt the statistical mechanics framework and we study the system embedded in a thermal bath at temperature T. The objective of this investigation is to examine the model's thermo-mechanical response at the thermodynamic equilibrium considering it in the Helmholtz ensemble corresponding to the application of the isometric conditions. Based on the previous premises, we can write the total energy of the system as

$$\Phi_H(y) = \frac{1}{2}l(Y-y)^2 + \frac{1}{2}ky^2 + E_b(y), \tag{2.1}$$

where the first and second addends are the potential energy contributions related to the l and k springs respectively while $E_b(y)$ is the exact potential energy contribution of the breakable spring

h defined as

$$E_b(y) = \begin{cases} \frac{1}{2}hy^2 & \text{if } |y| < Y_M, \\ \frac{1}{2}hY_M^2 & \text{if } |y| \geq Y_M. \end{cases} \tag{2.2}$$

We notice that, introducing the following characteristic function

$$\chi_A(y) = \begin{cases} 1 & \text{if } y \in A, \\ 0 & \text{if } y \notin A, \end{cases} \tag{2.3}$$

where $A = (-Y_M, Y_M)$, it is possible to write the previous Hamiltonian as

$$\Phi_H(y) = \frac{1}{2}l(Y-y)^2 + \frac{1}{2}ky^2 + \frac{1}{2}hy^2\chi_A(y) + \frac{1}{2}hY_M^2(1-\chi_A(y)). \tag{2.4}$$

We observe that, by considering the particular value that the characteristic function $\chi_A(y)$ assumes, we are able to establish if the system is in the intact configuration, when $\chi_A(y \in A) = 1$ (meaning that the breakable spring h is still intact), or in the broken configuration, when $\chi_A(y \notin A) = 0$ (meaning that the breakable spring h has overcome its maximum threshold Y_M). This is an important feature for the characteristic function because it can be then used as a helpful tool in the evaluation of some interesting quantities like the average number of intact breakable springs as we will see in the following discussion. Thanks to the Hamiltonian, we can evaluate the partition function of the system defined as

$$Z_H(Y) = \int_{\mathbb{R}} e^{-\frac{\Phi_H(y)}{K_B T}} \mathrm{d}y. \tag{2.5}$$

Writing explicitly the definition of $\chi_A(y)$ for the Hamiltonian $\Phi_H(y)$ in the previous integral, we can separate the partition function into three different domains of integration, namely

$$\begin{aligned} Z_H(Y) = &\int_{-\infty}^{-Y_M} e^{-\frac{l}{2K_BT}(Y-y)^2 - \frac{k}{2K_BT}y^2 - \frac{h}{2K_BT}Y_M^2} \mathrm{d}y \\ &+ \int_{-Y_M}^{Y_M} e^{-\frac{l}{2K_BT}(Y-y)^2 - \frac{k}{2K_BT}y^2 - \frac{h}{2K_BT}y^2} \mathrm{d}y \\ &+ \int_{Y_M}^{+\infty} e^{-\frac{l}{2K_BT}(Y-y)^2 - \frac{k}{2K_BT}y^2 - \frac{h}{2K_BT}Y_M^2} \mathrm{d}y. \end{aligned} \tag{2.6}$$

The last three integrals can be easily evaluated thanks to the following generalized Gaussian integral valid for a generic domain of integration $(a,b) \in \mathbb{R}$,

$$\int_a^b e^{-\alpha x^2 + \beta x} \mathrm{d}x = \frac{\sqrt{\pi} e^{\frac{\beta^2}{4\alpha}}}{2\sqrt{\alpha}} \left\{ \phi\left[\sqrt{\alpha}\left(b - \frac{\beta}{2\alpha}\right)\right] - \phi\left[\sqrt{\alpha}\left(a - \frac{\beta}{2\alpha}\right)\right] \right\}, \tag{2.7}$$

where $\phi(x)$ is the error function defined as

$$\phi(x) = \frac{2}{\sqrt{\pi}} \int_0^x e^{-t^2} \mathrm{d}t, \tag{2.8}$$

and, in particular, $\phi(\pm\infty) = \pm 1$ and $\phi(-x) = -\phi(x)$. After some long but straightforward calculations, we can write the partition function as

$$\begin{aligned} Z_H(Y) = e^{-\frac{hY_M^2}{2K_BT} - \frac{lkY^2}{2K_BT(l+k)}} \sqrt{\frac{\pi}{\alpha(l+k)}} \left[\frac{\Gamma(l+k)+2}{2}\right] \\ - e^{-\frac{l(k+h)Y^2}{2K_BT(l+k+h)}} \sqrt{\frac{\pi}{\alpha(l+k+h)}} \left[\frac{\Gamma(l+k+h)}{2}\right], \end{aligned} \tag{2.9}$$

where, for the sake of readability, we introduced the two following functions

$$\alpha(p) = \frac{p}{2K_BT}, \tag{2.10}$$

$$\Gamma(p) = \phi\left[\sqrt{\alpha(p)}\left(-Y_M - \frac{lY}{p}\right)\right] - \phi\left[\sqrt{\alpha(p)}\left(Y_M - \frac{lY}{p}\right)\right]. \tag{2.11}$$

Thanks to the partition function, we are now able to evaluate the average value of some interesting quantities. The first quantity we are interested in is the average force applied to the upper substrate, namely $\langle f \rangle$, that is given by

$$\langle f \rangle = \frac{1}{Z_H} \int_{\mathbb{R}} f e^{-\frac{\Phi_H(y)}{K_BT}} \mathrm{d}y. \tag{2.12}$$

Now, if we observe that the force can be derived from the potential energy as $f = \mathrm{d}\Phi_H/\mathrm{d}Y$, it is easy to prove the validity of the following alternative compact version for Eq.(2.12)

$$\langle f \rangle = -K_BT \frac{\partial \log Z_H}{\partial Y}. \tag{2.13}$$

Another interesting quantity is the average number of intact breakable springs that, thanks to the particular relation between the characteristic function $\chi_A(y)$ and the state of the breakable spring h, can be calculated as

$$\langle \chi_A(y) \rangle = \frac{1}{Z_H} \int_{\mathbb{R}} \chi_A(y) e^{-\frac{\Phi_H(y)}{K_BT}} \mathrm{d}y. \tag{2.14}$$

By deriving the logarithm of the partition function, $\log Z_H$, by Y_M, moreover, we obtain

$$-\frac{K_BT}{hY_M} \frac{\partial \log Z_H}{\partial Y_M} = \frac{1}{Z_H} \int_{\mathbb{R}} \big(1 - \chi_A(y)\big) e^{-\frac{\Phi_H(y)}{K_BT}} \mathrm{d}y = \langle 1 - \chi_A(y) \rangle, \tag{2.15}$$

that can be used to rewrite Eq.(2.14) in the following compact version

$$\langle \chi_A(y) \rangle = 1 + \frac{K_BT}{hY_M} \frac{\partial \log Z_H}{\partial Y_M}. \tag{2.16}$$

In Fig.2.3, we show the average force $\langle f \rangle$ (left panel) and the average number of intact breakable springs $\langle \chi_A(y) \rangle$ (right panel) versus the dimensionless elongation Y/Y_M for a system composed of springs of elastic constants identically equal to 1 ($l = k = h = 1$) while also varying the thermal to elastic energy ratio $K_BT/(hY_M^2)$. In the figure, we can observe the main effects of the presence of a breakable spring h in the system. As one can notice from the force-extension graph (left panel of Fig.2.3), in fact, one of the main effects of the breakable spring is that of

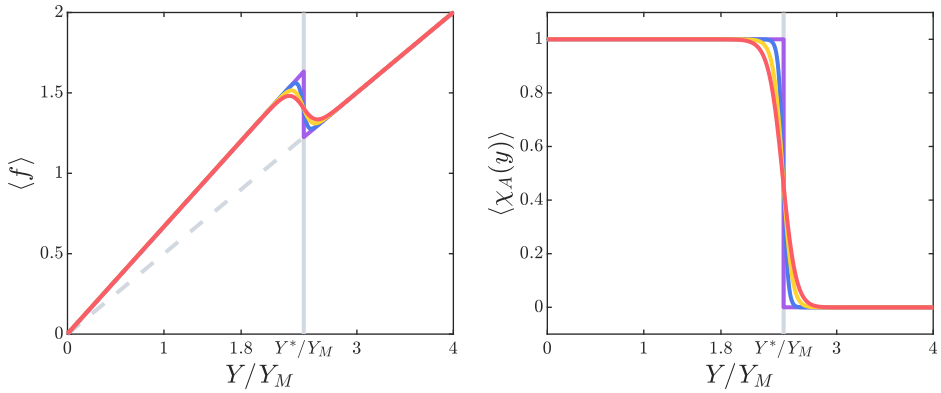

Figure 2.3: Behavior of the two-rigidity model with variable thermal to elastic energy ratio $K_BT/(hY_M^2) = \{0, 0.01, 0.02, 0.03\}$ (purple, blue, yellow and red curves respectively). Here, the purple curves correspond to the pure mechanical case at a null temperature. The average force $\langle f \rangle$ and the average number of intact breakable springs $\langle \chi_A(y) \rangle$ are presented versus the dimensionless elongation Y/Y_M, where, in both cases, $l = k = h = 1$ and $Y_M = 1$. In both panels is shown the dimensionless elongation Y^*/Y_M, responsible for the change in rigidity.

changing the rigidity of the system depending on the specific elongation parameter Y/Y_M. In the force-extension graph, we can notice that the slope of the curves changes from a steeper one to a less steep one in correspondence with the rupture of the breakable spring h at a specific total elongation that, for now, we will simply denote as Y^*/Y_M. Trying to explain the system behaviors observed in the figures, from a merely mechanical point of view, one could think that the system reaches its rupture point simply when the breakable spring h elongation reaches its breaking threshold Y_M. Keeping this in mind, if we consider the system just before its breaking point, we know that the force exerted by the spring l has to be equal to the one exerted by the combined actions of k and h springs, *i.e.* $l(Y - y) = (k + h)y$ (where Y is the total elongation of the system and y is the elongation of k and h parallel springs). If we then solve the latter identity for Y and we set the breakable spiring elongation equal to its breaking threshold, $y = Y_M$, we obtain a result, $Y/Y_M = 3$ (in the case of $l = k = h = 1$), apparently in disagreement with what we observe from the force-extension curves of Fig.2.3, where the actual breaking point Y^*/Y_M seems to anticipate our merely mechanical result $Y/Y_M = 3$. This apparent incongruity, fortunately, will be fully analyzed and explained in the following discussion thanks to the study of the same problem from an energy-balance point of view rather than relying on the use of the statistical mechanic's principles alone. In the right panel of Fig.2.3, it is shown the average number of intact breakable springs $\langle \chi_A(y) \rangle$ versus the adimensional elongation parameter Y/Y_M. In this graph, the average number of intact springs h, $\langle \chi_A(y) \rangle$, drops to zero in correspondence to the complete failure of the system *i.e.* when the elongation reaches its rupture point Y^*/Y_M. We remark again here that in the model used to obtain the results shown in the figure so far, we used three springs of elastic constant equal to one, $l = k = h = 1$, and an elongation threshold for the breakable spring h of $Y_M = 1$.

The two different slopes of the two linear branches in the force-extension curves correspond to the effective elastic constants of the system in the intact and broken configuration and can be evaluated using the following equation

$$k_{\text{eff}} = \left(\frac{1}{l} + \frac{1}{k+h} \right)^{-1} = \frac{l(k+h)}{l+k+h}. \tag{2.17}$$

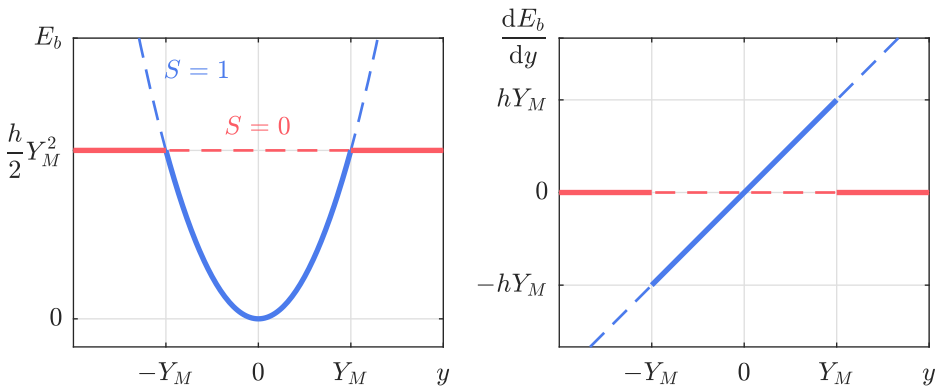

Figure 2.4: Spin approach on the potential energy of a breakable spring of elastic constant h (left) and resulting force (right). The spin assumes value $S=1$ when the spring is in the intact conformation and behaves like a standard linear spring (blue dashed curves) and $S=0$ when it is in the broken configuration (red dashed curves). The continuous curves are for reference and correspond to the exact potential energy profile.

The effective elastic constant, then, assumes the value $k_{\text{eff}}=\frac{2}{3}$ when $(Y/Y_M)<(Y^*/Y_M)$ and all the three springs are intact ($l=k=h=1$) and the smaller value $k_{\text{eff}}=\frac{1}{2}$ when $(Y/Y_M)>(Y^*/Y_M)$ in agreement to the fact that, in this second branch, the h spring has overcome its elongation threshold Y_M resulting in its breaking. Furthermore, looking at both panels of Fig.2.3, it is interesting to observe that the breaking elongation point Y^*/Y_M is independent of the temperature T while the only effect of the temperature on the system is that of smoothing out the curves. The independence from the temperature on the behavior of the transition of the system from the intact to the broken configuration is the direct result of the fact that this system is composed of a single unit. In the following discussion, we will see that the temperature does play a crucial role in the transition of the system when this is composed of many units interacting with each other.

2.2 Helmholtz ensemble with spin approximation

In this section, we adopt a statistical mechanics approach to study the system at equilibrium while introducing the spin variable approximation to deal with the non-convex potential energy of the breakable spring h. This means that, instead of considering the exact profile of the potential energy $E_b(y)$ of the breakable spring as defined in Eq.(2.2), we approximate it by introducing a new discrete variable called spin, S, in the phase space. This variable can assume only two values depending on the particular state of the spring h, namely $S=1$ when the h spring is intact ($|y|<Y_M$) or $S=0$ when it is in the broken state ($|y|>Y_M$). This new discrete variable S is then used to approximate the potential energy of the spring h with that of a standard intact linear spring of elastic constant h and elongation y, when $S=1$ (blu dashed curve in the left panel of Fig.2.4), or with a constant potential energy $\frac{1}{2}hY_M^2$ that corresponds to a null force, when $S=0$ (red dashed curve in the left panel of Fig.2.4). It is important to remark that the evaluation of the partition function based on the spin variable approach assumes that for both configurations, broken and intact, all the possible deformations y can be attained by the system. This, in general, could represent a problem in the calculation of the partition function but, as shown numerically in Ref.[91], with typical experimental temperatures, the effects of this approximation can be considered statistically negligible since these artificial configurations (superposition of dashed

curves in the left panel of Fig.2.4) have energy sensibly higher than real configurations (continuous curves of Fig.2.2). The new definition for the breakable spring contribution to the total potential energy is then described by

$$E_b(y) = \begin{cases} \frac{1}{2}hy^2 & \text{if } S = 1, \\ \frac{1}{2}hY_M^2 & \text{if } S = 0. \end{cases} \tag{2.18}$$

We can now use the spin variable S in the same way we previously used the characteristic function $\chi_A(y)$ in order to write the total potential energy of the system as follows

$$\Phi_H(y,S) = \frac{1}{2}l(Y-y)^2 + \frac{1}{2}ky^2 + \frac{1}{2}hy^2S + \frac{1}{2}hY_M^2(1-S), \tag{2.19}$$

depending on y and S. Observing Eq.(2.19), it is evident the similarity between the spin variable S and the characteristic function $\chi_A(y)$ defined in Eq.(2.3). The crucial difference between the two is that, now, the spin variable S belongs to the phase space. The parallelism between S and $\chi_A(y)$ will become clear once we evaluate the average number of intact breakable spring h for the spin approximation case. To evaluate the partition function of the system we have to sum over the spin variable values

$$Z_H(Y) = \sum_{S=0,1} \int_{\mathbb{R}} e^{-\frac{\Phi_H(y,S)}{K_BT}} \, \mathrm{d}y. \tag{2.20}$$

Writing explicitly the expression for the total energy and summing over the spin variable values, we obtain

$$\begin{aligned} Z_H(Y) = &\int_{\mathbb{R}} e^{-\frac{l}{2K_BT}(Y-y)^2 - \frac{k}{2K_BT}y^2 - \frac{h}{2K_BT}Y_M^2} \, \mathrm{d}y \\ &+ \int_{\mathbb{R}} e^{-\frac{l}{2K_BT}(Y-y)^2 - \frac{k}{2K_BT}y^2 - \frac{h}{2K_BT}y^2} \, \mathrm{d}y, \end{aligned} \tag{2.21}$$

that is easily solved, using the Gaussian integral, eventually obtaining

$$Z_H(Y) = \sqrt{\frac{2\pi K_BT}{l+k}} e^{-\frac{lkY^2}{2K_BT(l+k)} - \frac{hY_M^2}{2K_BT}} + \sqrt{\frac{2\pi K_BT}{l+k+h}} e^{-\frac{l(k+h)Y^2}{2K_BT(l+k+h)}}. \tag{2.22}$$

We note that thanks to the introduction of the spin variable approximation, the integrals that appeared in the calculation of the partition function were now evaluated on the entire real axis $\mathbb{R}$ instead of on limited domains of integration, as seen previously in the exact potential energy calculations. This represents a huge simplification for the calculation of the partition function and, consequently, for the evaluation of the interesting quantities like the average force $\langle f \rangle$, previously introduced in Eq.(2.13), or the average number of intact breakable springs that, now, corresponds exactly to $\langle S \rangle$. As briefly introduced before, we notice that the spin variable is defined exactly as the characteristic function $\chi_A(y)$ introduced in Eq.(2.3) and, since the spin variable appears in the definition of the potential energy Φ_H, in the same way that $\chi_A(y)$ did, it is easy to see that $\langle S \rangle$ is exactly the average number of intact breakable springs h, namely

$$\langle S \rangle = 1 + \frac{K_BT}{hY_M} \frac{\partial \log Z_H}{\partial Y_M}. \tag{2.23}$$

As shown in Fig.2.5, both the average force $\langle f \rangle$ and the average number of intact breakable springs $\langle S \rangle$ versus the dimensionless elongation Y/Y_M of the system obtained with the spin approximation (dashed curves) are in good agreement with the results obtained with the exact calculations (continuous curves). We notice that the spin approximation is more precise for

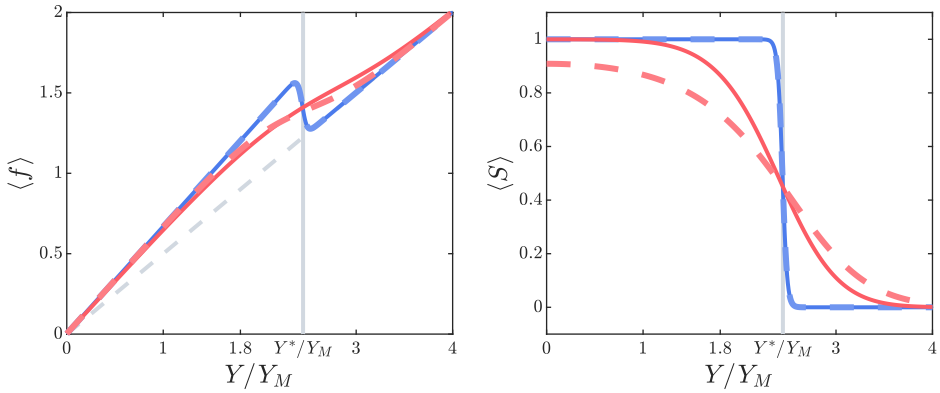

Figure 2.5: Comparison between the spin-approximated quantities (dashed curves) and the corresponding exact results (continuous curves) for $\langle f \rangle$ and $\langle S \rangle$ versus the adimensional elongation Y/Y_M. In both cases, the elastic constants are $l = k = h = 1$ and $Y_M = 1$, while the thermal to elastic energy ratio assumes the values $K_B T/(hY_M^2) = \{0.01, 0.2\}$ (respectively in blue and in red).

low temperatures. Furthermore, we observe that even in this case the rupture elongation does not correspond to the one someone would expect but, instead, is shifted as in the exact case. We remark again that the spin variable approximation provides a simpler and quicker way to evaluate the partition function of the system and this is even more useful while evaluating partition functions for a system made of several units as we will see in the next Chapters. In the following Section, thanks to the energy-balance approach, we will understand the reason behind the apparent discrepancy between the real breaking point of the system Y^*/Y_M and the one wrongfully predicted adopting a merely mechanic approach.

2.3 Helmholtz ensemble from an energetic perspective

In this section, we study the model in the isometric configuration adopting the principles of energy minimization which are valid under the zero temperature assumptions. By doing so, we can understand why it looks like the system tries to anticipate its breaking point in the force-extension curves seen before in both the exact and the approximated calculation cases (see Fig.2.3 and Fig.2.5).

In order to understand when the change in rigidity occurs, we need to understand in which state the system prefers to be from an energetic point of view given a prescribed elongation Y. The total potential energy of the system is

$$\Phi_H(y) = \begin{cases} \frac{1}{2}l(Y-y)^2 + \frac{1}{2}ky^2 + \frac{1}{2}hy^2 & \text{if } |y| < Y_M, \\ \frac{1}{2}l(Y-y)^2 + \frac{1}{2}ky^2 + \frac{1}{2}hY_M^2 & \text{if } |y| > Y_M. \end{cases} \tag{2.24}$$

Given a prescribed elongation Y, we search for the value of y, $y_{\min}$, that minimizes the potential energy. We start considering the $|y| < Y_M$ case, where the potential energy is defined as

$$\Phi_H(y) = \frac{1}{2}l(Y-y)^2 + \frac{1}{2}ky^2 + \frac{1}{2}hy^2. \tag{2.25}$$

Deriving $\Phi_H(y)$ by y and setting it equal to zero, $\frac{\partial \Phi_H(y)}{\partial y} = 0$, we obtain the following minimizing value for y

$$y_{\min} = \frac{l}{l+k+h} Y, \tag{2.26}$$

with the corresponding minimal potential energy

$$\Phi_H(y_{\min}) = \frac{l}{2}\left(\frac{k+h}{l+k+h}\right) Y^2. \tag{2.27}$$

If we go through the same process for the second range, $|y| > Y_M$, where the potential energy is defined as

$$\Phi_H(y) = \frac{1}{2} l (Y-y)^2 + \frac{1}{2} k y^2 + \frac{1}{2} h Y_M^2, \tag{2.28}$$

eventually, we obtain the following minimizing value for y

$$y_{\min} = \frac{l}{l+k} Y, \tag{2.29}$$

with the corresponding minimal potential energy

$$\Phi_H(y_{\min}) = \frac{1}{2}\frac{lk}{l+k} Y^2 + \frac{1}{2} h Y_M^2. \tag{2.30}$$

Now, by comparing when the first minimal potential energy, valid for the $|y| < Y_M$ case, is greater than the minimal potential energy valid for $|y| > Y_M$, we can find the total elongation Y^* that defines the threshold in which the system switches from the hard-rigidity to the soft-rigidity configuration,

$$\frac{l}{2}\left(\frac{k+h}{l+k+h}\right) Y^{*2} > \frac{1}{2}\frac{lk}{l+k} Y^{*2} + \frac{1}{2} h Y_M^2 \tag{2.31}$$

that, after some simple calculations, eventually gives

$$Y^* > \sqrt{\frac{(l+k)(l+k+h)}{l^2}}\, Y^M. \tag{2.32}$$

This value is in agreement with the results for the average force $\langle f \rangle$ and the average number of intact breakable springs $\langle \chi_A(y) \rangle$ (and $\langle S \rangle$) shown in Fig.2.3 (and Fig.2.5) where we can confirm that, given a system where $l = k = h = 1$ and $Y_M = 1$, the rupture elongation parameter is equal to $Y^*/Y_M = \sqrt{6}$. To conclude, this energetic approach (without thermal effects) is in agreement with both the exact and approximated approaches and offers a useful tool to be able to evaluate the correct threshold point of the entire system Y^*.

2.4 Exact Gibbs ensemble

We introduce the Gibbs ensemble, characterized by the presence of a prescribed force f (see right panel of Fig.2.1), by writing the corresponding exact Hamiltonian

$$\Phi_G(y, Y) = -fY + \frac{1}{2} l (Y-y)^2 + \frac{1}{2} k y^2 + E_b(y), \tag{2.33}$$

By observing the Hamiltonian, we can notice that the addition of the potential energy contribution deriving from the applied prescribed force f to the upper substrate is what differs from the Helmholtz case along with the fact that, now, Y belongs to the phase space as y does. The definition of $E_b(y)$ instead is equal to the one introduced in Eq.(2.2), namely

$$E_b(y) = \begin{cases} \frac{1}{2}hy^2 & \text{if } |y| < Y_M, \\ \frac{1}{2}hY_M^2 & \text{if } |y| \geq Y_M. \end{cases} \tag{2.34}$$

In the same spirit, adopting the same characteristic function $\chi_A(y)$ (Eq.(2.3)) introduced for the Helmholtz case, we can write the Hamiltonian of the system as

$$\Phi_G(y,Y) = -fY + \frac{1}{2}l(Y-y)^2 + \frac{1}{2}ky^2 + \frac{1}{2}hy^2\chi_A(y) + \frac{1}{2}hY_M^2(1-\chi_A(y)). \tag{2.35}$$

This potential energy can then be used to evaluate the partition function of the system

$$Z_G(f) = \int_{\mathbb{R}} \mathrm{d}y \int_{\mathbb{R}} e^{-\frac{\Phi_G(y,Y)}{K_BT}} \mathrm{d}Y, \tag{2.36}$$

that, now, is a function of the prescribed force f. We briefly observe that it is possible to swap the two integrals appearing in the definition of the partition function thanks to Fubini's theorem. Using the Gaussian integral introduced earlier in Eq.(2.7) we can perform the integrals present in $Z_G(f)$ eventually obtaining

$$\begin{aligned} Z_G(f) = &\frac{\pi K_BT}{\sqrt{lk}} e^{-\frac{hY_M^2}{2K_BT} + \frac{f^2}{2K_BT}\frac{l+k}{lk}} \left[\Lambda(k) + 2\right] \\ &- \frac{\pi K_BT}{\sqrt{l(k+h)}} e^{\frac{f^2}{2K_BT}\frac{l+k+h}{l(k+h)}} \Lambda(k+h), \end{aligned} \tag{2.37}$$

where, for the sake of readability, we use the function $\alpha(p)$, previously defined in Eq.(2.10), and we introduce a new function $\Lambda(p)$, similar to the function $\Gamma(p)$ defined in Eq.(2.11), as

$$\alpha(p) = \frac{p}{2K_BT}, \tag{2.38}$$

$$\Lambda(p) = \phi\left[\sqrt{\alpha(p)}\left(-Y_M - \frac{f}{p}\right)\right] - \phi\left[\sqrt{\alpha(p)}\left(Y_M - \frac{f}{p}\right)\right]. \tag{2.39}$$

Thanks to the partition function, we can now evaluate the average value of the elongation of the system $\langle Y \rangle$ and the average number of intact springs $\langle \chi_A(y) \rangle$, given a fixed applied force f

$$\langle Y \rangle = K_BT \frac{\partial \log Z_G}{\partial f}, \tag{2.40}$$

$$\langle \chi_A(y) \rangle = 1 + \frac{K_BT}{hY_M} \frac{\partial \log Z_G}{\partial Y_M}. \tag{2.41}$$

In Fig.2.6 we show the average adimensional elongation paramter $\langle Y \rangle / Y_M$ (left panel) and the average number of intact breakable springs $\langle \chi_A(y) \rangle$ (right panel) versus the prescribed force f for a system composed of springs of elastic constants $l = k = h = 1$ and for different thermal to elastic energy ration $K_BT/(hY_M^2)$. As we can see from the force-extension panel of the figure, the mechanical response to the variation of the prescribed force f, especially for low temperatures,

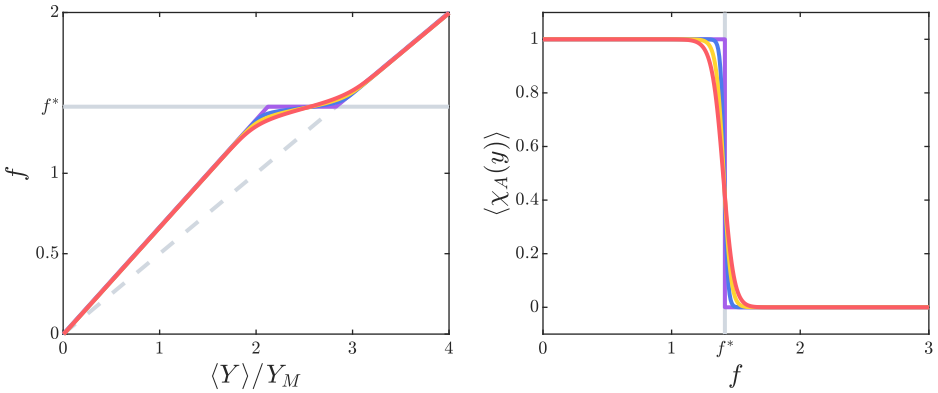

Figure 2.6: Behavior of the two-rigidity model with variable thermal to elastic energy ratio $K_BT/(hY_M^2) = \{0, 0.01, 0.02, 0.03\}$ (purple, blue, yellow and red curves respectively). The purple curves correspond to the pure mechanical case at a null temperature. The average elongation $\langle Y \rangle$ and the average number of intact breakable springs $\langle \chi_A(y) \rangle$ are presented versus the fixed force f, where, in both cases, $l = k = h = 1$ and $Y_M = 1$. In both panels, the force responsible for the change in rigidity, f^*, is shown.

presents a force plateau that corresponds to a transition for the system's rigidity. This change in rigidity occurs when the force f reaches a specific value $f = f^*$ that does not correspond to the result one could obtain basing the analysis only on mechanical principles (as seen before for the Helmholtz case). If we think about the system from a purely mechanical point of view, in fact, the force necessary to break the breakable spring h should be $f = (k+h)Y_M$ that, in the case shown in Fig.2.6 where the elastic constants are $l = k = h = 1$ and the elongation threshold is $Y_M = 1$, is equal to $f = 2$ that is higher than the correct one shown in the figure ($f = 2 > f^*$). This apparent discrepancy will be fully understood and explained in the following discussion while adopting an energy-balance approach as previously done for the Helmholtz case.

The difference between the two rigidity regimes emerges from the difference in slope of the two curve branches before and after the breaking force point and the same considerations done in the Helmholtz case hold in this case as well. The threshold force f^*, responsible for the transition between the two rigidity, is even more clear when observing the right panel of Fig.2.6 where the number of intact breakable spring h changes from 1 to 0 exactly at $f = f^*$. Furthermore, we stress the fact that, even in the Gibbs ensemble, f^* does not depend on the temperature that, instead, is responsible only for smoothing the curves while increasing. This temperature independence of the threshold force f^* is expected since the model is made of a single unit.

2.5 Gibbs ensemble with spin approximation

As introduced previously in the Helmholtz case, in this Section we adopt the spin variable approach to study the system in the Gibbs ensemble. As previously done, we introduce a spin variable S to help us approximate the total potential energy of the system. The spin variable will then assume the value $S = 0$ when the breakable spring is in the break state and $S = 1$ when it is in the intact conformation. By doing so, we are able to express the total energy as

$$\Phi_G(y, Y, S) = -fY + \frac{1}{2}l(Y-y)^2 + \frac{1}{2}ky^2 + \frac{1}{2}hy^2S + \frac{1}{2}hY_M^2(1-S), \tag{2.42}$$

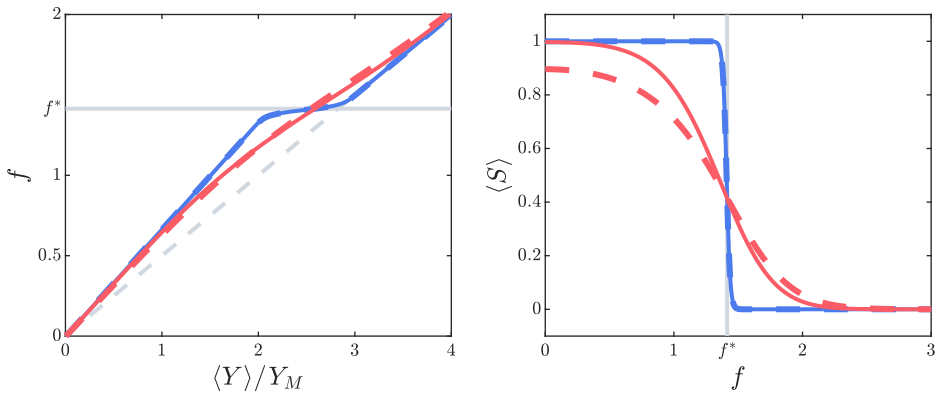

Figure 2.7: Comparison between the spin-approximated quantities (dashed curves) and the corresponding exact results (continuous curves) for $\langle Y\rangle/Y_M$ and $\langle S\rangle$ versus the applied force f. In both cases, the elastic constants are $l=k=h=1$ and $Y_M=1$, while the thermal to elastic energy ratio assumes the values $K_BT/(hY_M^2)=\{0.01,0.2\}$ (respectively in blue and in red).

that, now, is a function of y, Y and S. We proceed by evaluating the partition function of the system that, in the spin variable approximation, assumes the following definition

$$Z_G(f)=\sum_{S=0,1}\int_{\mathbb{R}}\mathrm{d}y\int_{\mathbb{R}}e^{-\frac{\Phi_G(y,Y,S)}{K_BT}}\mathrm{d}Y \tag{2.43}$$

Writing explicitly the expression for the total energy and explicitly expressing the sum over the spin values, we obtain

$$\begin{aligned}Z_G(f)=&\int_{\mathbb{R}}\mathrm{d}y\int_{\mathbb{R}}e^{\frac{fY}{K_BT}-\frac{l}{2K_BT}(Y-y)^2-\frac{k}{2K_BT}y^2-\frac{h}{2K_BT}Y_M^2}\mathrm{d}Y\\&+\int_{\mathbb{R}}\mathrm{d}y\int_{\mathbb{R}}e^{\frac{fY}{K_BT}-\frac{l}{2K_BT}(Y-y)^2-\frac{k}{2K_BT}y^2-\frac{h}{2K_BT}y^2}\mathrm{d}Y,\end{aligned} \tag{2.44}$$

that is easily solved using the Gaussian integral, eventually obtaining

$$Z_G(f)=\frac{2\pi K_BT}{\sqrt{lk}}e^{\frac{f^2}{2K_BT}\left(\frac{l+k}{lk}\right)-\frac{hY_M^2}{2K_BT}}+\frac{2\pi K_BT}{\sqrt{l(k+h)}}e^{\frac{f^2}{2K_BT}\left(\frac{l+k+h}{l(k+h)}\right)}. \tag{2.45}$$

Thanks to this approximated partition function we can evaluate the following quantities

$$\langle Y\rangle=K_BT\frac{\partial\log Z_G}{\partial f}, \tag{2.46}$$

$$\langle S\rangle=1+\frac{K_BT}{hY_M}\frac{\partial\log Z_G}{\partial Y_M}. \tag{2.47}$$

In Fig.2.7, we can see that the approximations obtained both for $\langle Y\rangle/Y_M$ and $\langle S\rangle$ versus the fixed force f are in good agreement with the results obtained with the exact calculations. As in the Helmholtz spin approximation, once again the spin approximation is more accurate for low temperatures as we should expect. Furthermore, we observe that even in this case the rupture force does not correspond to the one we would expect but, instead, is shifted as in the exact

case. In the following section, we will solve this apparent dilemma by adopting an energy-balance approach.

2.6 Gibbs ensemble from an energetic perspective

In this section, we study the model in the isotensional configuration adopting the principles of energy minimization in order to obtain the exact rupture force f^* responsible for the rigidity change of the system. The total potential energy of the system is given by

$$\Phi_G(y,Y) = \begin{cases} -fY + \frac{1}{2}l(Y-y)^2 + \frac{1}{2}ky^2 + \frac{1}{2}hy^2 & \text{if } |y| < Y_M, \\ -fY + \frac{1}{2}l(Y-y)^2 + \frac{1}{2}ky^2 + \frac{1}{2}hY_M^2 & \text{if } |y| > Y_M. \end{cases} \tag{2.48}$$

Given a fixed force f, we search for the quantities y and Y that minimize the potential energy. We start by considering our system in the $|y| < Y_M$ case, where the potential energy is defined as

$$\Phi_G(y,Y) = -fY + \frac{1}{2}l(Y-y)^2 + \frac{1}{2}ky^2 + \frac{1}{2}hy^2. \tag{2.49}$$

We derive $\Phi_G(y,Y)$ by y and Y separately, obtaining

$$\frac{\partial \Phi_G(y,Y)}{\partial y} = -l(Y-y) + hy + ky = 0, \tag{2.50}$$

$$\frac{\partial \Phi_G(y,Y)}{\partial Y} = -f + l(Y-y) = 0. \tag{2.51}$$

After some straightforward calculations, we obtain the two minimizing values

$$y_{\min} = \frac{f}{h+k}, \tag{2.52}$$

$$Y_{\min} = \frac{f}{h+k} + \frac{f}{l}. \tag{2.53}$$

that we use to evaluate the resulting minimal potential energy, obtaining

$$\Phi_G(y_{\min}, Y_{\min}) = -\frac{1}{2}\frac{f^2}{l} - \frac{1}{2}\frac{f^2}{h+k}. \tag{2.54}$$

Repeating the same process for the $|y| > Y_M$ case, we obtain the following minimized potential energy

$$\Phi_G(y_{\min}, Y_{\min}) = -\frac{1}{2}\frac{f^2}{k} - \frac{1}{2}\frac{f^2}{l} + \frac{1}{2}hY_M^2, \tag{2.55}$$

and, comparing the two minimized potential energy, we obtain the exact rupture force at which the system changes its rigidity, namely

$$f^* = \sqrt{k(h+k)}Y_M \tag{2.56}$$

We observe that using the same parameters of Fig.2.7, we have $f^* = \sqrt{2}$ in agreement with the results shown in the figure. Therefore, as in the Helmholtz ensemble, also in the present Gibbs case, the energetic approach (without thermal effects) is in perfect agreement with the exact calculation based on statistical mechanics and with the spin approximation. This confirms the

value of the rupture threshold given in Eq.(2.56) and underlines the fact that the correct approach to determining the rupture thresholds is the one based on energetic assumptions.

Chapter 3

Adhesion

3.1 Introduction

As introduced earlier, microinstabilities can be divided into two different classes. On the one side, we can have a bistable (or multistable) behavior between one ground state and one (or more) metastable state representing different conformations or configurations of the intact yet deformable system units, for example the conformational transitions in polymers or the martensitic transformations in solids. On the other side, we can also have transitions between the broken or unbroken states of some breakable units of the system. In this case, the system unit can switch from the intact condition to the damaged condition, and this process can be reversible or not depending on the specific situation. Examples of this scheme include the unzipping of hairpins, denaturation of macromolecules, and peeling of films.

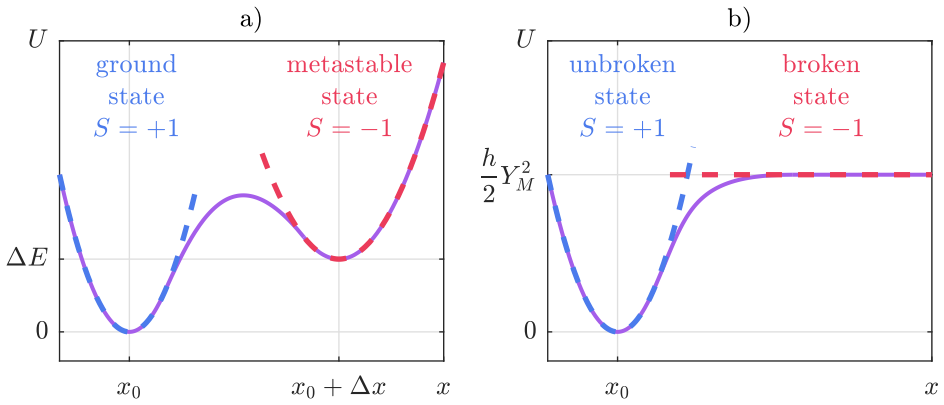

Figure 3.1: Paradigmatic potential energies of the system components for the two different classes of microinstabilities: bistability between a folded (ground) state and an unfolded (metastable) state (a), and damage process between the intact (unbroken) state and the damaged (broken) state (b).

To better appreciate the real difference between these two classes of micro-instabilities, we can observe from Fig.3.1 the potential energy $U(x)$ describing the behavior of the units in both cases

(we consider a one-dimensional geometry for the sake of simplicity). In the first case (Fig.3.1.a), we have an elastic unit with two configurations (*e.g.* folded and unfolded) corresponding to the two wells of the potential energy, having different equilibrium lengths and elastic constants. In the second case (Fig.3.1.b), we have a breakable mechanical unit with the unbroken configuration corresponding to the potential well, and the broken configuration corresponding to the horizontal portion of the curve (red dashed line). Indeed, in this region, the exerted force is zero, which means that we are in the broken state of the unit. In this Chapter, we will focus on the second class of microinstabilities concerning the switch between the intact and broken state of the system. The statistical mechanics of such a system can be studied by means of the spin variables approach introduced earlier in the discussion.

We would like to emphasize that the author of this thesis did not make a direct contribution to the model investigation presented in this chapter. However, it served as the initial inspiration for our study and contributed to our understanding of the prior research conducted by our team in this field. Nonetheless, we have included an examination of this model here to ensure continuity and clarity for the reader [93].

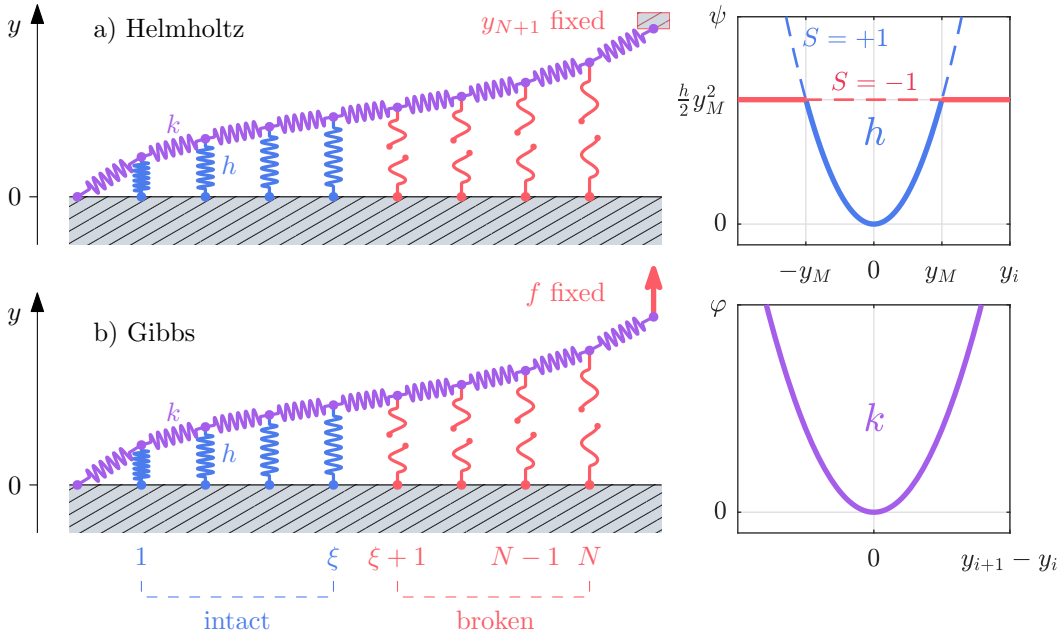

Figure 3.2: Scheme of the cohesion-decohesion process within both the Helmholtz (a) and the Gibbs (b) ensembles. While in the first case, we prescribe the position y_{N+1} and we measure the average force $\langle f \rangle$, in the second case we apply a fixed force f and we measure the average position $\langle y_{N+1} \rangle$. In both cases, we consider ξ unbroken vertical springs and $N - \xi$ broken vertical springs. The energy potentials φ and ψ correspond to the horizontal (continuous purple curve) and the vertical (continuous blu and red curves) springs, respectively. Moreover, in the breakable potential energy graph, the dashed curves correspond to the spin approximation.

We briefly recall that the main idea of the spin variables approach consists in introducing a series of discrete or *spin* variables to identify the state of the system units. More precisely, the bistable potential energy ψ of Fig.3.2, can be replaced by one quadratic function for the intact behavior of the system (dashed blu curve corresponding to $S = +1$ in the figure), and

a constant value for the broken part (dashed red line corresponding to $S = -1$ in the figure) that, then, results in a net zero force. The switching among them, then, is controlled by the associated spin variable. This strongly facilitates the calculation of the partition function and the corresponding thermodynamic quantities, useful to describe the system behavior. While the technique of the spin variables has been largely adopted to model units with transitions between ground and metastable states (see Fig.3.1.a), the case of units undergoing damage processes between unbroken ad broken states (Fig.3.1.b) has not been investigated by the same approach. As a matter of fact, the thermal effects on the damage processes are still far from being fully understood. Therefore, we propose here the analysis of the cohesion-decohesion process for a film deposited on a given substrate. This system is shown in Fig.3.2, where one can find the film represented by the horizontal mass-spring chain (purple springs of elastic constant k in the figure), and grounded to the substrate through a series of breakable springs (intact blu springs of elastic constant h and broken red springs exerting a null force). It is a simplified scheme paradigmatically representing several situations including *e.g.* hairpin unzipping, macromolecular denaturation, or film peeling.

The spin variables method allows for describing the system response, at a fixed temperature, within two different statistical ensembles. Indeed, the peeling of the film can be induced by prescribing a given extension (see Fig.3.2.a, Helmholtz ensemble), or by applying an external force to the last unit of the chain (see Fig.3.2.b, Gibbs ensemble). From the point of view of statistical mechanics, the analysis of both ensembles is very important since allows the investigation of the ensembles equivalence problem in the thermodynamic limit (*i.e.* for very large systems) [56, 98, 108–112]. By combining the spin variables approach with some peculiar features of the tridiagonal matrices, we are able to present the complete mathematical solution of the problem for an arbitrary number N of elements of the chain and we can also elaborate the limiting case for $N \to \infty$. We provide evidence that the peeling of the film in the thermodynamic limit ($N \to \infty$) occurs at a given temperature-dependent critical force, which is the same for both Helmholtz and Gibbs's statistical ensembles. As we will soon discover, in fact, for the peeling of a chain of breakable springs (with energy function ψ as in Fig.3.2), we will obtain an unexpected temperature-dependent force plateau. In particular, we prove that the force is a decreasing function of the temperature. This is coherent with the fact that thermal fluctuations foster the decohesion, allowing the escape from the well and, therefore, the exploration of the horizontal region of the ψ curve in Fig.3.2. The whole process is explained by means of a phase transition occurring at a given critical temperature, able to induce the complete decohesion of the film even without any external mechanical action. Although the critical force is the same for both Helmholtz and Gibbs's statistical ensembles, it is worth noticing that these ensembles are not equivalent in the thermodynamic limit. In fact, we verified that the ensembles exhibit different force-extension relations for $N \to \infty$.

To conclude, we underline that from the statistical mechanic's point of view, the system here investigated is particularly interesting for three reasons: (i) it can be analytically solved within both statistical ensembles; (ii) shows a phase transition at a critical temperature that can be calculated in closed form; and (iii) exhibits the ensembles nonequivalence in the thermodynamic limit, which is an unusual intriguing behavior.

The structure of this Chapter follows. In section 3.2, we define the system under investigation and the problems approached. In sections 3.3 and 3.4, we study the Helmholtz ensemble and its thermodynamic limit. Similarly, in sections 3.5 and 3.6, we study the Gibbs ensemble and its thermodynamic limit. In section 3.7 we show a good agreement between theoretical and experimental results concerning the unzipping of RNA and DNA hairpins. The conclusions (section 3.8) and a mathematical Appendix close this Chapter.

3.2 Problem statement

We take into consideration the scheme of Fig.3.2, where two configurations of the reversible and rate-independent cohesion-decohesion process are represented. This cohesion-decohesion scheme of an elastic layer from a substrate has been earlier introduced to describe a wide range of phenomena such as peeling of tapes, adhesion of geckos, and denaturation of DNA or other chemical structures [7, 8]. However, the thermal effects have been always neglected and represent the central point of the present investigation. In the first case (Fig.3.2.a), the process is controlled by the prescribed position y_{N+1} of the last element of the chain (isometric condition within the Helmholtz ensemble). In the second one (Fig.3.2.b), it is controlled by the applied force f (isotensional condition within the Gibbs ensemble). In both cases, the horizontal springs (elastic constant k) are purely harmonic with potential energy

$$\varphi = \frac{1}{2}k\left(y_{i+1} - y_i\right)^2, \tag{3.1}$$

while the vertical ones (elastic constant h) can be broken or unbroken being their state depending on their extension y_i. When $|y_i| > y_M$ they are broken and when $|y_i| < y_M$ they are unbroken. Therefore, an unbroken spring leads to a contribution to the potential energy equal to $\psi = \frac{1}{2}hy_i^2$ (when $|y_i| < y_M$) and a broken one a contribution equal to $\psi = \frac{1}{2}hy_M^2$ (when $|y_i| > y_M$). Indeed, we must impose the continuity of the potential energy over the whole configurational space (see the graph of ψ in Fig.3.2). The behaviors of both the intact springs k and the breakable springs h are shown in Fig.3.2.

The most important point, on which is grounded our approach, is that each vertical element is characterized by two different states (broken and unbroken configurations). In general, as previously anticipated, the statistical mechanics of a system of two-state units can be introduced by means of the so-called spin variables approach. Briefly, it consists in associating each unit of the system with a discrete spin variable, which can assume only two different values corresponding to the two possible states. In our case, these two different values correspond to the broken and unbroken states of each vertical element of the chain. Therefore, we should consider N spin variables S_i $(i = 1, \ldots, N)$, and the energy potential of each vertical spring should be written as

$$\psi = \frac{1}{4}(1 + S_i)hy_i^2 + \frac{1}{4}(1 - S_i)hy_M^2, \tag{3.2}$$

where $S_i = +1$ corresponds to the unbroken state and $S_i = -1$ corresponds to the broken one. With these assumptions, we have a phase space composed of the N continuous variables y_i and the N discrete variables S_i. The switching of the variable S_i and their statistics at thermodynamic equilibrium are directly controlled by the statistical ensemble (Helmholtz and Gibbs in our case) imposed on the system. This is the most general description of the system since we can envisage all the possible combinations of broken and unbroken elements along the chain. However, this complete model is rather complex and prevents the full mathematical analysis of the system. Nevertheless, since we are studying the cohesion-decohesion process under an external mechanical action applied to the right extremity of the system, we can simplify the model by assuming to have $N - \xi$ broken elements on the right of the chain and ξ unbroken elements on the left of the chain. It means that we suppose to have a single moving interface or domain wall between the intact region and the damaged region. This is a plausible hypothesis especially if we work at sufficiently low-temperature values. Under these hypotheses, the set of the two-state spin variables S_i are substituted by the single variable ξ belonging to the phase space of the system, and taking its values in the set $\{0, 1, 2, \ldots, N\} \ni \xi$. In this regard, the variable ξ can be considered

a multivalued spin variable. To conclude, it is worth underlining that the assumption to have a single moving domain wall between two regions with different physical states is similar to the one used in the so-called zipper model, largely used to describe the helix-coil transitions in proteins, the gel-sol transition of thermo-reversible gels, and the melting or denaturation of DNA [104–107].

The aim of this Chapter is to fully analyze the cohesion-decohesion process in both the Helmholtz and Gibbs ensembles, by providing a complete picture of the effect of the temperature on the system.

3.3 The Helmholtz ensemble

The Helmholtz ensemble is defined by a prescribed extension y_{N+1} of the last element of the chain, as represented in Fig.3.2.a (isometric condition). As previously anticipated, the variables belonging to the phase space of this system are the extensions y_i of the vertical springs ($i = 1, \dots, N$), and the number ξ of unbroken vertical springs. These considerations lead to a total potential energy of the system given by

$$\Phi = \sum_{i=0}^{N} \frac{1}{2} k (y_{i+1} - y_i)^2 + \sum_{i=1}^{\xi} \frac{1}{2} h y_i^2 + \sum_{i=\xi+1}^{N} \frac{1}{2} h y_M^2, \tag{3.3}$$

where $y_0 = 0$ and y_{N+1} are imposed. It is worth noticing that the last term of Φ is not an irrelevant additive constant since it depends implicitly on ξ, which is a variable of the phase space of the system. Eq.(3.3) can be easily rewritten as follows

$$\begin{aligned} \Phi = k \sum_{i=1}^{N} y_i^2 - k \sum_{i=1}^{N-1} y_i y_{i+1} + \frac{1}{2} k y_{N+1}^2 - k y_N y_{N+1} \\ + \frac{1}{2} h \sum_{i=1}^{\xi} y_i^2 + (N - \xi) \frac{1}{2} h y_M^2. \end{aligned} \tag{3.4}$$

For further convenience, the energy function Φ can be rearranged by means of the following matrix definition

$$\mathcal{A}_N^{\xi}(\eta) = \begin{pmatrix} a_1 & -1 & 0 & \cdots & \cdots & 0 \\ -1 & \ddots & \ddots & \ddots & & \vdots \\ 0 & \ddots & \ddots & \ddots & \ddots & 0 \\ \vdots & \ddots & \ddots & \ddots & \ddots & -1 \\ 0 & \cdots & \cdots & 0 & -1 & a_N \end{pmatrix} \in \mathcal{M}_{N,N}(\mathbb{R}). \tag{3.5}$$

where the diagonal elements are defined as follows

$$a_i = \begin{cases} 2 + \eta & \text{if } 1 \le i \le \xi, \\ 2 & \text{if } \xi + 1 \le i \le N, \end{cases} \tag{3.6}$$

The $\eta = h/k$ parameter appearing in the definition of the diagonal elements is the ratio between the elastic constants of vertical and horizontal elastic elements. The symbol $\mathcal{M}_{n,m}(\mathbb{R})$ represents

the linear space of the $n \times m$ matrices with real elements. We also define the vectors

$$\mathbf{y}^{\mathsf{T}} = \begin{pmatrix} y_1 & y_2 & \dots & y_N \end{pmatrix} \in \mathbb{R}^N, \tag{3.7}$$

$$\mathbf{v}^{\mathsf{T}} = \begin{pmatrix} 0 & \dots & 0 & 1 \end{pmatrix} \in \mathbb{R}^N. \tag{3.8}$$

These key premises allow rewriting the energy function as follows

$$\Phi\left(\mathbf{y}, \xi; y_{N+1}\right) = \frac{1}{2} k \mathbf{y}^{\mathsf{T}} \mathcal{A}_N^{\xi}(\eta) \mathbf{y} - k y_{N+1} \mathbf{v}^{\mathsf{T}} \mathbf{y} + \frac{1}{2} k y_{N+1}^2 + \frac{1}{2} k \eta (N - \xi) y_M^2, \tag{3.9}$$

where $\mathbf{y}$ and ξ are the main variables belonging to the phase space of the system and y_{N+1} is the externally applied extension of the last element of the chain. This expression of Φ is useful for the following developments since it is constituted by the sum of a quadratic form and a linear form in $\mathbf{y}$, with an additional term independent of $\mathbf{y}$. The partition function of the system analyzed within the Helmholtz ensemble can be therefore written as

$$Z_H(y_{N+1}) = \int_{\mathbb{R}^N} \sum_{\xi=0}^{N} e^{-\frac{\Phi(\mathbf{y}, \xi; y_{N+1})}{K_B T}} \mathrm{d}y_1 \dots \mathrm{d}y_N, \tag{3.10}$$

where we have integrated the continuous variable $\mathbf{y}$ and summed the discrete variable ξ. When Eq.(3.9) is substituted in Eq.(3.10), we get

$$\begin{aligned} Z_H(y_{N+1}) = e^{-\frac{k}{2K_B T} y_{N+1}^2} \sum_{\xi=0}^{N} e^{-\frac{1}{2K_B T} k \eta (N-\xi) y_M^2} \\ \times \int_{\mathbb{R}^N} e^{-\frac{1}{2K_B T} k \mathbf{y}^{\mathsf{T}} \mathcal{A}_N^{\xi}(\eta) \mathbf{y}} e^{\frac{k}{K_B T} y_{N+1} \mathbf{v}^{\mathsf{T}} \mathbf{y}} \mathrm{d}y_1 \dots \mathrm{d}y_N, \end{aligned} \tag{3.11}$$

where we can use the integral property

$$\int_{\mathbb{R}^N} e^{-\mathbf{y}^{\mathsf{T}} \mathcal{A} \mathbf{y}} e^{\mathbf{b}^{\mathsf{T}} \mathbf{y}} \mathrm{d}y_1 \dots \mathrm{d}y_N = \sqrt{\frac{\pi^N}{\det \mathcal{A}}} e^{\frac{1}{4} \mathbf{b}^{\mathsf{T}} \mathcal{A}^{-1} \mathbf{b}}, \tag{3.12}$$

holding for any symmetric and positive definite matrix $\mathcal{A}$. Indeed, by considering $\mathcal{A} = \frac{1}{2K_B T} k \mathcal{A}_N^{\xi}(\eta)$ and $\mathbf{b} = \frac{k}{K_B T} y_{N+1} \mathbf{v}$ in Eq.(3.12), we easily obtain

$$Z_H\left(y_{N+1}\right) = e^{-\frac{k y_{N+1}^2}{2K_B T}} \sum_{\xi=0}^{N} e^{-\frac{k y_M^2}{2K_B T} \eta (N-\xi)} \sqrt{\frac{(2\pi K_B T)^N}{k^N \det \mathcal{A}_N^{\xi}(\eta)}} e^{\frac{k y_{N+1}^2}{2K_B T} \mathbf{v}^{\mathsf{T}} \left[\mathcal{A}_N^{\xi}(\eta)\right]^{-1} \mathbf{v}}. \tag{3.13}$$

The knowledge of the partition function allows us to determine the average force necessary to prescribe the vertical extension y_{N+1} of the last element of the chain. As a matter of fact, a classical thermodynamic relation states that [98]

$$\langle f \rangle = -K_B T \frac{\partial \log Z_H}{\partial y_{N+1}} = -K_B T \frac{1}{Z_H} \frac{\partial Z_H}{\partial y_{N+1}}, \tag{3.14}$$

which can be elaborated to give the result

$$\begin{aligned}\langle f\rangle = ky_{N+1}\frac{1}{Z_H}\sum_{\xi=0}^{N}\sqrt{\frac{(2\pi K_BT)^N}{k^N\det\mathcal{A}_N^{\xi}(\eta)}}e^{-\frac{ky_M^2}{2K_BT}\eta(N-\xi)}\\ \times\left\{1-\mathbf{v}^{\mathsf{T}}\left[\mathcal{A}_N^{\xi}(\eta)\right]^{-1}\mathbf{v}\right\}e^{-\frac{ky_{N+1}^2}{2K_BT}\left\{1-\mathbf{v}^{\mathsf{T}}\left[\mathcal{A}_N^{\xi}(\eta)\right]^{-1}\mathbf{v}\right\}}.\end{aligned} \tag{3.15}$$

Another important quantity for describing the system behavior is the average value $\langle\xi\rangle$ of unbroken vertical springs. It can be directly evaluated through the expression

$$\langle\xi\rangle = \frac{1}{Z_H}\int_{\mathbb{R}^N}\sum_{\xi=0}^{N}\xi e^{-\frac{\Phi\left(\mathbf{y},\xi;y_{N+1}\right)}{K_BT}}\mathrm{d}y_1\ldots\mathrm{d}y_N. \tag{3.16}$$

Its calculation delivers

$$\langle\xi\rangle = \frac{1}{Z_H}\sum_{\xi=0}^{N}\xi\sqrt{\frac{(2\pi K_BT)^N}{k^N\det\mathcal{A}_N^{\xi}(\eta)}}e^{-\frac{ky_M^2}{2K_BT}\eta(N-\xi)-\frac{ky_{N+1}^2}{2K_BT}\left\{1-\mathbf{v}^{\mathsf{T}}\left[\mathcal{A}_N^{\xi}(\eta)\right]^{-1}\mathbf{v}\right\}}. \tag{3.17}$$

In addition, it is also interesting to determine the average value of the vector $\mathbf{y}$ defining the position of all the elements of the chain (corresponding to both broken and unbroken vertical springs). By definition of average value, we have

$$\langle\mathbf{y}\rangle = \frac{1}{Z_H}\int_{\mathbb{R}^N}\sum_{\xi=0}^{N}\mathbf{y}e^{-\frac{\Phi\left(\mathbf{y},\xi;y_{N+1}\right)}{K_BT}}\mathrm{d}y_1\ldots\mathrm{d}y_N. \tag{3.18}$$

Then, we can use the definition of Φ, by obtaining the more explicit form

$$\begin{aligned}\langle\mathbf{y}\rangle = e^{-\frac{k}{2K_BT}y_{N+1}^2}\frac{1}{Z_H}\sum_{\xi=0}^{N}e^{-\frac{1}{2K_BT}k\eta(N-\xi)y_M^2}\\ \times\int_{\mathbb{R}^N}\mathbf{y}e^{-\frac{1}{2K_BT}k\mathbf{y}^{\mathsf{T}}\mathcal{A}_N^{\xi}(\eta)\mathbf{y}+\frac{k}{K_BT}y_{N+1}\mathbf{v}^{\mathsf{T}}\mathbf{y}}\mathrm{d}y_1\ldots\mathrm{d}y_N.\end{aligned} \tag{3.19}$$

Now, by differentiating Eq.(3.12) with respect to an arbitrary element of the vector $\mathbf{b}$, we obtain a second integral property

$$\int_{\mathbb{R}^N}e^{-\mathbf{y}^{\mathsf{T}}\mathcal{A}\mathbf{y}}e^{\mathbf{b}^{\mathsf{T}}\mathbf{y}}\mathbf{y}\mathrm{d}y_1\ldots\mathrm{d}y_N = \frac{1}{2}\sqrt{\frac{\pi^N}{\det\mathcal{A}}}e^{\frac{1}{4}\mathbf{b}^{\mathsf{T}}\mathcal{A}^{-1}\mathbf{b}}\mathcal{A}^{-1}\mathbf{b}, \tag{3.20}$$

which holds, as before, for any symmetric and positive definite matrix $\mathcal{A}$ and that can be used to calculate the integral in Eq.(3.19). Straightforward calculations lead to the result

$$\begin{aligned}\langle\mathbf{y}\rangle = y_{N+1}\frac{1}{Z_H}\sum_{\xi=0}^{N}\sqrt{\frac{(2\pi K_BT)^N}{k^N\det\mathcal{A}_N^{\xi}(\eta)}}e^{-\frac{ky_M^2}{2K_BT}\eta(N-\xi)}\\ \times e^{-\frac{ky_{N+1}^2}{2K_BT}\left\{1-\mathbf{v}^{\mathsf{T}}\left[\mathcal{A}_N^{\xi}(\eta)\right]^{-1}\mathbf{v}\right\}}\left[\mathcal{A}_N^{\xi}(\eta)\right]^{-1}\mathbf{v}.\end{aligned} \tag{3.21}$$

Expressions for $\langle f\rangle$, $\langle \xi\rangle$ and $\langle \mathbf{y}\rangle$ in terms of the applied extension y_{N+1} represent the main results describing the behavior of the system under isometric conditions, *i.e.* within the Helmholtz ensemble. However, in order to obtain fully explicit representations for these quantities, we need to find closed-form expressions for the scalars $\det \mathcal{A}_N^\xi(\eta)$ and $\mathbf{v}^\mathsf{T}\left[\mathcal{A}_N^\xi(\eta)\right]^{-1}\mathbf{v}$, and the vector $\left[\mathcal{A}_N^\xi(\eta)\right]^{-1}\mathbf{v}$. This development is performed in the Appendix at the end of this Chapter, where we prove that

$$\det \mathcal{A}_N^\xi(\eta) = (N-\xi+1)G(\xi+1) - (N-\xi)G(\xi), \tag{3.22}$$

$$1 - \mathbf{v}^\mathsf{T}\left[\mathcal{A}_N^\xi(\eta)\right]^{-1}\mathbf{v} = \frac{G(\xi+1)-G(\xi)}{(N-\xi+1)G(\xi+1)-(N-\xi)G(\xi)}, \tag{3.23}$$

$$\left\{\left[\mathcal{A}_N^\xi(\eta)\right]^{-1}\mathbf{v}\right\}_i = \frac{\vartheta_{i-1}}{(N-\xi+1)G(\xi+1)-(N-\xi)G(\xi)}, \tag{3.24}$$

and where

$$G(z) = \frac{1}{\sqrt{\Delta}}\left(\frac{2+\eta+\sqrt{\Delta}}{2}\right)^z - \frac{1}{\sqrt{\Delta}}\left(\frac{2+\eta-\sqrt{\Delta}}{2}\right)^z, \tag{3.25}$$

with $\Delta = \eta^2 + 4\eta$ and

$$\begin{aligned}\vartheta_i = {} & \left[G(i+1) - (i-\xi+1)G(\xi+1) + (i-\xi)G(\xi)\right]\mathbf{1}(\xi-i) \\ & + \left[(i-\xi+1)G(\xi+1) - (i-\xi)G(\xi)\right].\end{aligned} \tag{3.26}$$

Here $\mathbf{1}(x)$ represents the Heaviside step function (see Appendix for details). The main results of this section can be therefore summed up as follows

$$\langle \mathcal{F}\rangle = 2\alpha\frac{\mathcal{Y}}{\mathcal{D}}\sum_{\xi=0}^{N}\frac{G(\xi+1)-G(\xi)}{\vartheta_N^{3/2}}e^{\alpha\eta\xi-\alpha\mathcal{Y}^2\frac{G(\xi+1)-G(\xi)}{\vartheta_N}}, \tag{3.27}$$

$$\langle \xi\rangle = \frac{1}{\mathcal{D}}\sum_{\xi=0}^{N}\frac{\xi}{\vartheta_N^{1/2}}e^{\alpha\eta\xi-\alpha\mathcal{Y}^2\frac{G(\xi+1)-G(\xi)}{\vartheta_N}}, \tag{3.28}$$

$$\begin{aligned}\langle \mathcal{Y}_i\rangle = {} & \frac{\mathcal{Y}}{\mathcal{D}}\sum_{\xi=0}^{i-1}\frac{(i-\xi)G(\xi+1)-(i-\xi-1)G(\xi)}{\vartheta_N^{3/2}}e^{\alpha\eta\xi-\alpha\mathcal{Y}^2\frac{G(\xi+1)-G(\xi)}{\vartheta_N}} \\ & + \frac{\mathcal{Y}}{\mathcal{D}}\sum_{\xi=i}^{N}\frac{G(i)}{\vartheta_N^{3/2}}e^{\alpha\eta\xi-\alpha\mathcal{Y}^2\frac{G(\xi+1)-G(\xi)}{\vartheta_N}},\end{aligned} \tag{3.29}$$

$$\mathcal{D} = \sum_{\xi=0}^{N}\frac{1}{\vartheta_N^{1/2}}e^{\alpha\eta\xi-\alpha\mathcal{Y}^2\frac{G(\xi+1)-G(\xi)}{\vartheta_N}}, \tag{3.30}$$

where we introduced the dimensionless quantities $\alpha = ky_M^2/(2K_BT)$, $\eta = h/k$, $\mathcal{Y} = y_{N+1}/y_M$, $\langle \mathcal{F}\rangle = \langle f\rangle y_M/(K_BT)$, $\langle \mathcal{Y}_i\rangle = \langle y_i\rangle/y_M$ $(i = 1,\ldots,N)$ and the quantity $\mathcal{D}$, proportional to the partition function Z_H. This form of the solutions is particularly useful to study the thermodynamic limit $(N\to\infty)$ of the Helmholtz ensemble, as discussed in the next Section.

A first example of application of the above results can be found in Fig.3.3, where we plotted the number of unbroken elements $\langle \xi\rangle$, the average force $\langle f\rangle$ and the average vector $\langle \mathbf{y}\rangle$ versus

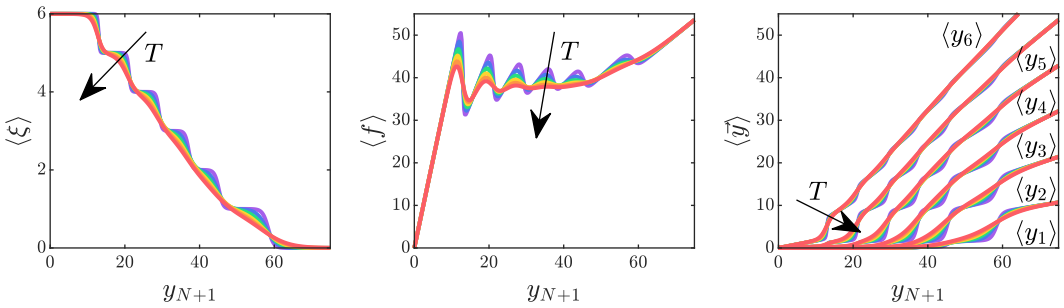

Figure 3.3: Number of unbroken elements $\langle \xi \rangle$, average force $\langle f \rangle$ and average vector $\langle \mathbf{y} \rangle$ versus y_{N+1} for a decohesion process (y_{N+1} increasing) under isometric conditions. We adopted the parameters $N = 6$, $k = 5$, $h = 20$, $y_M = 4$, and six values of $K_B T = 4, 7.2, 10.4, 13.6, 16.8$, and 20 (in arbitrary units).

y_{N+1}, for a case with $N = 6$. Since we adopted a quite large value of the rupture threshold y_M (*i.e.* $\alpha \gg 1$), we can identify all the distinct rupture occurrences in the decreasing steps of the quantity $\langle \xi \rangle$, and in the peaks of the force-extension ($\langle f \rangle$, y_{N+1}) curves. Besides, they can be also recognized in the behavior of the curves representing $\langle y_i \rangle$ versus y_{N+1}. It means that the discrete character of the decohesion process is directly reflected in the behavior of the main physical quantities describing the system. Of course, for large values of the temperature T, the curves are smoother and it is more difficult to recognize the single ruptures, due to the larger thermal fluctuations.

A second example, with a larger number of elements $N = 30$, is shown in Fig.3.4, where we plotted $\langle \xi \rangle$ and $\langle f \rangle$ versus y_{N+1}. In this case, we can identify some rupture events only for the smallest temperatures. While $\langle \xi \rangle$ is represented by the expected decreasing trend (going from $N = 30$ to 0), an interesting temperature-dependent plateau behavior can be observed in the force-extension curves. It means that the isometric detachment of a long chain from a substrate takes place at a given constant force, and this force is sensibly dependent on the temperature of the system. This behavior, which is related to the presence of a phase transition, is thoroughly studied in the next Section where we consider the limiting case for $N \to \infty$ by introducing the discrete to continuous transformation.

In Fig.3.3 and Fig.3.4, the behavior of $\langle \xi \rangle$ shows that the detachment of the elements occurs in a progressive way, described by a gradual change of $\langle \xi \rangle$ in response to the prescribed increasing extension y_{N+1}. This is a well known behavior characterizing the systems within the Helmholtz ensemble, already observed *e.g.* in the unfolding of proteins or other macromolecules under isometric conditions [91, 94, 110]. We will see that the behavior is completely different within the Gibbs (isotensional) ensemble, where all the vertical elements break quite simultaneously, at a given critical force. To conclude, we also observe that the behavior of the force-extension curves ($\langle f \rangle$ versus y_{N+1}) in Fig.3.3 and Fig.3.4, characterized by the force plateau, is in good qualitative agreement with several results obtained in peeling experiments and simulations concerning adhesive films and biological structures [244–248].

3.4 Thermodynamic limit in the Helmholtz ensemble

We consider the force-extension relationship given in Eq.(3.27), where we assume to have a large value of the number N of elements of the chain. This assumption corresponds to the

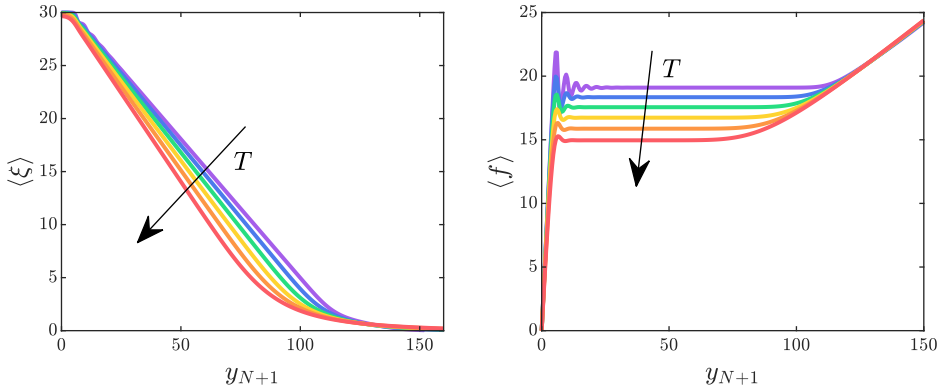

Figure 3.4: Number of unbroken elements $\langle \xi \rangle$ and average force $\langle f \rangle$ versus y_{N+1} for a system with $N = 30$, tested under isometric conditions. We adopted the parameters $k = 5$, $h = 20$, $y_M = 2$, and six values of $K_B T = 4, 7.2, 10.4, 13.6, 16.8$, and 20 (in arbitrary units).

thermodynamic limit and allows the approximation of the arbitrary sum $\sum_{\xi=0}^{N} \phi(\xi)$ in Eq.(3.27) with the integral $\int_0^N \phi(\xi) \mathrm{d}\xi$ (for any function ϕ depending on ξ). It means that the original discrete system can be considered as a continuous one for large values of N. To further simplify the expression, we can apply the change of variable $\xi = Nx$. So doing, the above integral assumes the form $N \int_0^1 \phi(Nx) \mathrm{d}x$. After these operations, we observe that in the new version of Eq.(3.27) we have several terms of the form $G(Nx)$ and $G(Nx+1)$. Under the hypothesis of large values of N, it is not difficult to realize that the function $G(z)$, defined in Eq.(3.25), can be approximated by $G(z) = b^z/\sqrt{\Delta}$, with $b = \frac{2+\eta+\sqrt{\Delta}}{2}$, since the second term can be neglected with respect to the first one. Indeed, in the second term of Eq.(3.25), the base $\frac{2+\eta-\sqrt{\Delta}}{2}$ is always strictly less than one, making the corresponding power negligible. It has been carefully verified also for the extreme cases with $\eta \gg 1$ and with $\eta \ll 1$. Therefore, we eventually obtain from Eq.(3.27) the expression

$$\langle \mathcal{F} \rangle = 2\alpha\mathcal{Y} \frac{\int_0^1 \frac{e^{Nx\left(\alpha\eta - \frac{1}{2}\log b\right)}}{\left[N(1-x)+\frac{b}{b-1}\right]^{3/2}} e^{-\alpha\mathcal{Y}^2 \frac{1}{N(1-x)+\frac{b}{b-1}}} \mathrm{d}x}{\int_0^1 \frac{e^{Nx\left(\alpha\eta - \frac{1}{2}\log b\right)}}{\left[N(1-x)+\frac{b}{b-1}\right]^{1/2}} e^{-\alpha\mathcal{Y}^2 \frac{1}{N(1-x)+\frac{b}{b-1}}} \mathrm{d}x}. \tag{3.31}$$

To simplify this result, we can apply the change of variable $s = N(1-x) + \frac{b}{b-1}$, by obtaining

$$\langle \mathcal{F} \rangle = 2\alpha\mathcal{Y} \frac{\int_{\frac{b}{b-1}}^{N+\frac{b}{b-1}} \frac{1}{s^{3/2}} e^{-s\left(\alpha\eta - \frac{1}{2}\log b\right) - \frac{1}{s}\alpha\mathcal{Y}^2} \mathrm{d}s}{\int_{\frac{b}{b-1}}^{N+\frac{b}{b-1}} \frac{1}{s^{1/2}} e^{-s\left(\alpha\eta - \frac{1}{2}\log b\right) - \frac{1}{s}\alpha\mathcal{Y}^2} \mathrm{d}s}. \tag{3.32}$$

This proves that a universal force-extension curve exists in the thermodynamic limit ($N \to \infty$) and its shape is given by the formula

$$\langle \mathcal{F} \rangle = 2\alpha \mathcal{Y} \frac{\int_{\frac{b}{b-1}}^{+\infty} \frac{1}{s^{3/2}} e^{-s\left(\alpha\eta - \frac{1}{2}\log b\right)} e^{-\frac{1}{s}\alpha\mathcal{Y}^2} \mathrm{d}s}{\int_{\frac{b}{b-1}}^{+\infty} \frac{1}{s^{1/2}} e^{-s\left(\alpha\eta - \frac{1}{2}\log b\right)} e^{-\frac{1}{s}\alpha\mathcal{Y}^2} \mathrm{d}s}, \tag{3.33}$$

where it is not difficult to verify that both integrals are well defined provided that $\alpha\eta - \frac{1}{2}\log b > 0$, a condition thoroughly discussed below. The result given in Eq.(3.33) can be used to introduce an important property of the system, concerning the force plateau observed for $N \to \infty$ and $\mathcal{Y} \to \infty$. To this aim, we introduce another change of variable defined by $1/z = \mathcal{Y}/s$. We easily get the relation

$$\langle \mathcal{F} \rangle = 2\alpha \frac{\int_{\frac{1}{\mathcal{Y}}\frac{b}{b-1}}^{+\infty} \frac{1}{z^{3/2}} e^{-\mathcal{Y}\left[\left(\alpha\eta - \frac{1}{2}\log b\right)z + \frac{\alpha}{z}\right]} \mathrm{d}z}{\int_{\frac{1}{\mathcal{Y}}\frac{b}{b-1}}^{+\infty} \frac{1}{z^{1/2}} e^{-\mathcal{Y}\left[\left(\alpha\eta - \frac{1}{2}\log b\right)z + \frac{\alpha}{z}\right]} \mathrm{d}z}, \tag{3.34}$$

which allows the calculation of the asymptotic value $\langle \mathcal{F} \rangle_{\mathrm{as}} = \lim_{\mathcal{Y}\to\infty} \langle \mathcal{F} \rangle$. First of all, we observe that

$$\lim_{\mathcal{Y}\to\infty} \int_0^{\frac{1}{\mathcal{Y}}\frac{b}{b-1}} \frac{1}{z^q} e^{-\mathcal{Y}\left[\left(\alpha\eta - \frac{1}{2}\log b\right)z + \frac{\alpha}{z}\right]} \mathrm{d}z = 0, \tag{3.35}$$

with $q = \frac{1}{2}, \frac{3}{2}$, provided that $\alpha\eta - \frac{1}{2}\log b > 0$, as before. Hence, we can write

$$\langle \mathcal{F} \rangle_{\mathrm{as}} = 2\alpha \lim_{\mathcal{Y}\to\infty} \frac{\int_0^{+\infty} \frac{1}{z^{3/2}} e^{-\mathcal{Y}\left[\left(\alpha\eta - \frac{1}{2}\log b\right)z + \frac{\alpha}{z}\right]} \mathrm{d}z}{\int_0^{+\infty} \frac{1}{z^{1/2}} e^{-\mathcal{Y}\left[\left(\alpha\eta - \frac{1}{2}\log b\right)z + \frac{\alpha}{z}\right]} \mathrm{d}z}, \tag{3.36}$$

where we can use the tabulated integral [249, 250]

$$\int_0^{+\infty} z^{\nu-1} e^{-\left(\gamma z + \frac{\beta}{z}\right)} \mathrm{d}z = 2\left(\frac{\beta}{\gamma}\right)^{\nu/2} K_\nu\left(2\sqrt{\beta\gamma}\right), \tag{3.37}$$

which is valid with $\beta > 0$ and $\gamma > 0$, and where $K_\nu(z)$ is a modified Bessel function of the second kind and order ν [249, 250]. Its application to Eq.(3.36) delivers

$$\begin{aligned} \langle \mathcal{F} \rangle_{\mathrm{as}} &= 2\alpha \lim_{\mathcal{Y}\to\infty} \frac{\left(\frac{\alpha}{\alpha\eta - \frac{1}{2}\log b}\right)^{-\frac{1}{4}} K_{-\frac{1}{2}}\left(2\mathcal{Y}\sqrt{\alpha\left(\alpha\eta - \frac{1}{2}\log b\right)}\right)}{\left(\frac{\alpha}{\alpha\eta - \frac{1}{2}\log b}\right)^{+\frac{1}{4}} K_{+\frac{1}{2}}\left(2\mathcal{Y}\sqrt{\alpha\left(\alpha\eta - \frac{1}{2}\log b\right)}\right)}, \\ &= 2\sqrt{\alpha\left(\alpha\eta - \frac{1}{2}\log b\right)}, \end{aligned} \tag{3.38}$$

where we used the property $K_\nu(z) = K_{-\nu}(z)$ [249, 250]. The result stated in Eq.(3.38) describes the asymptotic value of the force plateau in terms of the temperature and the other parameters of the system. It can be written in a more explicit form as

$$\langle f \rangle_{\mathrm{as}} = \sqrt{kh}\, y_M \sqrt{1 - \frac{K_B T}{h y_M^2} \log\left(\frac{2 + \eta + \sqrt{\eta^2 + 4\eta}}{2}\right)}, \tag{3.39}$$

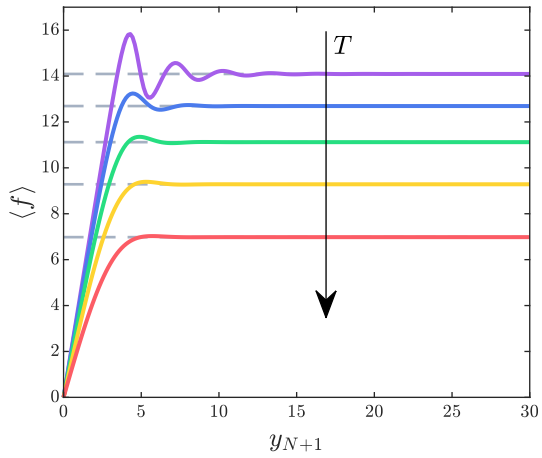

Figure 3.5: Comparison between the force-extension curves given in Eq.(3.15) or Eq.(3.27) (colored continuous curves) with the values of the force plateau obtained in Eq.(3.39) or Eq.(3.40) (gray dashed straight lines). We underline the agreement between the asymptotic force values for different system temperatures. We adopted the parameters $N = 100$, $k = 5$, $h = 20$, $y_M = 1.5$, and $K_B T = 3.0, 7.25, 11.5, 15.75$, and 20 (in arbitrary units).

or, equivalently,

$$\langle f \rangle_{\text{as}} = \sqrt{kh} y_M \sqrt{1 - \frac{T}{T_c}}, \tag{3.40}$$

where we introduced the critical temperature

$$T_c = \frac{1}{\frac{K_B}{h y_M^2} \log\left(\frac{2+\eta+\sqrt{\eta^2+4\eta}}{2}\right)}. \tag{3.41}$$

Since $\operatorname{arccosh}(x) = \log\left(x + \sqrt{x^2-1}\right)$, we can give the following alternative form for the critical temperature

$$T_c = \frac{1}{\frac{K_B}{h y_M^2} \operatorname{arccosh}\left(1 + \frac{\eta}{2}\right)}. \tag{3.42}$$

Importantly, it is not difficult to prove that the inequality $\alpha\eta - \frac{1}{2}\log b > 0$, assuring the convergence of the above integrals, simply means that we are working at subcritical temperatures, namely $T < T_c$.

The value of the plateau force obtained in Eq.(3.39) or Eq.(3.40) must be compared with the force-extension curve given in Eq.(3.15) or Eq.(3.27). This comparison can be found in Fig.3.5, where we considered a system with $N = 100$. We observe the perfect agreement of the solution for the original discrete system with the continuous approximation holding in the thermodynamic limit. This explains the variation of the plateau force with the temperature in terms of the presence of the phase transition occurring at the critical temperature T_c. The critical behavior of the asymptotic value of the force can be observed in Fig.3.6 where we plotted $\langle f \rangle_{\text{as}}$ versus $K_B T$ through Eq.(3.39) for different values of the ratio η. We note that the force approaches zero at the critical temperature T_c, and that T_c is an increasing function of the ratio η. It is important to remark that the value of the critical force for $T = 0$ is $\langle f \rangle_{\text{as}} = \sqrt{kh} y_M$, in perfect

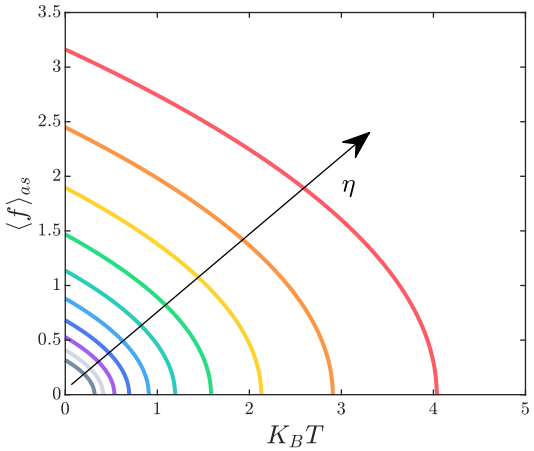

Figure 3.6: Critical behavior of the asymptotic force within the Helmholtz ensemble. We plotted $\langle f \rangle_{\text{as}}$ versus $K_B T$ (see Eq.(3.39)) for different values of the ratio $\eta = h/k$ between the elastic constants of the vertical and horizontal elements. We adopted the parameters $k = 1$, $y_M = 1$ (in arbitrary units) and we plotted ten curves with $10^{-1} \leq \eta \leq 10^{+1}$.

agreement with the recent literature concerning the pure mechanical peeling [7]. Moreover, we also remark that the critical behavior characterized by the phase transition can be obtained, from the mathematical point of view, only if the system approaches the thermodynamic limit, *i.e.* for $N \to \infty$.

To better elucidate the meaning of the critical temperature and of the associated phase transition we further analyze the behavior of the variable $\langle \xi \rangle$ given in Eq.(3.28), measuring the average number of unbroken vertical springs. As before, by assuming a large value of N, we can substitute the sums with the pertinent integrals and we easily find

$$\langle \xi \rangle = N \frac{\int_0^1 \frac{x e^{Nx\left(\alpha\eta - \frac{1}{2}\log b\right)}}{\left[N(1-x)+\frac{b}{b-1}\right]^{1/2}} e^{-\alpha \mathcal{Y}^2 \frac{1}{N(1-x)+\frac{b}{b-1}}} \mathrm{d}x}{\int_0^1 \frac{e^{Nx\left(\alpha\eta - \frac{1}{2}\log b\right)}}{\left[N(1-x)+\frac{b}{b-1}\right]^{1/2}} e^{-\alpha \mathcal{Y}^2 \frac{1}{N(1-x)+\frac{b}{b-1}}} \mathrm{d}x}. \tag{3.43}$$

We can now apply the change of variable $s = N(1-x) + \frac{b}{b-1}$, and we get the number $\langle \zeta \rangle = N - \langle \xi \rangle$ of broken vertical springs in the form

$$\langle \zeta \rangle = \frac{\int_{\frac{b}{b-1}}^{N+\frac{b}{b-1}} s^{1/2} e^{-s\left(\alpha\eta - \frac{1}{2}\log b\right)} e^{-\frac{1}{s}\alpha \mathcal{Y}^2} \mathrm{d}s}{\int_{\frac{b}{b-1}}^{N+\frac{b}{b-1}} s^{-1/2} e^{-s\left(\alpha\eta - \frac{1}{2}\log b\right)} e^{-\frac{1}{s}\alpha \mathcal{Y}^2} \mathrm{d}s} - \frac{b}{b-1}. \tag{3.44}$$

In the thermodynamic limit, we have that $N \to \infty$ and we can write the expression

$$\langle \zeta \rangle = \frac{\int_{\frac{b}{b-1}}^{+\infty} s^{1/2} e^{-s\left(\alpha\eta - \frac{1}{2}\log b\right)} e^{-\frac{1}{s}\alpha \mathcal{Y}^2} \mathrm{d}s}{\int_{\frac{b}{b-1}}^{+\infty} s^{-1/2} e^{-s\left(\alpha\eta - \frac{1}{2}\log b\right)} e^{-\frac{1}{s}\alpha \mathcal{Y}^2} \mathrm{d}s} - \frac{b}{b-1}, \tag{3.45}$$

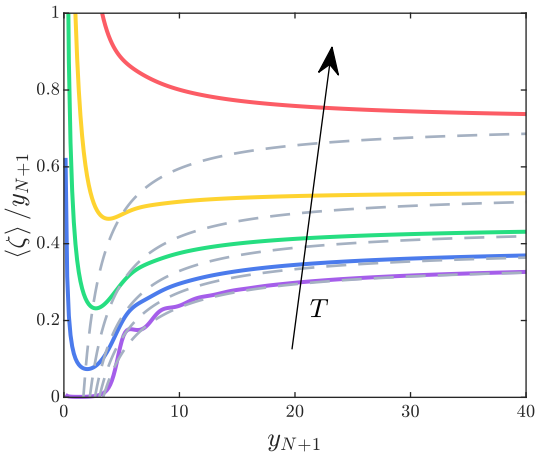

Figure 3.7: Asymptotic behavior of the number of broken elements $\langle\zeta\rangle$ within the Helmholtz ensemble and with $y_{N+1} \to \infty$. The quantities $\langle\zeta\rangle/y_{N+1} = (N - \langle\xi\rangle)/y_{N+1}$ (colored continuous lines), calculated through Eq.(3.17) or Eq.(3.28), and $\langle\zeta\rangle|_{y_{N+1}\to\infty}/y_{N+1}$ (gray dashed lines), obtained from Eq.(3.50), are represented versus y_{N+1}. They show the same asymptotic behavior. We adopted the parameters $N = 100$, $k = 5$, $h = 20$, $y_M = 1.5$, and $K_B T = 3.0, 7.25, 11.5, 15.75$, and 20 (in arbitrary units).

which proves that $\langle\zeta\rangle = N - \langle\xi\rangle$ is independent of N for large N. This is the expected behavior since for a long chain the number of broken elements must depend only on the applied extension $\mathcal{Y}$ and on the temperature T. This result allows us to give a clear physical interpretation of the phase transition corresponding to the critical temperature T_c. We consider separately the cases with $\mathcal{Y} = 0$ and with large values of $\mathcal{Y}$. For $\mathcal{Y} = 0$ we have to calculate

$$\langle\zeta\rangle|_{\mathcal{Y}=0} = \frac{\int_{\frac{b}{b-1}}^{+\infty} s^{1/2} e^{-s\left(\alpha\eta - \frac{1}{2}\log b\right)} \mathrm{d}s}{\int_{\frac{b}{b-1}}^{+\infty} s^{-1/2} e^{-s\left(\alpha\eta - \frac{1}{2}\log b\right)} \mathrm{d}s} - \frac{b}{b-1}. \tag{3.46}$$

Both integrals in the numerator and denominator can be calculated in closed form (if $\alpha\eta - \frac{1}{2}\log b > 0$, as before), and we eventually obtain the result

$$\langle\zeta\rangle|_{\mathcal{Y}=0} = \frac{b}{b-1}\frac{1}{\Theta}\left[\frac{1}{2} - \Theta + \sqrt{\frac{\Theta}{\pi}}\frac{e^{-\Theta}}{1 - \mathrm{erf}\left(\sqrt{\Theta}\right)}\right], \tag{3.47}$$

where

$$\Theta = \frac{b}{b-1}\left(\alpha\eta - \frac{1}{2}\log b\right) = \frac{hy_M^2}{2K_B T}\frac{e^{\frac{hy_M^2}{K_B T_c}}}{e^{\frac{hy_M^2}{K_B T_c}} - 1}\left(1 - \frac{T}{T_c}\right). \tag{3.48}$$

So, we directly deduce that for $\Theta \to \infty$ (or $T \to 0$) we have $\langle\zeta\rangle|_{\mathcal{Y}=0} = 0$ and for $\Theta \to 0$ (or $T \to T_c$) we have $\langle\zeta\rangle|_{\mathcal{Y}=0} \to \infty$. It means that at low temperatures we have no vertical springs broken and at the critical temperature we have all the vertical springs broken. Hence, we observe the characteristic divergence of $\langle\zeta\rangle|_{\mathcal{Y}=0}$ for $T \to T_c$. This behavior can be found in Fig.3.8, where we plotted $\langle\zeta\rangle|_{\mathcal{Y}=0}$ versus $K_B T$ for different values of η.

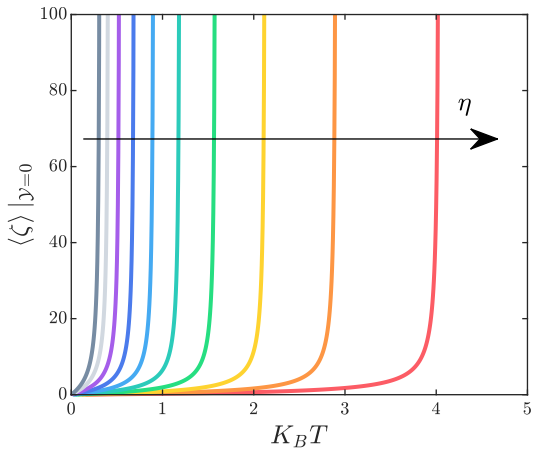

Figure 3.8: Critical behavior of the number of broken elements within the Helmholtz ensemble and with $\mathcal{Y}=0$. We plotted $\langle\zeta\rangle|_{\mathcal{Y}=0}$ versus K_BT (see Eq.(3.47)) for different values of the ratio $\eta=h/k$ between the elastic constants of the vertical and horizontal elements. We adopted the parameters $k=1$, $y_M=1$ (in arbitrary units) and we plotted ten curves with $10^{-1}\leq\eta\leq10^{+1}$.

We can state that, at the critical temperature, all the vertical springs are broken independently of the prescribed extension applied to the infinite chain. Indeed, this can be proved also for large values of $\mathcal{Y}$. In this case, we consider Eq.(3.45) where we apply the change of variable $1/z=\mathcal{Y}/s$. We eventually obtain, for large values of $\mathcal{Y}$, the relation

$$\begin{aligned}
\langle\zeta\rangle|_{\mathcal{Y}\to\infty} &\to \mathcal{Y}\frac{\int_0^{+\infty} z^{1/2}e^{-\mathcal{Y}z\left(\alpha\eta-\frac{1}{2}\log b\right)}e^{-\frac{1}{z}\alpha\mathcal{Y}}\mathrm{d}z}{\int_0^{+\infty} z^{-1/2}e^{-\mathcal{Y}z\left(\alpha\eta-\frac{1}{2}\log b\right)}e^{-\frac{1}{z}\alpha\mathcal{Y}}\mathrm{d}z}-\frac{b}{b-1}\\
&=\mathcal{Y}\frac{\left(\frac{\alpha}{\alpha\eta-\frac{1}{2}\log b}\right)^{\frac{3}{4}}K_{\frac{3}{2}}\left(2\mathcal{Y}\sqrt{\alpha\left(\alpha\eta-\frac{1}{2}\log b\right)}\right)}{\left(\frac{\alpha}{\alpha\eta-\frac{1}{2}\log b}\right)^{\frac{1}{4}}K_{\frac{1}{2}}\left(2\mathcal{Y}\sqrt{\alpha\left(\alpha\eta-\frac{1}{2}\log b\right)}\right)}-\frac{b}{b-1}\\
&\to\mathcal{Y}\left(\frac{\alpha}{\alpha\eta-\frac{1}{2}\log b}\right)^{\frac{1}{2}}-\frac{b}{b-1}\\
&=\mathcal{Y}\sqrt{\frac{k}{h}}\frac{1}{\sqrt{1-\frac{T}{T_c}}}-\frac{e^{\frac{hy_M^2}{K_BT_c}}}{e^{\frac{hy_M^2}{K_BT_c}}-1},
\end{aligned}\tag{3.49}$$

where we used the integral given in Eq.(3.37) and the asymptotic relation of the modified Bessel functions $K_\nu(z)\to\sqrt{\frac{\pi}{2z}}e^{-z}\ \forall\nu$ for $z\to\infty$ [249, 250]. It means that the number of broken elements $\langle\zeta\rangle=N-\langle\xi\rangle$, increasing with the applied extension $\mathcal{Y}$, is described by the straight line given in Eq.(3.49), at least for large values of $\mathcal{Y}$. In other words, we have a linear relation between $\langle\zeta\rangle$ and $\mathcal{Y}$ for $\mathcal{Y}\to\infty$. This behavior is confirmed in Fig.3.7, where for convenience we plotted $\langle\zeta\rangle/y_{N+1}=(N-\langle\xi\rangle)/y_{N+1}$, calculated through Eq.(3.17) or (3.28), and $\langle\zeta\rangle|_{y_{N+1}\to\infty}/y_{N+1}$,

obtained from Eq.(3.49) and explicitly given by

$$\frac{\langle\zeta\rangle|_{y_{N+1}\to\infty}}{y_{N+1}} = \frac{1}{y_M}\sqrt{\frac{k}{h}}\frac{1}{\sqrt{1-\frac{T}{T_c}}} - \frac{1}{y_{N+1}}\frac{e^{\frac{hy_M^2}{K_BT_c}}}{e^{\frac{hy_M^2}{K_BT_c}}-1}. \tag{3.50}$$

We observe the same asymptotic behavior of both quantities for different values of the temperature. This proves that the transition from discrete to continuous systems is legitimate to analyze the thermodynamic limit. Moreover, from Eq.(3.50), we observe that $\langle\zeta\rangle|_{y_{N+1}\to\infty}$ diverges to infinity when $T \to T_c$. At the same time, we have no finite values of the prescribed y_{N+1} able to entirely detach the system for subcritical temperatures $T < T_c$. It means that, for $T < T_c$, we must have $y_{N+1} \to \infty$ for inducing the complete detachment of the chain. Therefore, we conclude that for $T \to T_c$ we have a phase transition corresponding to the rupture of all the vertical elements of the chain, *i.e.* to the complete detachment of the chain from the substrate. For this reason, the critical temperature can also be referred to as the denaturation temperature of the system. This is the terminology often adopted in the biological context [77–79]. More details on the application of our theory to RNA and DNA hairpins will be given in Section 3.7.

3.5 The Gibbs ensemble

The Gibbs ensemble is characterized by the applied force f, which induces the detachment of the chain from the substrate, as shown in Fig.3.2.b (isotensional condition). To calculate the Gibbs partition function, we observe that the total energy of the system can be written as $\Phi - fy_{N+1}$, where Φ is the energy function introduced within the Helmholtz ensemble in Eq.(3.9). The Gibbs partition function can be therefore written as

$$\begin{aligned} Z_G(f) &= \int_{\mathbb{R}^{N+1}} \sum_{\xi=0}^{N} e^{-\frac{\Phi\left(\mathbf{y},\xi;y_{N+1}\right)}{K_BT}} e^{\frac{fy_{N+1}}{K_BT}} \mathrm{d}y_1 \dots \mathrm{d}y_N \mathrm{d}y_{N+1} \\ &= \int_{-\infty}^{+\infty} Z_H(y_{N+1})\, e^{\frac{fy_{N+1}}{K_BT}} \mathrm{d}y_{N+1}, \end{aligned} \tag{3.51}$$

which corresponds to the Laplace transform of the Helmholtz partition function. By using Eq.(3.13), we immediately get

$$\begin{aligned} Z_G(f) = &\sum_{\xi=0}^{N} \sqrt{\frac{(2\pi K_BT)^N}{k^N \det \mathcal{A}_N^{\xi}(\eta)}} e^{-\frac{ky_M^2}{2K_BT}\eta(N-\xi)} \\ &\times \int_{-\infty}^{+\infty} e^{-\frac{ky_{N+1}^2}{2K_BT}\left\{1-\mathbf{v}^{\mathsf{T}}\left[\mathcal{A}_N^{\xi}(\eta)\right]^{-1}\mathbf{v}\right\}} e^{\frac{fy_{N+1}}{K_BT}} \mathrm{d}y_{N+1}, \end{aligned} \tag{3.52}$$

where the integral can be easily performed thanks to the classical result (see Eq.(3.12) with $N = 1$)

$$\int_{-\infty}^{+\infty} e^{-\lambda z^2} e^{\gamma z} \mathrm{d}z = \sqrt{\frac{\pi}{\lambda}} e^{\frac{\gamma^2}{4\lambda}}, \quad \lambda > 0. \tag{3.53}$$

Straightforward simplifications lead to

$$Z_G(f) = \sum_{\xi=0}^{N} \sqrt{\frac{(2\pi K_B T/k)^{N+1}}{\det \mathcal{A}_N^{\xi}(\eta)\left\{1 - \mathbf{v}^{\mathsf{T}}\left[\mathcal{A}_N^{\xi}(\eta)\right]^{-1}\mathbf{v}\right\}}} \times e^{-\frac{ky_M^2}{2K_B T}\eta(N-\xi)} e^{\frac{f^2}{2kK_B T}\left\{1-\mathbf{v}^{\mathsf{T}}\left[\mathcal{A}_N^{\xi}(\eta)\right]^{-1}\mathbf{v}\right\}^{-1}}. \tag{3.54}$$

The knowledge of the partition function allows determining the average extension $\langle y_{N+1}\rangle$ of the last element of the chain induced by the applied force f. A classical thermodynamic relation states indeed that [98]

$$\langle y_{N+1}\rangle = K_B T \frac{\partial \log Z_G}{\partial f} = K_B T \frac{1}{Z_G}\frac{\partial Z_G}{\partial f}, \tag{3.55}$$

and gives the result

$$\langle y_{N+1}\rangle = \frac{f}{k}\frac{1}{Z_G}\sum_{\xi=0}^{N} \sqrt{\frac{(2\pi K_B T/k)^{N+1}}{\det \mathcal{A}_N^{\xi}(\eta)\left\{1 - \mathbf{v}^{\mathsf{T}}\left[\mathcal{A}_N^{\xi}(\eta)\right]^{-1}\mathbf{v}\right\}^3}} \times e^{-\frac{ky_M^2}{2K_B T}\eta(N-\xi)} e^{\frac{f^2}{2kK_B T}\left\{1-\mathbf{v}^{\mathsf{T}}\left[\mathcal{A}_N^{\xi}(\eta)\right]^{-1}\mathbf{v}\right\}^{-1}}. \tag{3.56}$$

Similarly, we can also determine the average number of unbroken vertical springs defined as

$$\langle \xi\rangle = \frac{1}{Z_G}\int_{\mathbb{R}^{N+1}} \sum_{\xi=0}^{N} \xi e^{-\frac{\Phi\left(\mathbf{y},\xi;y_{N+1}\right)}{K_B T}} e^{\frac{y_{N+1}}{K_B T}} \mathrm{d}y_1 \ldots \mathrm{d}y_N \mathrm{d}y_{N+1}. \tag{3.57}$$

The explicit expression can be found in the form

$$\langle \xi\rangle = \frac{1}{Z_G}\sum_{\xi=0}^{N} \xi \sqrt{\frac{(2\pi K_B T/k)^{N+1}}{\det \mathcal{A}_N^{\xi}(\eta)\left\{1 - \mathbf{v}^{\mathsf{T}}\left[\mathcal{A}_N^{\xi}(\eta)\right]^{-1}\mathbf{v}\right\}}} \times e^{-\frac{ky_M^2}{2K_B T}\eta(N-\xi)} e^{\frac{f^2}{2kK_B T}\left\{1-\mathbf{v}^{\mathsf{T}}\left[\mathcal{A}_N^{\xi}(\eta)\right]^{-1}\mathbf{v}\right\}^{-1}}. \tag{3.58}$$

Finally, we can evaluate the average value of the positions of all the elements of the chain. This quantity is defined by the expression

$$\langle \mathbf{y}\rangle = \frac{1}{Z_G}\int_{\mathbb{R}^{N+1}} \sum_{\xi=0}^{N} \mathbf{y} e^{-\frac{\Phi\left(\mathbf{y},\xi;y_{N+1}\right)}{K_B T}} e^{\frac{f y_{N+1}}{K_B T}} \mathrm{d}\mathbf{y} \mathrm{d}y_{N+1}. \tag{3.59}$$

The comparison of Eq.(3.59) with Eqs.(3.18) and (3.21) yields the partial result

$$\begin{aligned}\langle \mathbf{y} \rangle = \frac{1}{Z_G} \int_{-\infty}^{+\infty} y_{N+1} \sum_{\xi=0}^{N} \sqrt{\frac{(2\pi K_B T)^N}{k^N \det \mathcal{A}_N^{\xi}(\eta)}} e^{-\frac{k y_M^2}{2K_B T}\eta(N-\xi)} \\ \times e^{-\frac{k y_{N+1}^2}{2K_B T}\left\{1-\mathbf{v}^{\mathsf{T}}\left[\mathcal{A}_N^{\xi}(\eta)\right]^{-1}\mathbf{v}\right\}} e^{\frac{f y_{N+1}}{K_B T}} \left[\mathcal{A}_N^{\xi}(\eta)\right]^{-1} \mathbf{v} \mathrm{d} y_{N+1},\end{aligned} \tag{3.60}$$

where the last integral can be evaluated by means of the relation (see Eq.(3.20) with $N = 1$)

$$\int_{-\infty}^{+\infty} e^{-\lambda z^2} e^{\gamma z} z \mathrm{d} z = \frac{\gamma}{2\lambda} \sqrt{\frac{\pi}{\lambda}} e^{\frac{\gamma^2}{4\lambda}}, \quad \lambda > 0. \tag{3.61}$$

The calculation can be performed to eventually give the final result in the form

$$\begin{aligned}\langle \mathbf{y} \rangle = \frac{f}{k} \frac{1}{Z_G} \sum_{\xi=0}^{N} \sqrt{\frac{(2\pi K_B T/k)^{N+1}}{\det \mathcal{A}_N^{\xi}(\eta) \left\{1 - \mathbf{v}^{\mathsf{T}} \left[\mathcal{A}_N^{\xi}(\eta)\right]^{-1} \mathbf{v}\right\}^3}} \\ \times e^{-\frac{k y_M^2}{2K_B T}\eta(N-\xi)} e^{\frac{f^2}{2kK_B T}\left\{1-\mathbf{v}^{\mathsf{T}}\left[\mathcal{A}_N^{\xi}(\eta)\right]^{-1}\mathbf{v}\right\}^{-1}} \left[\mathcal{A}_N^{\xi}(\eta)\right]^{-1} \mathbf{v}.\end{aligned} \tag{3.62}$$

The three major achievements of this Section, describing the behavior of $\langle y_{N+1} \rangle$, $\langle \xi \rangle$ and $\langle \mathbf{y} \rangle$ as functions of f, must be complemented with the expressions for $\det \mathcal{A}_N^{\xi}(\eta)$, $\mathbf{v}^{\mathsf{T}} \left[\mathcal{A}_N^{\xi}(\eta)\right]^{-1} \mathbf{v}$, and $\left[\mathcal{A}_N^{\xi}(\eta)\right]^{-1} \mathbf{v}$ shown in Eqs.(3.22), (3.23) and (3.24), respectively (fully demonstrated in Appendix). The explicit results can be summed up by using dimensionless quantities as follows

$$\langle \mathcal{Y} \rangle = \frac{\mathcal{F}}{2\alpha \mathcal{E}} \sum_{\xi=0}^{N} e^{\alpha\eta\xi} \frac{\vartheta_N}{[G(\xi+1) - G(\xi)]^{3/2}} e^{\frac{1}{4\alpha}\mathcal{F}^2 \frac{\vartheta_N}{G(\xi+1)-G(\xi)}}, \tag{3.63}$$

$$\langle \xi \rangle = \frac{1}{\mathcal{E}} \sum_{\xi=0}^{N} \xi e^{\alpha\eta\xi} \frac{1}{[G(\xi+1) - G(\xi)]^{1/2}} e^{\frac{1}{4\alpha}\mathcal{F}^2 \frac{\vartheta_N}{G(\xi+1)-G(\xi)}}, \tag{3.64}$$

$$\begin{aligned}\langle \mathcal{Y}_i \rangle = \left\{ \sum_{\xi=0}^{i-1} e^{\alpha\eta\xi} \frac{(i-\xi)G(\xi+1) - (i-\xi-1)G(\xi)}{[G(\xi+1) - G(\xi)]^{3/2}} e^{\frac{1}{4\alpha}\mathcal{F}^2 \frac{\vartheta_N}{G(\xi+1)-G(\xi)}} \right. \\ \left. + \sum_{\xi=i}^{N} e^{\alpha\eta\xi} \frac{G(i)}{[G(\xi+1) - G(\xi)]^{3/2}} e^{\frac{1}{4\alpha}\mathcal{F}^2 \frac{\vartheta_N}{G(\xi+1)-G(\xi)}} \right\} \frac{\mathcal{F}}{2\alpha\mathcal{E}},\end{aligned} \tag{3.65}$$

$$\mathcal{E} = \sum_{\xi=0}^{N} e^{\alpha\eta\xi} \frac{1}{[G(\xi+1) - G(\xi)]^{1/2}} e^{\frac{1}{4\alpha}\mathcal{F}^2 \frac{\vartheta_N}{G(\xi+1)-G(\xi)}}, \tag{3.66}$$

where we introduced $\alpha = k y_M^2/(2K_B T)$, $\eta = h/k$, $\langle \mathcal{Y} \rangle = \langle y_{N+1} \rangle / y_M$, $\mathcal{F} = f y_M/(K_B T)$, $\langle \mathcal{Y}_i \rangle = \langle y_i \rangle / y_M$ $(i = 1, \ldots, N)$ and the quantity $\mathcal{E}$, proportional to the partition function Z_G. This dimensionless form of the solutions is particularly useful to study the thermodynamic limit $(N \to \infty)$ of the Gibbs ensemble, as discussed in the next Section.

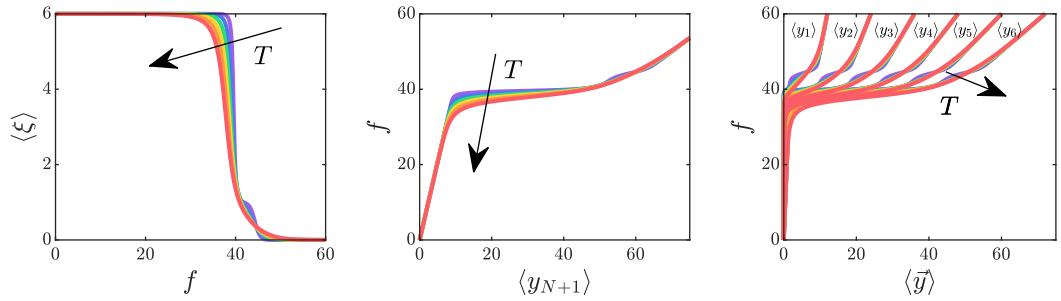

Figure 3.9: Number of unbroken elements $\langle\xi\rangle$, average position $\langle y_{N+1}\rangle$ and average vector $\langle\mathbf{y}\rangle$ versus f for a decohesion process (f increasing) under isotensional conditions. We adopted the parameters $N=6$, $k=5$, $h=20$, $y_M=4$, and six values of $K_BT=4, 7.2, 10.4, 13.6, 16.8$, and 20 (in arbitrary units).

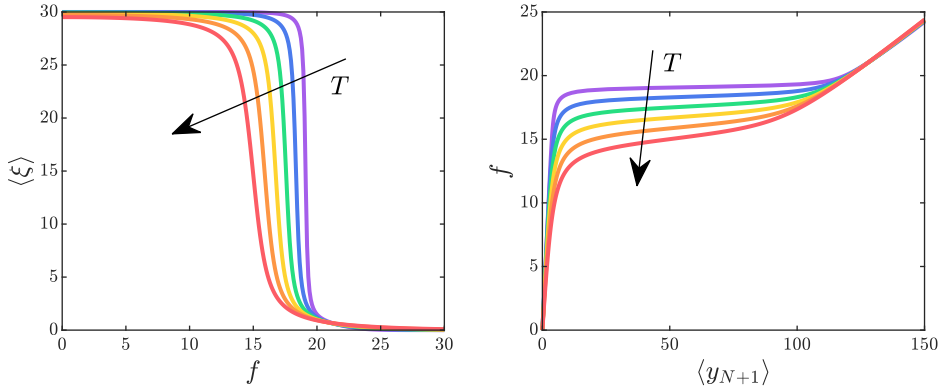

Figure 3.10: Number of unbroken elements $\langle\xi\rangle$ and average position $\langle y_{N+1}\rangle$ versus f for a system with $N=30$, tested under isotensional conditions. We adopted the parameters $k=5$, $h=20$, $y_M=2$, and six values of $K_BT=4, 7.2, 10.4, 13.6, 16.8$, and 20 (in arbitrary units).

An application of the obtained results can be found in Fig.3.9, where we show the behavior of $\langle\xi\rangle$, $\langle y_{N+1}\rangle$, and $\langle\mathbf{y}\rangle$ as functions of f, for a small system with $N=6$. Important differences between the Helmholtz and the Gibbs responses can be recognized by comparing Fig.3.3 with Fig.3.9. In Fig.3.9 the behavior of the number of unbroken elements $\langle\xi\rangle$ within the Gibbs ensemble shows that the detachment process corresponds to the simultaneous breaking of all the vertical elements, occurring when the force f reaches a given threshold value. On the contrary, we observed in Fig.3.3 a completely different behavior of $\langle\xi\rangle$ within the Helmholtz ensemble. Indeed, in that case, we deduced that the breaking of the elements is a sequential phenomenon, induced by the progressive increase of the extension y_{N+1}. This dissimilarity between the Helmholtz and the Gibbs ensembles is sometimes underlined by affirming that the isotensional condition produces a cooperative response while the isometric condition generates a non-cooperative response [91, 94, 110].

Another important difference concerns the shape of the force-extension curves measured within the two statistical ensembles. While the isometric case leads to a series of peaks corresponding to the rupture occurrences, the isotensional case is characterized by a monotone force-extension curve. Also, this feature can be explained by the quite simultaneous rupture of all the elements observed within the Gibbs ensemble. Again, the simultaneous or cooperative ruptures can be identified

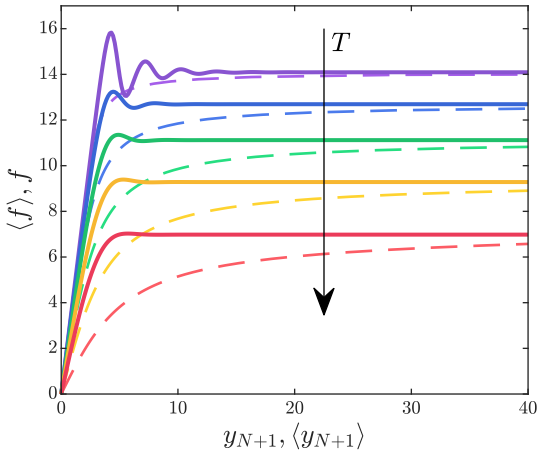

Figure 3.11: Comparison between the Helmholtz force-extension curves ($\langle f \rangle$ versus y_{N+1}, solid curves) and the Gibbs force-extension curves (f versus $\langle y_{N+1} \rangle$, dashed lines) proving the nonequivalence of the two statistical ensembles in the thermodynamic limit. We adopted the parameters $N = 100$, $k = 5$, $h = 20$, $y_M = 1.5$, and $K_B T = 3.0, 7.25, 11.5, 15.75$, and 20 (in arbitrary units).

in the isotensional behavior of $\langle \mathbf{y} \rangle$, plotted in Fig.3.9, while the sequential or non-cooperative ruptures were observed in the isometric behavior of $\langle \mathbf{y} \rangle$, plotted in Fig.3.3. All these features are typically observed when studying the behavior of small systems within the Gibbs or Helmholtz ensemble. In particular, they concern the folding/unfolding processes in chains of bistable units [91, 94, 110]. However, in our study of the cohesion-decohesion process, we obtain a peculiar and unusual behavior characterized by the temperature-dependent force plateau in the force-extension curves (observed for large values of N). This point is also confirmed for the Gibbs ensemble as one can see in Fig.3.10, where we plotted $\langle \xi \rangle$ and $\langle y_{N+1} \rangle$ versus f for a system with $N = 30$. Here, we observe a temperature-dependent threshold force for the detachment process in the plot of $\langle \xi \rangle$ and a temperature-dependent force plateau in the plot of $\langle y_{N+1} \rangle$. This behavior is thoroughly studied in the next Section by considering the discrete to continuous transition for $N \to \infty$ (thermodynamic limit).

3.6 The thermodynamic limit in the Gibbs ensemble

We consider now the behavior of the system under isotensional condition when N is very large. We apply the same technique described in Section 3.4, and, then, we substitute the sums with the corresponding integrals. Moreover, we assume, as before, that the function $G(z)$ can be approximated by the exponential form $G(z) = \frac{1}{\sqrt{\Delta}} b^z$. To begin, we consider the force-extension relation given in Eq.(3.63), and we get the first asymptotic expression

$$\langle \mathcal{Y} \rangle = \frac{\mathcal{F}}{2\alpha} \frac{\int_0^1 \frac{e^{Nx\left(\alpha\eta - \frac{1}{2}\log b\right)}}{\left[N(1-x)+\frac{b}{b-1}\right]^{-1}} e^{\frac{1}{4\alpha}\mathcal{F}^2\left[N(1-x)+\frac{b}{b-1}\right]} \mathrm{d}x}{\int_0^1 e^{Nx\left(\alpha\eta - \frac{1}{2}\log b\right)} e^{\frac{1}{4\alpha}\mathcal{F}^2\left[N(1-x)+\frac{b}{b-1}\right]} \mathrm{d}x}. \tag{3.67}$$

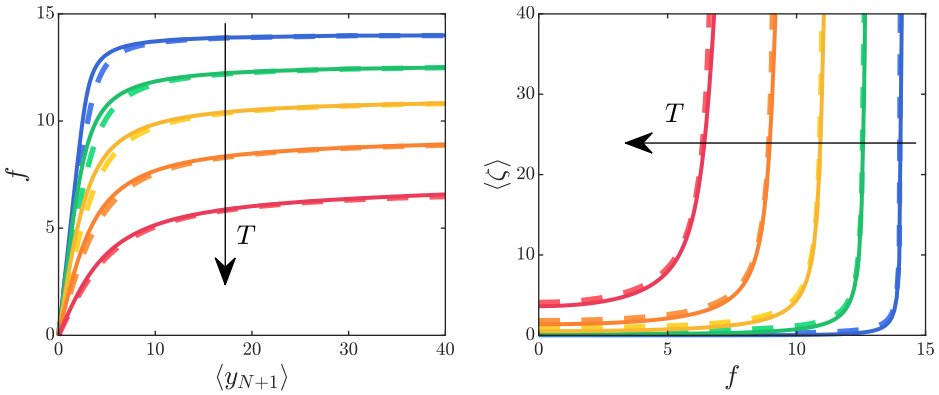

Figure 3.12: Behavior of the thermodynamic limit within the Gibbs ensemble in terms of force-extension relation and the average number of broken elements. We compare the results of the continuous approach given in Eqs.(3.78) and (3.79) (dashed lines) with their discrete counterparts given in Eqs.(3.63) and (3.64) (continuous lines), applied to a system with $N = 100$. We adopted the parameters $k = 5$, $h = 20$, $y_M = 1.5$, and $K_BT = 3.0, 7.25, 11.5, 15.75$, and 20 (in arbitrary units).

In order to obtain a simpler mathematical form, we apply the change of variable $s = N(1-x)+\frac{b}{b-1}$, yielding the result

$$\langle \mathcal{Y} \rangle = \frac{\mathcal{F}}{2\alpha} \frac{\int_{\frac{b}{b-1}}^{N+\frac{b}{b-1}} e^{-\left(\alpha\eta - \frac{1}{2}\log b\right)s} e^{\frac{1}{4\alpha}\mathcal{F}^2 s} s \mathrm{d}s}{\int_{\frac{b}{b-1}}^{N+\frac{b}{b-1}} e^{-\left(\alpha\eta - \frac{1}{2}\log b\right)s} e^{\frac{1}{4\alpha}\mathcal{F}^2 s} \mathrm{d}s}. \tag{3.68}$$

Since we are working at the thermodynamic limit, we have that $N \to \infty$ and we get

$$\langle \mathcal{Y} \rangle = \frac{\mathcal{F}}{2\alpha} \frac{\int_{\frac{b}{b-1}}^{+\infty} e^{-\left(\alpha\eta - \frac{1}{2}\log b - \frac{1}{4\alpha}\mathcal{F}^2\right)s} s \mathrm{d}s}{\int_{\frac{b}{b-1}}^{+\infty} e^{-\left(\alpha\eta - \frac{1}{2}\log b - \frac{1}{4\alpha}\mathcal{F}^2\right)s} \mathrm{d}s}. \tag{3.69}$$

This result proves that the thermodynamic limit exists also for the Gibbs ensemble and that we have a universal force-extension curve describing the cohesion-decohesion process. Indeed, the two integrals in Eq.(3.69) are both convergent if $\alpha\eta - \frac{1}{2}\log b - \frac{1}{4\alpha}\mathcal{F}^2 > 0$ and can be easily calculated yielding the following very simple closed form expression for the dimensionless force-extension curve

$$\langle \mathcal{Y} \rangle = \frac{\mathcal{F}}{2\alpha}\left(\frac{b}{b-1} + \frac{1}{\alpha\eta - \frac{1}{2}\log b - \frac{1}{4\alpha}\mathcal{F}^2}\right). \tag{3.70}$$

This relation shows that the extension is divergent for a given value of force, thus exhibiting a behavior similar to the one observed within the Helmholtz ensemble. It means that also in this case we observe a force plateau characterizing the detachment process. Moreover, we can observe that the value of this force plateau is given by the relation $\alpha\eta - \frac{1}{2}\log b - \frac{1}{4\alpha}\mathcal{F}^2 = 0$, exactly corresponding to Eq.(3.38), obtained in Section 3.4. However, if we observe the shape of the force-extension curves of the two different statistical ensembles (Gibbs and Helmholtz) in the thermodynamic limit ($N \to \infty$), we can see that they are considerably different, thus proving the nonequivalence of the ensembles for the cohesion-decohesion process under investigation. This

behavior can be found in Fig.3.11, where we plotted Eqs.(3.27) and (3.63) for a large value of N and for different values of the temperature. This nonequivalence can be also appreciated by comparing Eqs.(3.33) and (3.70), representing the force-extension curves in the continuous limit. Indeed, this point can be formally proved by comparing the slopes of the curves given in Eqs.(3.33) and (3.70) for small force or extension. Their calculation give

$$\left.\frac{\partial\langle\mathcal{F}\rangle}{\partial\mathcal{Y}}\right|_{\mathcal{Y}=0} = 4\alpha\frac{b-1}{b}\left[\sqrt{\frac{\Theta}{\pi}}\frac{e^{-\Theta}}{1-\mathrm{erf}\left(\sqrt{\Theta}\right)}-\Theta\right], \tag{3.71}$$

$$\left.\frac{\partial\mathcal{F}}{\partial\langle\mathcal{Y}\rangle}\right|_{\mathcal{F}=0} = 4\alpha\frac{b-1}{b}\left[\frac{\Theta}{2\left(1+\Theta\right)}\right], \tag{3.72}$$

for the Helmholtz ensemble and the Gibbs ensemble, respectively. Here, we defined $\Theta = \frac{b}{b-1}\left(\alpha\eta-\frac{1}{2}\log b\right)$, coherently with Eq.(3.48). By defining $p=\sqrt{\frac{\Theta}{\pi}}\frac{e^{-\Theta}}{1-\mathrm{erf}(\sqrt{\Theta})}-\Theta$ and $q=\frac{\Theta}{2(1+\Theta)}$, we can observe that p and q are two monotonically increasing functions of Θ with $p(0)=q(0)=0$ and $p(+\infty)=q(+\infty)=1/2$. Importantly, we have that $p>q$ over the whole interval $0<\Theta<+\infty$, confirming the nonequivalence of the ensembles in the thermodynamic limit. We remark that this behavior of the force-extension slopes is coherent with the results of Fig.3.11.

Although the equivalence of the Gibbs and Helmholtz statistical ensemble has been proved for a large class of systems (namely single flexible polymer chains without confinement effects and with a continuous pairing interaction potential between neighboring monomers [56, 108–112]), it is difficult to prove general results for other structures and configurations. In any case, other classes of problems, *e.g.* concerning the escape of a polymer confined between two surfaces and the desorption of a polymer initially tethered onto a surface, exhibit an unusual non-equivalence between the defined statistical ensembles [113–116]. These results have been theoretically proved and confirmed by molecular dynamic simulations. Such investigations are coherent with our achievements and prove the possibility to have a real nonequivalence between different (canonical) ensembles in statistical mechanics.

The other important parameter of the system is the number of unbroken vertical elements, which can be calculated through Eq.(3.64). This expression can be elaborated in the limiting case of $N\to\infty$, eventually obtaining the asymptotic form

$$\langle\xi\rangle = \frac{\int_0^1 Nx e^{Nx\left(\alpha\eta-\frac{1}{2}\log b\right)}e^{\frac{1}{4\alpha}\mathcal{F}^2\left[N(1-x)+\frac{b}{b-1}\right]}\mathrm{d}x}{\int_0^1 e^{Nx\left(\alpha\eta-\frac{1}{2}\log b\right)}e^{\frac{1}{4\alpha}\mathcal{F}^2\left[N(1-x)+\frac{b}{b-1}\right]}\mathrm{d}x}. \tag{3.73}$$

As done before, we can use the change of variable $s=N(1-x)+\frac{b}{b-1}$, which delivers

$$\langle\xi\rangle = \frac{\int_{\frac{b}{b-1}}^{N+\frac{b}{b-1}}\left(N+\frac{b}{b-1}-s\right)e^{-\left(\alpha\eta-\frac{1}{2}\log b\right)s}e^{\frac{1}{4\alpha}\mathcal{F}^2 s}\mathrm{d}s}{\int_{\frac{b}{b-1}}^{N+\frac{b}{b-1}}e^{-\left(\alpha\eta-\frac{1}{2}\log b\right)s}e^{\frac{1}{4\alpha}\mathcal{F}^2 s}\mathrm{d}s}. \tag{3.74}$$

From now on, it is better to consider the number of broken vertical elements $\langle\zeta\rangle = N-\langle\xi\rangle$ given

by

$$\langle\zeta\rangle = \frac{\int_{\frac{b}{b-1}}^{N+\frac{b}{b-1}} e^{-\left(\alpha\eta-\frac{1}{2}\log b\right)s} e^{\frac{1}{4\alpha}\mathcal{F}^2 s} s\mathrm{d}s}{\int_{\frac{b}{b-1}}^{N+\frac{b}{b-1}} e^{-\left(\alpha\eta-\frac{1}{2}\log b\right)s} e^{\frac{1}{4\alpha}\mathcal{F}^2 s}\mathrm{d}s} - \frac{b}{b-1}. \tag{3.75}$$

This result proves that the limit of ζ for $N \to \infty$ exists and can be written as follows

$$\langle\zeta\rangle = \frac{\int_{\frac{b}{b-1}}^{+\infty} e^{-\left(\alpha\eta-\frac{1}{2}\log b\,\frac{1}{4\alpha}\mathcal{F}^2\right)s} s\mathrm{d}s}{\int_{\frac{b}{b-1}}^{+\infty} e^{-\left(\alpha\eta-\frac{1}{2}\log b-\frac{1}{4\alpha}\mathcal{F}^2\right)s}\mathrm{d}s} - \frac{b}{b-1}. \tag{3.76}$$

In contrast to the calculation concerning the Helmholtz ensemble, here we can evaluate Eq.(3.76) in closed form and we eventually find that

$$\langle\zeta\rangle = \frac{1}{\alpha\eta - \frac{1}{2}\log b - \frac{1}{4\alpha}\mathcal{F}^2}. \tag{3.77}$$

Also in this case, we observe the divergence of $\langle\zeta\rangle$ for a value of force exactly given by Eq.(3.38) of Section 3.4, dealing with the isometric condition. This point confirms the presence of the phase transition for the isotensional condition as well. To conclude, Eqs.(3.70) and (3.77) completely describe the behavior of the cohesion-decohesion process within the Gibbs ensemble for a system attaining the thermodynamic limit. These results can be written as follows, by making explicit the real physical quantities

$$\langle y_{N+1}\rangle = \frac{f}{k}\left[\frac{e^{\frac{hy_M^2}{K_B T_c}}}{e^{\frac{hy_M^2}{K_B T_c}}-1} + \frac{1}{\frac{hy_M^2}{2K_B T}\left(1-\frac{T}{T_c}-\frac{f^2}{khy_M^2}\right)}\right], \tag{3.78}$$

$$\langle\zeta\rangle = \frac{1}{\frac{hy_M^2}{2K_B T}\left(1-\frac{T}{T_c}-\frac{f^2}{khy_M^2}\right)}, \tag{3.79}$$

where the critical temperature T_c is given in Eq.(3.41). While the first equation represents the force-extension relation during the cohesion-decohesion process, the second one indicates the number of broken vertical elements in terms of the applied force and the temperature. These two results have been compared in Fig.3.12 with their discrete counterparts given in Eqs.(3.63) and (3.64), applied to a system with $N = 100$. The good agreement obtained in Fig.3.12 proves that the discrete and the continuous approaches give very similar results in the thermodynamic limit. In both plots, we can identify the temperature-dependent critical force able to generate the complete detachment of the chain. In addition, although we have proved the nonequivalence of the ensembles in the thermodynamic limit, we observe that the value of the asymptotic force and the corresponding critical temperature are the same for both the Gibbs and the Helmholtz ensembles.

To conclude, it is interesting to remark that Eq.(3.79) can be used to trace the phase diagram of the system, where we can identify two different regions corresponding to the states "completely detached" and "partially detached". When $\langle\zeta\rangle$, obtained through Eq.(3.79), is positive, or equivalently when $1-\frac{T}{T_c}-\frac{f^2}{khy_M^2} > 0$, we are in a situation of partial detachment and we can

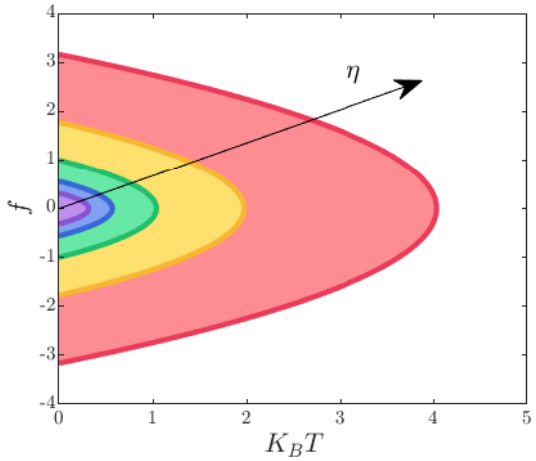

Figure 3.13: Phase diagram of the isotensional detachment process obtained for different values of the ratio η. While the external region corresponds to the complete detachment, the internal one to the partial detachment. We adopted the parameters $k = 1$, $y_M = 1$, and $\eta = 0.1, 0.316, 1, 3.16, 10$ (in arbitrary units).

increase the force and/or the temperature to bring the detachment to an end. In this case, we are in the internal shaded areas of Fig.3.13. On the other hand, when $1 - \frac{T}{T_c} - \frac{f^2}{khy_M^2} < 0$, the chain is completely detached and we are in the external areas of Fig.3.13. We observe from Fig.3.13 that, for a value of the applied force f in a given range, we have a value of the temperature able to denaturate the system. In the particular case with $f = 0$, such a temperature is identical to the critical temperature given in Eq.(3.41). In other words, for any subcritical temperature $T < T_c$, we can identify a value of force inducing the complete detachment of the chain. In this respect, the critical behavior of the Helmholtz ensemble is different. In fact, in the isometric condition, we have no finite values of the prescribed y_{N+1} able to denaturate the system for subcritical temperatures $T < T_c$. This difference between the Helmholtz and the Gibbs ensembles is consistent with their non-cooperative and cooperative interpretation, respectively. Indeed, for the Gibbs ensemble, we can have a value of f inducing complete decohesion for $T < T_c$ since all vertical elements break simultaneously and, therefore, the critical force can induce the denaturation. Conversely, for the Helmholtz ensemble, the number of broken elements is proportional to y_{N+1} (for y_{N+1} large enough, see Eq.(3.49)) and therefore we can not entirely detach the system with a finite value of y_{N+1} for $T < T_c$.

3.7 Application to nucleic acid hairpins

Recently, the mechanical unfolding of nucleic acid hairpins has been experimentally and numerically investigated in order to determine the phase diagram in the force-temperature plane [251, 252]. Hairpins are closed loops composed of nucleobases of DNA or RNA as shown in Fig.3.14. The force spectroscopy techniques are applied to measure the force necessary to open the hairpin's structures. Since the geometry of the hairpin experiments is very similar to the one adopted in the investigation concerning adhesion/deadhesion processes, and because of the generality of our results, we can show here the comparison between experimental and theoretical findings. In particular, the theory previously developed can be applied to give a theoretical

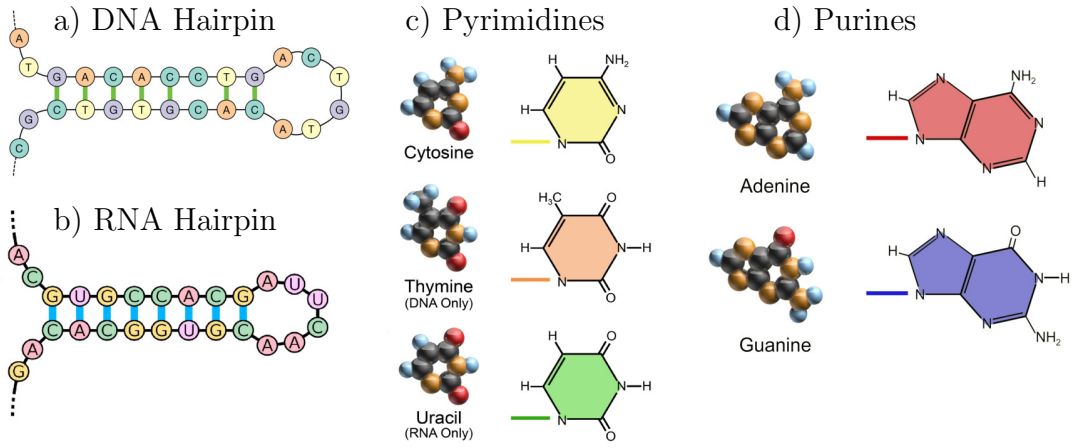

Figure 3.14: Hairpin structures. a) DNA hairpin example composed of C, T, A, and G bases. b) RNA hairpin example composed of C, U, A, and G bases. c) Pyrimidine nucleobases cytosine (C), thymine (T), and uracil (U) consist of simple ring molecules. d) Purine nucleobases adenine (A) and guanine (G) consist of fused-ring molecules. The images are adapted from Wikipedia under CC BY 3.0 license.

interpretation of the experimental results obtained through the unfolding of RNA and DNA hairpins by optical-thermal tweezers [253, 254]. Concerning RNA, the unfolding of a 20-base-pair tetraloop hairpin was studied under different ionic conditions and at temperatures ranging from 22 °C to 42 °C [253]. Aluminum heating plates with thermoelectric coolers have been used to heat the system and the temperature has been measured by a thin thermocouple. At each temperature, single hairpin molecules have been held at constant force (Gibbs ensemble), and the transition force has been measured versus the controlled temperature of the experiment (see Fig.3.15, top right panel). The experimental data are also plotted in Fig.3.15 (bottom panel, red down-pointing triangles) together with the theoretical curve obtained through Eqs.(3.40) and (3.41), with $k = 0.6$ N/m, $h = 86.3$ N/m and $y_M = 7.77$ pm. Concerning DNA, a 6.8 kbp hairpin obtained from λ-DNA has been used in a temperature-jump optical trap for single-molecule manipulation [254]. In this case, the temperature is controlled by a heating laser with a wavelength highly absorbed by water in order to have a quite broad range of temperatures between 5 °C and 50 °C (see Fig.3.15, top left panel). The resulting transition force is also plotted in Fig.3.15 (bottom panel, blue up-pointing triangles) against the theoretical curve obtained, as before, through Eqs.(3.40) and (3.41), and now with $k = 1$ N/m, $h = 5.34$ N/m, and $y_M = 19.5$ pm. In Fig.3.15, bottom panel, we also added a green square symbol corresponding to the measured denaturation temperature of DNA (here also assumed for RNA) [255, 256]. We remark however that the denaturation temperature is rather sensible to the solvent conditions and the base composition of the nucleic acids [257]. The value $k = 1$ N/m for DNA has been imposed since a Young modulus of 300MPa has been estimated for the linear elasticity of DNA [258]. Indeed, by assuming a Young modulus $E = 300$ MPa, a DNA radius $r = 1$ nm and a distance between base pairs $\ell = 0.34$ nm, we easily obtained $k = \pi r^2 E/\ell \simeq 1$ N/m. Concerning the RNA stretching modulus, we adopted the value $k = 0.6$ N/m since calculations and experiments indicate that the stretch modulus of dsDNA is nearly twofold larger than that of dsRNA [259, 260]. The different mechanical behaviors of DNA and RNA are thoroughly explained in the recent literature [259, 260]. The other parameters (h and y_M) have been fitted to obtain a good agreement between experimental and theoretical

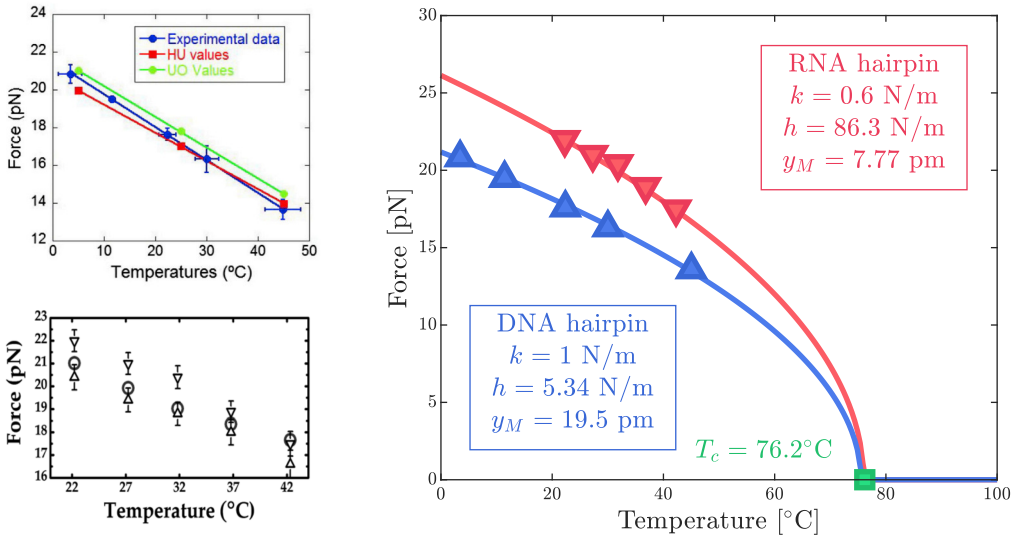

Figure 3.15: Top left panel: DNA hairpin unfolding experimental data; reproduced with permission [254]. The experimental data (blue points) are compared with two theoretical predictions, HU and UO, described by [254]. Bottom left panel: RNA hairpin unfolding experimental data; reproduced with permission [253]. The down-pointing triangles correspond to the unfolding, the up-pointing triangles to the refolding and the circles to the equilibrium force (at which the unfolding and refolding rate constants are equal). Right panel: comparison between experimental results for the unzipping of RNA and DNA hairpins. Red down-pointing triangles: RNA hairpins [253]; blue up-pointing triangles: DNA hairpins [254]. Both sets of results are shown in the first two panels, and our theoretical predictions are here represented by continuous lines. The green square symbol corresponds to a measurement of the denaturation temperature [255, 256].

results for both RNA and DNA hairpins. It is interesting to note that the curves are able to jointly represent both the experimental data with the applied force at different temperatures [253, 254], and the measurements concerning the denaturation temperature [255, 256]. Moreover, the obtained values of h are larger than k, coherently with other DNA models based on the Morse potential [80]. To conclude, also the values of the extension threshold y_M are reasonable being lesser than the distance between base pairs $\ell = 0.34$ nm, which is a characteristic length for nucleic acids.

3.8 Conclusion

In this Chapter, we elaborated a model to describe the cohesion/decohesion process related to a film deposited on a substrate, by focusing on the effects of the thermal fluctuations. We analyzed this process under an additional mechanical action, represented by either an external force or a prescribed extension applied to the end-terminal of the chain. These two conditions correspond to the Gibbs and the Helmholtz ensembles of statistical mechanics, respectively. To approach the problem, we combined the method based on the spin variables [91, 92] with a refined analysis of

the properties of some tridiagonal matrices [96, 97], characterizing the system under investigation. Firstly, we developed the theory for the Helmholtz ensemble and then we obtained the results for the Gibbs one through the Laplace transform describing the relationship between the partition functions of the two ensembles [98]. Eventually, for both statistical ensembles, we obtained explicit results giving the force-extension relation, the average number of broken units, and the average extension of all the elements of the chain as functions of the temperature and of the external mechanical action (a force for the Gibbs ensemble and an extension for the Helmholtz one). These achievements, summarized in Eqs.(3.27)-(3.30) (Helmholtz) and Eqs.(3.63)-(3.66) (Gibbs), and obtained for an arbitrary number N of elements of the chain, are useful to fully understand the behavior of the system, to compare with existing results concerning the folding/unfolding of macromolecular bistable chains, and finally to perform the analysis of the thermodynamic limit. Indeed, when $N \to \infty$, the sums in Eqs.(3.27)-(3.30) (Helmholtz) and Eqs.(3.63)-(3.66) (Gibbs) can be substituted by suitable integrals by introducing a discrete to continuous transformation. Such an analysis allows proving that, in the thermodynamic limit, the peeling of the film from the substrate takes place at a given critical force, which is temperature dependent. In the cohesion/decohesion process, the origin of the temperature-dependent peeling force is explained through the observation of a phase transition taking place at a given critical temperature able to fully detach the film from the substrate. In the subcritical regime, the thermal fluctuations promote the detachment of the film, and, therefore, a lower peeling force is needed for higher temperatures. The decreasing trend of the peeling force with the temperature is the same for both statistical ensembles. However, these latter are nonequivalent in the thermodynamic limit since they show a different force-extension curve. The obtained relation for the temperature-dependent denaturation force has been tested against experimental data concerning the unzipping of RNA and DNA hairpins, eventually obtaining a good agreement between theory and measurements.

While the presented model is interesting since leads to a fully analytic approach able to explain the emergence of the phase transition and the nonequivalence of the ensembles, it could be generalized to take into consideration more complex situations. For instance, the spin variable methodology, here employed to calculate the partition functions, is limited to the study of equilibrium thermodynamics. It could be interesting to generalize it to the dynamic regime, where the real energy function describing the units of the system plays an important role [99–101]. Moreover, our approach could be applied to different system configurations including fiber bundles with breakable strands, buckling of films deposited over substrates, cracks propagation in brittle or plastic solids, and rupture phenomena in polymer networks.

3.9 Appendix

3.9.1 Tridiagonal matrix

We prove here some properties concerning the matrix $\mathcal{A}_N^{\xi}(\eta)$, defined in Eq.(3.5). To begin, we consider the following arbitrary tridiagonal matrix $\mathcal{T}$

$$\mathcal{T} = \begin{pmatrix} a_1 & b_1 & 0 & \cdots & 0 \\ c_1 & \ddots & \ddots & \ddots & \vdots \\ 0 & \ddots & \ddots & \ddots & 0 \\ \vdots & \ddots & \ddots & \ddots & b_{N-1} \\ 0 & \cdots & 0 & c_{N-1} & a_N \end{pmatrix} \in \mathcal{M}_{N,N}(\mathbb{R}), \tag{3.80}$$

where the diagonal is composed by the elements $(a_1,\dots,a_N)$, the superdiagonal by $(b_1,\dots,b_{N-1})$ and the subdiagonal by $(c_1,\dots,c_{N-1})$. It has been proved [96, 97] that the elements of the inverse matrix $\mathcal{T}^{-1}$ can be represented as

$$\left[\mathcal{T}^{-1}\right]_{ij} = \begin{cases} \dfrac{1}{\vartheta_N}(-1)^{i+j} b_i \times \cdots \times b_{j-1}\vartheta_{i-1}\varphi_{j+1}, & \text{if } i<j \\ \dfrac{1}{\vartheta_N}\vartheta_{i-1}\varphi_{i+1}, & \text{if } i=j \\ \dfrac{1}{\vartheta_N}(-1)^{i+j} c_j \times \cdots \times c_{i-1}\vartheta_{j-1}\varphi_{i+1}, & \text{if } i>j \end{cases} \tag{3.81}$$

where the sequences ϑ_i and φ_i are given by the recursive laws

$$\begin{cases} \vartheta_i = a_i\vartheta_{i-1} - b_{i-1}c_{i-1}\vartheta_{i-2}, \\ \vartheta_{-1}=0,\ \vartheta_0=1,\ i=1,2,\dots,N \end{cases} \tag{3.82}$$

and

$$\begin{cases} \varphi_i = a_i\varphi_{i+1} - b_i c_i \varphi_{i+2}, \\ \varphi_{N+2}=0,\ \varphi_{N+1}=1,\ i=N,\dots,1 \end{cases} \tag{3.83}$$

While Eq.(3.82) is an increasing recursive law going from $i=1$ to $i=N$, Eq.(3.83) is a decreasing recursive law going from $i=N$ to $i=1$. We also remember that $\det\mathcal{T}=\vartheta_N$ [96, 97]. In the case of the matrix $\mathcal{A}_N^{\xi}(\eta)$, we have that $b_i=-1\forall i$ and $c_i=-1\forall i$. Under this hypothesis, the general result can be simplified as follows

$$\left[\mathcal{T}^{-1}\right]_{ij} = \begin{cases} \dfrac{1}{\vartheta_N}\vartheta_{i-1}\varphi_{j+1}, & \text{if } i<j \\ \dfrac{1}{\vartheta_N}\vartheta_{i-1}\varphi_{i+1}, & \text{if } i=j \\ \dfrac{1}{\vartheta_N}\vartheta_{j-1}\varphi_{i+1}, & \text{if } i>j \end{cases} \tag{3.84}$$

where the sequences ϑ_i and φ_i are given by the reduced recursive laws

$$\begin{cases} \vartheta_i = a_i\vartheta_{i-1} - \vartheta_{i-2}, \\ \vartheta_{-1}=0,\ \vartheta_0=1,\ i=1,2,\dots,N \end{cases} \tag{3.85}$$

and

$$\begin{cases} \varphi_i = a_i\varphi_{i+1} - \varphi_{i+2}, \\ \varphi_{N+2}=0,\ \varphi_{N+1}=1,\ i=N,\dots,1 \end{cases} \tag{3.86}$$

Since we need to determine $\det \mathcal{A}_N^{\xi}(\eta)$, $\mathbf{v}^{\mathsf{T}}\left[\mathcal{A}_N^{\xi}(\eta)\right]^{-1}\mathbf{v}$, and $\left[\mathcal{A}_N^{\xi}(\eta)\right]^{-1}\mathbf{v}$, it is sufficient to calculate only the sequence ϑ_i associated to the matrix $\mathcal{A}_N^{\xi}(\eta)$. Indeed, we have that

$$\det \mathcal{A}_N^{\xi}(\eta) = \vartheta_N, \tag{3.87}$$

$$\begin{aligned}\mathbf{v}^{\mathsf{T}}\left[\mathcal{A}_N^{\xi}(\eta)\right]^{-1}\mathbf{v} &= \left[\mathcal{A}_N^{\xi}(\eta)\right]^{-1}_{NN} \\ &= \vartheta_{N-1}\varphi_{N+1}/\vartheta_N = \vartheta_{N-1}/\vartheta_N,\end{aligned} \tag{3.88}$$

$$\left\{\left[\mathcal{A}_N^{\xi}(\eta)\right]^{-1}\mathbf{v}\right\}_i = \vartheta_{i-1}\varphi_{N+1}/\vartheta_N = \vartheta_{i-1}/\vartheta_N. \tag{3.89}$$

Therefore, we consider Eq.(3.85) with $a_1 = \cdots = a_\xi = 2+\eta$ and $a_{\xi+1} = \cdots = a_N = 2$. Then, for $i \le \xi$, we have the difference equation $\vartheta_i = (2+\eta)\vartheta_{i-1} - \vartheta_{i-2}$, whose general solution can be written as

$$\vartheta_i = p\left(\frac{2+\eta+\sqrt{\Delta}}{2}\right)^i + q\left(\frac{2+\eta-\sqrt{\Delta}}{2}\right)^i, \tag{3.90}$$

with $\Delta = \eta^2 + 4\eta$ and where the coefficients p and q must be fixed through the conditions $\vartheta_{-1} = 0$ and $\vartheta_0 = 1$. A straightforward calculation leads to the explicit solution for $i \le \xi$

$$\vartheta_i = \frac{1}{\sqrt{\Delta}}\left(\frac{2+\eta+\sqrt{\Delta}}{2}\right)^{i+1} - \frac{1}{\sqrt{\Delta}}\left(\frac{2+\eta-\sqrt{\Delta}}{2}\right)^{i+1}. \tag{3.91}$$

For $i > \xi$, we have the simpler difference equation $\vartheta_i = 2\vartheta_{i-1} - \vartheta_{i-2}$, with the general solution $\vartheta_i = r + si$. In this case, the coefficients r and s must be obtained by imposing $\vartheta_{\xi-1}$ and ϑ_ξ by means of Eq.(3.90). Hence, the result for $i > \xi$ can be eventually found as

$$\vartheta_i = (i-\xi+1)\vartheta_\xi - (i-\xi)\vartheta_{\xi-1}, \tag{3.92}$$

where $\vartheta_{\xi-1}$ and ϑ_ξ are given by Eq.(3.90). The obtained results can be summarized through the final expression holding for $1 \le i \le N$

$$\vartheta_i = \begin{cases} G(i+1), & \text{if } i \le \xi \\ (i-\xi+1)G(\xi+1) - (i-\xi)G(\xi), & \text{if } i > \xi \end{cases} \tag{3.93}$$

where the function $G(z)$ is defined as follows

$$G(z) = \frac{1}{\sqrt{\Delta}}\left(\frac{2+\eta+\sqrt{\Delta}}{2}\right)^z - \frac{1}{\sqrt{\Delta}}\left(\frac{2+\eta-\sqrt{\Delta}}{2}\right)^z. \tag{3.94}$$

A more compact form of the solution can be also written as

$$\begin{aligned}\vartheta_i = {} & [G(i+1) - (i-\xi+1)G(\xi+1) + (i-\xi)G(\xi)]\mathbf{1}(\xi-i) \\ & + [(i-\xi+1)G(\xi+1) - (i-\xi)G(\xi)],\end{aligned} \tag{3.95}$$

in terms of the Heaviside step function $\mathbf{1}(x)$, defined as $\mathbf{1}(x) = 1$ if $x \geq 0$, and $\mathbf{1}(x) = 0$ if $x < 0$. To conclude, Eqs.(3.87)-(3.89) assume the final form

$$\det \mathcal{A}_N^{\xi}(\eta) = (N-\xi+1)G(\xi+1) - (N-\xi)G(\xi), \tag{3.96}$$

$$1 - \mathbf{v}^{\mathsf{T}} \left[\mathcal{A}_N^{\xi}(\eta)\right]^{-1} \mathbf{v} = \frac{G(\xi+1) - G(\xi)}{(N-\xi+1)G(\xi+1) - (N-\xi)G(\xi)}, \tag{3.97}$$

$$\left\{ \left[\mathcal{A}_N^{\xi}(\eta)\right]^{-1} \mathbf{v} \right\}_i = \frac{\vartheta_{i-1}}{(N-\xi+1)G(\xi+1) - (N-\xi)G(\xi)}, \tag{3.98}$$

where ϑ_i is given in Eq.(3.95) and the function $G(z)$ in Eq.(3.94).

Chapter 4

Thermal effects on adhesion processes with the softening mechanism

4.1 Introduction

Here we introduce an important generalization of the model presented in Chapter 3, by introducing a softening mechanism in the breakable units of the system. More specifically, we study a one-dimensional lattice of masses linked by harmonic springs and connected to a substrate by breakable links subjected to a softening mechanism (see Fig.4.1). This geometry has been previously introduced to describe a wide range of phenomena such as the peeling of tapes, adhesion of geckos, and denaturation of macromolecules [7, 8]. However, the thermal fluctuations and the softening mechanism have been neglected in these works, even though, in the physical systems recalled above, they can play a crucial role that is analyzed in detail in the following development.

From the mechanical point of view, we consider two different kinds of loading, which induce the decohesion of the system from the substrate. The decohesion process can be induced by either prescribing a given extension of the last element of the chain (Fig.4.1.a) or by applying an external force to the last unit of the chain (Fig.4.1.b). On one hand, the first isometric condition corresponds to the Helmholtz ensemble of statistical mechanics and can be generated by hard devices. On the other hand, the isotensional condition corresponds to the Gibbs ensemble of the statistical mechanics and can be generated by soft devices. Indeed, these two boundary conditions can be deduced as limiting cases of real loading experiments, when the stiffness of the device is large (hard device) or is negligible (soft device) as compared with the loaded system one, respectively [94, 95]. From a theoretical point of view, an intriguing problem concerns the equivalence of the two ensembles in the thermodynamic limit (*i.e.* for very large systems) [56, 98, 108–112]. Interestingly, we will prove, in our case, the non-equivalence of the ensembles in the thermodynamic limit. Moreover, we are able to study the force necessary to detach the chain from the substrate as a function of the temperature and of the external mechanical action applied to the system. In this context, we obtain a critical behavior described by specific phase transitions. Also, the evolution of the number of intact, softened, and broken elements are thoroughly investigated in both isometric and isotensional conditions. To conclude, the aim of this part is to fully analyze the cohesion-decohesion process with a softening mechanism in both the Helmholtz and Gibbs ensembles, thus providing a complete picture of the effect of the temperature and loading type on this prototypical physical system.

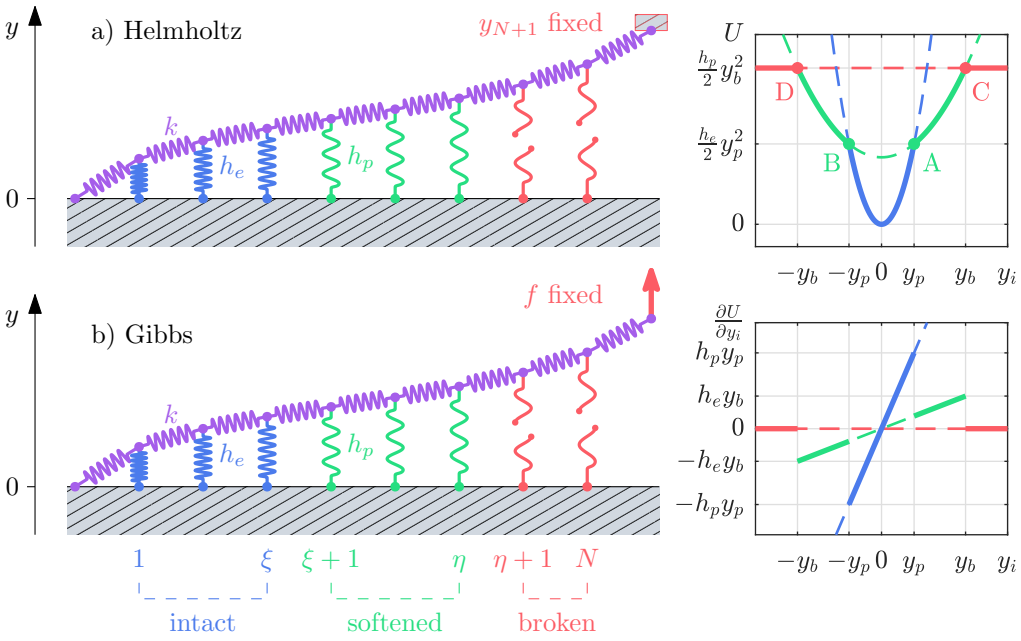

Figure 4.1: Scheme of the cohesion-decohesion process within both the Helmholtz (a) and the Gibbs (b) ensembles. While in the first case, we prescribe the position y_{N+1} and we measure the average force $\langle f \rangle$, in the second case we apply a force f and we measure the average position $\langle y_{N+1} \rangle$. In both cases, we consider a linear elastic behavior for the horizontal springs (in purple) and a breakable response with softening mechanism (blu, green and red springs corresponding to the intact, softened and broken configuration of the breakable springs) for the vertical elements. The energy potential U (top right) and its resulting force $\partial U/\partial y_i$ (bottom right) corresponding to the horizontal breakable springs are showed.

This Chapter is organized as follows. In Section 4.2 we define the problem and we simplify the spin variable methods through the zipper assumption. Then, in Section 4.3, we introduce the system behavior under isometric conditions, and in Section 4.4, we analyze its thermodynamic limit. Similarly, in Section 4.5, we introduce the system behavior under isotensional conditions, and in Section 4.6, we analyze its thermodynamic limit. The conclusions (Section 4.8) and two mathematical Appendices close the Chapter.

4.2 Problem statement

Our prototypical system is represented in Fig.4.1. The horizontal springs of the lattice are purely harmonic, characterized by the elastic constant k, with potential energy

$$W(y_{i+1} - y_i) = \frac{1}{2} k (y_{i+1} - y_i)^2. \tag{4.1}$$

On the other hand, the vertical ones can be in three different states, depending on their extension y_i (as shown in the right panel of Fig.4.1). When $|y_i| < y_p$, they are intact (elastic constant h_e), when $y_p < |y_i| < y_b$ they are softened (elastic constant $h_p < h_e$), and when $|y_i| > y_b$ they are broken (they do not support forces). This scheme represents the softening mechanism of

the breakable bonds. We describe such behavior in a spin formalism by introducing a discrete variable S_i associated with each vertical spring. Hence, we can write the potential energy of the breakable bonds in the form

$$\begin{aligned} U(y_i, S_i) = \frac{S_i(1+S_i)}{2}\frac{1}{2}h_e y_i^2 + (1+S_i)(1-S_i)\left(\frac{1}{2}h_p y_i^2 + \Delta E\right) \\ - \frac{S_i(1-S_i)}{2}\left(\frac{1}{2}h_p y_b^2 + \Delta E\right), \end{aligned} \tag{4.2}$$

where $S_i = +1$ corresponds to the intact state, $S_i = 0$ corresponds to the softened state, and $S_i = -1$ corresponds to the broken state ($i = 1, \ldots, N$). With these assumptions, we have a phase space composed of the N continuous variables $y_i \in \mathbb{R}$ and the N discrete variables $S_i \in \{+1, 0, -1\}$. Therefore, when we calculate the partition function, we have to integrate over all the continuous variables and sum over all the discrete ones. In doing so, the switching of the variable S_i and their statistics at thermodynamic equilibrium are directly controlled by the statistical ensemble (Helmholtz or Gibbs in our case) imposed on the system.

The assumption of considering independent spins for all the breakable bonds is the most rigorous approach in order to analyze the system behavior. However, on this assumption, the statistical mechanics of the system under investigation cannot be analytically developed and also its numerical implementation is quite expensive. Indeed, the calculation of the partition function is rather prohibitive because of the sum over all the possible spin combinations. Nevertheless, since we are studying the cohesion-decohesion process under an external mechanical action applied to one endpoint of the system, suppose the right one, we can simplify the model by assuming to have $N - \eta$ broken elements on the right region of the chain, $\eta - \xi$ softened elements on the central region of the chain and ξ intact or unbroken elements on the left region of the chain (see Fig.4.1). In other words, we suppose to have two moving interfaces or domain walls between the three regions of the chain. This hypothesis strongly reduces the mathematical complexity of the problem and is reasonable if we work at temperatures sufficiently low and at an applied mechanical load sufficiently large (either extension or force). Indeed, the set of the three-state spin variables S_i is substituted by the two variables η and ξ, assuming values in the set $\{0, 1, 2, \ldots, N\}$. In this sense, η and ξ can be viewed as multi-valued spin variables. Moreover, this hypothesis is similar to the one adopted in the so-called zipper model, largely used to describe the helix-coil transitions in proteins, the gel-sol transition of thermo-reversible gels, and the melting or denaturation of DNA [104–107]. By implementing this simplified scheme, we deduce a fully analytical solution of both Helmholtz and Gibbs boundary problems for an arbitrary number N of elements of the chain, and also in the thermodynamic limit ($N \to \infty$).

One of the most important results concerns the analytic expressions of the temperature-dependent debonding force (or system strength) in both cases of isotensional and isometric loading. This temperature-dependent behavior can be interpreted by observing that the thermal fluctuations may foster the decohesion, allowing the escape from the energy well shown in the U graph of Fig.4.1. More rigorously, we prove that this behavior can be explained in terms of a phase transition occurring at a given critical temperature. In particular, it means that the system can be completely detached from the substrate for supercritical temperatures even without any external mechanical action.

This behavior has been observed in several polymeric systems subjected to a force [261–263]. In particular, several important results have been obtained for the pulling processes of adsorbed polymers on a surface. They were found by means of directed or partially directed walk models of lattice polymers adsorbed at a surface under the influence of an applied force [264, 265]. In this context, a temperature-dependent critical force has been derived for semi-flexible polymers

[266], polymers subject to an arbitrarily oriented force[267], heterogeneous adsorption surfaces [268], striped adsorption surfaces [269], and self-avoiding chains [270–272]. From a theoretical point of view, the main difference between these approaches and ours is that they use lattice polymer techniques whereas we adopt continuous geometric variables. Interestingly, the lattice methods can also describe bubbles with different physical states along the chain, without needing the zipper simplifying assumption. In our case neglecting such simplifying assumption would lead to a numerical treatment of the subject and we preferred the analytical clearness of the results. Importantly, in our continuous model, we also introduced the softening mechanism, which is the main topic of this Chapter and represents, as we show in the following, an important ingredient to distinguish different observed regimes in the decohesion behavior.

In our system, although the decohesion force for subcritical temperatures is the same for both statistical ensembles, they are not equivalent in the thermodynamic limit since the force-extension curves are different under isometric and isotensional conditions. Importantly, the softening mechanism in the breakable elements generates a strength-temperature curve composed of two branches connected, with continuity, at a given temperature T_0. From the physical point of view, this is the temperature at which all the elements are at least softened. The interesting point is that this transition has been experimentally observed in the strength behavior of some systems including sapphire whiskers [33] and a number of high-entropy and medium-entropy alloys [35, 38]. In these cases, the softening mechanism comes from the emergence of a population of dislocations beyond a certain threshold of deformation.

Another fundamental effect induced by the bonds softening is the possibility of describing a temperature-dependent process zone that for enough high temperatures anticipates the propagation front. As a result, we may obtain a transition between different regimes, experimentally observed for example in polymeric materials [273, 274].

Summarizing, the proposed system is particularly important for the following reasons: (i) once previous crucial assumptions are considered, the model can be analytically solved in both isometric and isotensional statistical ensembles; (ii) the solution shows a phase transition at a critical temperature that can be calculated in closed form; (iii) the studied system manifestly shows the ensembles non-equivalence in the thermodynamic limit, which is an unusual feature in statistical mechanics; (iv) finally, the model describes the existence of a two-branch curve for the strength-temperature behavior, observed in real materials, as a result of a softening anticipating breaking effects.

4.3 Hard device: Helmholtz ensemble

We consider the cohesion-decohesion process in the system represented in Fig.4.1.a, where the detachment is generated by imposing the extension y_{N+1} of the last element of the chain. This condition corresponds to the Helmholtz ensemble of the statistical mechanics and it is obtained in the case of loading with hard devices (with a very large, ideally infinity, intrinsic elastic constant). We identify the longitudinal springs with the potential energy $W(z) = \frac{1}{2}kz^2$ for any $z \in \mathbb{R}$, and the transverse springs with the potential energy $U(y) = \frac{1}{2}h_e y^2$ if $|y| \leq y_p$ (intact), $U(y) = \frac{1}{2}h_p y^2 + \Delta E$ if $y_p < |y| \leq y_b$ (softened), and $U(y) = \frac{1}{2}h_p y_b^2 + \Delta E$ if $|y| > y_b$ (broken). The values $\pm y_p$ of the extension correspond to the softening points A and B of the breakable spring, where the elastic constant switch from h_e to $h_p < h_e$. The force jump at $y = \pm y_p$ is given by $\sqrt{2\Delta E(h_e - h_p)}$ (see bottom right panel of Fig.4.1). We simply calculate that $y_p = \sqrt{2\Delta E/(h_e - h_p)}$, and we must always impose the inequality $y_b > y_p$, where $\pm y_b$ are the extensions at the breaking points C and D of the transverse elements. As anticipated, we assume that a first group of ξ elements of the chain are intact ($i = 1, \ldots, \xi$), a second group of $\eta - \xi$ elements are softened ($i = \xi + 1, \ldots, \eta$), and

a third group of $N-\eta$ elements are broken ($i=\eta+1,\dots,N$). These premises allow us to write the total potential energy of the system in the following form

$$\begin{aligned}\Phi &= \sum_{i=0}^{N} W\left(y_{i+1}-y_i\right)+\sum_{i=1}^{N} U\left(y_i\right)\\ &=\sum_{i=0}^{N}\frac{1}{2}k\left(y_{i+1}-y_i\right)^2+\sum_{i=1}^{\xi}\frac{1}{2}h_e y_i^2+\sum_{i=1+\xi}^{\eta}\left[\frac{1}{2}h_p y_i^2+\Delta E\right]\\ &\quad+\sum_{i=1+\eta}^{N}\left[\frac{1}{2}h_p y_b^2+\Delta E\right],\end{aligned} \tag{4.3}$$

where the applied extension y_{N+1} is considered as a parameter and we fix $y_0=0$. The variables belonging to the phase space are the extensions $y_1,\dots,y_N$, and the two configurational numbers ξ and η, characterizing the state of the breakable elements. For further convenience, the energy function Φ can be further arranged as follows

$$\begin{aligned}\Phi(\mathbf{y},\xi,\eta;y_{N+1}) = \frac{1}{2}k\mathbf{y}^{\mathsf{T}}\mathcal{A}(\xi,\eta)\mathbf{y}-ky_{N+1}\mathbf{v}^{\mathsf{T}}\mathbf{y}+\frac{1}{2}ky_{N+1}^2\\ +(N-\xi)\Delta E+(N-\eta)\frac{1}{2}h_p y_b^2,\end{aligned} \tag{4.4}$$

where we defined

$$\mathbf{y}^{\mathsf{T}}=\begin{pmatrix}y_1 & y_2 & \dots & y_N\end{pmatrix}\in\mathbb{R}^N, \tag{4.5}$$

$$\mathbf{v}^{\mathsf{T}}=\begin{pmatrix}0 & \dots & 0 & 1\end{pmatrix}\in\mathbb{R}^N, \tag{4.6}$$

and the tridiagonal (symmetric and positive definite) matrix

$$\mathcal{A}(\xi,\eta)=\begin{pmatrix}a_1 & -1 & 0 & \cdots & 0\\ -1 & \ddots & \ddots & \ddots & \vdots\\ 0 & \ddots & \ddots & \ddots & 0\\ \vdots & \ddots & \ddots & \ddots & -1\\ 0 & \cdots & 0 & -1 & a_N\end{pmatrix}\in\mathcal{M}_{N,N}(\mathbb{R}). \tag{4.7}$$

We observe that ξ and η must fulfill the condition $0\le\xi\le\eta\le N$. Moreover, this matrix has all the subdiagonal and superdiagonal elements equal to -1, and the diagonal elements are defined as follows

$$a_i=\begin{cases}2+\alpha & \text{if } 1\le i\le\xi,\\ 2+\beta & \text{if } \xi+1\le i\le\eta,\\ 2 & \text{if } \eta+1\le i\le N,\end{cases} \tag{4.8}$$

where we introduced the rescaled elastic constants

$$\alpha=\frac{h_e}{k},\quad \beta=\frac{h_p}{k}. \tag{4.9}$$

The algebraic properties of the matrix $\mathcal{A}(\xi,\eta)$ are thoroughly studied in the Appendix, where we evaluate the quantities needed to obtain the temperature-dependent relations among the

observables during the cohesion-decohesion process.

It is well known that the equilibrium statistical mechanics of a system in contact with a reservoir at temperature T is described by the canonical distribution. The expectation values of physical observables can be obtained by evaluating the partition function that, within the Helmholtz ensemble, can be written as

$$Z_H(y_{N+1}) = \sum_{\eta=0}^{N}\sum_{\xi=0}^{\eta}\int_{\mathbb{R}^N} e^{-\frac{\Phi(\mathbf{y},\xi,\eta;y_{N+1})}{K_B T}}\,\mathrm{d}y_1\ldots\mathrm{d}y_N, \tag{4.10}$$

where we have to integrate the continuous variables represented by the vector $\mathbf{y}$ and sum over the discrete variables ξ and η, describing the state (intact, softened, or broken) of the elements of the chain ($0 \le \xi \le \eta \le N$). Using Eq.(4.4), Z_H can be evaluated using the property of Gaussian integrals

$$\int_{\mathbb{R}^N} e^{-\frac{1}{2}\mathbf{y}^\mathsf{T}\mathcal{M}\mathbf{y}} e^{\mathbf{b}^\mathsf{T}\mathbf{y}}\mathrm{d}y_1\ldots\mathrm{d}y_N = \sqrt{\frac{(2\pi)^N}{\det\mathcal{M}}}\, e^{\frac{1}{2}\mathbf{y}^\mathsf{T}\mathcal{M}^{-1}\mathbf{b}}, \tag{4.11}$$

holding for any symmetric and positive definite matrix $\mathcal{M}$. In particular, we can introduce $\mathcal{M} = \frac{k}{K_B T}\mathcal{A}$ and $\mathbf{b} = \frac{k y_{N+1}}{K_B T}\mathbf{v}$ to obtain

$$Z_H(y_{N+1}) = \left[\sqrt{\frac{2\pi K_B T}{k}} e^{-\frac{2\Delta E + k\beta y_b^2}{2K_B T}}\right]^N \sum_{\eta=0}^{N}\sum_{\xi=0}^{\eta}\Gamma_{\xi,\eta}(T, y_{N+1}), \tag{4.12}$$

where

$$\Gamma_{\xi,\eta}(T, y_{N+1}) = \frac{\exp\left\{\xi\frac{\Delta E}{K_B T} + \eta\frac{k\beta y_b^2}{2K_B T} - \frac{k y_{N+1}^2}{2K_B T}\left[1 - \mathcal{A}^{-1}_{NN}(\xi,\eta)\right]\right\}}{\sqrt{\det\mathcal{A}(\xi,\eta)}}, \tag{4.13}$$

and $\mathcal{A}^{-1}_{NN}(\xi,\eta) = \mathbf{v}^\mathsf{T}\mathcal{A}^{-1}(\xi,\eta)\mathbf{v}$. We can thus determine the average force associated with the vertical extension y_{N+1} of the last element of the chain as [98]

$$\langle f\rangle = -K_B T\frac{\partial \log Z_H}{\partial y_{N+1}} = -\frac{K_B T}{Z_H}\frac{\partial Z_H}{\partial y_{N+1}}. \tag{4.14}$$

We obtain

$$\langle f\rangle = \frac{\sum_{\eta=0}^{N}\sum_{\xi=0}^{\eta}\left\{1 - \mathcal{A}^{-1}_{NN}(\xi,\eta)\right\}\Gamma_{\xi,\eta}(T, y_{N+1})}{\sum_{\eta=0}^{N}\sum_{\xi=0}^{\eta}\Gamma_{\xi,\eta}(T, y_{N+1})} k y_{N+1}. \tag{4.15}$$

This expression represents the force-extension relation for the system within the Helmholtz ensemble, or equivalently, under isometric conditions. It is also important to calculate the average value of the number of broken elements $\langle N - \eta\rangle$ and the average number of softened elements

$\langle \eta - \xi \rangle$. These quantities can be directly evaluated through the expressions

$$\begin{aligned}\langle N-\eta\rangle &= \frac{1}{Z_H}\sum_{\eta=0}^{N}\sum_{\xi=0}^{\eta}\int_{\mathbb{R}^N}(N-\eta)e^{-\frac{\Phi\left(\boldsymbol{y},\xi,\eta;y_{N+1}\right)}{K_BT}}\,\mathrm{d}y_1\ldots\mathrm{d}y_N \\ &= \frac{\sum_{\eta=0}^{N}\sum_{\xi=0}^{\eta}(N-\eta)\Gamma_{\xi,\eta}(T,y_{N+1})}{\sum_{\eta=0}^{N}\sum_{\xi=0}^{\eta}\Gamma_{\xi,\eta}(T,y_{N+1})}, \qquad (4.16)\\ \langle \eta-\xi\rangle &= \frac{1}{Z_H}\sum_{\eta=0}^{N}\sum_{\xi=0}^{\eta}\int_{\mathbb{R}^N}(\eta-\xi)e^{-\frac{\Phi\left(\boldsymbol{y},\xi,\eta;y_{N+1}\right)}{K_BT}}\,\mathrm{d}y_1\ldots\mathrm{d}y_N \\ &= \frac{\sum_{\eta=0}^{N}\sum_{\xi=0}^{\eta}(\eta-\xi)\Gamma_{\xi,\eta}(T,y_{N+1})}{\sum_{\eta=0}^{N}\sum_{\xi=0}^{\eta}\Gamma_{\xi,\eta}(T,y_{N+1})}. \qquad (4.17)\end{aligned}$$

In order to simplify the analysis it is useful to rescale the applied extension y_{N+1} with respect to y_b (*i.e.* the extension corresponding to the breaking of the link) and define the non-dimensional extension

$$\mathcal{Y} = \frac{y_{N+1}}{y_b}. \qquad (4.18)$$

In order to further simplify the formula previously derived, we can consider the rescaled energies

$$\delta = \frac{k\,y_b^2}{2K_BT}, \quad \varphi = \frac{\Delta E}{K_BT}. \qquad (4.19)$$

Thus, introducing Eqs.(4.18) and (4.19) into the expression of $\langle f\rangle$, $\langle N-\eta\rangle$ and $\langle \eta-\xi\rangle$, we obtain

$$\langle \mathcal{F}\rangle = \frac{\langle f\rangle}{k y_b} = \frac{\mathcal{Y}}{\mathcal{Z}_H}\sum_{\eta=0}^{N}\sum_{\xi=0}^{\eta}\frac{1-\mathcal{A}^{-1}_{NN}(\xi,\eta)}{\sqrt{\det\mathcal{A}(\xi,\eta)}}e^{\varphi\xi+\beta\delta\eta-\delta\mathcal{Y}^2\left\{1-\mathcal{A}^{-1}_{NN}(\xi,\eta)\right\}}, \qquad (4.20)$$

$$\langle N-\eta\rangle = \frac{1}{\mathcal{Z}_H}\sum_{\eta=0}^{N}\sum_{\xi=0}^{\eta}\frac{N-\eta}{\sqrt{\det\mathcal{A}(\xi,\eta)}}e^{\varphi\xi+\beta\delta\eta-\delta\mathcal{Y}^2\left\{1-\mathcal{A}^{-1}_{NN}(\xi,\eta)\right\}}, \qquad (4.21)$$

$$\langle \eta-\xi\rangle = \frac{1}{\mathcal{Z}_H}\sum_{\eta=0}^{N}\sum_{\xi=0}^{\eta}\frac{\eta-\xi}{\sqrt{\det\mathcal{A}(\xi,\eta)}}e^{\varphi\xi+\beta\delta\eta-\delta\mathcal{Y}^2\left\{1-\mathcal{A}^{-1}_{NN}(\xi,\eta)\right\}}, \qquad (4.22)$$

where we have used Eqs.(4.12) and (4.13) to define the (rescaled) partition function

$$\mathcal{Z}_H(\mathcal{Y}) = \sum_{\eta=0}^{N}\sum_{\xi=0}^{\eta}\frac{1}{\sqrt{\det\mathcal{A}(\xi,\eta)}}e^{\varphi\xi+\beta\delta\eta-\delta\mathcal{Y}^2\left\{1-\mathcal{A}^{-1}_{NN}(\xi,\eta)\right\}}. \qquad (4.23)$$

Using the properties of $\mathcal{A}(\xi,\eta)$ and the relations in Eqs.(4.94) and (4.95), it is possible to find explicit expressions for $\det\mathcal{A}(\xi,\eta)$ and $\mathcal{A}^{-1}_{NN}(\xi,\eta)$ so to obtain the behavior of the relevant physical quantities of the system.

Previous results are represented in Fig.4.2, where we study the dependence of the relevant quantities on the temperature and size of the system. In particular, we plotted $\langle\mathcal{F}\rangle$, $\langle\xi\rangle$, $\langle\eta-\xi\rangle$ and $\langle N-\eta\rangle$ versus the applied rescaled extension $\mathcal{Y}$ (changing the temperature) for two different cases: the first one concerns a short chain with $N=5$ (first row), and the second one a larger chain with $N=50$ (second row). For $N=5$ (first row), and for low values of the temperature, we

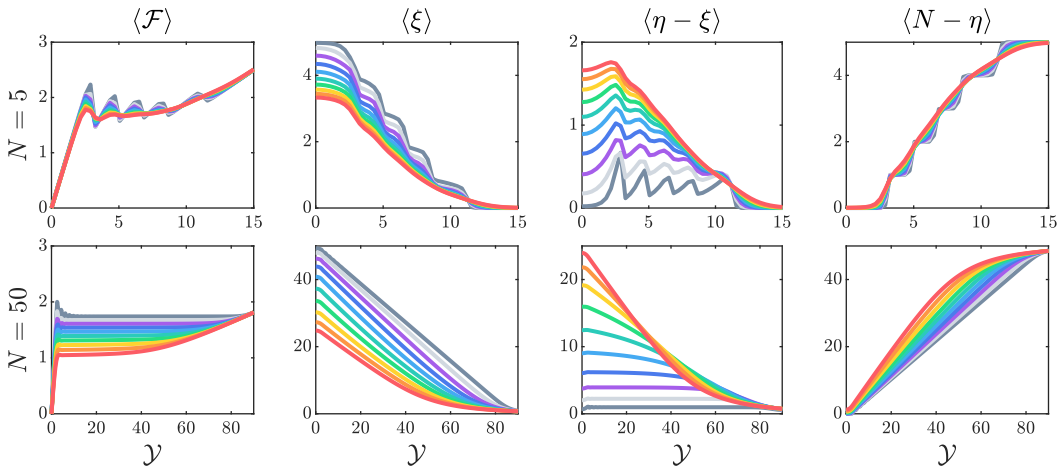

Figure 4.2: From left to right columns: force-extension curve and distribution of intact, softened, and broken elements during the detachment of a film from a substrate for the Helmholtz ensemble (hard device, extension applied to the last element of the chain). First row: we considered $N = 5$, and 10 values of K_BT from 0.5 to 5 (a.u.) from gray to red curves. Second row: we considered $N = 50$, and 10 values of K_BT from 2 to 20 (a.u.). The adopted parameters follows: $h_e = 20$, $h_p = 15$, $\Delta E = 2$, $y_b = 2y_p$ and $k = 5$ (all in arbitrary units).

easily identify the partial and complete rupture occurrences (see the peaks and/or steps in the curves of $\langle \mathcal{F} \rangle$, $\langle \xi \rangle$, $\langle \eta - \xi \rangle$ and $\langle N - \eta \rangle$). However, for larger values of the temperature, the curves are smoother because of the increasing thermal fluctuations. We also observe that the detachment of the elements of the chain occurs in a progressive way in response to the increasing extension $\mathcal{Y}$. This is a specific feature of the Helmholtz ensemble, typically observed in the folding/unfolding process of bistable macromolecules stretched by hard devices [91, 92, 94, 95, 102, 103]. For $N = 50$ (second row), we can identify two important properties of the detachment process in large systems: first, increasing $\mathcal{Y}$ the curve approximately exhibits a temperature-dependent plateau; second, during the decohesion process the number of softened elements is temperature dependent and approximately constant for small values of temperature in a certain range of $\mathcal{Y}$. Although these features can be observed in the $N = 50$ case of Fig.4.2 only for low values of the temperature, we will deduce in the thermodynamic limit (*i.e.*, when $N \to \infty$) that this behavior can be explained in terms of a phase transition (see Section 4.4). The existence of a constant finite softened domain shows the possibility of analytically describing the existence of a process zone regulating the advancing of the decohesion front as observed in cohesive fracture phenomena [273]. Interestingly, the size of the process zone increases with temperature, so that in accordance with the experimental behavior the decohesion is "fragile" at low temperature and "ductile" at higher values of the temperature [274].

4.4 Thermodynamic limit within the Helmholtz ensemble

We study here the thermodynamic limit within the Helmholtz ensemble, defined by a very large number of elements in the chain (macroscopic limit valid for large systems). To this aim we have to study the behavior of Eqs.(4.20), (4.21), (4.22), and (4.23) for $N \to \infty$. In order to perform the analysis in this limit, we formally substitute the sums appearing in these expressions

by integrals. In particular, we will use the approximation $\sum_{\chi=0}^{n}\phi(\chi)\simeq\int_0^n\phi(\chi)\mathrm{d}\chi$ for an generic function $\phi(\chi)$. A better approximation could be adopted by using the Euler-McLaurin formula [250]. However, this approach, discussed in Ref.[93], is not necessary for the purposes of the present analysis. Moreover, due to the fact that we are considering the case of N large, it is possible to use the simplified expressions of $\det\mathcal{A}(\xi,\eta)$ and $\mathcal{A}^{-1}_{NN}(\xi,\eta)$, obtained in Eqs.(4.98) and (4.99).

From Eqs.(4.20) and (4.23) we get the following explicit result for the force-extension relation

$$\langle\mathcal{F}\rangle=\mathcal{Y}\frac{\int_0^N e^{\left(\beta\delta-\frac{\log\beta_0}{2}\right)\eta-\delta\mathcal{Y}^2B_\eta^{-1}}B_\eta^{-\frac{3}{2}}\mathrm{d}\eta\int_0^\eta e^{\left(\varphi+\frac{1}{2}\log\frac{\beta_0}{\alpha_0}\right)\xi}\mathrm{d}\xi}{\int_0^N e^{\left(\beta\delta-\frac{\log\beta_0}{2}\right)\eta-\delta\mathcal{Y}^2B_\eta^{-1}}B_\eta^{-\frac{1}{2}}\mathrm{d}\eta\int_0^\eta e^{\left(\varphi+\frac{1}{2}\log\frac{\beta_0}{\alpha_0}\right)\xi}\mathrm{d}\xi},\tag{4.24}$$

where

$$\alpha_0=\frac{2+\alpha+\sqrt{\alpha^2+4\alpha}}{2},\quad \beta_0=\frac{2+\beta+\sqrt{\beta^2+4\beta}}{2}.\tag{4.25}$$

and where we introduced the function $B(x)$ defined as

$$B(x)=N-x+\frac{\beta_0}{\beta_0-1}\triangleq B_x\tag{4.26}$$

To better understand the behavior of the force-extension response for large values of N, we first perform the integration on the variable ξ, and then we fully apply the change of variable $N-\eta+\beta_0/(\beta_0-1)=s$, delivering the following result

$$\langle\mathcal{F}\rangle=\mathcal{Y}\frac{\int_{\frac{\beta_0}{\beta_0-1}}^{\frac{\beta_0}{\beta_0-1}+N}\left[e^{\left(\varphi+\frac{1}{2}\log\frac{\beta_0}{\alpha_0}\right)\left(N-s+\frac{\beta_0}{\beta_0-1}\right)}-1\right]e^{-\left(\beta\delta-\frac{1}{2}\log\beta_0\right)s-\frac{\delta\mathcal{Y}^2}{s}}\frac{\mathrm{d}s}{s^{3/2}}}{\int_{\frac{\beta_0}{\beta_0-1}}^{\frac{\beta_0}{\beta_0-1}+N}\left[e^{\left(\varphi+\frac{1}{2}\log\frac{\beta_0}{\alpha_0}\right)\left(N-s+\frac{\beta_0}{\beta_0-1}\right)}-1\right]e^{-\left(\beta\delta-\frac{1}{2}\log\beta_0\right)s-\frac{\delta\mathcal{Y}^2}{s}}\frac{\mathrm{d}s}{s^{1/2}}}.\tag{4.27}$$

The behavior of the previous expression depends on the sign of the quantity $\varphi+\frac{1}{2}\log\frac{\beta_0}{\alpha_0}$, appearing in the exponential term within the square brackets in both numerator and denominator. From Eq.(4.19) we have

$$\Theta=\varphi+\frac{1}{2}\log\frac{\beta_0}{\alpha_0}\gtrless 0\quad\Rightarrow\quad T\lessgtr\frac{2\Delta E}{K_B\log\frac{\alpha_0}{\beta_0}}\triangleq T_0,\tag{4.28}$$

where we have defined the temperature T_0, corresponding to a transition in the system behavior (we will prove that all elements are at least softened for $T>T_0$). If $T<T_0$ and we consider large values of N (thermodynamic limit), the exponential term in the square brackets of Eq.(4.27) is dominant. On the other hand, if $T>T_0$ the exponential term in the square brackets of Eq.(4.27) is negligible for large values of N. Thus, for $N\to\infty$ we obtain

$$\langle\mathcal{F}\rangle=\mathcal{Y}\frac{\int_{\frac{\beta_0}{\beta_0-1}}^{+\infty}e^{-\left(\beta\delta-\frac{1}{2}\log\alpha_0+\varphi\right)s-\frac{\delta\mathcal{Y}^2}{s}}\frac{\mathrm{d}s}{s^{3/2}}}{\int_{\frac{\beta_0}{\beta_0-1}}^{+\infty}e^{-\left(\beta\delta-\frac{1}{2}\log\alpha_0+\varphi\right)s-\frac{\delta\mathcal{Y}^2}{s}}\frac{\mathrm{d}s}{s^{1/2}}},\quad\text{for}\quad T<T_0\tag{4.29}$$

and

$$\langle \mathcal{F} \rangle = \mathcal{Y} \frac{\int_{\frac{\beta_0}{\beta_0-1}}^{+\infty} e^{-\left(\beta\delta-\frac{1}{2}\log\beta_0\right)s-\frac{\delta\mathcal{Y}^2}{s}} \frac{\mathrm{d}s}{s^{3/2}}}{\int_{\frac{\beta_0}{\beta_0-1}}^{+\infty} e^{-\left(\beta\delta-\frac{1}{2}\log\beta_0\right)s-\frac{\delta\mathcal{Y}^2}{s}} \frac{\mathrm{d}s}{s^{1/2}}}, \quad \text{for} \quad T > T_0. \tag{4.30}$$

In order to ensure the convergence of the integrals in Eqs.(4.29) and (4.30) it is necessary that the following conditions hold

$$\beta\delta - \frac{1}{2}\log\alpha_0 + \varphi > 0, \quad \text{if } T < T_0, \tag{4.31}$$

$$\beta\delta - \frac{1}{2}\log\beta_0 > 0, \quad \text{if } T > T_0. \tag{4.32}$$

These conditions have a physical interpretation that will be discussed in the following. The integrals appearing in Eqs.(4.29)-(4.30) can be evaluated in terms of error functions as discussed in 4.9.2. To simplify the form of the results, we define

$$\lambda_1 = \beta\delta - \frac{1}{2}\log\alpha_0 + \varphi, \quad \lambda_2 = \beta\delta - \frac{1}{2}\log\beta_0, \quad c = \frac{\beta_0}{\beta_0 - 1}. \tag{4.33}$$

We thus obtain

$$\langle \mathcal{F} \rangle = \sqrt{\frac{\lambda_1}{\delta}} \left[\frac{2}{1 + e^{4\mathcal{Y}\sqrt{\lambda_1\delta}} \frac{1-\mathrm{erf}\left(\sqrt{\frac{\delta}{c}}\mathcal{Y} + \sqrt{\lambda_1 c}\right)}{1+\mathrm{erf}\left(\sqrt{\frac{\delta}{c}}\mathcal{Y} - \sqrt{\lambda_1 c}\right)}} - 1 \right] \quad \text{for } T < T_0, \tag{4.34}$$

$$\langle \mathcal{F} \rangle = \sqrt{\frac{\lambda_2}{\delta}} \left[\frac{2}{1 + e^{4\mathcal{Y}\sqrt{\lambda_2\delta}} \frac{1-\mathrm{erf}\left(\sqrt{\frac{\delta}{c}}\mathcal{Y} + \sqrt{\lambda_2 c}\right)}{1+\mathrm{erf}\left(\sqrt{\frac{\delta}{c}}\mathcal{Y} - \sqrt{\lambda_2 c}\right)}} - 1 \right] \quad \text{for } T > T_0. \tag{4.35}$$

It is possible to see that the quantities in the brackets in Eqs.(4.34) and (4.35) converge to 1 when $\mathcal{Y} \to \infty$. Thus, the expectation value of the force $\langle \mathcal{F} \rangle$ is characterized by an asymptotic force $\langle \mathcal{F} \rangle_{as}$ for large values of $\mathcal{Y}$ (coherently with Fig.4.2.b). In particular, we get the following asymptotic values

$$\langle \mathcal{F} \rangle_{as} = \sqrt{\frac{\lambda_1}{\delta}} = \sqrt{\frac{\beta\delta - \frac{1}{2}\log\alpha_0 + \varphi}{\delta}} = \sqrt{\frac{2\Delta E}{k y_b^2} + \frac{h_p}{k}} \sqrt{1 - \frac{T}{T_b}} \quad \text{for } T < T_0, \tag{4.36}$$

where

$$T_b = \frac{2\Delta E + h_p y_b^2}{K_B \log\alpha_0} = \frac{2\Delta E + h_p y_b^2}{K_B \log\frac{2+\alpha+\sqrt{\alpha^2+4\alpha}}{2}}, \tag{4.37}$$

and

$$\langle \mathcal{F} \rangle_{as} = \sqrt{\frac{\lambda_2}{\delta}} = \sqrt{\frac{\beta\delta - \frac{1}{2}\log\beta_0}{\delta}} = \sqrt{\frac{h_p}{k}}\sqrt{1 - \frac{T}{T_c}} \quad \text{for } T > T_0, \tag{4.38}$$

where

$$T_c = \frac{h_p y_b^2}{K_B \log\beta_0} = \frac{h_p y_b^2}{K_B \log\frac{2+\beta+\sqrt{\beta^2+4\beta}}{2}}. \tag{4.39}$$

The parameters T_b and T_c represent two critical temperatures for the system with $\langle \mathcal{F} \rangle_{as} = 0$ in Eqs.(4.36) and (4.38), respectively. As we will discuss in detail, it means that all the bonds are certainly broken for supercritical temperatures. These results also show that the conditions in Eq.(4.31), introduced to ensure the convergence of the integrals, correspond to requiring that the system is working at subcritical temperatures. It is possible to observe the emergence of two different cases depending on the parameters of the system. From Eq.(4.28) and (4.39), we find

$$\frac{h_p y_b^2}{2\Delta E}\frac{T_0}{T_c} = \frac{\log\beta_0}{\log\alpha_0 - \log\beta_0}. \tag{4.40}$$

As a consequence, we have

$$\frac{h_p y_b^2}{2\Delta E} \lessgtr \frac{\log\beta_0}{\log\alpha_0 - \log\beta_0} \quad \Rightarrow \quad T_c \lessgtr T_0. \tag{4.41}$$

We remark that this analysis is valid if $y_b > y_p$, *i.e.* if the softening region exists. It is possible to verify the continuity of $\langle \mathcal{F} \rangle_{as}$ for $T = T_0$ from Eqs.(4.36) and (4.38). As a matter of fact, from the definitions of T_0, T_b and T_c in Eqs. (4.28), (4.37) and (4.39) one can verify the equality

$$\sqrt{\frac{2\Delta E}{k y_b^2} + \frac{h_p}{k}}\sqrt{1 - \frac{T_0}{T_b}} = \sqrt{\frac{h_p}{k}}\sqrt{1 - \frac{T_0}{T_c}}. \tag{4.42}$$

Moreover, from this equality, we obtain that

$$\frac{k y_b^2}{2\Delta E} = \frac{T_c}{T_0}\frac{T_b - T_0}{T_c - T_b}. \tag{4.43}$$

Thus, for the case with $T_c > T_0$ (*i.e.* when T_0 represents the crossover temperature for the force-extension curves) in Eq.(4.41), the positivity of $k y_b^2/2\Delta E$ implies that $T_c > T_b > T_0$.

This scenario is illustrated in Fig.4.3, where Eq.(4.20) is compared, for a large value of N, with Eqs.(4.36) and (4.38), corresponding to the thermodynamic limit. In order to show the effect of the condition in Eq.(4.41), we have fixed the values of the constitutive parameters but different values of the breaking extension y_b in the top and bottom panels (smaller value in top panels). This choice is reflected by the different sizes of the softening region of the potential energy U in panels b and e. In panels a and d we plotted the force-extension curves from Eq.(4.20) for increasing temperatures and compared it with the proper asymptotic values obtained from Eqs.(4.36) and (4.38). The good agreement observed proves that the theoretical procedure adopted to analyze the thermodynamic limit is correct and that the decrease of the asymptotic force, when the temperature increases, is explained by the presence of a phase transition. The critical point depends on the constitutive parameters of the system. When $\frac{h_p y_b^2}{2\Delta E} < \frac{\log\beta_0}{\log\alpha_0 - \log\beta_0}$, we have that $T_0 > T_c$ and, thus, the force-extension curve follows Eq.(4.36). As a consequence, the phase

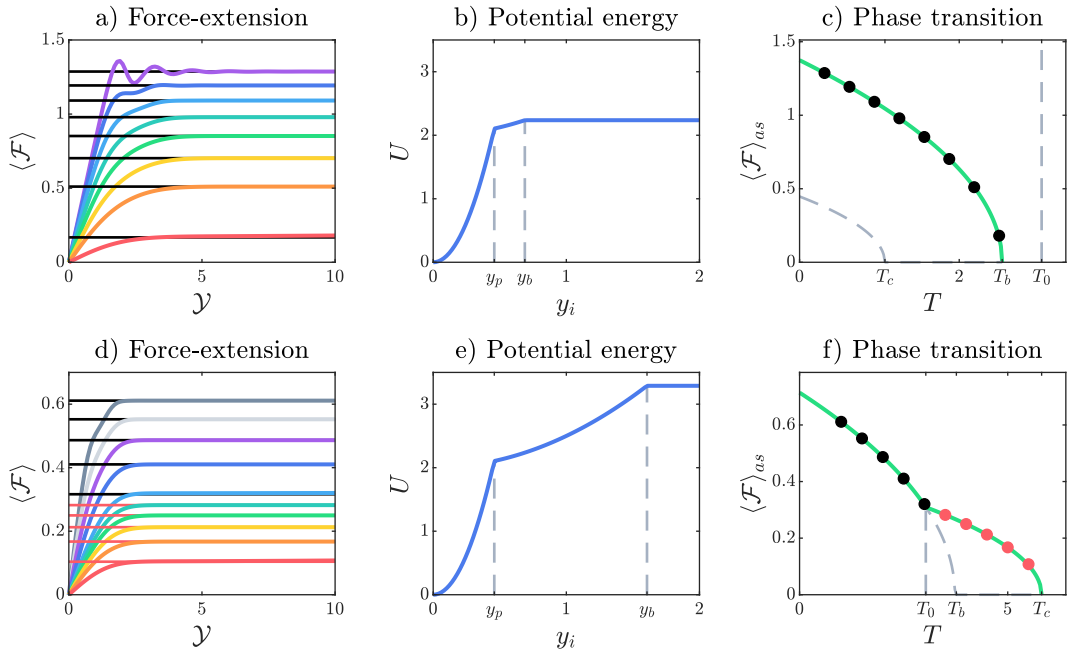

Figure 4.3: Behavior of the asymptotic force versus the temperature for a small (panels a, b, and c) and a large (panels d, e, and f) value of the breaking extension y_b. Panels a and d: comparison between Eq.(4.20) with $N = 300$ (colored curves) and Eqs.(4.36) (black straight lines) and (4.38) (red straight lines) at the thermodynamic limit (in panel a, we used 8 values of T between 0 and T_b, from purple to red curves; in panel d, we used 10 values of T between 0 and T_c, from dark gray to red). Panels b and e: potential energy of the adopted breakable elements with different y_b ($y_b = 1.5y_p$ in panel b and $y_b = 3.5y_p$ in panel e). Panels c and f: asymptotic force versus temperature (the green lines correspond to Eqs.(4.36) and (4.38); the circles to the colored curves of panels a and d for $\mathcal{Y} = 10$). The adopted parameters follows: $h_e = 20$, $h_p = 1$, $\Delta E = 2$, $k = 5$, and $K_B = 1$ (all in arbitrary units).

transition appears at the critical temperature T_b. On the other hand, when $\frac{h_p y_b^2}{2\Delta E} > \frac{\log \beta_0}{\log \alpha_0 - \log \beta_0}$, we have $T_0 < T_c$. In this case, the force-extension follows Eq.(4.36) until the temperature reaches the value T_0; when the temperature is increased, the behavior of the force is described by Eq.(4.38) and the phase transition occurs at the critical temperature T_c. From panels c and f of Fig.4.3, we deduce that the force needed to obtain the complete detachment of the system monotonically decreases to zero for increasing values of the temperature. This process terminates at $T = T_b$ in panel c, and at $T = T_c$ in panel f. It means that the thermal fluctuations are able to promote the fracture of the breakable elements and that the critical temperatures T_b and T_c are sufficient to induce complete denaturation of the system even if the resulting force experienced by the system is zero. This phenomenon can be better clarified by studying the behavior of $\langle N - \eta \rangle$ (average number of broken elements) and $\langle \eta - \xi \rangle$ (average number of softened elements).

We will evaluate $\langle N - \eta \rangle$ and $\langle \eta - \xi \rangle$ in the limiting case of $N \to \infty$. By performing the analysis used for the force-extension relation, starting from Eqs.(4.21), (4.22) and (4.23), we

obtain

$$\langle N-\eta\rangle = \frac{\int_0^N e^{\left(\beta\delta-\frac{1}{2}\log\beta_0\right)\eta-\frac{\delta\mathcal{Y}^2}{B_\eta}}(N-\eta)\frac{\mathrm{d}\eta}{\sqrt{B_\eta}}\int_0^\eta e^{\left(\varphi+\frac{1}{2}\log\frac{\beta_0}{\alpha_0}\right)\xi}\mathrm{d}\xi}{\int_0^N e^{\left(\beta\delta-\frac{1}{2}\log\beta_0\right)\eta-\frac{\delta\mathcal{Y}^2}{B_\eta}}\frac{\mathrm{d}\eta}{\sqrt{B_\eta}}\int_0^\eta e^{\left(\varphi+\frac{1}{2}\log\frac{\beta_0}{\alpha_0}\right)\xi}\mathrm{d}\xi}, \tag{4.44}$$

$$\langle \eta-\xi\rangle = \frac{\int_0^N\int_0^\eta(\eta-\xi)e^{\left(\varphi+\frac{1}{2}\log\frac{\beta_0}{\alpha_0}\right)\xi+\left(\beta\delta-\frac{1}{2}\log\beta_0\right)\eta-\frac{\delta\mathcal{Y}^2}{B_\eta}}\frac{\mathrm{d}\xi\mathrm{d}\eta}{\sqrt{B_\eta}}}{\int_0^N\int_0^\eta e^{\left(\varphi+\frac{1}{2}\log\frac{\beta_0}{\alpha_0}\right)\xi+\left(\beta\delta-\frac{1}{2}\log\beta_0\right)\eta-\frac{\delta\mathcal{Y}^2}{B_\eta}}\frac{\mathrm{d}\xi\mathrm{d}\eta}{\sqrt{B_\eta}}}. \tag{4.45}$$

Where, for the sake of readability, we used again $B_\eta = N-\eta+\beta_0/(\beta_0-1)$. After the evaluation of the integral on ξ, we apply the change of variable $N-\eta+\beta_0/(\beta_0-1)=s$. We get

$$\langle N-\eta\rangle = \frac{\int_{\frac{\beta_0}{\beta_0-1}}^{\frac{\beta_0}{\beta_0-1}+N}\left(s-\frac{\beta_0}{\beta_0-1}\right)\left[e^{\Theta B_s}-1\right]e^{-\left(\beta\delta-\frac{1}{2}\log\beta_0\right)s-\frac{\delta\mathcal{Y}^2}{s}}\frac{\mathrm{d}s}{\sqrt{s}}}{\int_{\frac{\beta_0}{\beta_0-1}}^{\frac{\beta_0}{\beta_0-1}+N}\left[e^{\Theta B_s}-1\right]e^{-\left(\beta\delta-\frac{1}{2}\log\beta_0\right)s-\frac{\delta\mathcal{Y}^2}{s}}\frac{\mathrm{d}s}{\sqrt{s}}}, \tag{4.46}$$

$$\langle \eta-\xi\rangle = \frac{\int_{\frac{\beta_0}{\beta_0-1}}^{\frac{\beta_0}{\beta_0-1}+N}\left[-B_s+\frac{1}{\Theta}e^{\Theta B_s}-\frac{1}{\Theta}\right]e^{-\left(\beta\delta-\frac{1}{2}\log\beta_0\right)s-\frac{\delta\mathcal{Y}^2}{s}}\frac{\mathrm{d}s}{\sqrt{s}}}{\int_{\frac{\beta_0}{\beta_0-1}}^{\frac{\beta_0}{\beta_0-1}+N}\left[e^{\Theta B_s}-1\right]e^{-\left(\beta\delta-\frac{1}{2}\log\beta_0\right)s-\frac{\delta\mathcal{Y}^2}{s}}\frac{\mathrm{d}s}{\sqrt{s}}}, \tag{4.47}$$

where we used $\Theta=\varphi+\frac{1}{2}\log\frac{\beta_0}{\alpha_0}$ defined in Eq.(4.28). As for the force-extension relation, in the limit with $N\to\infty$, we can consider separately the cases with $\Theta>0$ ($T<T_0$, exponential term in the brackets is dominant) and $\Theta<0$ ($T>T_0$, exponential term in the brackets is negligible). As a result, we get

$$T<T_0\begin{cases}\langle N-\eta\rangle = \dfrac{\int_{\frac{\beta_0}{\beta_0-1}}^{+\infty}\left(s-\frac{\beta_0}{\beta_0-1}\right)e^{-\left(\beta\delta-\frac{1}{2}\log\alpha_0+\varphi\right)s-\frac{\delta\mathcal{Y}^2}{s}}\frac{\mathrm{d}s}{\sqrt{s}}}{\int_{\frac{\beta_0}{\beta_0-1}}^{+\infty}e^{-\left(\beta\delta-\frac{1}{2}\log\alpha_0+\varphi\right)s-\frac{\delta\mathcal{Y}^2}{s}}\frac{\mathrm{d}s}{\sqrt{s}}},\\ \langle \eta-\xi\rangle = \dfrac{1}{\Theta} = \dfrac{1}{\varphi+\frac{1}{2}\log\frac{\beta_0}{\alpha_0}}.\end{cases} \tag{4.48}$$

$$T>T_0\begin{cases}\langle N-\eta\rangle = \dfrac{\int_{\frac{\beta_0}{\beta_0-1}}^{+\infty}\left(s-\frac{\beta_0}{\beta_0-1}\right)e^{-\left(\beta\delta-\frac{1}{2}\log\beta_0\right)s-\frac{\delta\mathcal{Y}^2}{s}}\frac{\mathrm{d}s}{\sqrt{s}}}{\int_{\frac{\beta_0}{\beta_0-1}}^{+\infty}e^{-\left(\beta\delta-\frac{1}{2}\log\beta_0\right)s-\frac{\delta\mathcal{Y}^2}{s}}\frac{\mathrm{d}s}{\sqrt{s}}},\\ \langle \eta-\xi\rangle \to +\infty.\end{cases} \tag{4.49}$$

We observe that the average number of softened elements $\langle\eta-\xi\rangle$ is independent of $\mathcal{Y}$ and is varying only with the temperature T for $T<T_0$. It means that the two domain walls between intact and softened elements, and between softened and broken elements, move simultaneously with increasing $\mathcal{Y}$ conserving a constant distance between them (which means a constant number

of softened elements). On the other hand, the value of $\langle \eta - \xi \rangle$ is divergent to infinity when $T > T_0$. This divergence means that we have no intact elements and the vertical springs can be either softened or broken. Therefore, the transition at the temperature T_0 can be characterized by the partial breaking of all the elements of the chain induced by the thermal fluctuations.

The two integrals appearing in Eqs.(4.48) and (4.49) can be calculated by using the formulas given in Appendix B. Using the definitions of λ_1, λ_2 and c in Eq.(4.33), we obtain

$$\langle N - \eta \rangle = \begin{cases} \dfrac{\Upsilon(\lambda_1)}{\Psi(\lambda_1)} - c & \text{for } T < T_0, \\ \dfrac{\Upsilon(\lambda_2)}{\Psi(\lambda_2)} - c & \text{for } T > T_0, \end{cases} \tag{4.50}$$

where the functions $\Upsilon(\lambda)$ and $\Psi(\lambda)$ are defined as follows

$$\begin{aligned} \Upsilon(\lambda) = \frac{1}{2}\sqrt{\frac{\pi}{\lambda}} \Bigg\{ & e^{2\mathcal{Y}\sqrt{\lambda\delta}} \left[1 - \operatorname{erf}\left(\sqrt{\frac{\delta}{c}}\mathcal{Y} + \sqrt{\lambda c} \right) \right] \\ & + e^{-2\mathcal{Y}\sqrt{\lambda\delta}} \left[1 + \operatorname{erf}\left(\sqrt{\frac{\delta}{c}}\mathcal{Y} - \sqrt{\lambda c} \right) \right] \Bigg\}, \end{aligned} \tag{4.51}$$

$$\begin{aligned} \Psi(\lambda) = \frac{1}{4\lambda}\sqrt{\frac{\pi}{\lambda}} \Bigg\{ & e^{2\mathcal{Y}\sqrt{\lambda\delta}} \left(1 - 2\mathcal{Y}\sqrt{\lambda\delta} \right) \left[1 - \operatorname{erf}\left(\sqrt{\frac{\delta}{c}}\mathcal{Y} + \sqrt{\lambda c} \right) \right] \\ & + e^{-2\mathcal{Y}\sqrt{\lambda\delta}} \left(1 + 2\mathcal{Y}\sqrt{\lambda\delta} \right) \left[1 + \operatorname{erf}\left(\sqrt{\frac{\delta}{c}}\mathcal{Y} - \sqrt{\lambda c} \right) \right] \Bigg\} \\ & + \frac{\sqrt{c}}{\lambda} e^{-\lambda c} e^{-\frac{\delta}{c}\mathcal{Y}^2}. \end{aligned} \tag{4.52}$$

We can evaluate the asymptotic behavior of $\langle N - \eta \rangle$ for large values of $\mathcal{Y}$ for both $T < T_0$ and $T > T_0$. By means of previous results, and using the asymptotic expression $1 - \operatorname{erf}(x) \sim e^{-x^2}/(x\sqrt{\pi})$ for $x \to \infty$, we easily get the asymptotic formulas for $\mathcal{Y} \to \infty$

$$\langle N - \eta \rangle \simeq \begin{cases} \mathcal{Y}\sqrt{\dfrac{\delta}{\lambda_1}} & \text{for} \quad T < T_0, \\ \mathcal{Y}\sqrt{\dfrac{\delta}{\lambda_2}} & \text{for} \quad T > T_0. \end{cases} \tag{4.53}$$

The final asymptotic result can be therefore written as

$$T < T_0 \begin{cases} \langle N - \eta \rangle \simeq \dfrac{\mathcal{Y}}{\sqrt{\frac{2\Delta E}{k y_b^2} + \frac{h_p}{k}}\sqrt{1 - \frac{T}{T_b}}} & \text{for } \mathcal{Y} \to \infty, \\ \langle \eta - \xi \rangle = \dfrac{1}{\varphi + \frac{1}{2}\log\frac{\beta_0}{\alpha_0}} = \dfrac{K_B T}{\Delta E}\dfrac{1}{1 - \frac{T}{T_0}}, \end{cases} \tag{4.54}$$

$$T > T_0 \begin{cases} \langle N - \eta \rangle \simeq \dfrac{\mathcal{Y}}{\sqrt{\frac{h_p}{k}}\sqrt{1 - \frac{T}{T_c}}} & \text{for } \mathcal{Y} \to \infty, \\ \langle \eta - \xi \rangle \to +\infty. \end{cases} \tag{4.55}$$

This result shows that the increase of the broken elements is linear with $\mathcal{Y}$ (for $\mathcal{Y}$ large), confirming the progressive detachment process induced by the Helmholtz (isometric) condition. We can combine Eqs.(4.36) and (4.38) with Eqs.(4.54) and (4.55) to obtain the simple relation $\langle N-\eta\rangle\langle\mathcal{F}\rangle_{as}=\mathcal{Y}$, which is valid for any temperature T, and for large values of the extension $\mathcal{Y}$. This relation, rewritten in terms of the real physical quantities for large y_{N+1}, reads

$$\langle f\rangle_{as}=\frac{k}{\langle N-\eta\rangle}y_{N+1}. \tag{4.56}$$

The behavior of the system within the Helmholtz ensemble in the thermodynamic limit is summarized in Fig.4.4, where we plot the most important quantities versus the temperature by considering the two cases identified in Eq.(4.41). In particular, we fix the values of the constitutive parameters of the system but consider two different values of y_b. For small values of y_b (left panels), the temperature T_0 is larger than T_b and T_c. Therefore, only the valid equations for $T<T_0$ must be considered (panel a). On the other hand, for larger values of y_b (right panels), T_0 is smaller than T_b and T_c: thus, the force-extension exhibits different regimes for $T<T_0$ and $T>T_0$ (panel b). In panel a ($T_c<T_b<T_0$), the asymptotic force $\langle\mathcal{F}\rangle_{as}$ shows a monotone decreasing behavior terminating at the critical temperature T_b corresponding to a phase transition. The number of the softened elements $\langle\eta-\xi\rangle$ is constant with respect to $\mathcal{Y}$ but is an increasing function of the temperature until point A, corresponding to the phase transition. It means that the region of softened elements exhibits a fixed length and is gradually moved leftward by the increasing extension $\mathcal{Y}$. The extension of this region represents the temperature-dependent analytic measure of the process zone. Coherently, the number of broken elements $\langle N-\eta\rangle$ is linearly increasing with $\mathcal{Y}$ and nonlinearly increasing with T (for this reason we plotted the ratio $\langle N-\eta\rangle/\mathcal{Y}$ which is only temperature dependent). We observe that $\langle N-\eta\rangle/\mathcal{Y}$ diverges at the critical temperature T_b. Therefore, $\langle N-\eta\rangle\to\infty$ for $T\to T_b$ for any value of the extension $\mathcal{Y}$ (for large values of $\mathcal{Y}$). It means that the phase transition can be explained through the total detachment of the system induced by the strong thermal fluctuations. In panel b ($T_0<T_b<T_c$), the asymptotic force $\langle\mathcal{F}\rangle_{as}$ is a decreasing function of the temperature with a first transition at the point B (temperature T_0) and a second final transition at temperature T_c, where we have the complete detachment. The transition at T_0 can be explained by observing the behavior of the number of softened elements $\langle\eta-\xi\rangle$ versus the temperature. We see that $\langle\eta-\xi\rangle\to\infty$ for $T\to T_0$, proving that all elements are (at least) softened for temperatures larger than T_0. Therefore, we have the first transition at T_0 where all the elements are softened and a second transition at T_c where all the elements are broken. This is coherent with the plot of $\langle N-\eta\rangle/\mathcal{Y}$ versus the temperature, from which we deduce that $\langle N-\eta\rangle\to\infty$ for $T\to T_c$ for any value of the extension $\mathcal{Y}$. Point C shows the slope transition in the evolution of the broken elements at the temperature T_0. To complete the description of Fig.4.4, we underline that the vertical dashed lines in all panels are useful to easily identify the characteristic temperatures T_c, T_b, and T_0. Moreover, the dashed curved lines correspond to solutions that are not relevant to the behavior of the system. More specifically, they correspond to Eqs.(4.38) and (4.55) in panel a and to Eqs.(4.36) and (4.54) in panel b.

To conclude, the behavior of the system under isometric conditions can be usefully described by analyzing the phase diagrams represented in Fig.4.5. Two cases are described: $T_c<T_b<T_0$ (panel a); $T_0<T_b<T_c$ (panel b). Observe that, since the system is symmetric (bilateral), in the figure we considered both positive and negative values of $\mathcal{Y}$. We can identify three possible phases for the system: $\mathcal{L}$ corresponds to all the elements broken; $\mathcal{M}$ corresponds to a combination of softened and broken elements; finally, $\mathcal{N}$ corresponds to a mix of intact, softened and broken elements. These phases are separated by vertical lines corresponding to the phase transitions.

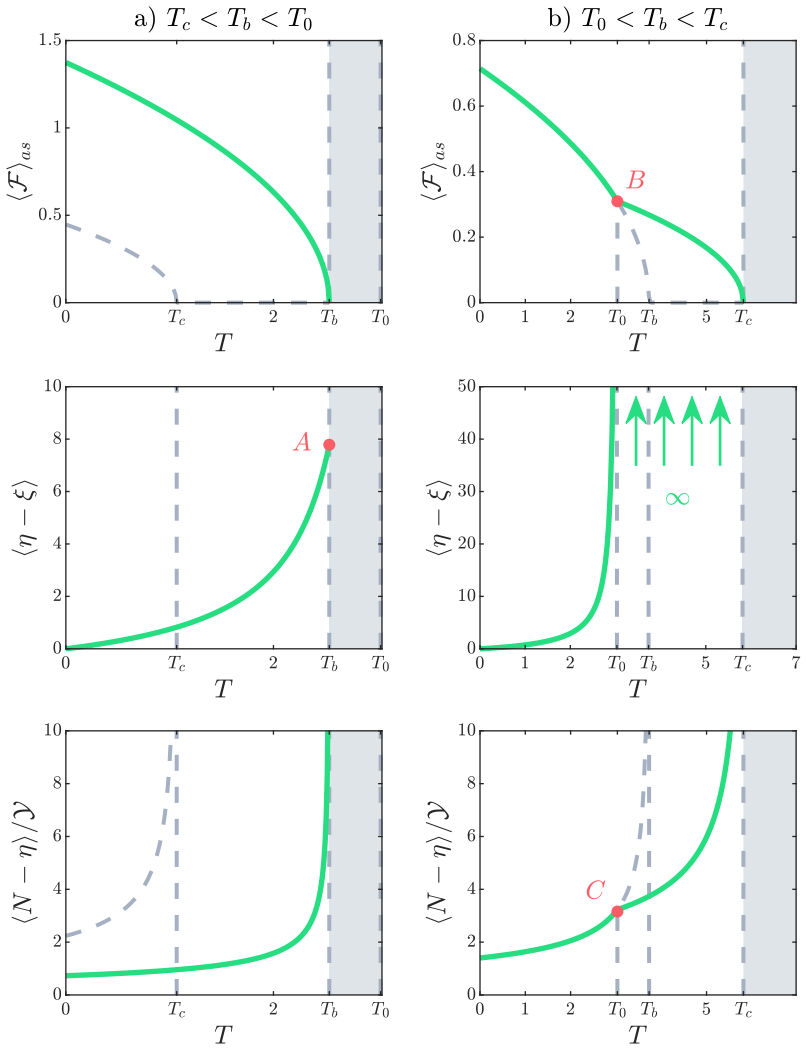

Figure 4.4: Behavior of the main quantities describing the system in the thermodynamic limit versus the temperature for a small (panels a, where $T_c < T_b < T_0$) and a large (panels b, where $T_0 < T_b < T_c$) value of the breaking extension y_b ($y_b = 1.5y_p$ in panel a and $y_b = 3.5y_p$ in panel b). In each case, we plotted the asymptotic or critical force $\langle \mathcal{F} \rangle_{as}$ given in Eqs.(4.36) and (4.38), the average number of softened elements $\langle \eta - \xi \rangle$, and the average number of broken elements divided by the applied extension $\langle N - \eta \rangle / \mathcal{Y}$. These plots correspond to the results given in Eqs.(4.54) and (4.55). The shaded areas correspond to supercritical temperatures. The adopted parameters follows: $h_e = 20$, $h_p = 1$, $\Delta E = 2$, $k = 5$, and $K_B = 1$ (all in arbitrary units).

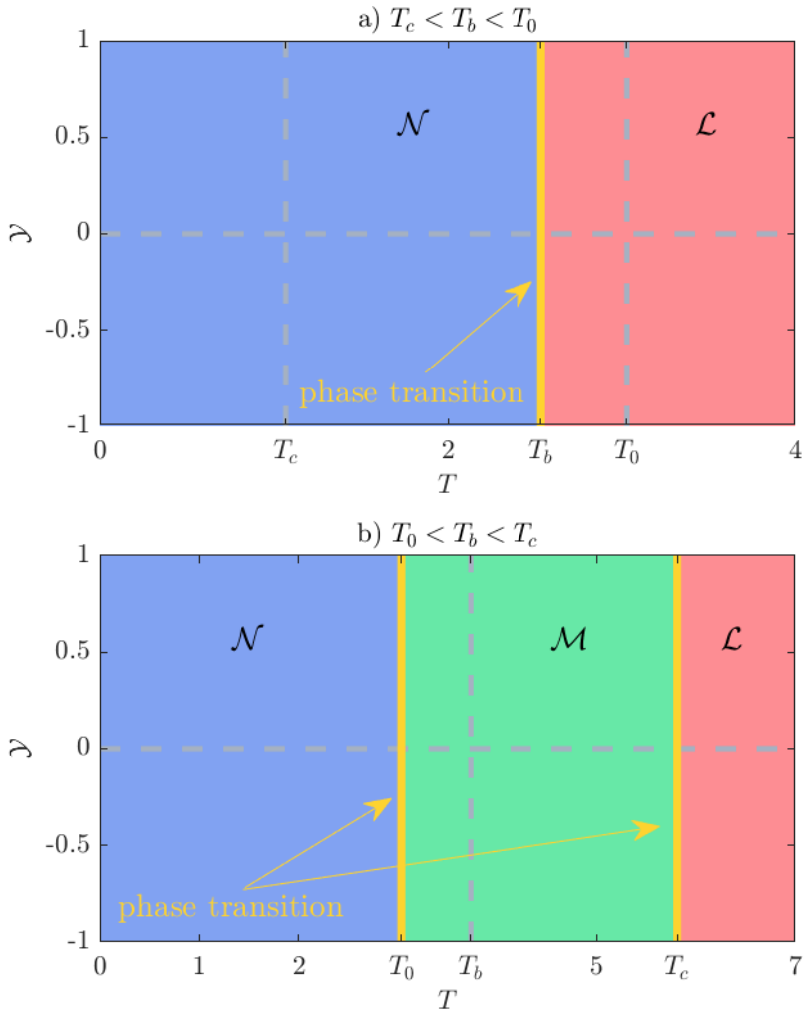

Figure 4.5: Phase diagrams for the system in the thermodynamic limit under Helmholtz isometric condition for the case with $T_c < T_b < T_0$ (panel a, where $y_b = 1.5y_p$) and for the case with $T_0 < T_b < T_c$ (panel b, where $y_b = 3.5y_p$). We can identify three possible phases for the system: $\mathcal{L}$ corresponds to a phase with all the elements broken; $\mathcal{M}$ corresponds to a combination of softened and broken elements; finally, $\mathcal{N}$ corresponds to a mix of intact, softened and broken elements. The adopted parameters follows: $h_e = 20$, $h_p = 1$, $\Delta E = 2$, $K_B = 1$ and $k = 5$ (all in arbitrary units).

Therefore, the phase diagrams explain clearly that, for Helmholtz isometric condition, we have no finite values of the prescribed extension $\mathcal{Y}$ able to induce the whole system detachment for subcritical temperatures. We will see that the Gibbs isotensional condition leads to different behavior.

4.5 Soft device: Gibbs ensemble

In this Section, we determine the properties of the detachment process realized within the Gibbs ensemble, which corresponds to a soft device able to apply a force to the last element of the chain. If we consider a force f applied to the last element with vertical extension y_{N+1}, the total potential energy of the system is given by $\Phi - f y_{N+1}$, where Φ is the Helmholtz potential energy defined in Eq.(4.4). It follows that the Gibbs partition function is given by the Laplace transform of the Helmholtz partition function [109]. Moreover, the knowledge of the Gibbs partition function allows the calculation of the average extension of the last element of the chain by using classical thermodynamic relations [98]. We can introduce the non-dimensional quantities (analogous the those used in Section 4.3)

$$\mathcal{F} = \frac{f}{k y_b}, \quad \langle \mathcal{Y} \rangle = \frac{\langle y_{N+1} \rangle}{y_b}, \tag{4.57}$$

representing the rescaled applied force and average extension, respectively. Thus, we can write the relations

$$\mathcal{Z}_G(\mathcal{F}) = \int_{-\infty}^{+\infty} \mathcal{Z}_H(\mathcal{Y}) e^{2\delta \mathcal{F} \mathcal{Y}} \mathrm{d}\mathcal{Y}, \tag{4.58}$$

$$\langle \mathcal{Y} \rangle = \frac{1}{2\delta} \frac{1}{\mathcal{Z}_G(\mathcal{F})} \frac{\partial \mathcal{Z}_G(\mathcal{F})}{\partial \mathcal{F}}. \tag{4.59}$$

We can easily determine the Gibbs partition function through Eqs.(4.23) and (4.58) as a gaussian integral. We obtain (up to a multiplicative constant)

$$\mathcal{Z}_G(\mathcal{F}) = \sum_{\eta=0}^{N} \sum_{\xi=0}^{\eta} \frac{e^{\varphi \xi} e^{\beta \delta \eta}}{\sqrt{\det \mathcal{A}(\xi,\eta) \left\{ 1 - \mathcal{A}^{-1}_{NN}(\xi,\eta) \right\}}} e^{\frac{\delta \mathcal{F}^2}{1 - \mathcal{A}^{-1}_{NN}(\xi,\eta)}}, \tag{4.60}$$

where δ and φ have been defined in Eq.(4.19). By applying Eq.(4.59), we directly obtain the force-extension relation as

$$\langle \mathcal{Y} \rangle = \frac{\mathcal{F}}{\mathcal{Z}_G} \sum_{\eta=0}^{N} \sum_{\xi=0}^{\eta} \frac{e^{\varphi \xi} e^{\beta \delta \eta}}{\sqrt{\det \mathcal{A}(\xi,\eta)} \left\{ 1 - \mathcal{A}^{-1}_{NN}(\xi,\eta) \right\}^{3/2}} e^{\frac{\delta \mathcal{F}^2}{1 - \mathcal{A}^{-1}_{NN}(\xi,\eta)}}. \tag{4.61}$$

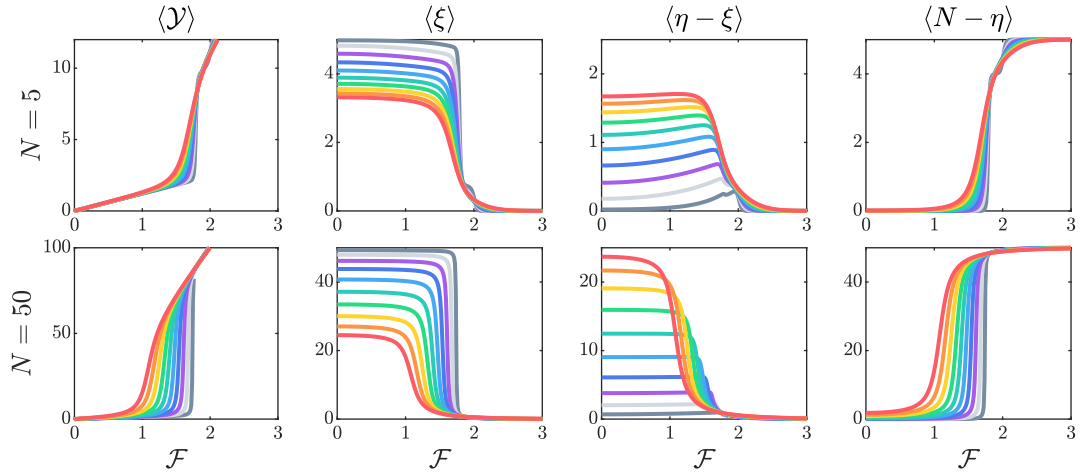

Figure 4.6: Force-extension curve and distribution of intact, softened, and broken elements during the detachment of a film from a substrate for the Gibbs ensemble (soft device, applied force to the last element of the chain). Panel a): we considered $N = 5$, and 10 values of K_BT from 0.5 to 5 (a.u.). Panel b): we considered $N = 50$, and 10 values of K_BT from 2 to 20 (a.u.), from gray to red colors. The adopted parameters follows: $h_e = 20$, $h_p = 15$, $\Delta E = 2$, $y_b = 2y_p$ and $k = 5$ (all in arbitrary units).

We can finally calculate the average value of the number of broken elements $\langle N - \eta \rangle$ and the average number of softened elements $\langle \eta - \xi \rangle$, eventually obtaining

$$\langle N - \eta \rangle = \frac{1}{\mathcal{Z}_G} \sum_{\eta=0}^{N} \sum_{\xi=0}^{\eta} \frac{(N-\eta) e^{\varphi\xi + \beta\delta\eta + \frac{\delta\mathcal{F}^2}{1-\mathcal{A}_{NN}^{-1}(\xi,\eta)}}}{\sqrt{\det \mathcal{A}(\xi,\eta) \left\{1 - \mathcal{A}_{NN}^{-1}(\xi,\eta)\right\}}}, \tag{4.62}$$

$$\langle \eta - \xi \rangle = \frac{1}{\mathcal{Z}_G} \sum_{\eta=0}^{N} \sum_{\xi=0}^{\eta} \frac{(\eta-\xi) e^{\varphi\xi + \beta\delta\eta + \frac{\delta\mathcal{F}^2}{1-\mathcal{A}_{NN}^{-1}(\xi,\eta)}}}{\sqrt{\det \mathcal{A}(\xi,\eta) \left\{1 - \mathcal{A}_{NN}^{-1}(\xi,\eta)\right\}}}. \tag{4.63}$$

An example of application of these results can be found in Fig.4.6, where we plotted $\langle \mathcal{Y} \rangle$, $\langle \xi \rangle$, $\langle \eta - \xi \rangle$ and $\langle N - \eta \rangle$ versus the applied force $\mathcal{F}$ (using the temperature as a parameter) for two different cases: the first one concerns a short chain with $N = 5$ (panel a), and the second one a larger chain with $N = 50$ (panel b). Concerning the case with $N = 5$, it is interesting to note the differences between the Gibbs and the Helmholtz ensemble. We, therefore, compare panel a) of Fig.4.2 with panel a) of Fig.4.6. While the detachment of the elements is quite simultaneous within the Gibbs ensemble (cooperative process occurring at a given threshold force), the same phenomenon is sequential within the Helmholtz ensemble, where we observe a gradual and progressive bond breaking (non-cooperative response). This different behavior is well known in the context of the stretching of macromolecules by means of force-spectroscopy techniques [91, 92, 94, 95, 102, 103]. Another difference concerns the fact that, in the Gibbs ensemble, we are not able to identify peaks or steps in the curves of Fig.4.6, corresponding to the single-breaking occurrences. Also, this point is clearly related to the cooperative response characterizing the Gibbs ensemble. If we look at the case with $N = 50$ (panel b of Fig.4.6), we can clearly see a force plateau corresponding to the cooperative detachment of the elements.

This force plateau is temperature dependent, as already observed within the Helmholtz ensemble. Moreover, we also deduce that the number of softened elements remains approximately constant and only temperature dependent before the complete rupture of the elements. These properties of the detachment process will be thoroughly analyzed in the next Section, by introducing the thermodynamic limit of the Gibbs ensemble.

4.6 Thermodynamic limit within the Gibbs ensemble

In this Section, we analyze the thermodynamic limit within the Gibbs ensemble and consider the behavior of Eqs.(4.60), (4.61), (4.62), and (4.63) for $N \to \infty$. Following the procedure shown in Section 4.4 and using the formula in 4.9, Eqs.(4.60) and (4.61), give the force-extension response of the system within the Gibbs ensemble as

$$\langle \mathcal{Y} \rangle = \mathcal{F} \frac{\int_0^N B_\eta e^{\left(\beta\delta - \frac{1}{2}\log\beta_0\right)\eta + \delta\mathcal{F}^2 B_\eta} \mathrm{d}\eta \int_0^\eta e^{\left(\varphi + \frac{1}{2}\log\frac{\beta_0}{\alpha_0}\right)\xi} \mathrm{d}\xi}{\int_0^N e^{\left(\beta\delta - \frac{1}{2}\log\beta_0\right)\eta + \delta\mathcal{F}^2 B_\eta} \mathrm{d}\eta \int_0^\eta e^{\left(\varphi + \frac{1}{2}\log\frac{\beta_0}{\alpha_0}\right)\xi} \mathrm{d}\xi}, \tag{4.64}$$

where α_0 and β_0 have been defined in Eq.(4.25) and B_η has been defined in Eq.(4.26). After the integration over ξ we can apply the change of variable $N - \eta + \beta_0/(\beta_0 - 1) = s$ thus obtaining

$$\langle \mathcal{Y} \rangle = \mathcal{F} \frac{\int_{\frac{\beta_0}{\beta_0-1}}^{\frac{\beta_0}{\beta_0-1}+N} \left[e^{\left(\varphi + \frac{1}{2}\log\frac{\beta_0}{\alpha_0}\right)B_s} - 1 \right] e^{-\left(\beta\delta - \frac{1}{2}\log\beta_0\right)s + \delta\mathcal{F}^2 s} s \, \mathrm{d}s}{\int_{\frac{\beta_0}{\beta_0-1}}^{\frac{\beta_0}{\beta_0-1}+N} \left[e^{\left(\varphi + \frac{1}{2}\log\frac{\beta_0}{\alpha_0}\right)B_s} - 1 \right] e^{-\left(\beta\delta - \frac{1}{2}\log\beta_0\right)s + \delta\mathcal{F}^2 s} \mathrm{d}s}. \tag{4.65}$$

As before, this expression depends on the sign of the quantity $\Theta = \varphi + \frac{1}{2}\log\frac{\beta_0}{\alpha_0}$. In the limit with $N \to \infty$, we consider separately the cases with $\Theta > 0$ ($T < T_0$, exponential term in the brackets is dominant) and $\Theta < 0$ ($T > T_0$, exponential term in the brackets is negligible). We eventually get (for $N \to \infty$)

$$\langle \mathcal{Y} \rangle = \mathcal{F} \frac{\int_{\frac{\beta_0}{\beta_0-1}}^{+\infty} e^{-\left(\beta\delta - \frac{1}{2}\log\alpha_0 + \varphi\right)s + \delta\mathcal{F}^2 s} s \mathrm{d}s}{\int_{\frac{\beta_0}{\beta_0-1}}^{+\infty} e^{-\left(\beta\delta - \frac{1}{2}\log\alpha_0 + \varphi\right)s + \delta\mathcal{F}^2 s} \mathrm{d}s} \qquad \text{for } T < T_0, \tag{4.66}$$

$$\langle \mathcal{Y} \rangle = \mathcal{F} \frac{\int_{\frac{\beta_0}{\beta_0-1}}^{+\infty} e^{-\left(\beta\delta - \frac{1}{2}\log\beta_0\right)s + \delta\mathcal{F}^2 s} s \mathrm{d}s}{\int_{\frac{\beta_0}{\beta_0-1}}^{+\infty} e^{-\left(\beta\delta - \frac{1}{2}\log\beta_0\right)s + \delta\mathcal{F}^2 s} \mathrm{d}s} \qquad \text{for } T > T_0. \tag{4.67}$$

Finally, we obtain the force-extension formulas for $N \to \infty$ under the same conditions for the Helmholtz ensemble (see Eqs.(4.31) and (4.32)) as

$$\langle \mathcal{Y} \rangle = \mathcal{F}\left(\frac{\beta_0}{\beta_0 - 1} + \frac{1}{\beta\delta - \frac{1}{2}\log\alpha_0 + \varphi - \delta\mathcal{F}^2}\right) \qquad \text{for } T < T_0, \tag{4.68}$$

$$\langle \mathcal{Y} \rangle = \mathcal{F}\left(\frac{\beta_0}{\beta_0 - 1} + \frac{1}{\beta\delta - \frac{1}{2}\log\beta_0 - \delta\mathcal{F}^2}\right) \qquad \text{for } T > T_0. \tag{4.69}$$

We remark that these expressions reveal an asymptotic behavior corresponding to a force plateau, as already observed within the Helmholtz ensemble. In particular, the values of the asymptotic force are the same for the two statistical ensembles. Indeed, for $T < T_0$, we deduce from Eq.(4.68) that the asymptotic force is solution of the quadratic equation $\beta\delta - \frac{1}{2}\log\alpha_0 + \varphi - \delta\mathcal{F}^2 = 0$, which is exactly solved by the Helmholtz result stated in Eq.(4.36). Similarly, for $T > T_0$, we deduce from Eq.(4.69) that the asymptotic force is solution of the quadratic equation $\beta\delta - \frac{1}{2}\log\beta_0 - \delta\mathcal{F}^2 = 0$, which is exactly solved by the Helmholtz result stated in Eq.(4.38). While the asymptotic forces are the same for the Helmholtz and Gibbs ensembles, it is not difficult to verify that the shape of the force-extension response is sensibly different for the two ensembles. This can be done by comparing the analytical solutions for the force-extension response obtained at the thermodynamic limit in Eqs.(4.34)-(4.35) (Helmholtz) and Eqs.(4.68)-(4.69) (Gibbs). It means that the two statistical ensembles are nonequivalent in the thermodynamic limit. For instance, this point can be shown by calculating the slopes of the force-extensions curves at the origin (for small forces and extensions) for both ensembles and by observing that these quantities are different. More details, concerning the case of the adhesion-decohesion process without the softening mechanism, can be found in [93].

To complete the analysis, we determine the average value of the number of broken elements $\langle N - \eta \rangle$ and the average number of softened elements $\langle \eta - \xi \rangle$ in the limiting case of $N \to \infty$. To this aim, we apply the same procedure already used for the force-extension relation. From Eqs.(4.62) and (4.63), combined with the partition function given in Eq.(4.60), we obtain

$$\langle N - \eta \rangle = \frac{\int_0^N (N-\eta) e^{\left(\beta\delta - \frac{1}{2}\log\beta_0\right)\eta + \delta\mathcal{F}^2 B_\eta} \mathrm{d}\eta \int_0^\eta e^{\left(\varphi + \frac{1}{2}\log\frac{\beta_0}{\alpha_0}\right)\xi} \mathrm{d}\xi}{\int_0^N e^{\left(\beta\delta - \frac{1}{2}\log\beta_0\right)\eta + \delta\mathcal{F}^2 B_\eta} \mathrm{d}\eta \int_0^\eta e^{\left(\varphi + \frac{1}{2}\log\frac{\beta_0}{\alpha_0}\right)\xi} \mathrm{d}\xi}, \tag{4.70}$$

$$\langle \eta - \xi \rangle = \frac{\int_0^N e^{\left(\beta\delta - \frac{1}{2}\log\beta_0\right)\eta - \delta\mathcal{F}^2 B_\eta} \mathrm{d}\eta \int_0^\eta (\eta-\xi) e^{\left(\varphi + \frac{1}{2}\log\frac{\beta_0}{\alpha_0}\right)\xi} \mathrm{d}\xi}{\int_0^N e^{\left(\beta\delta - \frac{1}{2}\log\beta_0\right)\eta - \delta\mathcal{F}^2 B_\eta} \mathrm{d}\eta \int_0^\eta e^{\left(\varphi + \frac{1}{2}\log\frac{\beta_0}{\alpha_0}\right)\xi} \mathrm{d}\xi}. \tag{4.71}$$

After the integration over ξ and the change of variable $N-\eta+\beta_0/(\beta_0-1)=s$ we obtain

$$\langle N-\eta\rangle=\frac{\int_{\frac{\beta_0}{\beta_0-1}}^{\frac{\beta_0}{\beta_0-1}+N}\left(s-\frac{\beta_0}{\beta_0-1}\right)\left[e^{\Theta B_s}-1\right]e^{-\left(\beta\delta-\frac{1}{2}\log\beta_0-\delta\mathcal{F}^2\right)s}\mathrm{d}s}{\int_{\frac{\beta_0}{\beta_0-1}}^{\frac{\beta_0}{\beta_0-1}+N}\left[e^{\Theta B_s}-1\right]e^{-\left(\beta\delta-\frac{1}{2}\log\beta_0-\delta\mathcal{F}^2\right)s}\mathrm{d}s}, \tag{4.72}$$

$$\langle \eta-\xi\rangle=\frac{\int_{\frac{\beta_0}{\beta_0-1}}^{\frac{\beta_0}{\beta_0-1}+N}\left[-B_s+\frac{1}{\Theta}e^{\Theta B_s}-\frac{1}{\Theta}\right]e^{-\left(\beta\delta-\frac{1}{2}\log\beta_0-\delta\mathcal{F}^2\right)s}\mathrm{d}s}{\int_{\frac{\beta_0}{\beta_0-1}}^{\frac{\beta_0}{\beta_0-1}+N}\left[e^{\Theta B_s}-1\right]e^{-\left(\beta\delta-\frac{1}{2}\log\beta_0-\delta\mathcal{F}^2\right)s}\mathrm{d}s}, \tag{4.73}$$

where, as in Section 4.4, we considered $\Theta=\varphi+\frac{1}{2}\log\frac{\beta_0}{\alpha_0}$. To complete the analysis, we consider the cases with $\Theta>0$ ($T<T_0$, exponential term in the brackets is dominant) and $\Theta<0$ ($T>T_0$, exponential term in the brackets is negligible). We get

$$T<T_0\begin{cases}\langle N-\eta\rangle=\dfrac{1}{\beta\delta-\frac{1}{2}\log\alpha_0+\varphi-\delta\mathcal{F}^2},\\ \langle \eta-\xi\rangle=\dfrac{1}{\Theta}=\dfrac{1}{\varphi+\frac{1}{2}\log\frac{\beta_0}{\alpha_0}},\end{cases} \tag{4.74}$$

$$T>T_0\begin{cases}\langle N-\eta\rangle=\dfrac{1}{\beta\delta-\frac{1}{2}\log\beta_0-\delta\mathcal{F}^2},\\ \langle \eta-\xi\rangle\to+\infty.\end{cases} \tag{4.75}$$

These results can be used to understand the behavior of the detachment process within the Gibbs ensemble in the thermodynamic limit as shown in Figs. 4.7 and 4.8. In both figures, we have fixed the constitutive parameters of the model but the values of y_b (small value in the left panel, larger value in the right panel). We recall that in the Helmholtz ensemble, we obtained two different responses depending on the parameters, as stated in Eq.(4.41). In panel a of Fig.4.7 and Fig.4.8 we show the results for the case with $T_c<T_b<T_0$ ($y_b=1.5y_p$), and in panel b those of the case with $T_0<T_b<T_c$ ($y_b=3.5y_p$). While in Fig.4.7 we show the behavior of the relevant quantities as a function of the applied force (using the temperature as a parameter), in Fig.4.8 we show the same quantities as a function of the temperature (now using the applied force as a parameter).

In Fig.4.7 we draw a comparison between Eqs.(4.60), (4.61), (4.62), and (4.63) with a large value of N and Eqs.(4.68), (4.69), (4.74), and (4.75) obtained for $N\to\infty$. This comparison proves that the mathematical treatment of the thermodynamic limit here developed is consistent with the model of detachment proposed. Indeed, we find a very good agreement between the general results, applied to a system with a large value of N, and the theoretical ones obtained in the thermodynamic limit. Concerning panel a, the force-extension curves exhibit the force plateau discussed above, which is very similar to the behavior observed within the Helmholtz ensemble. The average number of softened elements remains constant with $\mathcal{F}$ and depends on the temperature T. Finally, the number of broken elements diverges to infinity when the force approaches its critical value. The situation is more complicated in panel b, where we have an intermediate transition describing the partial breaking of all the elements of the system. In this case, when $T<T_0$ (black solid curves), the behavior is very similar to the one described in panel a. On the other hand, when $T>T_0$ (red solid curves), all the elements are softened due to the

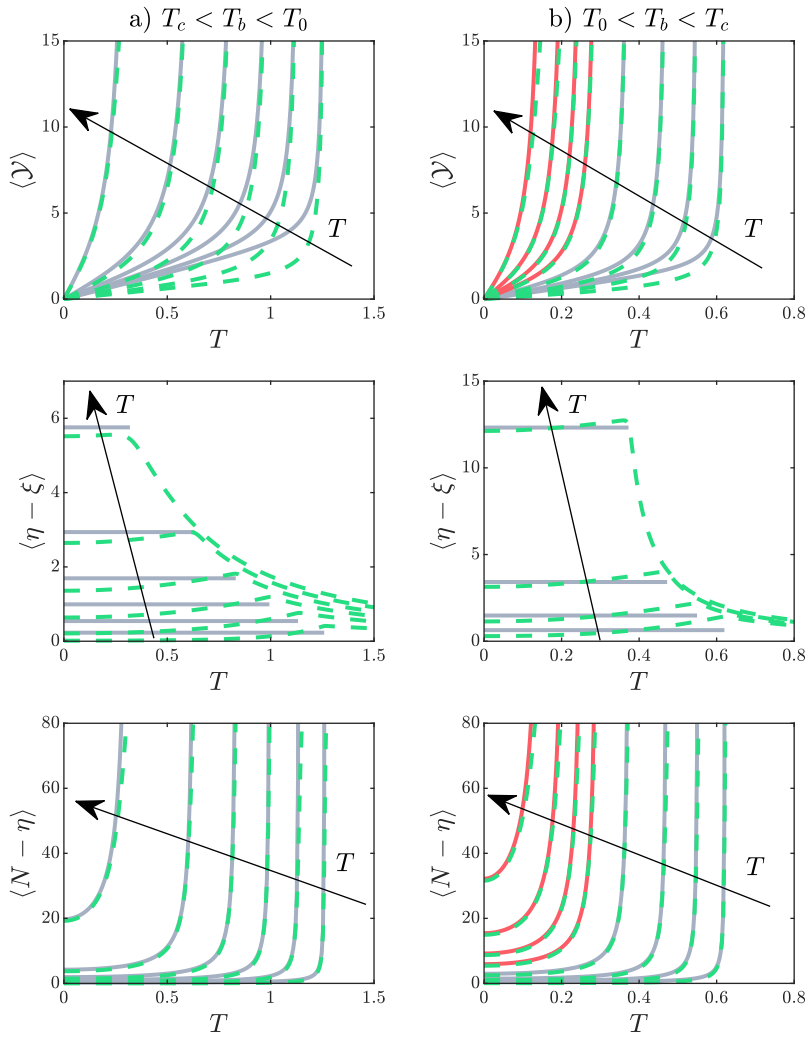

Figure 4.7: Force-extension curve and distribution of softened and broken elements during the detachment of a film from a substrate with a soft device (Gibbs ensemble) in the thermodynamic limit. Panel a: comparison of Eqs.(4.60), (4.61), (4.62), and (4.63) with $N = 250$ (green dashed curves) and Eqs.(4.68), (4.69), (4.74), and (4.75) obtained for $N \to \infty$ (gray solid curves) for the case with $T_c < T_b < T_0$ ($y_b = 1.5 y_p$). We adopted 6 values of T between 0.4 and 2.4. Panel b: comparison of Eqs.(4.60), (4.61), (4.62), and (4.63) with $N = 250$ (green dashed curves) and Eqs.(4.68), (4.69), (4.74), and (4.75) obtained for $N \to \infty$ (gray solid curves for $T < T_0$ and red solid curves for $T > T_0$) for the case with $T_0 < T_b < T_c$ ($y_b = 3.5 y_p$). We used 8 values of T between 0.9 and 5.1. The adopted parameters follows: $h_e = 20$, $h_p = 1$, $\Delta E = 2$, $K_B = 1$, and $k = 5$ (all in arbitrary units).

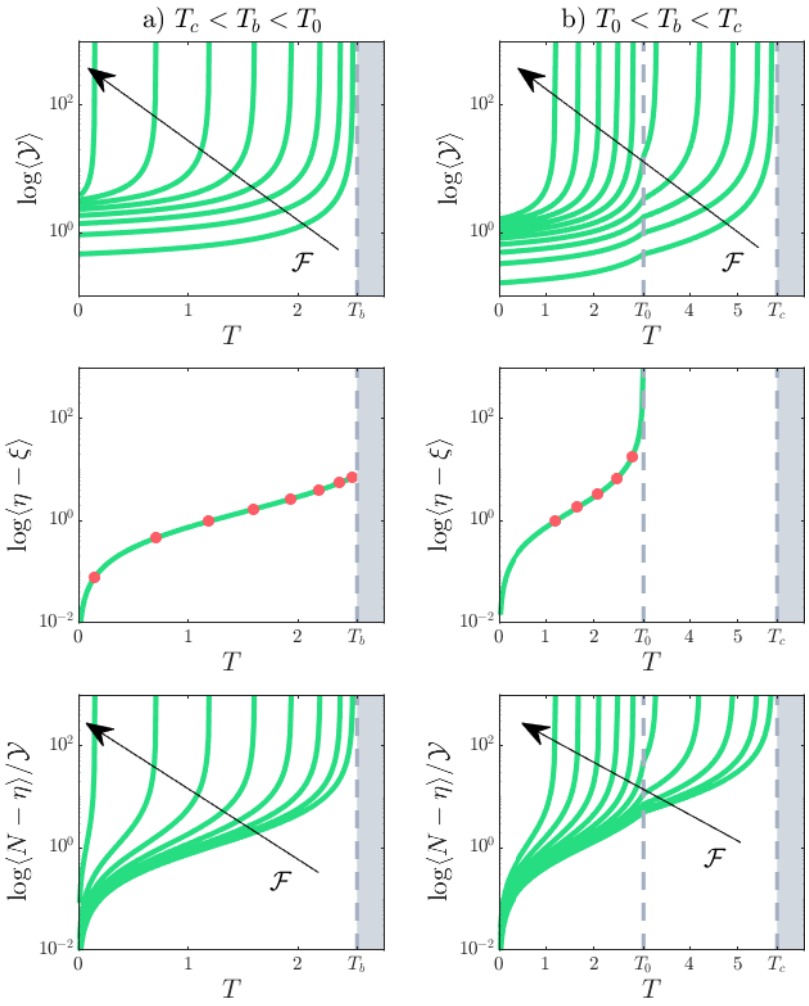

Figure 4.8: Extension $\langle\mathcal{Y}\rangle$, the average number of softened elements $\langle\eta-\xi\rangle$, and the average number of broken elements $\langle N-\eta\rangle$ versus the temperature during the detachment of a film from a substrate with a soft device (Gibbs ensemble) in the thermodynamic limit. Panel a: plots of Eqs.(4.68), (4.69), (4.74), and (4.75) for different values of the applied force $\mathcal{F}$ (8 values from 0.16 to 1.3) for the case with $T_c < T_b < T_0$ ($y_b = 1.5y_p$). Panel b: plots of Eqs.(4.68), (4.69), (4.74), and (4.75) for different values of the applied force $\mathcal{F}$ (10 values from 0.058 to 0.58) for the case with $T_0 < T_b < T_c$ ($y_b = 3.5y_p$). In both panels, shaded areas correspond to supercritical temperatures. The adopted parameters follows: $h_e = 20$, $h_p = 1$, $\Delta E = 2$, $K_B = 1$ and $k = 5$ (all in arbitrary units).

thermal fluctuations, and, therefore, $\langle \eta - \xi \rangle \to \infty$ (for this reason no red curves are shown in the plot of $\langle \eta - \xi \rangle$ versus $\mathcal{F}$). It means that the detachment process consists of the complete break of all the elements already softened.

Also in Fig.4.8, we separately show the behavior of the system with $T_c < T_b < T_0$ (panel a with $y_b = 1.5 y_p$), and the system with $T_0 < T_b < T_c$ (panel b with $y_b = 3.5 y_p$). We used a logarithmic scale to better appreciate the shape of the plots. The representation of the extension $\langle \mathcal{Y} \rangle$, the average number of softened elements $\langle \eta - \xi \rangle$, and the average number of broken elements $\langle N - \eta \rangle$ versus the temperature is particularly useful to identify a crucial difference between the Helmholtz and the Gibbs ensembles. For the isometric condition (Helmholtz ensemble), we have no finite values of the prescribed extension $\mathcal{Y}$ able to completely detach the system for subcritical temperatures. Indeed, since the detachment progress is gradual or progressive in response to the prescribed extension, only an infinite value of extension can cause a complete detachment of the chain (see Fig.4.4). Differently, for the isotensional condition (Gibbs ensemble), for any subcritical temperature, we can identify a value of force inducing the complete detachment of the chain. This can be seen by looking at the force-extension curves in panels a and b of Fig.4.8. Here, we observe that for any value of the temperature, we can identify a force producing an asymptotic behavior of $\langle \mathcal{Y} \rangle$, which corresponds to the total detachment of the system. The relationships between force and temperature are given by $\beta\delta - \frac{1}{2}\log\alpha_0 + \varphi - \delta\mathcal{F}^2 = 0$ for $T < T_0$, and by $\beta\delta - \frac{1}{2}\log\beta_0 - \delta\mathcal{F}^2 = 0$ for $T > T_0$, as stated in Eqs. (4.68) and (4.69) (we remember that δ and φ, defined in Eq.(4.19), depend on T). This is coherent with the fact that within the Gibbs ensemble all the element break simultaneously or cooperatively, thus allowing the force to completely detach the chain independently of the (subcritical) temperature of the system. The average number of softened elements $\langle \eta - \xi \rangle$ is independent of the force and therefore we find a single curve ($\forall \mathcal{F}$) in the corresponding plot. However, for any applied force we have a different critical temperature of the system and then the curve of $\langle \eta - \xi \rangle$ must be considered valid up to the red circle symbols shown in Fig.4.8. Indeed, these symbols correspond to the critical temperature, which is, in turn, determined by the applied force. Finally, the curves of the average number of broken elements $\langle N - \eta \rangle$ show a divergence at the critical temperature of the system, representing the complete detachment of the chain from the substrate. The important difference between panel a and panel b consists in the presence of the additional transition at the temperature T_0 in the case with $T_0 < T_b < T_c$ (large breaking extension $y_b = 3.5 y_p$). In this case, we observe that for $T \to T_0$ we have $\langle \eta - \xi \rangle \to \infty$ even if $\langle N - \eta \rangle$ is finite. It means that at the temperature $T \geq T_0$ all the vertical elements are spontaneously softened (due to the thermal fluctuations), and the detachment process is realized by completing their rupture thanks to the applied force.

To conclude the discussion concerning the thermodynamic limit in the Gibbs ensemble, in Fig.4.9 we show the phase diagram of the system in the force-temperature plane. We separately considered the two cases with $T_c < T_b < T_0$ (panel a) and with $T_0 < T_b < T_c$ (panel b). Again, due to symmetry, we considered both positive and negative values of $\mathcal{F}$ (see the scheme in Fig.4.1 (panel b)). Moreover, we observe the same three possible cases obtained in the hard device: the region $\mathcal{L}$ corresponds to a phase with all broken elements; the region $\mathcal{M}$ corresponds to a combination of softened and broken elements; finally, the region $\mathcal{N}$ corresponds to a mixture of intact, softened and broken elements. In Fig.4.9 we can identify the critical points (C_b in panel a, and C_c in panel b), whose meaning is now quite clear: for temperatures larger than those of the critical points, the chain is always completely detached from the substrate. In panel b of Fig.4.9, we can see the triple points P^+ and P^-, where the three phases of the system coexist. In any case, we observe that for a value of the applied force $\mathcal{F}$ (in a suitable range), we have a value of the temperature able to detach the chain. When $\mathcal{F} = 0$, such a temperature corresponds to the critical temperature of the system. In other words, for any subcritical temperature, we can identify a

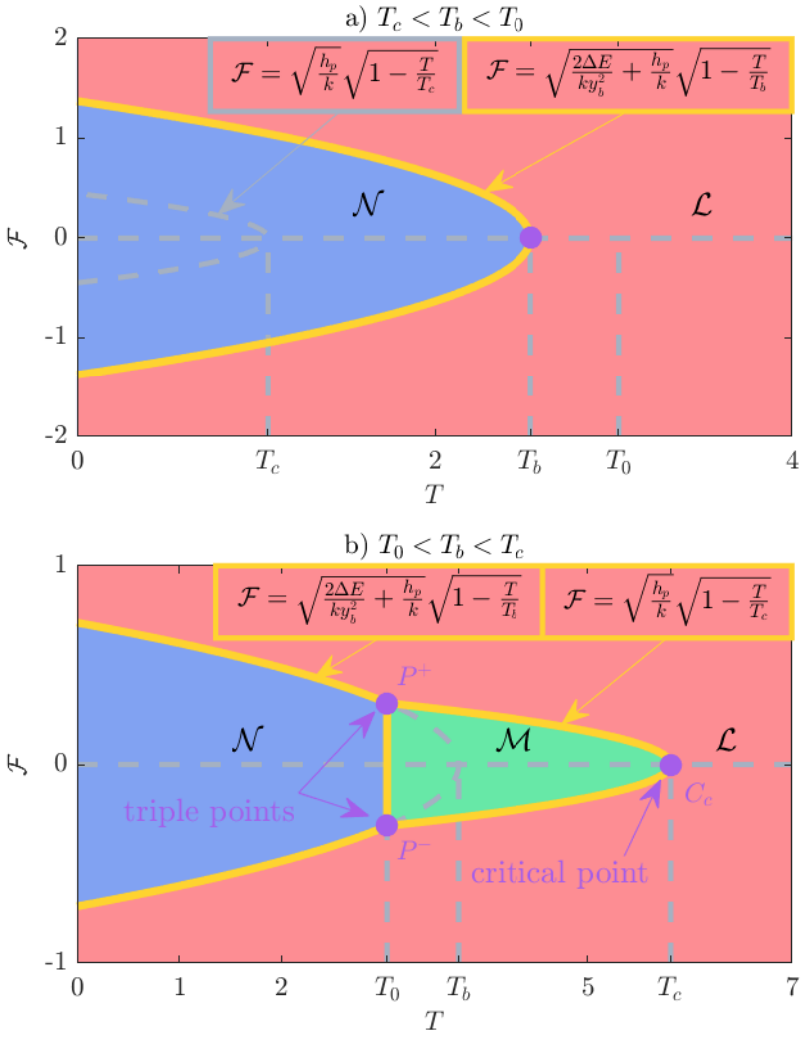

Figure 4.9: Phase diagrams for the system in the thermodynamic limit under Gibbs isotensional condition for the case with $T_c < T_b < T_0$ (panel a, where $y_b = 1.5y_p$) and for the case with $T_0 < T_b < T_c$ (panel b, where $y_b = 3.5y_p$). We can identify three possible phases for the system: $\mathcal{L}$ corresponds to a phase with all the elements broken; $\mathcal{M}$ corresponds to a combination of softened and broken elements; finally, $\mathcal{N}$ corresponds to a mix of intact, softened and broken elements. We can also identify the critical points (C_b in panel a, and C_c in panel b) and the triple points P^+ and P^- in panel b, where the three phases of the system coexist. The adopted parameters follows: $h_e = 20$, $h_p = 1$, $\Delta E = 2$, $K_B = 1$ and $k = 5$ (all in arbitrary units).

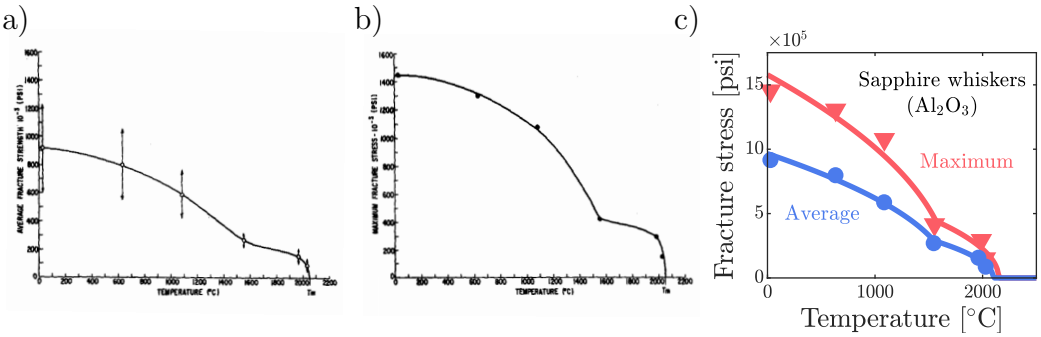

Figure 4.10: Mechanical behavior of sapphire whiskers at elevated temperatures. The experimental average fracture strength (panel a) and the experimental maximum fracture stress (panel b), as a function of temperature, are reproduced with permission from [33]. Panel c): comparison between theoretical and experimental average and maximum strengths based on Eqs.(4.36) and (4.38).

value of force inducing the complete detachment of the chain. As previously discussed, the critical behavior of the Helmholtz ensemble is different. In fact, for isometric conditions, we have no finite values of the prescribed extension able to detach the system for subcritical temperatures, as shown in Fig.4.5. This difference between the Helmholtz and the Gibbs ensembles is consistent with their non-cooperative and cooperative interpretation, respectively.

4.7 Comparison with experimental results

In this Section, we use the obtained results to give an interpretation of some experiments conducted to determine the tensile behavior of different materials at elevated temperatures, under an applied mechanical load.

The first case concerns filamentary crystals or whiskers of sapphire (Al_2O_3) with a diameter between 8 and 40 μm [33]. In these structures, the damage can be generated by the propagation of the decohesion process that, at the microscopic scale, can be modeled by our theory. Indeed, the decohesion process can be viewed as a sequence of ruptures, representing the breaking of the chemical bonds along a direction of the crystal structure. In particular, our model will be used to analyze the effect of the temperature on this damaging process. If we consider whiskers free of dislocations, or, at least, without applied stress, and for low temperatures, we can assume that the magnitudes of their strengths represent a good indication of the stresses required either for crack propagation or for dislocation nucleation. The temperature dependence of these stresses has been measured by [33]. The experimental average fracture strength and the experimental maximum fracture stress as a function of temperature are reported in panels a) and b) of Fig.4.10, respectively [33]. The transition at around $T = 1550$ °C in the stress decrease suggests a change in the mechanism of failure leading to the complete fracture. In its studies, Brenner has proposed the following scenario [33]. First of all, it is supposed that some defects are distributed within the whiskers (formed during the crystal growth) and they are able to intensify the applied stress through Griffith and/or Eshelby-like mechanisms. At a given level of applied stress, the locally intensified stress around the defects can generate propagation of the crack or nucleation of dislocations. Brenner provides evidence that at lower temperatures, the enhanced stress causes crack propagation without dislocation nucleation while at elevated temperatures, dislocations are generated before the fracture propagation. In the latter case, the population of dislocations is able to reduce the elastic stiffness of the material. In our model, the generation of dislocations can

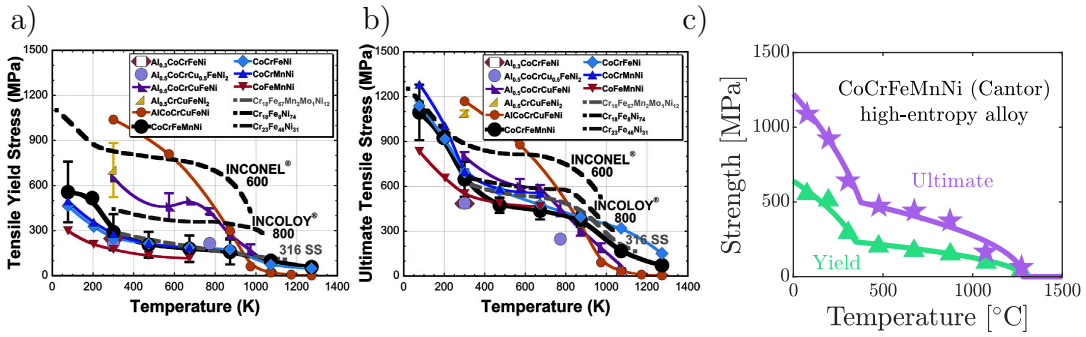

Figure 4.11: Mechanical behavior of high-entropy and medium-entropy alloys over a large temperatures range. The experimental tensile yield stress (panel a) and the experimental ultimate tensile stress (panel b), as a function of temperature, are reproduced with permission from [35]. Panel c): comparison between theoretical and experimental results for the quinary CrMnFeCoNi alloy (also named Cantor alloy), based on Eqs.(4.36) and (4.38).

be therefore represented by the softening mechanism described by the transition of the stiffness of the vertical springs between h_e and h_p, shown in Fig.4.1. It is interesting to observe that the theoretical behavior of the strength shows a transitional behavior at T_0, as shown in Fig.4.3, panel f. The temperature T_0 is therefore around 1550 °C for the sapphire whiskers. The decohesion forces given by Eqs.(4.36) and (4.38) are able to represent the experimental results on the strength of the sapphire whiskers, as shown in panel c) of Fig.4.10. Quite a good agreement between theory and experiments can be noticed.

Another class of materials where our theory can be applied is represented by high-entropy alloys. These systems are typically composed of five or more elements with equal (or relatively equal) stoichiometric coefficients. These materials are named high-entropy alloys since the mixing entropy is maximized if the components are present in equal proportions, and it is an increasing function of the number of components. Consequently, when these systems are composed of two to four components, then they are typically named medium-entropy alloys. From a historical point of view, the idea of creating alloys has been used to generate desirable properties in a given artificial material. High-entropy alloys represent a new strategy introduced to exploit a multi-dimensional compositional space in order to induce exceptional properties to these recent exotic materials. Today, only a small region of this multi-dimensional space has been explored and many other alloys can be discovered in the future [34]. In Fig.4.11, one can find the experimental data concerning the tensile yield stress (panel a) and the ultimate tensile stress (panel b) of several high-entropy alloys and medium-entropy alloys [35]. The mechanisms at the origin of the mechanical response in these systems are very complex. The distribution of defects plays a crucial role in defining mechanical properties. At the atomic scale, typical defects include vacancies, dislocations, and grain boundaries. At a larger scale, other defects are represented by pores, precipitates, cracks, and residual stresses. The static and dynamic interplay of these microstructures is able to determine the overall mechanical response of the whole material. In spite of this complexity, the yield and ultimate strengths, shown in panels a) and b) of Fig.4.11, decrease continuously over the full range of temperatures. More specifically, a first region characterized by a steep drop is followed by a second region where the decrease is slower. As before, the transition between these regions can be interpreted as a change in the underlying damaging physical mechanism.

As a paradigmatic example, we consider the quinary CrMnFeCoNi alloy (also named Cantor alloy), which is one of the first high-entropy alloys investigated [36]. This structure crystallizes

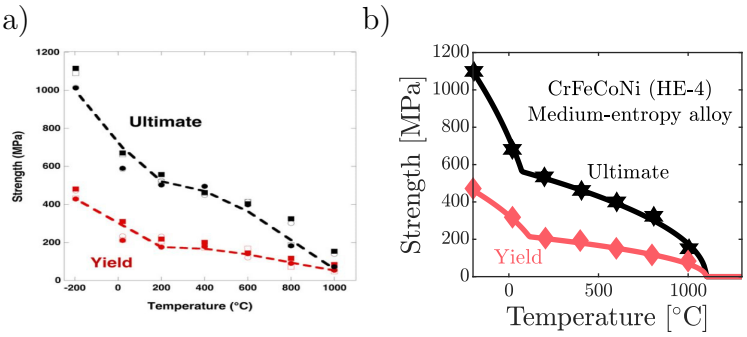

Figure 4.12: Mechanical behavior of the medium-entropy alloy CrFeCoNi over a large temperatures range. The experimental tensile yield stress and ultimate tensile stress (panel a), as a function of temperature, are reproduced with permission from [38]. Panel b): comparison between theoretical and experimental results for the CrFeCoNi alloy (also named HE-4), based on Eqs.(4.36) and (4.38).

as a single-phase FCC solid. The strength of this alloy exhibits a strong drop for temperatures below 350 °K, and a weaker temperature dependence at elevated temperatures up to around 1270 °K. There is therefore a behavioral transition at the temperature $T_0 = 350$ °K. From the microstructural point of view, this can be explained as follows. For small deformation, the CoCrFeMnNi alloy exhibits the development of planar dislocation glide, which is typical for FCC metals [37]. For larger strains, dislocations lose their planar character and organize into cell structures [37]. This modification induces a larger ductility and a lower stiffness of the overall material. Finally, this process is represented in our model by the softening of the vertical breakable springs, which change their elastic coefficients from h_e to h_p, as shown in Fig.4.1. In panel c) of Fig.4.11, we draw a comparison between the experimental and theoretical results for both the yield and ultimate stress of the quinary CrMnFeCoNi alloy. As before, we remark that the model is able to capture the transition in the behavior of the strength as a function of the temperature. Another example is given in Fig.4.12, where we take into consideration the mechanical properties of the medium-entropy alloy CrFeCoNi (also named HE-4). In panel a) of Fig.4.12, experimental ultimate and yield stresses are reported [38]. As before, a transition can be observed for a temperature around 200 °C. Also in this case, this transition can be interpreted by a different structure and mobility of the dislocations with different strains and temperatures [38]. The comparison with the theoretical results is drawn in panel b) of Fig.4.12, where a good agreement can be underlined.

We described the application of the softening mechanism to the strength behavior of sapphire whiskers and of high-entropy and medium-entropy alloys. For these material systems, we provided evidence that the theory is able to describe the behavior of both yield and ultimate stress as a function of the temperature.

4.8 Conclusions

We considered the cohesion/decohesion process under thermal fluctuations by means of a paradigmatic system represented by a linear mass-spring chain, connected to a substrate through breakable elements. These elements are described by a softening mechanism, *i.e.*, by three operating regions as follows: the first linear region corresponds to intact elements (small deformation), the second region corresponds to softened elements with a reduced stiffness

(intermediate deformation), and finally, the third region corresponds to broken elements (large deformation). This paradigmatic system has been studied under the assumption to be embedded in a thermal bath at a given temperature and loaded by an external mechanical action. This latter can be either a prescribed extension (hard device) or an applied force (soft device) to the last element of the chain. These two configurations correspond to the Helmholtz ensemble (isometric condition) and the Gibbs ensemble (isotensional condition) of the equilibrium statistical mechanics, respectively. In order to cope with the mathematical analysis of the problem, we adopted the spin variable approach for defining the state of any breakable element [91, 92, 94, 95, 102, 103], we introduced the zipper model hypothesis with two domain walls for describing the three operating regions of the bonds chain [104–107], and we finally exploited some analytical properties of the tridiagonal matrices [96, 97] to obtain closed form results under isometric and isotensional conditions. In both cases, we obtained the general solution of the problem for a chain composed of a number N of elements. These solutions, in both cases, lead to a constant decohesion force, which represents the strength of the system. Importantly, this strength is temperature dependent, and its value is decreasing with increasing temperature. The physical interpretation of this behavior can be done by observing that the thermal fluctuations foster the damaging of the breakable elements, thus reducing the strength of the system. Also, the number of broken and softened elements has been determined as a function of the temperature and of the external mechanical action for both statistical ensembles. Interestingly, we proved that the number of softened elements depends only on the temperature and it is independent of the external mechanical action. The increasing size of the softened region with the temperature gives a thorough interpretation of the fragile-to-ductile transition of several materials. This analysis provides a complete picture of the system behavior with a finite number N of elements. To better understand the meaning of these results, we analyzed the system behavior under the hypothesis of thermodynamic limit, *i.e.* for $N \to \infty$. In this case, the sums appearing in the partition functions of both ensembles and in the macroscopic averages of the relevant thermodynamic variables can be substituted by integrals, eventually leading to useful closed-form expressions. The analysis of these results delivers a clear explanation of the temperature-dependent strength in terms of phase transitions. Indeed, a first critical temperature exists for the system and corresponds to the partial breaking of all the elements of the chain. Then, a second critical temperature describes the complete breaking of all the bonds. This complex critical scenario is able to give a rigorous explanation of the relationship between strength and temperature in systems where a transition in the breaking mechanism occurs (here represented by the bonds softening). In several experimental measurements, a two-branch curve for the strength-temperature relation has been indeed observed [33, 35, 38]. Another interesting result concerns the non-equivalence of the ensembles in the thermodynamic limit. It means that the force-extension curves are different for the Helmholtz and the Gibbs ensembles, also for $N \to \infty$. It is well known that the equivalence of the Gibbs and Helmholtz statistical ensemble has been proved for a large class of physical systems including, *e.g.*, single flexible polymer chains without confinement effects and with a continuous pairing interaction potential between neighboring monomers [56, 108–112]. However, it is difficult to prove the ensemble's equivalence for more general systems or structures. For instance, other problems, concerning for example the escape of a polymer confined between two planes or the desorption of a polymer tethered on a surface, lead to the non-equivalence between the defined statistical ensembles [113–118]. Interestingly, these investigations are coherent with our results and definitively prove the possibility to have ensembles non-equivalence between different statistical ensembles in relevant physical systems. Generalizations of the theory may include the dynamic behavior of cohesion/decohesion processes (where the barriers between the wells of the energetic landscape play an important role [99–101]), or the multi-state softening *i.e.* composed of several steps with different stiffness (described by several domain walls in the chain).

4.9 Appendix

4.9.1 Tridiagonal matrix

In this appendix, we will recall some properties of tridiagonal matrices used in the text. In particular, we consider the matrix $\mathcal{A}(\xi,\eta)$ defined in Eq.(4.7) and obtain the formulas for $\det[\mathcal{A}(\xi,\eta)]$ and $1-\mathcal{A}^{-1}_{NN}(\xi,\eta)$.

For sake of generality, let us consider $\mathcal{T}$ defined as

$$\mathcal{T}=\begin{pmatrix} a_1 & b_1 & 0 & \cdots & 0 \\ c_1 & \ddots & \ddots & \ddots & \vdots \\ 0 & \ddots & \ddots & \ddots & 0 \\ \vdots & \ddots & \ddots & \ddots & b_{N-1} \\ 0 & \cdots & 0 & c_{N-1} & a_N \end{pmatrix} \in \mathcal{M}_{N,N}(\mathbb{R}), \tag{4.76}$$

where the diagonal is composed by the elements $(a_1,\ldots,a_N)$, the superdiagonal by $(b_1,\ldots,b_{N-1})$ and the subdiagonal by $(c_1,\ldots,c_{N-1})$.

The elements of the inverse matrix $\mathcal{T}^{-1}$ can be written as [96, 97]

$$\left[\mathcal{T}^{-1}\right]_{ij}=\begin{cases} \dfrac{1}{\vartheta_N}(-1)^{i+j}b_i\times\cdots\times b_{j-1}\vartheta_{i-1}\varphi_{j+1}, & \text{if } i<j \\ \dfrac{1}{\vartheta_N}\vartheta_{i-1}\varphi_{i+1}, & \text{if } i=j \\ \dfrac{1}{\vartheta_N}(-1)^{i+j}c_j\times\cdots\times c_{i-1}\vartheta_{j-1}\varphi_{i+1}, & \text{if } i>j \end{cases} \tag{4.77}$$

where the sequences ϑ_i and φ_i are obtained using the recursive rules

$$\begin{cases} \vartheta_i=a_i\vartheta_{i-1}-b_{i-1}c_{i-1}\vartheta_{i-2}, \\ \vartheta_{-1}=0,\ \vartheta_0=1,\ i=1,2,\ldots,N \end{cases} \tag{4.78}$$

and

$$\begin{cases} \varphi_i=a_i\varphi_{i+1}-b_ic_i\varphi_{i+2}, \\ \varphi_{N+2}=0,\ \varphi_{N+1}=1,\ i=N,\ldots,1 \end{cases} \tag{4.79}$$

Notice that while Eq.(4.78) is an increasing recursive rule going from $i=1$ to $i=N$, Eq.(4.79) is a decreasing recursive rule for $i=N$ to $i=1$. It is possible to show [96, 97] that

$$\det\mathcal{T}=\vartheta_N. \tag{4.80}$$

These formulas can be specialized to the case where $b_i=c_i=-1 \quad \forall i$ (such as for matrix $\mathcal{A}(\xi,\eta)$ in Eq.(4.7)). The general result can thus be simplified as

$$\left[\mathcal{T}^{-1}\right]_{ij}=\begin{cases} \dfrac{1}{\vartheta_N}\vartheta_{i-1}\varphi_{j+1}, & \text{if } i<j \\ \dfrac{1}{\vartheta_N}\vartheta_{i-1}\varphi_{i+1}, & \text{if } i=j \\ \dfrac{1}{\vartheta_N}\vartheta_{j-1}\varphi_{i+1}, & \text{if } i>j \end{cases} \tag{4.81}$$

where the sequences ϑ_i and φ_i are given by the reduced recursive laws

$$\begin{cases} \vartheta_i = a_i \vartheta_{i-1} - \vartheta_{i-2}, \\ \vartheta_{-1} = 0, \vartheta_0 = 1, i = 1, 2, \ldots, N \end{cases} \tag{4.82}$$

and

$$\begin{cases} \varphi_i = a_i \varphi_{i+1} - \varphi_{i+2}, \\ \varphi_{N+2} = 0, \varphi_{N+1} = 1, i = N, \ldots, 1 \end{cases} \tag{4.83}$$

In order to evaluate the physical quantities in Section 4.3 and 4.5 we need to compute $\det \mathcal{A}(\xi, \eta)$ and $\mathcal{A}^{-1}_{NN}(\xi, \eta)$. We have that

$$\det \mathcal{A}(\xi, \eta) = \vartheta_N, \tag{4.84}$$

$$\mathcal{A}^{-1}_{NN}(\xi, \eta) = \vartheta_{N-1}\varphi_{N+1}/\vartheta_N = \vartheta_{N-1}/\vartheta_N. \tag{4.85}$$

Let us consider Eq.(4.82) with $a_1 = \cdots = a_\xi = 2 + \alpha$, $a_{\xi+1} = \cdots = a_\eta = 2 + \beta$, and $a_{\eta+1} = \cdots = a_N = 2$. Then, for $i \leq \xi$ we have the difference equation $\vartheta_i = (2+\alpha)\vartheta_{i-1} - \vartheta_{i-2}$, whose general solution can be written as

$$\vartheta_i = p \left(\frac{2 + \alpha + \sqrt{\Delta}}{2} \right)^i + q \left(\frac{2 + \alpha - \sqrt{\Delta}}{2} \right)^i, \tag{4.86}$$

with $\Delta = \alpha^2 + 4\alpha$ and where the coefficients p and q must be fixed using the conditions $\vartheta_{-1} = 0$ and $\vartheta_0 = 1$. A straightforward calculation leads to the explicit solution for $i \leq \xi$

$$\vartheta_i = \frac{1}{\sqrt{\Delta}} \left(\frac{2 + \alpha + \sqrt{\Delta}}{2} \right)^{i+1} - \frac{1}{\sqrt{\Delta}} \left(\frac{2 + \alpha - \sqrt{\Delta}}{2} \right)^{i+1}. \tag{4.87}$$

Let us define the function

$$\mathcal{G}(\gamma, z) = \frac{1}{\sqrt{\gamma^2 + 4\gamma}} \left[\left(\frac{2 + \gamma + \sqrt{\gamma^2 + 4\gamma}}{2} \right)^z - \left(\frac{2 + \gamma - \sqrt{\gamma^2 + 4\gamma}}{2} \right)^z \right], \tag{4.88}$$

which satisfies the properties $\mathcal{G}(\gamma, 0) = 0$, $\mathcal{G}(\gamma, 1) = 1$, and $\mathcal{G}(\gamma, -1) = -1$. We can write the final result for $i \leq \xi$ as

$$\vartheta_i = \mathcal{G}(\alpha, i + 1). \tag{4.89}$$

For $\xi + 1 \leq i \leq \eta$, we have the difference equation $\vartheta_i = (2 + \beta)\vartheta_{i-1} - \vartheta_{i-2}$, with the general solution

$$\vartheta_i = r \left(\frac{2 + \beta + \sqrt{\Sigma}}{2} \right)^i + s \left(\frac{2 + \beta - \sqrt{\Sigma}}{2} \right)^i, \tag{4.90}$$

where $\Sigma = \beta^2 + 4\beta$. In this case, the coefficients r and s must be obtained by imposing $\vartheta_{\xi-1}$ and ϑ_ξ by means of Eq.(4.89). A long but straightforward calculation yields the final solution for $\xi + 1 \leq i \leq \eta$ in the form

$$\vartheta_i = \mathcal{G}(\beta, i - \xi + 1)\mathcal{G}(\alpha, \xi + 1) - \mathcal{G}(\beta, i - \xi)\mathcal{G}(\alpha, \xi). \tag{4.91}$$

For $i \geq \eta + 1$, we have the simpler difference equation $\vartheta_i = 2\vartheta_{i-1} - \vartheta_{i-2}$, with the general solution

$\vartheta_i = v + wi$. In this case, the coefficients v and w must be obtained by imposing $\vartheta_{\eta-1}$ and ϑ_η by means of Eq.(4.91). Hence, the result for $i \geq \eta+1$ can be eventually found as

$$\vartheta_i = (i-\eta+1)\vartheta_\eta - (i-\eta)\vartheta_{\eta-1}, \tag{4.92}$$

where $\vartheta_{\eta-1}$ and ϑ_η are given by Eq.(4.91). The result for $i \geq \eta+1$ can be therefore written in the following final form

$$\begin{aligned}\vartheta_i = (i-\eta+1)&[\mathcal{G}(\beta,\eta-\xi+1)\mathcal{G}(\alpha,\xi+1) - \mathcal{G}(\beta,\eta-\xi)\mathcal{G}(\alpha,\xi)] \\ -(i-\eta)&[\mathcal{G}(\beta,\eta-\xi)\mathcal{G}(\alpha,\xi+1) - \mathcal{G}(\beta,\eta-\xi-1)\mathcal{G}(\alpha,\xi)].\end{aligned} \tag{4.93}$$

From Eq.(4.84) we finally find

$$\begin{aligned}\det\mathcal{A}(\xi,\eta) = (N-\eta+1)&\left[\mathcal{G}(\beta,\eta-\xi+1)\mathcal{G}(\alpha,\xi+1) - \mathcal{G}(\beta,\eta-\xi)\mathcal{G}(\alpha,\xi)\right] \\ -(N-\eta)&\left[\mathcal{G}(\beta,\eta-\xi)\mathcal{G}(\alpha,\xi+1) - \mathcal{G}(\beta,\eta-\xi-1)\mathcal{G}(\alpha,\xi)\right],\end{aligned} \tag{4.94}$$

and

$$\begin{aligned}1-\mathcal{A}^{-1}_{NN}(\xi,\eta) = &\frac{\mathcal{G}(\alpha,\xi+1)}{\det\mathcal{A}(\xi,\eta)}\left[\mathcal{G}(\beta,\eta-\xi+1) - \mathcal{G}(\beta,\eta-\xi)\right] \\ &- \frac{\mathcal{G}(\alpha,\xi)}{\det\mathcal{A}(\xi,\eta)}\left[\mathcal{G}(\beta,\eta-\xi) - \mathcal{G}(\beta,\eta-\xi-1)\right].\end{aligned} \tag{4.95}$$

These formulas are used in Section 4.3 and 4.5.

The function $\mathcal{G}(\gamma,z)$ defined in Eq.(4.88) can be simplified by observing that, the second term is defined by a power with a base always strictly less than one. Thus, for large values of z, the second term can be neglected with respect to the first one. More specifically, we have two different cases:

$$\mathcal{G}(\alpha,z) \simeq \frac{1}{\sqrt{\Delta}}\alpha_0^z \quad \text{with} \quad \alpha_0 = (2+\alpha+\sqrt{\Delta})/2, \Delta = \alpha^2+4\alpha, \tag{4.96}$$

$$\mathcal{G}(\beta,z) \simeq \frac{1}{\sqrt{\Sigma}}\beta_0^z \quad \text{with} \quad \beta_0 = (2+\beta+\sqrt{\Sigma})/2, \Sigma = \beta^2+4\beta. \tag{4.97}$$

These results can be used to simplify Eq.(4.94)-(4.95) leading to

$$\begin{aligned}\det\mathcal{A}(\xi,\eta) = &\frac{\alpha_0\beta_0-1}{\sqrt{\Delta\Sigma}}\beta_0^{\eta-\xi-1}\alpha_0^{\xi}\times \\ &[(N-\eta+1)\beta_0 - (N-\eta)],\end{aligned} \tag{4.98}$$

$$1-\mathcal{A}^{-1}_{NN}(\xi,\eta) = \frac{1}{N-\eta+\frac{\beta_0}{\beta_0-1}}. \tag{4.99}$$

These expressions are used to evaluate the formulas in Sections 4.4 and 4.6.

4.9.2 Useful integrals

In order to develop Eqs.(4.29) and (4.30) in closed form we have to consider the integrals

$$I_1 = \int e^{-ax}e^{-\frac{b}{x}}\frac{\mathrm{d}x}{x^{3/2}}, \quad I_2 = \int e^{-ax}e^{-\frac{b}{x}}\frac{\mathrm{d}x}{x^{1/2}}, \tag{4.100}$$

where a and b are two real and positive constants. For obtaining an explicit expression for these integrals, we define the quantities

$$I^{+} = \sqrt{b} I_1 + \sqrt{a} I_2, \quad I^{-} = \sqrt{b} I_1 - \sqrt{a} I_2. \tag{4.101}$$

We can therefore write

$$I^{\mp} = \int \left(\sqrt{\frac{b}{x^3}} \mp \sqrt{\frac{a}{x}} \right) e^{-ax} e^{-\frac{b}{x}} \mathrm{d}x. \tag{4.102}$$

Now, we can observe that

$$\left(\sqrt{\frac{b}{x}} \pm \sqrt{ax} \right)^2 = \frac{b}{x} + ax \pm 2\sqrt{ab}, \tag{4.103}$$

and hence, we can write Eq.(4.102) in the form

$$I^{\mp} = \int \left(\sqrt{\frac{b}{x^3}} \mp \sqrt{\frac{a}{x}} \right) e^{-\left(\sqrt{\frac{b}{x}} \pm \sqrt{ax} \right)^2 \pm 2\sqrt{ab}} \mathrm{d}x. \tag{4.104}$$

To conclude, by remembering the definition of the error function [250]

$$\mathrm{erf}(x) = \frac{2}{\sqrt{\pi}} \int_0^x e^{-t^2} \mathrm{d}t, \tag{4.105}$$

we can observe that

$$\frac{\mathrm{d}}{\mathrm{d}x} \mathrm{erf}\left(\sqrt{\frac{b}{x}} \pm \sqrt{ax} \right) = -\frac{1}{\sqrt{\pi}} e^{-\left(\sqrt{\frac{b}{x}} \pm \sqrt{ax} \right)^2} \left(\sqrt{\frac{b}{x^3}} \mp \sqrt{\frac{a}{x}} \right), \tag{4.106}$$

and we directly obtain the first important result

$$I^{\mp} = -\sqrt{\pi} e^{\pm 2\sqrt{ab}} \mathrm{erf}\left(\sqrt{\frac{b}{x}} \pm \sqrt{ax} \right). \tag{4.107}$$

Since from Eq.(4.101) we have that $I^{+} + I^{-} = 2\sqrt{b} I_1$ and $I^{+} - I^{-} = 2\sqrt{a} I_2$, we get the final results

$$I_1 = -\frac{1}{2} \sqrt{\frac{\pi}{b}} \left[e^{+2\sqrt{ab}} \mathrm{erf}\left(\sqrt{\frac{b}{x}} + \sqrt{ax} \right) + e^{-2\sqrt{ab}} \mathrm{erf}\left(\sqrt{\frac{b}{x}} - \sqrt{ax} \right) \right], \tag{4.108}$$

$$I_2 = +\frac{1}{2} \sqrt{\frac{\pi}{a}} \left[e^{+2\sqrt{ab}} \mathrm{erf}\left(\sqrt{\frac{b}{x}} + \sqrt{ax} \right) - e^{-2\sqrt{ab}} \mathrm{erf}\left(\sqrt{\frac{b}{x}} - \sqrt{ax} \right) \right]. \tag{4.109}$$

The two integrals appearing in Eqs.(4.48) and (4.49) can be developed by evaluating

$$I = \int \sqrt{x} e^{-ax} e^{-\frac{b}{x}} dx. \tag{4.110}$$

Since

$$\frac{\mathrm{d}}{\mathrm{d}x} \left(\sqrt{x} e^{-ax} e^{-\frac{b}{x}} \right) = e^{-ax} e^{-\frac{b}{x}} \left(-ax^{1/2} + \frac{b}{x^{3/2}} + \frac{1}{2x^{1/2}} \right), \tag{4.111}$$

we get the relation

$$\sqrt{x}e^{-ax}e^{-\frac{b}{x}} = \int e^{-ax}e^{-\frac{b}{x}}\left(-ax^{1/2} + \frac{b}{x^{3/2}} + \frac{1}{2x^{1/2}}\right)\mathrm{d}x. \tag{4.112}$$

Therefore, we easily obtain

$$\begin{aligned} I + \frac{\sqrt{x}}{a}e^{-ax}e^{-\frac{b}{x}} &= I + \int e^{-ax}e^{-\frac{b}{x}}\left(-x^{1/2} + \frac{b}{ax^{3/2}} + \frac{1}{2ax^{1/2}}\right)\mathrm{d}x \\ &= \frac{b}{a}I_1 + \frac{1}{2a}I_2. \end{aligned} \tag{4.113}$$

This expression allows writing the final result in the form

$$\begin{aligned} I = \frac{\sqrt{\pi}}{2a}\Bigg[& e^{+2\sqrt{ab}}\left(\frac{1}{2\sqrt{a}} - \sqrt{b}\right)\mathrm{erf}\left(\sqrt{\frac{b}{x}} + \sqrt{ax}\right) \\ & -e^{-2\sqrt{ab}}\left(\frac{1}{2\sqrt{a}} + \sqrt{b}\right)\mathrm{erf}\left(\sqrt{\frac{b}{x}} - \sqrt{ax}\right)\Bigg] - \frac{\sqrt{x}}{a}e^{-ax}e^{-\frac{b}{x}}. \end{aligned} \tag{4.114}$$

Chapter 5

Phase transformations in materials science

5.1 Introduction

Several natural and artificial systems, as typically encountered in biology and modern nanotechnology, exhibit a combination of fundamental effects of non-locality and non-convexity, resulting in a variety of rather complex physical responses [29, 275–277]. A deep understanding of these phenomena is therefore essential for the analysis and design of such systems. The non-convexity feature is related to the possibility that the potential energy of the system may have different basins leading to wiggly energy landscapes and possibly many competing metastable states. Often, these systems are composed of several units (which may be identical, or inhomogeneous) and each unit is characterized by bistability or, in general, multistability. This assumption describes the possibility for each unit to be in two (or more) distinct states. In this framework, non-locality describes the possibility that the units can be in strong interaction with each other and thus the state in which one unit is found affects the state of the others, particularly those that are spatially closer. In the biological context, this form of interaction is sometimes referred to as cooperativity [278] and may be fundamental in many crucial biological and medical phenomena such as protein folding/unfolding, DNA degradation and resulting diseases [84, 132]. The complex response of such systems is the result of the energy competition among the many metastable configurations, regulated by the temperature-controlled exploration of the overall energy landscape. We show how three different statistical mechanics approaches, taking care of the elastic properties of the different configurations, can give important insights into many observed physical and biophysical phenomena.

Many examples can be theoretically inscribed into the previously introduced conceptual framework. For example, in the biological field, we may consider the conformational transitions in bio-polymeric chains [49–52, 169, 171, 172, 215, 221, 222, 224], and the sarcomeres behavior in skeletal muscles [70–76, 279]. On the other hand, concerning artificial systems, we can think of waves propagation in bistable lattices [11–15, 280], energy harvesting through multistable chains [16–18], and the plasticity and hysteresis in phase transitions and martensitic transformations of solids [19–24, 27, 281–290].

In this Chapter, we are interested in the observed thermal effects in previous examples, which become increasingly important as the size of the system decreases. The analysis is therefore relevant in systems of nanoscopic dimensions [230] or when, as in biological and polymeric soft matter, the competing contributions are of the entropic type with small energy differences

and low barriers [165]. For this reason, in order to have a correct physical description of the static and dynamic features of these systems, it is not sufficient to rely on classical discrete or continuous mechanics, but we must take into account the equilibrium or non-equilibrium statistical mechanics. By so doing, we can obtain important information on the thermodynamic picture of the folding/unfolding process in a macromolecular chain or a detailed description of the thermal effects on the microstructure evolution in a two-phase solid material.

Concerning materials science, and in particular the mechanics of solids for multiphase materials, many approaches can be found in the literature to describe the microstructure evolution. The Ericksen pioneering work proposed a variational energetic approach in the context of non-linear continuum elasticity theory with non-convex energy densities [19]. This methodology has been further generalized to describe phase transformations at the microstructure level [281–283]. Nevertheless, these continuum variational approaches neglect interfacial energy effects and non-local interactions, which are crucial contributions to the description of the realistic microstructure evolutions [284]. As a matter of fact, the minimization of the non-convex elastic energy without non-local interactions cannot completely describe the nucleation and propagation of finite domains [27, 285]. Therefore, surface energy contributions have been introduced by means of higher gradient energy terms [286, 287], and by non-local interactions [288]. A similar research line, in the context of discrete mechanics, has been developed from the pioneering work of Müller and Villaggio [20]. The basic model is composed of a one-dimensional lattice of units with non-convex potential energy and an intrinsic length-scale [21]. This scheme allows the description of energy barriers, metastable states, quasi-plastic and pseudo-elastic behaviors [23, 289]. Also in this context, the model has been extended with non-local energy terms able to capture the different features of phase nucleation and propagation [22]. Further generalizations consider the influence of boundary conditions, enabling a more detailed identification of the internal and boundary phase nucleations [24, 290]. Recent models investigate the austenite to martensite phase transitions in wires, eventually describing the shape memory alloy behavior under uniaxial tension [291–293].

Many similar methods have been elaborated to describe the configurational transitions in biological macromolecules (mainly proteins), undergoing folding/unfolding processes. In particular, those theories are able to explain the saw-tooth-like force-extension response observed in several experiments. A model has been proposed for macromolecules unfolded in atomic force microscopes, and validated for titin and RNA hairpins [294]. An approach based on the equilibrium statistical mechanics is based on a Landau-like free energy and predicts a sequence of first-order phase transitions in correspondence to the unfolding processes [53, 54]. Further investigations are based on the energy minimization of a bistable system and agree with the pattern observed in titin experiments [55]. Also, the Monte-Carlo implementation of a two-state theory for single-molecule stretching experiments has been proposed [110]. Finally, the mechanical unfolding of proteins have been also modeled through domain interactions described by the Ising model [102, 295].

In order to properly introduce the thermodynamics on non-convex, non-local systems, we adopt the method of the spin variables. So doing, we can consider two separated and different quadratic functions representing the wells of the potential energy, instead of the more complicated original bistable function. The introduction of the spin variables strongly simplifies the calculation of the partition functions and, consequently, the analysis of the macroscopic thermodynamic quantities. Indeed, in order to calculate these partition functions, we sum over the spin variables and integrate over the classical continuous variables. Since the separated wells are represented by quadratic terms, the integration can be performed straightforwardly since it acts on Gaussian functions. This theoretical approach is therefore able to yield closed-form results useful to better understand the underlying physics. Moreover, by means of this technique, we can study different ensembles of statistical mechanics, corresponding to different mechanical boundary conditions. On one hand, we can analyze the behavior of the system under an applied force (isotensional

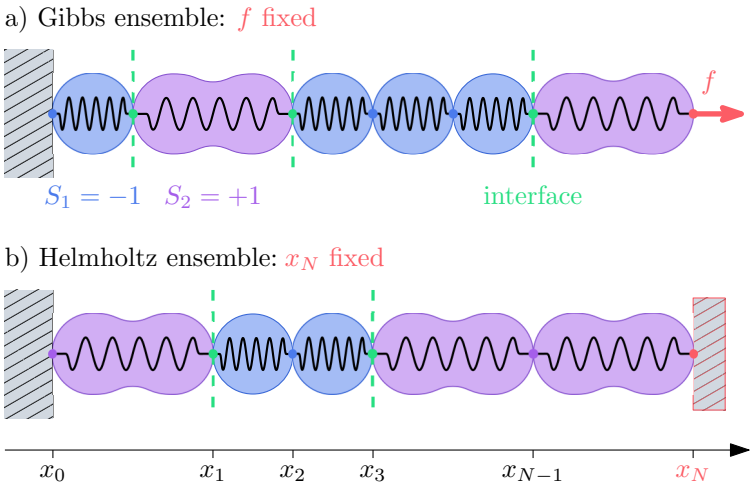

Figure 5.1: Scheme of the discrete system with variable phase configuration. Top panel: isotensional loading (Gibbs ensemble) of the chain with applied force f. Bottom panel: isometric loading (Helmholtz ensemble) of the chain with the prescribed extension x_N. Each chain unit, in both ensembles, feels an Ising interaction energy J due to the nearest neighbors. As an example, in the Gibbs and Helmholtz schemes, we show respectively three and two interfaces between folded and unfolded domains.

condition), corresponding to the Gibbs ensemble. On the other hand, we can also investigate the features of the system with prescribed extension (isometric condition), corresponding to the Helmholtz ensemble. As described in Ref.[94], these boundary conditions can be considered as limiting configurations of the more realistic case of an elastic device interacting with the system. Moreover, from a theoretical point of view, the comparison of the force-extension response within different ensembles is an important point useful to understand the concept of ensembles' equivalence in the thermodynamic limit, as discussed below. The spin variable method has been successfully used to study the nanomechanics of macromolecules [91, 92, 94, 95, 103, 163], the denaturation of macromolecules [82, 218], the non-local or cooperative effects [102, 165], skeletal muscles [73–76], and systems with transitions between unbroken and broken states [1, 30–32, 93]. It is interesting to observe that spin-string (in one dimension) and spin-membrane (in two dimensions) models, which are similar in spirit to the model presented here, have been developed also to describe transitions between zero-curvature phases and non-zero-curvature phases [296, 297]. These models are useful to give a theoretical interpretation to experimental and numerical results concerning the buckling of low-dimensional systems [298–300].

Here, we analyze a discrete chain with N bistable units (see Fig.5.1), where the two potential energy wells of each unit are characterized by different elastic constants k (pristine or folded state) and αk (extended or unfolded state), where $\alpha > 0$ (see Fig.5.2). In addition, the two states are separated by an energy jump ΔE, representing the (Helmholtz) transition energy, and have their equilibrium lengths equal to ℓ and $\chi\ell$, with a rise in length of $\Delta x = \ell(\chi - 1)$, where $\chi > 1$ (see Fig.5.2). The assumption of considering two different elastic constants of the wells, already considered in the purely mechanical case in Ref.[289], involves important novelties compared to the case with identical constants. Indeed, when the folded and unfolded elastic constants are equal ($\alpha = 1$), the conformational transitions correspond to a temperature-independent average plateau force [91, 92, 94, 95, 103, 163, 165]. This result can be simply explained in the

framework of the Bell relation $f = \Delta E/\Delta x$, discovered in the context of cell adhesion [59, 60, 110]. This plateau force, which depends neither on the spring constant nor on the temperature T, can be explained as follows. We consider two potential energies $U_f(x) = \frac{1}{2}k(x-\ell)^2 - fx$ and $U_u(x) = \Delta E + \frac{1}{2}k(x-\chi\ell)^2 - fx$, corresponding to the folded and unfolded states of the unit under force f when $\alpha = 1$. In both cases, the equilibrium lengths are defined by $\partial U_f/\partial x = 0$ and $\partial U_u/\partial x = 0$ and we get $x_f = \ell + f/k$ and $x_u = \chi\ell + f/k$. Finally, the unfolded configuration is more favorable than the folded one when $U_u(x_u) < U_f(x_f)$, which corresponds to $f > \Delta E/\Delta x$. The quantity $f_M = \Delta E/\Delta x$ is the so-called Maxwell force for the case with $\alpha = 1$. This approach can be easily generalized to the case with $\alpha \neq 1$ and $T = 0$ (purely mechanical behavior). The same analysis yields in fact the following quadratic equation for the transition force f_M

$$f_M^2(1-\alpha) + 2\alpha k f_M \Delta x - 2\alpha k \Delta E = 0, \tag{5.1}$$

where $\Delta x = \ell(\chi - 1)$, as before. This value of force has two important properties (both valid for $\alpha < 1$ and $\alpha > 1$): (i) on the plane (U, x) it is represented by an inclined straight line that is the common tangent to the two parabolas of the wells (see solid green lines in Fig.5.2, top panels); (ii) on the plane $(\mathrm{d}U/\mathrm{d}x, x)$ is represented by a horizontal straight line (see solid green lines in Fig.5.2, bottom panels) that makes equal the two areas of the indicated triangles (see shaded regions in Fig.5.2, bottom panels). This last property gives the name Maxwell force to the transition force because the equality of the two triangles is reminiscent of Maxwell's construction on the isothermal Van der Waals curves in the pressure-volume plane of a real gas [301]. The situation becomes much more complicated when $\alpha \neq 1$ and $T > 0$ and the transition force f_M, based on statistical mechanics analysis, is temperature dependent. Indeed, the asymmetry of energy wells makes entropic contributions crucial. It means that a temperature-dependent term must be added to Eq.(5.1) when $\alpha \neq 1$ and $T > 0$. This point is the focus of this Chapter and it is extensively examined in the following development.

Other two special values of the force are of interest in this discussion and represent the maximum (roof) f_R and the minimum (floor) f_F values of the force, such that for $f \in (f_F, f_R)$ both the first phase and the second phase can exist. They can be simply obtained as

$$f_R = k\,(x^* - \ell)\,, \tag{5.2}$$

$$f_F = \alpha k\,(x^* - \chi\ell)\,, \tag{5.3}$$

where x^* represents the point of intersection of the two parabolas (where the top of the energy barrier is reached, see Fig.5.2).

We also introduce in the discrete lattice of non-convex elements (see Fig.5.1) a non-local interaction described through an Ising scheme. This feature is crucial in order to take into consideration a form of cooperativity in the biological context or, equivalently, a sort of interface energy between folded and unfolded domains in the materials science context. The Ising interaction energy J can be considered positive (cooperative case) when adjacent units prefer to be in the same state, and negative (anti-cooperative case) when they prefer to be in two different states. To focus mainly on the interesting temperature-dependent force plateau behavior, in this study we will discuss only the ferromagnetic-like interactions, with $J > 0$. The important theoretical novelty with respect to classical spin models in physics is the fundamental role of elasticity and, in particular, the effect generated by the different elastic behavior of the two phases. Furthermore, for these systems, we can determine the analytic expression of the partition function in both Gibbs and Helmholtz ensembles (isotensional and isometric conditions, as shown in Fig.5.1). This can be done by means of an *ad hoc* implementation of the transfer matrix technique for the Gibbs case [302], and by using the Laplace transform relation between the partition functions of

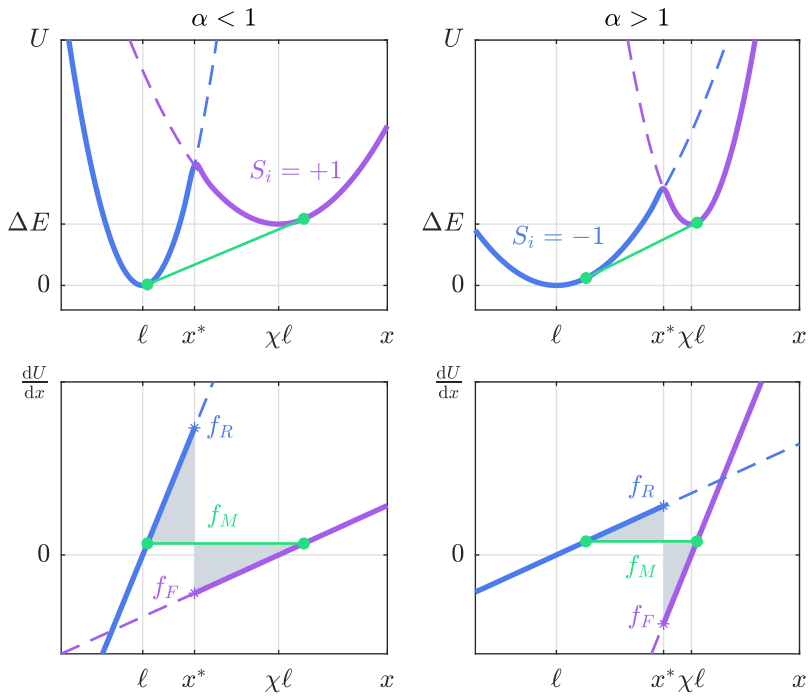

Figure 5.2: Elastic behavior of the chain units. Top panels: bistable potential energy $U = U(x)$ versus x for each unit, where $x = x_i - x_{i-1}$. The folded well corresponds to $S_i = -1$ and it is characterized by $L(-1) = \ell$, $Q(-1) = 0$, $K(-1) = k$. The unfolded well, identified by $S_i = +1$, is defined by $L(+1) = \chi\ell$, $Q(+1) = \Delta E$, $K(+1) = \alpha k$. Bottom panels: we show the quantity $\mathrm{d}U/\mathrm{d}x$ versus x (the force applied by the bistable unit, with a negative sign), exhibiting the characteristic force jump. Both the cases with $\alpha < 1$ and $\alpha > 1$ are shown on the left and on the right, respectively. In all plots, the solid green lines represent the transition paths (at $T = 0$), discussed in the main text.

conjugated ensembles for the Helmholtz case [98].

The first analysis, within the Gibbs ensemble, provides evidence that the force plateau is temperature-dependent and gives us the tools to obtain its expression in the limit of large values of N and large (positive) values of the ratio J/K_BT (K_B being the Boltzmann constant), which represents the strongly ferromagnetic case in the thermodynamic limit. Defining $\beta = 1/K_BT$, we can introduce the quantity $\tilde{\beta} = J\beta$ that represents the competition between the Ising interaction energy and the entropic contributions. Moreover, for isometric loading, in the Helmholtz ensemble, we find a peak force at the beginning of the plateau, representing the nucleation of a new domain with unfolded units. This is an important feature, typically observed in experimental measurements [303–308], and in molecular dynamics simulations of the microstructure evolution in nano-systems [230–234, 309–317]. In this Ising model, the microstructure evolution of folded and unfolded domains comes naturally and is regulated by the competition between interface energies and entropic contributions and, as we will show, the stress peak is an effect induced by the introduction of interface energy terms. The number of interfaces may vary in the whole range between 0 and $N - 1$ and typically it increases with the temperature [165]. The knowledge of the partition function allows a full analysis of the configurational properties of the system leading to the quantitative evaluation of the average number of unfolded units and the average number of

interfaces. In particular, this allows us to observe that the microstructure evolution, under increasing extension, is characterized by a single moving domain wall between folded and unfolded regions only when $\tilde{\beta} \gg 1$, *i.e.* when the system is strongly ferromagnetic, whereas for $\tilde{\beta} \ll 1$, *i.e.* when temperature increases, entropic energy terms favor solutions with an increasing number of interfaces.

An interesting point concerning these systems is the equivalence of the ensembles in the thermodynamic limit (*i.e.*, for $N \to \infty$) [56, 108, 109, 111, 112]. Two conjugated ensembles are said to be equivalent when the macroscopic behavior described by the force-extension relation is the same for $N \to \infty$. In general, it is difficult to prove for a given system if two statistical ensembles are equivalent. Although there are some particular rules, there are no general criteria or theorems for determining whether a system satisfies such an equivalence [111]. Several examples of non-equivalence are well known in the literature [113–118]. In our case, the analysis of the equivalence is rather difficult, mainly due to the overly complicated mathematical form of the Helmholtz partition function. But, since the systems with positive and sufficiently intense Ising interaction ($\tilde{\beta} \gg 1$) are the most interesting for practical applications, we can limit our analysis to the case of a system where the number of interfaces can take only the values 0 and 1. This observation is at the origin of the second approach proposed here, called the zipper model, previously adopted in other statistical mechanics investigations [104–107]. The main assumption is the analysis of solutions with none or one interface, which correspond to the previous Ising scheme only when $\tilde{\beta} \gg 1$. This simplification makes the thermodynamic limit analysis more transparent and, in this zipper case, we can explicitly prove the equivalence of the isotensional and isometric ensembles for $N \to \infty$. In addition, the result obtained under the zipper assumption, within the Helmholtz ensemble, can be further simplified by means of the stationary phase method (large values of N), leading to the third approach here discussed to describe non-convex discrete systems with non-local interactions. This final approximation is particularly useful since yields a compact mathematical expression for the force-extension curve and it allows the explicit calculation of the force peak in the Helmholtz ensemble, which is a crucial quantity in several experiments and numerical simulations, as discussed above. On one side, it leads to inferring some comparisons between our theoretical results and data from the literature; on the other side, it suggests both the possibility of designing new materials with required transition properties and the possibility of controlling them through external thermal fields.

The structure of this Chapter is the follows. In Section 5.2 we introduce the Ising scheme and we discuss in detail the proposed solutions for the Gibbs and Helmholtz ensembles. In Section 5.3 we explain how to obtain the thermodynamic limit within the Gibbs ensemble and we discuss the important effect of temperature-dependent force plateaux. In Section 5.4 we introduce the zipper model: we discuss the Gibbs and Helmholtz ensembles and we draw a comparison with the previous Ising scheme. In Section 5.5 we study the approximation based on the stationary phase and we perform a detailed analysis of the first peak force within the Helmholtz ensemble. Finally, in Section 5.6, to support the obtained analytical results, we discuss some explicit, quantitative comparisons with data from the literature concerning the behavior of nanowires with microstructural evolution.

5.2 Two-state chain with Ising non-local interactions

Consider a discrete chain of N two-state elements, each described by a bistable potential energy (see Figs.5.1 and 5.2), that interact also non-locally. We distinguish the two phases using the spin variable S_i assuming values in $\{-1, +1\}$. In particular, $S_i = -1$ corresponds to the first well (folded element), whereas $S_i = +1$ corresponds to the second well (unfolded element). The

main hypothesis of this new model is that the two phases are characterized by two different elastic constants $K(S_i)$, associated with two natural lengths $L(S_i)$ and two basal energies $Q(S_i)$. Specifically, we assume, without loss of generality, that $L(-1) = \ell$, $L(+1) = \chi\ell$, $Q(-1) = 0$, $Q(+1) = \Delta E$, $K(-1) = k$, $K(+1) = \alpha k$, where $\alpha > 0$, $\chi > 1$ and ΔE is the energy jump between the states. In these hypotheses, and introducing Ising non-local interaction terms, the overall Hamiltonian assumes the compact form

$$H = \sum_{i=1}^{N} \left\{ Q(S_i) + \frac{K(S_i)}{2} \left[(\lambda_i - \lambda_0(S_i))\, \ell \right]^2 \right\} - J \sum_{i=1}^{N-1} S_i S_{i+1}. \tag{5.4}$$

Here, the non dimensional parameter $\lambda_i = (x_i - x_{i-1})/\ell$ is the ratio between the i-th spring length and the folded rest length $L(-1) = \ell$, *i.e.* the spring stretch and $\lambda_0(S_i) = L(S_i)/\ell$, *i.e.* the natural (zero-force) spring stretch. The parameter J measures the non-local interaction strength. We remark that $J > 0$ corresponds to the ferromagnetic case, favoring states coalescence. It is useful to take into account the adimensional Hamiltonian $\tilde{H}$, obtained dividing H by the interface energy J

$$\tilde{H} = \sum_{i=1}^{N} \left\{ \tilde{Q}(S_i) + \frac{\tilde{K}(S_i)}{2} \left(\lambda_i - \lambda_0(S_i) \right)^2 \right\} - \varpi \sum_{i=1}^{N-1} S_i S_{i+1}, \tag{5.5}$$

where $\tilde{Q}(S_i) = Q(S_i)/J$, $\tilde{K}(S_i) = K(S_i)\ell^2/J$ and $\varpi = 1$ is a constant that we inserted in order to be able, later on, to calculate the average number of interfaces. We also introduce $\tilde{k} = k\ell^2/J$ so that $\tilde{K}(-1) = \tilde{k}$ and $\tilde{K}(+1) = \alpha\tilde{k}$. We remark that the spin variables approach can be adopted only when we work not far from the thermodynamic equilibrium [91, 163]. Indeed when rate effects are considered, the relaxation times of the system strongly depend on the energy barriers between the potential wells, which are neglected within our approach (see Ref.[99] and recent generalizations in Refs.[100, 101]). On the other hand, in the rate-independent regime considered here, this approach allows us to describe non-convexity through the discrete parameters S_i, in the sense that a for fixed phases configuration (S_i, i=1,...,N), the energy is convex with respect to other (stretch) variables. This energy structure also ensures that the equilibrium solutions represent local elastic energy minima (metastable equilibrium states). It is also important to remark that the application of the spin variable approach is correct only when the energy barrier between the two states is sufficiently larger than the thermal energy $K_B T$.

For completeness, in Appendix 5.8.1, we prove that the Hamiltonian function given in Eq.(5.4), based on Ising interactions among spins, can be obtained through an approximation of the Hamiltonian function defined by non-local next-nearest-neighbor (NNN) elastic interactions. Observe that this is coherent with the results in Refs.[24, 290], where it is shown that for small values of J the non-local interaction energy is, as in the case of the Ising model, proportional to the number of interfaces plus possible higher order boundary energy terms (that are neglected here). This is an important point since some previous investigations on thermal effects for multi-stable lattices considered NNN interactions [165]. The resulting analysis was complex enough to prevent a fully analytical solution, whereas the scheme with Ising interactions proposed here represents an important step forward because the results are obtained in closed form.

Here we analyze separately the two cases of assigned force (Gibbs ensemble) and assigned displacement (Helmholtz ensemble). We remark that detailed computations are reported in Appendix 5.8.2 and 5.8.3.

5.2.1 Ising model within the Gibbs ensemble

The statistical mechanics in the case of assigned force f, within the Gibbs ensemble (see Fig.5.1, top panel), can be introduced by calculating the canonical partition function

$$Z_G(f) = \sum_{\{S_i\}} \int_{\mathbb{R}^N} e^{-\beta(H - f x_N)} \mathrm{d}x_1 \dots \mathrm{d}x_N. \tag{5.6}$$

Due to the fact that it is more useful to consider dimensionless parameters, in Eq.(5.6), we substitute x_i with the stretch λ_i and introduce the dimensionless force $\tilde{f} = f\ell/J$ and energy $\tilde{H} = H/J$ together with the main non-dimensional parameter $\tilde{\beta} = \beta J$. We end up with the following partition function expression

$$Z_G(\tilde{f}) = \ell^N \sum_{\{S_i\}} \int_{\mathbb{R}^N} e^{-\tilde{\beta}\left(\tilde{H} - \tilde{f}\sum_{i=1}^N \lambda_i\right)} \mathrm{d}\lambda_1 \dots \mathrm{d}\lambda_N. \tag{5.7}$$

The sums over $\{S_i\}$ are to be considered extended to the values $+1$ and -1 for each spin variable ($i = 1, \dots, N$). Moreover, we have that $\sum_{i=1}^N \lambda_i \ell = x_N$ (where, without loss of generality, to avoid rigid motions, we have assumed $x_0 = 0$). Following the calculations in Appendix 5.8.2, we obtain

$$Z_G(\tilde{f}) = \frac{\ell^N}{2\cosh\tilde{\beta}} \left[\hat{\lambda}_1^N + \hat{\lambda}_2^N + e^{-2\tilde{\beta}} \left(\hat{\lambda}_1^N - \hat{\lambda}_2^N \right) \frac{\hat{\lambda}_1 + \hat{\lambda}_2}{\hat{\lambda}_1 - \hat{\lambda}_2} \right], \tag{5.8}$$

where $\hat{\lambda}_{1,2}$ ($\hat{\lambda}_1 > \hat{\lambda}_2$) are the eigenvalues of the transfer matrix defined in Eq.(5.80) (see Appendix 5.8.2). This result is similar to the one obtained in Ref.[102], where however the elastic constants were considered equal ($\alpha = 1$), and where a three-dimensional structure was studied to deal with polymeric cooperative systems.

The knowledge of the Gibbs partition function allows us to calculate the expected value $\langle x_N \rangle$ of the chain length (*i.e.*, the average value of the last position x_N, that from now on we rename x for simplicity of notation), the average number of unfolded units $\langle n_u \rangle$, and the average number of interfaces $\langle \iota \rangle$ between folded and unfolded units. Since

$$\sum_{i=1}^{N-1} S_i S_{i+1} = N - 1 - 2\iota, \tag{5.9}$$

using the dimensionless parameters introduced before, we get

$$\langle \tilde{x} \rangle = \frac{1}{\tilde{\beta}} \frac{\partial \log Z_G(\tilde{f})}{\partial \tilde{f}}, \tag{5.10}$$

$$\langle n_u \rangle = -\frac{1}{\tilde{\beta}} \frac{\partial \log Z_G(\tilde{f})}{\partial \Delta\tilde{E}}, \tag{5.11}$$

$$\langle \iota \rangle = \frac{N-1}{2} - \frac{1}{2\tilde{\beta}} \frac{\partial \log Z_G(\tilde{f})}{\partial \varpi}, \tag{5.12}$$

where $\tilde{x} = x/\ell$ and $\Delta\tilde{E} = \Delta E/J$. In Fig.5.3, the behavior of the mechanical quantities defined in Eqs.(5.10), (5.11), and (5.12) is shown by varying the values of $\tilde{\beta}$ (different colors) and α (different rows). More precisely, each row of Fig.5.3 corresponds to different values of α (namely, 1/3, 1, and 3 in the first, second, and third row, respectively), while $\tilde{\beta} = J/K_B T$ varies in every single

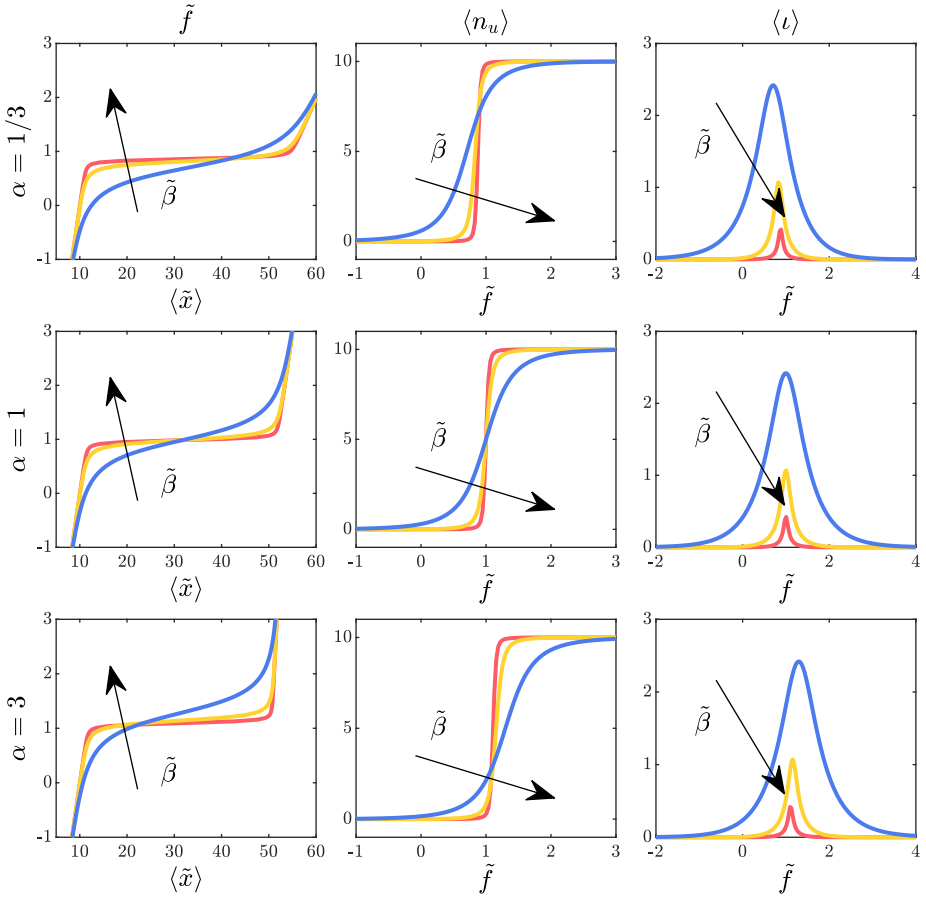

Figure 5.3: Behavior within the Gibbs ensemble with variable Ising coefficient $\tilde{\beta}$ and parameter α. The quantities $\langle \tilde{x} \rangle$, $\langle n_u \rangle$ and $\langle \iota \rangle$ are represented versus the dimensionless force $\tilde{f}$, with a variable Ising coefficient $\tilde{\beta} = \{1/2, 1, 3/2\}$. In the first row, we used $\alpha = 1/3$, in the second one $\alpha = 1$, and in the third one $\alpha = 3$. We adopted the parameters $N = 10$, $\tilde{k} = 6$, $Q(-1) = 0$, $Q(+1) = \Delta\tilde{E} = 4$, $\chi = 5$. The arrows indicate the direction in which $\tilde{\beta}$ increases.

plot (assuming the values 1/2, 1 and 3/2 for the blue, yellow and red curves, respectively). The first column shows the average chain length $\langle \tilde{x} \rangle$, the second one the average number of unfolded units $\langle n_u \rangle$, and the third one the average number of interfaces $\langle \iota \rangle$.

To begin, considering the force-extension figure in the case with identical wells $\alpha = 1$, we can notice that at the higher dimensionless Ising parameter $\tilde{\beta} = 3/2$ (red curve) there is a force plateau that corresponds to a cooperative unfolding of the chain units, a typical behavior characterizing the Gibbs ensemble [24]. At the lower value $\tilde{\beta} = 1/2$ (blue curve), when interaction terms decrease, this plateau is less sharp due to the fact that thermal fluctuations induce the system to explore a larger part of the wiggly energy landscape, eventually smoothing the force plateau. Again for $\alpha = 1$, the cooperative behavior is further confirmed by the expectation value of the number of unfolded units $\langle n_u \rangle$ that shows a transition from 0 to N at the same threshold of the force-extension curve. In the plot of the average number of interfaces $\langle \iota \rangle$ (always with $\alpha = 1$), we can notice that increasing the parameter $\tilde{\beta}$ decreases the number of interfaces due to the fact

that, in a ferromagnetic scenario, all the units tend to be in the same configuration (either folded or unfolded). Furthermore, in this plot, we can easily notice that the force thresholds that are responsible for the synchronized unfolding of the chain units are the same for different values of $\tilde{\beta}$. This is due to the fact that, in the second row, we have considered chain units that present the same elastic constant for both wells ($\alpha = 1$). Consider now the first row ($\alpha = 1/3$), when the second well is more compliant (softening regime). In this case, the fully unfolded configuration force-extension curve has a lower slope than the homogeneous folded one. The most interesting aspect here is that the force plateau occurs at different thresholds depending on the value of $\tilde{\beta}$ and, then, on the temperature T. This behavior is further confirmed by the shift of the peak in the average number of interfaces $\langle \iota \rangle$, corresponding to a force threshold depending on the value of $\tilde{\beta}$. In this plot, in fact, we can observe that the force threshold increases with $\tilde{\beta}$, meaning that the force plateau decreases with the temperature. All these considerations hold even in the third row ($\alpha = 3$), when the second state is stiffer (hardening regime), with the only difference that now the force plateau increases with the temperature.

While these results, representing the main physical effects of the proposed model, can already be qualitatively discussed, as described above, in the limiting cases of $N \to \infty$ and $\tilde{\beta} \gg 1$ this dependence can be quantitatively described, so that a more detailed analysis is postponed later.

5.2.2 Ising model within the Helmholtz ensemble

Consider now the isometric loading condition, described by the Helmholtz ensemble (see Fig.5.1, bottom panel). In this case, the total elongation of the chain is fixed by assigning x_N. As shown in Ref.[165], one may use an inverse Laplace transform to obtain the canonical partition function in the Helmholtz ensemble, starting from the Gibbs one given in Eq.(5.6). Using the change of variable $f \to -i\omega/\beta$, we can write

$$Z_H(x_N) = \frac{1}{2\pi} \int_{-\infty}^{+\infty} Z_G \left(-\frac{i\omega}{\beta} \right) e^{i\omega x_N} \mathrm{d}\omega, \tag{5.13}$$

and we obtain (see Appendix 5.8.3 for the detailed calculation)

$$Z_H(\tilde{x}_N) = \frac{\ell^{N-1} e^{N\tilde{\beta}}}{2\cosh\tilde{\beta}} \left(\frac{\pi}{2\tilde{\beta}} \right)^{\frac{N-1}{2}} \left\{ \sum_{k=0}^{\left[\frac{N}{2}\right]} \binom{N}{2k} \mathcal{W}_k + e^{-2\tilde{\beta}} \sum_{k=0}^{\left[\frac{N-1}{2}\right]} \binom{N}{2k+1} \mathcal{W}_k \right\}, \tag{5.14}$$

where

$$\begin{aligned} \mathcal{W}_k = & \sum_{j=0}^{k} \sum_{s=0}^{N-2j} \binom{k}{j} \binom{N-2j}{s} e^{-(s+j)\tilde{\beta}\Delta\tilde{E}} \sqrt{\frac{1}{\tilde{k}^{N-s-j}(\alpha\tilde{k})^{s+j}}} \\ & \times (-1)^j 4^j \left(1 - e^{-4\tilde{\beta}}\right)^j \sqrt{\frac{1}{\left(\frac{N-s-j}{\tilde{k}} + \frac{s+j}{(\alpha\tilde{k})}\right)}} \\ & \times \exp\left\{ -\frac{\tilde{\beta}}{2} \frac{\left[\tilde{x}_N - (N - s - j + \chi s + \chi j)\right]^2}{\left(\frac{N-s-j}{\tilde{k}} + \frac{s+j}{(\alpha\tilde{k})}\right)} \right\}. \end{aligned} \tag{5.15}$$

This partition function allows us to evaluate the expectation values $\langle f \rangle$ of the force conjugated to the assigned displacement, the average value of the number of unfolded units $\langle n_u \rangle$, and the

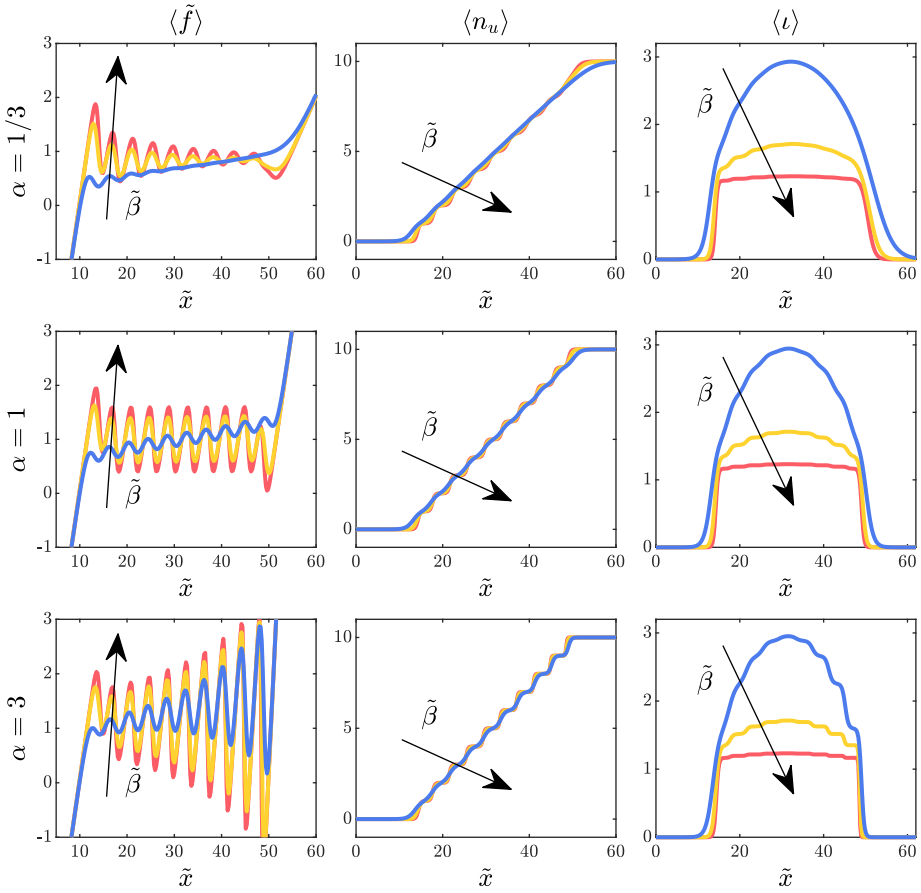

Figure 5.4: Behavior of the non-convex non-local chain within the Helmholtz ensemble with variable Ising coefficient $\tilde{\beta}$ and parameter α. The quantities $\langle \tilde{f} \rangle$, $\langle n_u \rangle$ and $\langle \iota \rangle$ are represented versus the dimensionless extension $\tilde{x}$, with variable $\tilde{\beta} = \{1/2, 1, 3/2\}$. In the first row, we used $\alpha = 1/3$, in the second one $\alpha = 1$, and in the third one $\alpha = 3$. Here $N = 10$, $\tilde{k} = 6$, $Q(-1) = 0$, $Q(+1) = \Delta\tilde{E} = 4$, $\chi = 5$. The arrows indicate the direction in which $\tilde{\beta}$ increases.

expectation value of the number of interfaces $\langle \iota \rangle$. We have

$$\langle \tilde{f} \rangle = -\frac{1}{\tilde{\beta}} \frac{\partial \log Z_H(\tilde{x}_N)}{\partial \tilde{x}_N}, \tag{5.16}$$

$$\langle n_u \rangle = -\frac{1}{\tilde{\beta}} \frac{\partial \log Z_H(\tilde{x}_N)}{\partial \Delta\tilde{E}}, \tag{5.17}$$

$$\langle \iota \rangle = \frac{N-1}{2} - \frac{1}{2\tilde{\beta}} \frac{\partial \log Z_H(\tilde{x}_N)}{\partial \varpi}. \tag{5.18}$$

In Fig.5.4, we show the behavior of the system within the Helmholtz ensemble. As before, we have different values for α in different rows (namely, $\alpha = 1/3, 1, 3$ in the first, second, and third row, respectively) and, in every single plot, $\tilde{\beta}$ is variable (namely, $\tilde{\beta} = 1/2, 1, 3/2$ for the blue, yellow and red curves, respectively). The average values $\langle \tilde{f} \rangle$, $\langle n_u \rangle$ and $\langle \iota \rangle$ are represented versus

$\tilde{x}$ in the first, second and third column of Fig.5.4. We can observe that the expectation values of the normalized force versus the applied extension always exhibit the typical saw-tooth path associated with a non-synchronized phase transition of the units. In the Helmholtz ensemble, in fact, due to the prescribed total elongation of the chain, we observe a sequential unfolding rather than a synchronized unfolding of the units, as seen previously within the Gibbs ensemble. In the plots of the average number of interfaces (third column), we can notice that at the highest $\tilde{\beta}$ value, there is only one single domain wall throughout the whole unfolding process. This means that with high values of the Ising parameter (or, similarly, for lower values of the temperature) it is strongly disadvantaged to create more than one interface in the course of the sequential unfolding process. The important result to underline, as already shown in Ref.[165], is that when a large ferromagnetic Ising coefficient is considered ($\tilde{\beta} \gg 1$), the system favors the generation of a single propagating interface, with a nucleation stress peak corresponding to the sudden transition of a chain fraction in the unfolded conformation. The asymmetry of the curves representing the number of interfaces and the dependence of the force plateau on the temperature (through $\tilde{\beta}$) are related once again to the presence of different elastic constants for the folded and unfolded wells (for the cases with $\alpha \neq 1$).

We remark that from a theoretical point of view, the unfolding of the last unit is characterized by a downward force peak that represents the coalescence of the folded phase to the unfolded one. Actually, in real experiments, this down peak is typically not attained for early specimen failure or for the presence of grips (or clamps) forbidding full propagation of the new phase in the terminal region. This point can be further discussed as follows. The energy of an interface corresponds to the Ising energy of two different adjacent states. Thus, the generation of the first interface costs more energy than its propagation. In fact, during propagation, the number of interfaces remains constant and equal to one (if $\tilde{\beta} \gg 1$) and no additional energy has to be spent for interface creation. This explains the first upward nucleation peak: the higher force is required to store enough energy to create an interface in the original homogeneous chain. During the traction, the interface approaches the right end of the chain until it reaches the last unit. When the last unit also unfolds, the interface disappears and the system energy decreases. This last phase is then energetically favored and requires less mechanical effort than propagation. This explains the last downward coalescence peak. Even if this latter phenomenon is not easy to be observed experimentally, it has already been underlined by some previous theoretical models [292, 293].

Moreover, when $\tilde{\beta}$ is low (meaning that the thermal fluctuations are high compared to the Ising parameter J), we can observe a reduction of the force peaks resulting in a smoothing of the force-extension curve, as shown in the first column of the figure. The behavior of the first peak is largely analyzed in the following Sections. The steps observed in the curves representing the number of unfolded units $\langle n_u \rangle$ versus the rising normalized extension are also smoothed with a decreasing $\tilde{\beta}$. Similarly, the number of interfaces $\langle \iota \rangle$ increases with lower values of $\tilde{\beta}$.

5.3 Thermodynamic limit with strongly ferromagnetic behavior in the Gibbs ensemble

As anticipated, the plateau force observed in the force-extension curves, corresponding to the so-called Maxwell stress in the purely mechanical case [289], sensibly depends on $\tilde{\beta}$ and, therefore, on the temperature in both the cases with applied force (Gibbs) and with total fixed elongation (Helmholtz). Here, to obtain an analytical measure of such an important effect, we consider strongly Ising interactions, *i.e.* with $\tilde{\beta} = \frac{J}{k_B T}$ sufficiently large, and we study the system in the thermodynamic limit ($N \to \infty$). An analogous limit was considered in Ref.[290] for a

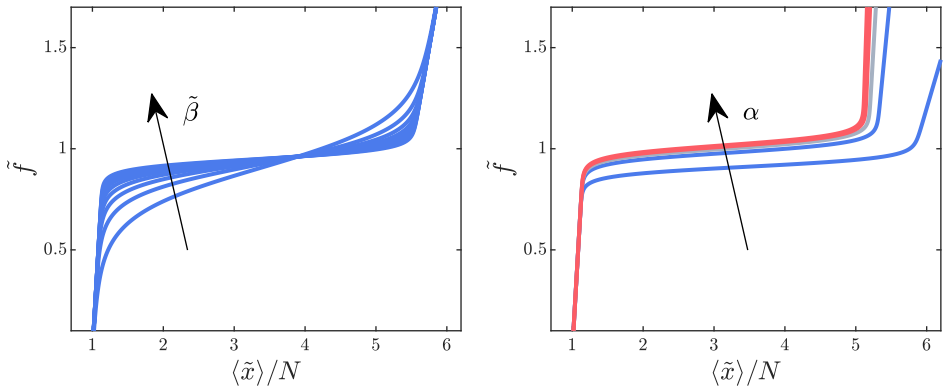

Figure 5.5: Force-extension curves within the Gibbs ensemble in the thermodynamic limit. In the left panel, $\tilde{\beta} = \{2,3,\dots,10\}$ is varied while $\alpha = 1/3$ is constant. On the right panel, instead, $\tilde{\beta} = 10$ is constant while $\alpha = \{0.2, 0.6, 1, 1.4, 1.8\}$ is variable. The curves are blue for $\alpha < 1$ and red for $\alpha > 1$ (the grey curve corresponds to $\alpha = 1$). The other parameters are $\tilde{k} = 6$, $\tilde{Q}(-1) = 0$, $\tilde{Q}(+1) = \Delta\tilde{E} = 4$, $\chi = 5$, $N = 10$. The arrows indicate the direction in which $\tilde{\beta}$ and α increase.

purely mechanical system. We remark that this limit, due to the complexity of the system, is performed here only for the Gibbs ensemble. In the following Sections, we will introduce particular hypotheses to get more analytical results also in the Helmholtz ensemble.

Let us consider first the thermodynamic limit for the Gibbs ensemble. Thus, from Eq.(5.8) we have

$$\log Z_G \underset{N\to\infty}{\simeq} N \log \hat{\lambda}_1, \tag{5.19}$$

where we exploited the property $\hat{\lambda}_1 > \hat{\lambda}_2$ (see Eq.(5.80) for details). From Eq.(5.10) we find

$$\langle\tilde{x}\rangle \simeq \frac{N}{\tilde{\beta}} \frac{\partial \log \hat{\lambda}_1}{\partial \tilde{f}}. \tag{5.20}$$

A direct evaluation of the derivative in Eq.(5.20) gives

$$\frac{\langle\tilde{x}\rangle}{N} \simeq \frac{1}{2}\left[\left(1 + \frac{c_- - c_+}{\sqrt{\Delta}}\right)\left(1 + \frac{\tilde{f}}{\tilde{k}}\right) + \left(1 - \frac{c_- - c_+}{\sqrt{\Delta}}\right)\left(\chi + \frac{\tilde{f}}{\alpha\tilde{k}}\right)\right], \tag{5.21}$$

where c_- and c_+ also depend on $\tilde{f}$ and are defined in Eq.(5.78) and Δ in Eq.(5.81) (see Appendix 5.8.2). In Fig.5.5, we show an example of an application of Eq.(5.21), where some force-extension curves are plotted with different values of $\tilde{\beta}$ (left panel) and α (right panel). Specifically, on the left panel of Fig.5.5, we can observe that increasing $\tilde{\beta}$ has both the effect of reducing the slope of the force plateau and of increasing the Maxwell force, confirming once again that the force plateau depends on the value of $\tilde{\beta}$ and then on the temperature T. Observe that here we are considering a fixed value of $\alpha = 1/3$ with the second phase softer than the first one. On the right panel of Fig.5.5, instead, we can see that keeping $\tilde{\beta}$ constant and increasing α we induce an increase in the force plateau, proving that the Maxwell force strictly depends on the asymmetry of the elastic constants of the two energy wells, as already observed in the purely mechanical case when constant force plateaux depending on α are observed.

Interestingly, it is possible to link the expectation value of the number of unfolded units to

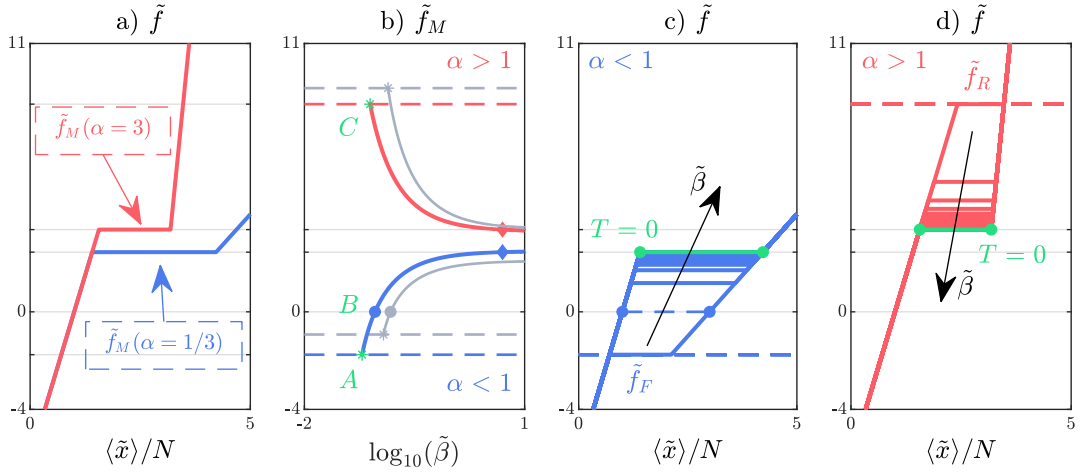

Figure 5.6: Dependence of the Maxwell force by $\tilde{\beta}$. Panel a): piecewise linear force-extension response in the thermodynamic limit under strong ferromagnetic assumption $\tilde{\beta} \gg 1$. We used $\alpha = 1/3$ (solid blue line) and $\alpha = 3$ (solid red line). Moreover, we adopted $\tilde{\beta} = 5$ for both curves. Panel b): dimensionless Maxwell force versus β with $\alpha = 1/3$ and $\alpha = 3$ (solid blue and solid red curves, respectively). Also, the curves for $\alpha = 1/6$ and $\alpha = 6$ are shown for completeness (solid grey curves). The theoretical maximum (roof) and minimum (floor) values of the Maxwell forces $\tilde{f}_M(\tilde{\beta}^*) = \tilde{f}_R$ and $\tilde{f}_M(\tilde{\beta}^*) = \tilde{f}_F$ are represented by dashed blue ($\alpha < 1$) and red ($\alpha > 1$) curves. Panels c) and d): evolution of the force plateau in the force-extension curve as $\tilde{\beta}$ changes for the two cases of $\alpha < 1$ (panel c) and $\alpha > 1$ (panel d). Green plateaux correspond to $T = 0$ (see Fig.5.2). Adopted parameters: $\tilde{k} = 6$, $\tilde{Q}(-1) = 0$, $\tilde{Q}(+1) = \Delta\tilde{E} = 6$, $\chi = 3$.

the assigned force in the thermodynamic limit. Indeed, by using Eq.(5.11) for $N \to \infty$, we get

$$\frac{\langle n_u \rangle}{N} \simeq -\frac{1}{\tilde{\beta}} \frac{\partial \log \hat{\lambda}_1}{\partial \Delta \tilde{E}} = \frac{1}{2}\left(1 - \frac{c_- - c_+}{\sqrt{\Delta}}\right), \tag{5.22}$$

$$\frac{\langle n_f \rangle}{N} = 1 - \frac{\langle n_u \rangle}{N} = \frac{1}{2}\left(1 + \frac{c_- - c_+}{\sqrt{\Delta}}\right). \tag{5.23}$$

where again c_- and c_+ depend on $\tilde{f}$ and are defined in Eq.(5.78). Thus we may write Eq.(5.21) in the form

$$\frac{\langle \tilde{x} \rangle}{N} \simeq \frac{\langle n_f \rangle}{N}\left(1 + \frac{\tilde{f}}{\tilde{k}}\right) + \frac{\langle n_u \rangle}{N}\left(\chi + \frac{\tilde{f}}{\alpha \tilde{k}}\right). \tag{5.24}$$

We notice that Eq.(5.24), derived from Eqs.(5.21), (5.22), and (5.23), gives a direct physical interpretation of the transition process with the expected value of the elongation obtained as a convex combination of the stretch-force relations in the purely folded and purely unfolded phases, depending on their percentage. In particular, when $\langle n_u \rangle = 0$, all units are in the folded phase and the system follows the first branch as obtained without temperature and non-local interaction effects. On the other hand, in the opposite extreme case with $\langle n_u \rangle = N$, all the bistable units are unfolded and the elongation is now given by $\langle \tilde{x} \rangle = \chi N + (N/\alpha\tilde{k})\tilde{f}$. These two homogeneous regimes, where the energy is convex and temperature has no effects, are connected by a force plateau whose height and slope depend on both temperature and Ising coefficient J through $\tilde{\beta}$.

Now we introduce the hypothesis of strong ferromagnetic interactions with respect to temper-

ature, $\tilde{\beta} \gg 1$. More precisely, from the definition of Δ in Eq.(5.81), it is possible to consider the approximation

$$\Delta \simeq (c_- - c_+)^2, \tag{5.25}$$

valid if

$$\frac{4c_+c_-e^{-4\tilde{\beta}}}{(c_- - c_+)^2} \ll 1. \tag{5.26}$$

Taking into account the form of $c_\pm$ (see Eqs.(5.73) and (5.78) in Appendix B), this condition corresponds to

$$\tilde{\beta} \gg \frac{1}{4}\log\left[\frac{2}{\cosh(\delta)-1}\right], \tag{5.27}$$

where

$$\delta = \frac{1}{2}\log\left(\frac{1}{\alpha}\right) - \tilde{\beta}\left[\Delta\tilde{E} - (\chi-1)\tilde{f} - \left(\frac{1}{\alpha}-1\right)\frac{\tilde{f}^2}{2\tilde{k}}\right]. \tag{5.28}$$

In particular, one verifies that in the limit $\tilde{\beta} \to +\infty$ (with $\delta \neq 0$) the ratio in Eq. (5.26) goes to zero. Using this approximation, Eq.(5.21) shows the two following different regimes, corresponding to the two homogeneous folded and unfolded fractions, depending on the force $\tilde{f}$ through the parameters $c_- = c_-(\tilde{f})$ and $c_+ = c_+(\tilde{f})$

$$\frac{\langle\tilde{x}\rangle}{N} \simeq \begin{cases} 1 + \dfrac{\tilde{f}}{\tilde{k}} & \text{if } c_- > c_+, \\ \chi + \dfrac{\tilde{f}}{\alpha\tilde{k}} & \text{if } c_- < c_+. \end{cases} \tag{5.29}$$

Thus under the assumption of large $\tilde{\beta}$, we get a horizontal force plateau, as shown in Fig.5.6 (panel a), obtained by imposing $c_- = c_+$, or, by using Eq.(5.73), given by the condition

$$\delta = 0, \tag{5.30}$$

where δ has been defined in Eq.(5.28). In this way we obtain the main result of this part, *i.e.* that for large enough interface energy J and for a large value of N, the system is characterized by a temperature-dependent transition force. This is controlled by a new temperature-dependent term in Eq.(5.30), not present in Eq.(5.1). Moreover, we can obtain an explicit analytic expression of the dimensionless Maxwell force $\tilde{f}_M$ as follows

$$\tilde{f}_M(\tilde{\beta}) = \left(\sqrt{\mathcal{D}} - 1\right)\left(\frac{\alpha}{1-\alpha}\right)\tilde{k}\,(\chi-1), \tag{5.31}$$

where

$$\mathcal{D} = 1 - \frac{2}{\tilde{\beta}(\chi-1)^2\tilde{k}}\left(\frac{1-\alpha}{\alpha}\right)\left(\frac{1}{2}\log\frac{1}{\alpha} - \tilde{\beta}\Delta\tilde{E}\right). \tag{5.32}$$

Due to the different elastic constants ($\alpha \neq 1$), the Maxwell force obtained from Eq.(5.31) depends on the temperature T (through $\tilde{\beta}$). A simpler dependence can be obtained by expanding Eq.(5.31) up to the first order in the difference $(1-\alpha)/\alpha$, measuring the difference from the case when the two wells are identical $\alpha = 1$. We obtain

$$\tilde{f}_M(\tilde{\beta}) \simeq \frac{\Delta\tilde{E}}{\chi-1} - \left[\frac{\Delta\tilde{E}^2}{2\tilde{k}(\chi-1)^3} + \frac{1}{2\tilde{\beta}(\chi-1)}\right]\left(\frac{1-\alpha}{\alpha}\right), \tag{5.33}$$

which is valid for $|(1-\alpha)/\alpha| \ll 1$. When $\alpha = 1$ we retrieve the expression $\tilde{f} = \Delta\tilde{E}/(\chi-1)$, well known in literature [59, 60, 91, 92], and discussed in the Introduction. On the other hand, if T approaches zero, Eq.(5.30) simplifies to Eq.(5.1).

The dependence of the Maxwell force on $\tilde{\beta}$ is shown in Fig.5.6 (panel b). We can observe the opposite behaviors exhibited in the hardening case with $\alpha > 1$ (solid blue curve with $\alpha = 1/3$) and in the softening case with $\alpha < 1$ (solid red curve with $\alpha = 3$). We can also notice that when $\tilde{\beta} \to \infty$ the Maxwell force reads

$$\tilde{f}_M \simeq \tilde{k}(\chi-1)\frac{\alpha}{1-\alpha}\left[\sqrt{1+\frac{2\Delta\tilde{E}}{(\chi-1)^2\tilde{k}}\left(\frac{1-\alpha}{\alpha}\right)}-1\right] > 0, \tag{5.34}$$

with a first order correction $\mathcal{O}(1/\tilde{\beta})$. In particular, when $\alpha < 1$, if $\tilde{\beta}$ decreases (as the temperature increases), the Maxwell force decreases as well. The corresponding variation in the stress-strain diagram is shown in Fig.5.6 (panel c). In particular, from Eqs.(5.31) and (5.32), we deduce that when the value of $\tilde{\beta}$ satisfies the equality $\log(1/\alpha)/2\Delta\tilde{E} = \tilde{\beta}$, the Maxwell force characterizing the plateau is $\tilde{f}_M = 0$ (see the point B in Fig.5.6, panel b). Thus, at this value, $\tilde{\beta} = \tilde{\beta}_0$, the Maxwell plateau at zero applied force connects the two natural configurations with $\langle\tilde{x}\rangle/N \simeq 1$ and $\langle\tilde{x}\rangle/N \simeq \chi$ corresponding to the completely folded and completely unfolded states, respectively. In other words, the system undergoes a transition to the second state at zero applied force. It is important to observe that solutions with zero or even negative Maxwell forces have been considered in the case of phase transitions in shape memory alloys [318]. In this case, a consistent definition of the reference configuration assumed to be stable, should be temperature dependent, so that for positive (negative) Maxwell stress the reference configuration is the homogeneous folded (unfolded) phase configuration.

It is important to observe that, for this case with $\alpha < 1$, the Maxwell stress can decrease until the limit value $\tilde{f}_F$, as defined in Eq.(5.3), because after this value the energy of the unfolded state is not defined (see the point A in Fig.5.6, panel b, and the floor plateau in Fig.5.6, panel c). We denote $\tilde{\beta}^*$ the value of $\tilde{\beta}$, for which we attain the plateau at $\tilde{f}_F$. Interestingly, for $\alpha < 1$, the equation $\tilde{f}_M(\tilde{\beta}^*) = \tilde{f}_F$ is solved by

$$\tilde{\beta}^* = \frac{\frac{1}{2}\log\frac{1}{\alpha}}{\Delta\tilde{E}(1-\alpha)+\frac{1}{2}\alpha\tilde{k}(1-\chi)^2}. \tag{5.35}$$

In the case with $\alpha > 1$, represented in Fig.5.6, panel b (red solid curve), we observe that the Maxwell stress always increases with the temperature (decreasing $\tilde{\beta}$). In this situation, the Maxwell force is always positive. However, the plateau stops existing at $\tilde{\beta}^*$ corresponding to the value of force $\tilde{f}_R$, defined in Eq.(5.2), when the energy of the first well ceases to be defined (see the point C in Fig.5.6, panel b, and the roof plateau in Fig.5.6, panel d). Interestingly, for $\alpha > 1$, the equation $\tilde{f}_M(\tilde{\beta}^*) = \tilde{f}_R$ is solved by

$$\tilde{\beta}^* = \frac{\frac{1}{2}\alpha\log\alpha}{\Delta\tilde{E}(1-\alpha)+\frac{1}{2}\alpha\tilde{k}(1-\chi)^2}. \tag{5.36}$$

It is important to point out that, due to the use of the spin variables method, the temperature is always limited by the fact that the barrier between the two energy wells must always be sufficiently larger than K_BT.

In this Section, we obtained an analytical expression ($\delta = 0$) linking the Maxwell force to the temperature in the thermodynamic limit ($N \to \infty$) and with the assumption of strong ferromagnetic interaction (under the isotensional condition). This result is related to the difference

of stiffness between the two energy wells ($\alpha \neq 1$) and explains the mechanical response observed in several nanosystems [230–234, 309–317]. Interestingly enough, if for $\alpha > 1$ ($\alpha < 1$) we increase (decrease) the stress starting from the homogeneous folded (unfolded) state, the system keeps this configuration even for values of the stress for which this configuration is characterized by a higher elastic energy than the other homogeneous state, due to entropic effects. This counter-intuitive behavior, tending to stabilize the softer phase, is observable only in the case of different wells and was named entropic stabilization [318].

5.4 The zipper model

In this Section, we further extend the study of the non-local non-convex chain of bistable units under the assumption of strong ferromagnetic behavior ($\tilde{\beta} \gg 1$). As previously discussed, this hypothesis leads to the existence of a single domain wall [165, 290], *i.e* a single interface between the folded and unfolded regions that propagates through the chain (see Fig.5.7). We underline that this single interface wall propagates continuously throughout the entirety of the system without showing any pinning phenomena that could obstacle the motion since we fully neglect any possible defect (dislocations, vacancy or interstitial defects) in our structure (such pinning behavior has been thoroughly investigated in [319–321]). In this framework, we derive simplified analytical expressions for both the Gibbs and Helmholtz ensembles and we prove their equivalence in the thermodynamic limit. Accordingly, we consider a chain composed of $N-\xi$ units in the folded state and the remaining ξ units in the unfolded one, being ξ a discrete variable assuming values in the set $\{0,1,2,\dots,N\}$, representing the position, in terms of chain units, of the moving domain wall between folded and unfolded regions. This discrete variable can vary depending on both mechanical and thermal effects and this simplified scheme is typically called zipper model [104–107].

To begin with, let us consider the Hamiltonian in Eq.(5.5), where the last sum over the $N-1$ spins can be divided into two parts by means of the zipper assumptions. By introducing ι, the number of changes (interfaces) in the spins sequence $S_1,\dots,S_N$, we have ι addends with value -1 and $N-1-\iota$ addends with value $+1$, see Eq.(5.9). Thus

$$\tilde{H}_Z = \sum_{i=1}^{N} \left\{ \tilde{Q}(S_i) + \frac{\tilde{K}(S_i)}{2} \left(\lambda_i - \lambda_0(S_i)\right)^2 \right\} - [N-1-2\iota(\xi)]. \tag{5.37}$$

In particular, we assume the possibility to have $\iota(\xi)=0$ if $\xi \in \{0,N\}$ (no interface) and $\iota(\xi)=1$ if $1 \leq \xi \leq N-1$ (only one interface). Accordingly: (i) if $i \leq N-\xi$ (folded units), then we have $\tilde{Q}(i)=0$, $\tilde{K}(i)=\tilde{k}$, $\lambda_0(i)=1$, and (ii) if $i \geq N-\xi+1$ (unfolded units), then $\tilde{Q}(i)=\Delta\tilde{E}$, $\tilde{K}(i)=\alpha\tilde{k}$, $\lambda_0(i)=\chi$.

By separating the folded and unfolded contributions we may rearrange the Hamiltonian as

$$\begin{aligned} \tilde{H}_Z(\xi) = &\sum_{i=1}^{N-\xi} \left\{ \frac{\tilde{k}}{2} \left(\lambda_i - 1\right)^2 \right\} + \sum_{i=N-\xi+1}^{N} \left\{ \Delta\tilde{E} + \frac{\alpha\tilde{k}}{2} \left(\lambda_i - \chi\right)^2 \right\} \\ &- [N-1-2\iota(\xi)]. \end{aligned} \tag{5.38}$$

From now on, the discrete variable ξ belongs to the phase space of the system together with the continuous displacements λ_i.

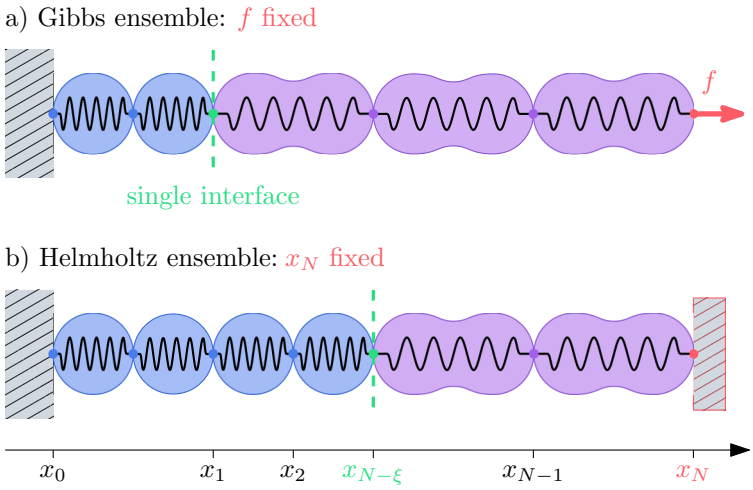

Figure 5.7: Scheme of the zipper model of the non-local non-convex chain. Top panel: isotensional configuration (Gibbs ensemble). Bottom panel: isometric configuration (Helmholtz ensemble). In both cases, we always have only one interface between folded and unfolded regions.

5.4.1 Zipper model within the Gibbs ensemble

Let us evaluate the canonical partition function in the Gibbs ensemble by using the Hamiltonian in Eq.(5.38). By definition we have

$$Z_G(\tilde{f}) = \ell^N \sum_{\xi=0}^{N} \int_{\mathbb{R}^N} e^{-\tilde{\beta}\left(\tilde{H}_Z - \tilde{f}\left(\sum_{i=1}^{N}\lambda_i\right)\right)} \mathrm{d}\lambda_1 \ldots \mathrm{d}\lambda_N, \tag{5.39}$$

that can be evaluated by a Gaussian integration giving

$$\begin{aligned} Z_G(\tilde{f}) = \sum_{\xi=0}^{N} \frac{1}{\alpha^{\frac{\xi}{2}}} e^{-\tilde{\beta}\left\{2\iota(\xi)+\Delta\tilde{E}\xi-\tilde{f}[N+(\chi-1)\xi]-\frac{\tilde{f}^2}{2\tilde{k}}\left[N-\xi+\frac{\xi}{\alpha}\right]\right\}} \\ \times \ell^N \left(\frac{2\pi}{\tilde{\beta}\tilde{k}}\right)^{\frac{N}{2}} e^{\tilde{\beta}(N-1)}. \end{aligned} \tag{5.40}$$

Following the same reasoning as in Section 5.2, one may evaluate the expectation values of the mechanical macroscopic observables of the system, namely $\langle\tilde{x}\rangle$, $\langle n_u\rangle$ and $\langle\iota\rangle$ (see Eqs.(5.10), (5.11) and (5.12)), where we use again $\tilde{x}$ to indicate $\tilde{x}_N$. In Fig.5.8, the behavior of the mechanical quantities $\langle\tilde{x}\rangle$, $\langle n_u\rangle$ and $\langle\iota\rangle$ is shown by varying the values of $\tilde{\beta}$ (different colors) and α (different rows). Each row of Fig.5.8 corresponds to a different constant α (namely, 1/3, 1 and 3 in the first, second and third row, respectively) while $\tilde{\beta} = J/K_BT$ varies within every single plot ($\tilde{\beta} = 1, 2, 3$ for the blue, yellow and red curves, respectively). The first column shows the average chain length $\langle\tilde{x}\rangle$, the second one the average number of unfolded units $\langle n_u\rangle$ and the third the average number of interfaces $\langle\iota\rangle$. By looking at the force-extension curve and at the average number of unfolded units, one observes again the typical synchronized behavior of the Gibbs ensemble, where all the units unfold cooperatively. A difference with respect to the exact Ising model is that the number of interfaces is smaller, limited by the presence of the zipper assumption.

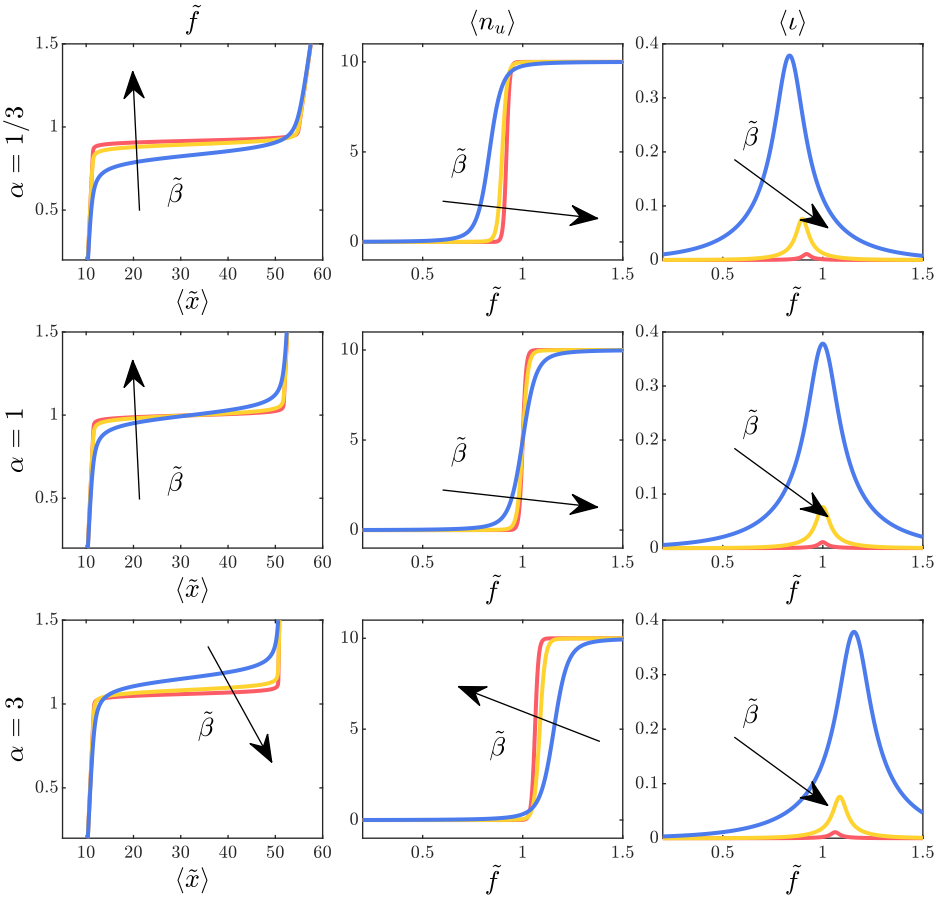

Figure 5.8: Behavior of the zipper model within the Gibbs ensemble with variable Ising coefficient $\tilde{\beta}$ and parameter α. The quantities $\langle \tilde{x} \rangle$, $\langle n_u \rangle$ and $\langle \iota \rangle$ are represented versus the dimensionless force $\tilde{f}$, with a variable Ising coefficient $\tilde{\beta} = \{1, 2, 3\}$. In the first row, we used $\alpha = 1/3$, in the second one $\alpha = 1$, and in the third one $\alpha = 3$. We adopted the parameters $N = 10$, $\tilde{k} = 6$, $Q(-1) = 0$, $Q(+1) = \Delta\tilde{E} = 4$, $\chi = 5$. The arrows indicate the direction in which $\tilde{\beta}$ increases.

In particular, we may study $\langle x \rangle$, evaluated through Eq.(5.10) and the partition function in Eq.(5.40). After some straightforward calculations, one obtains

$$\frac{\langle \tilde{x} \rangle}{N} = \frac{\left[1 + \frac{\tilde{f}}{\tilde{k}} + \left(\chi + \frac{\tilde{f}}{\alpha \tilde{k}}\right) e^{N\delta}\right] \left(1 - e^{-2\tilde{\beta}}\right) + e^{-2\tilde{\beta}} \sum_{\xi=0}^{N} e^{\delta\xi} A_\xi}{\left[1 + e^{N\delta}\right] \left(1 - e^{-2\tilde{\beta}}\right) + e^{-2\tilde{\beta}} \sum_{\xi=0}^{N} e^{\delta\xi}}, \tag{5.41}$$

where δ is defined in Eq.(5.28) and

$$A_\xi = \frac{\xi}{N} \left(\chi + \frac{\tilde{f}}{\alpha \tilde{k}}\right) + \left(1 - \frac{\xi}{N}\right) \left(1 + \frac{\tilde{f}}{\tilde{k}}\right). \tag{5.42}$$

We can now use the following sums

$$\sum_{\xi=0}^{N} \mathrm{y}^{\xi} = \frac{1-\mathrm{y}^{N+1}}{1-\mathrm{y}}, \tag{5.43}$$

$$\sum_{\xi=0}^{N} \xi \mathrm{y}^{\xi} = \frac{\mathrm{y}}{(1-\mathrm{y})^2}[1-(N+1)\mathrm{y}^{N}+N\mathrm{y}^{N+1}], \tag{5.44}$$

which allows us to obtain the explicit expressions

$$\begin{aligned}\Sigma_1 = \sum_{\xi=0}^{N} e^{\delta\xi} A_{\xi} = \left(1+\frac{\tilde{f}}{\tilde{k}}\right)\frac{1-e^{\delta(N+1)}}{1-e^{\delta}} + \left[\left(\chi+\frac{\tilde{f}}{\alpha\tilde{k}}\right)-\left(1+\frac{\tilde{f}}{\tilde{k}}\right)\right] \\ \times \frac{1}{N}\frac{e^{\delta}}{(1-e^{\delta})^2}\left[1-(N+1)e^{N\delta}+Ne^{\delta(N+1)}\right],\end{aligned} \tag{5.45}$$

$$\Sigma_2 = \sum_{\xi=0}^{N} e^{\delta\xi} = \frac{1-e^{\delta(N+1)}}{1-e^{\delta}}. \tag{5.46}$$

Thus, Eq.(5.41) reads

$$\frac{\langle\tilde{x}\rangle}{N} = \frac{\left[1+\frac{\tilde{f}}{\tilde{k}}+\left(\chi+\frac{\tilde{f}}{\alpha\tilde{k}}\right)e^{N\delta}\right]\left(1-e^{-2\tilde{\beta}}\right)+e^{-2\tilde{\beta}}\Sigma_1}{\left[1+e^{N\delta}\right]\left(1-e^{-2\tilde{\beta}}\right)+e^{-2\tilde{\beta}}\Sigma_2}, \tag{5.47}$$

which provides the Gibbs force-extension relation in the approximations of a single interface and large ferromagnetic interaction (zipper model). Observe that, thanks to this hypothesis, we are able to obtain for the zipper model exact explicit relations for the material response of the system also in the discrete case with finite arbitrary N.

On the other hand, in the thermodynamic limit ($N \to \infty$), we can confirm the results obtained in Section 5.3 for the complete Ising scheme. In particular, when $N \to \infty$, the value of $\langle\tilde{x}\rangle/N$ depends on the sign of δ. If $\delta < 0$ we have

$$\lim_{N\to\infty} \Sigma_1 = \left(1+\frac{\tilde{f}}{\tilde{k}}\right)\frac{1}{1-e^{\delta}}, \quad \lim_{N\to\infty} \Sigma_2 = \frac{1}{1-e^{\delta}}, \tag{5.48}$$

and we get (in the limit $N \to \infty$)

$$\frac{\langle\tilde{x}\rangle}{N} \simeq 1+\frac{\tilde{f}}{\tilde{k}}, \tag{5.49}$$

that represents the elastic branch of the response observed when all units are folded. Conversely, if $\delta > 0$, we can show that

$$\lim_{N\to\infty} \Sigma_1 e^{-N\delta} = -\left(\chi+\frac{\tilde{f}}{\alpha\tilde{k}}\right)\frac{e^{\delta}}{1-e^{\delta}}, \quad \lim_{N\to\infty} \Sigma_2 e^{-N\delta} = -\frac{e^{\delta}}{1-e^{\delta}}. \tag{5.50}$$

Hence, a manipulation of Eq.(5.47) gives (in the limit $N \to \infty$)

$$\frac{\langle\tilde{x}\rangle}{N} \simeq \chi+\frac{\tilde{f}}{\alpha\tilde{k}}, \tag{5.51}$$

representing the unfolded elastic branch. Thus, the two elastic branches for $\delta < 0$ and $\delta > 0$ are linked by a force plateau (see Fig.5.6, panel a), corresponding to Eq. $\delta = 0$. This is exactly the same condition found in Eq.(5.30), proving that the results obtained within the zipper approximation in the thermodynamic limit coincide with the ones obtained in Section 5.3 under the strong ferromagnetic assumption.

5.4.2 Zipper model within the Helmholtz ensemble

Let us then consider the Helmholtz ensemble under the zipper assumption. In this case, the partition function can be obtained as in Eq.(5.13), by the application of a Fourier transform. Indeed, using Eq.(5.40), we get

$$Z_H(\tilde{x}_N) = \left(\frac{2\pi\ell^2 e^{2\tilde{\beta}}}{\tilde{\beta}}\right)^{\frac{N-1}{2}} \sum_{\xi=0}^{N} \sqrt{\frac{1}{\left(\frac{N-\xi}{\tilde{k}} + \frac{\xi}{\alpha\tilde{k}}\right)\tilde{k}^{N-\xi}(\alpha\tilde{k})^{\xi}}} \times e^{-\tilde{\beta}\left(\frac{[\tilde{x}_N-(N+(\chi-1)\xi)]^2}{2}\left(\frac{N-\xi}{\tilde{k}}+\frac{\xi}{\alpha\tilde{k}}\right)^{-1}+2\iota(\xi)+\Delta\tilde{E}\xi\right)}. \tag{5.52}$$

The average macroscopic property of the zipper model within the Helmholtz ensemble can be found through Eqs.(5.16), (5.17) and (5.18). In Fig.5.9 we show $\langle\tilde{f}\rangle$, $\langle n_u\rangle$ and $\langle\iota\rangle$ as function of the prescribed extension $\tilde{x}_N$ for different values of the Ising coefficient $\tilde{\beta}$ and different elastic constants ratio α. We recover the same macroscopic behavior of the exact Ising model characterized by the sequential unfolding of the units and represented by the typical saw-tooth path of the force-extension curve. In particular, it is important to observe that the value of the number of interfaces remains constantly at 1, due to the zipper assumption, and it is 0 only when $\xi = 0$ or $\xi = N$, coherently with the model introduced. It is interesting to notice that in the force-extension curve, we can see the first upward force peak, corresponding to the nucleation of a new phase with unfolded units, and the last downward peak, representing the coalescence of the folded region to the unfolded one. Observing the sequential unfolding of the units in the force-extension plots of Fig.5.9, we can notice that there are three different behaviors depending on the elastic constants ratio: in the case with $\alpha = 1/3$, the force needed to unfold a single unit decreases while the number of unfolded units increases; in the case with $\alpha = 1$, except for the nucleation (first peak) and the coalescence (last peak) forces, all the other forces needed to unfold the units are equal; finally, in the case with $\alpha = 3$, we have the opposite behavior to the case with $\alpha = 1/3$, *i.e.* the unfolding forces increase with the number of unfolded units. This result is perfectly coherent with the previously introduced concept of entropic stabilization of the softer configuration. Moreover, we remark that by considering a higher number of elements (not reported for compactness), it is possible to observe an initial nucleation of a segment with more than one single element passing to the new unfolded state. This aspect is discussed in detail in the next section where we consider the system behavior for large values of N. In this case, we can analyze the amplitude of the first peak and of the first nucleated segment analytically leading to a useful result for comparing the model with experiments and numerical simulations.

5.5 Stationary phase analysis of the zipper model within the Helmholtz ensemble

Here, we want to study the thermodynamic limit of the Helmholtz zipper model. The aim of this development is to obtain three important results: (i) a simplified expression of the force-

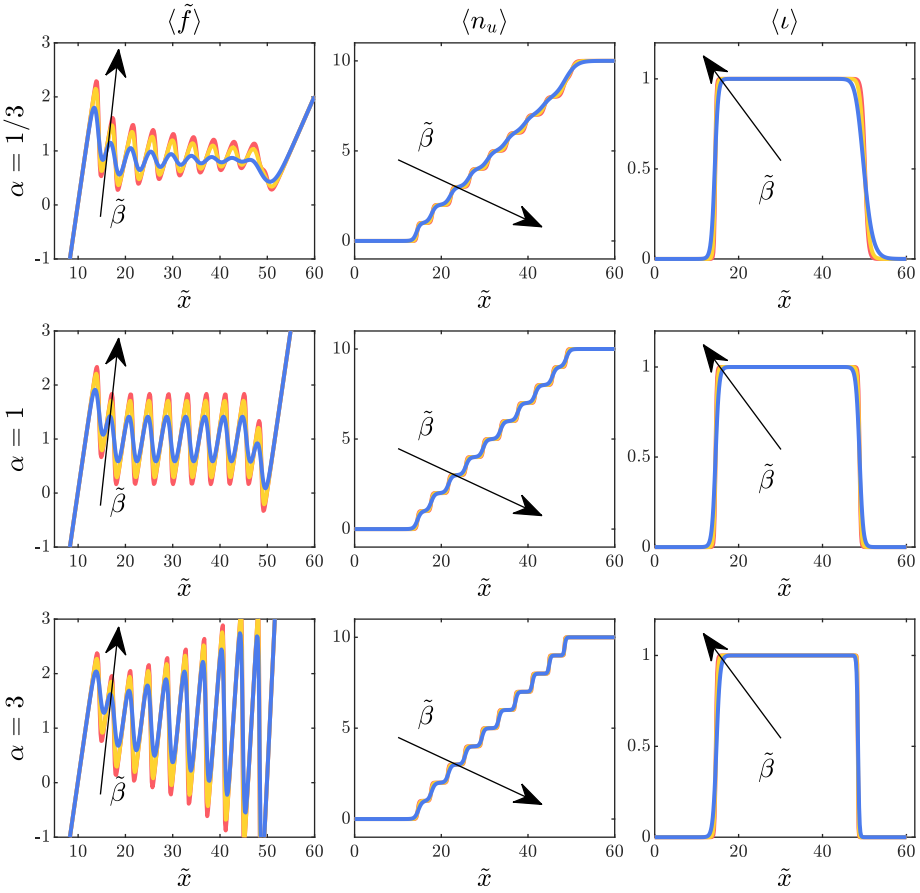

Figure 5.9: Behavior of the zipper model within the Helmholtz ensemble with variable Ising coefficient $\tilde{\beta}$ and parameter α. The quantities $\langle \tilde{f} \rangle$, $\langle n_u \rangle$ and $\langle \iota \rangle$ are represented versus the strain $\tilde{x}$, with a variable Ising coefficient $\tilde{\beta} = \{1, 2, 3\}$. In the first row, we used $\alpha = 1/3$, in the second one $\alpha = 1$, and in the third one $\alpha = 3$. We adopted the parameters $N = 10$, $\tilde{k} = 6$, $Q(-1) = 0$, $Q(+1) = \Delta\tilde{E} = 4$, $\chi = 5$. The arrows indicate the direction in which $\tilde{\beta}$ increases.

extension relation under isometric conditions valid for large values of N and for $\tilde{\beta} \gg 1$, (ii) an explicit expression for the amplitude of the first force peak, representing the nucleation of the unfolded phase, and (iii) a rigorous demonstration of the equivalence of the Gibbs and Helmholtz ensembles for the zipper model.

By using Eqs.(5.16) and (5.52), we can obtain the force-extension relation under isometric conditions for the zipper model. A refined analysis of this relation for large values of N, developed by means of the stationary phase method, is discussed in Appendix 5.8.4, where one can find the rigorous demonstration of the equivalence of the Gibbs and Helmholtz ensembles and the following simplified expression written in terms of the average chain stretch $\bar{\lambda} = \frac{x_N}{\ell N}$

$$\langle \tilde{f} \rangle = \frac{\mathcal{C}_N \left[e^{\Delta g_0 N} (\bar{\lambda} - 1) \tilde{k}^{\frac{1}{2}} + e^{\Delta g_1 N} (\bar{\lambda} - \chi)(\alpha \tilde{k})^{\frac{3}{2}} \right] + \tilde{f}_M}{\mathcal{C}_N \left[\sqrt{\tilde{k}}\, e^{\Delta g_0 N} + \sqrt{\alpha \tilde{k}}\, e^{\Delta g_1 N} \right] + 1}, \tag{5.53}$$

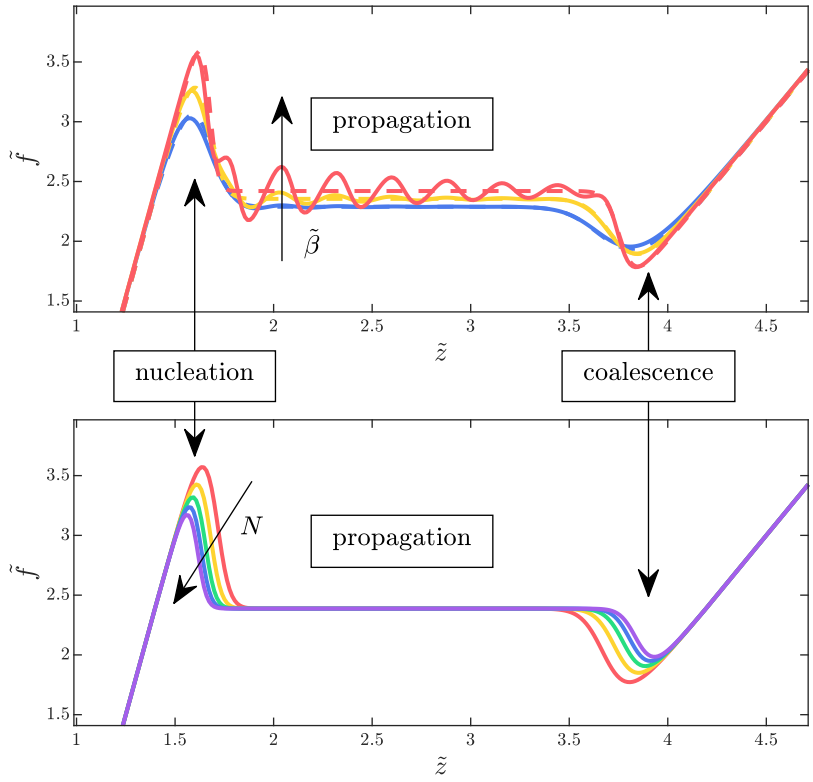

Figure 5.10: Top panel: Comparison between the isometric force-extension response of the exact zipper model, obtained by the partition function in Eq.(5.52) (solid lines), and the result of the stationary phase method, stated in Eq.(5.53) (dashed lines). We considered different values of the Ising dimensionless parameter $\tilde{\beta} = \{1, 1.5, 3\}$. Adopted parameters: $N = 10$, $\tilde{k} = 6$, $\tilde{h} = 2$, $\alpha = 1/3$, $\tilde{Q}(-1) = 0$, $\tilde{Q}(+1) = \Delta\tilde{E} = 6$, $\chi = 3$. Bottom panel: Evolution of the isometric force-extension curve, stated in Eq.(5.53) as obtained by the stationary phase method, with an increasing number N of units. Adopted parameters: $\tilde{k} = 6$, $\tilde{h} = 2$, $\alpha = 1/3$, $\tilde{Q}(-1) = 0$, $\tilde{Q}(+1) = \Delta\tilde{E} = 6$, $\chi = 3$, $\tilde{\beta} = 2$, $N = \{8, 10, 12, 14, 16\}$.

where

$$\Delta g_0 = -\frac{\tilde{\beta}\tilde{k}}{2}\left[\bar{\lambda} - \left(1 + \frac{\tilde{f}_M}{\tilde{k}}\right)\right]^2, \tag{5.54}$$

$$\Delta g_1 = -\frac{\tilde{\beta}\alpha\tilde{k}}{2}\left[\bar{\lambda} - \left(\chi + \frac{\tilde{f}_M}{\alpha\tilde{k}}\right)\right]^2, \tag{5.55}$$

$$\mathcal{C}_N = \frac{2e^{2\tilde{\beta}} - 1}{2}\sqrt{\frac{\tilde{\beta}}{2\pi N}}\left[\chi + \frac{\tilde{f}_M}{\alpha\tilde{k}} - \left(1 + \frac{\tilde{f}_M}{\tilde{k}}\right)\right]. \tag{5.56}$$

This important analytical expression for the force-extension relation contains all the physical features describing the Helmholtz ensemble, as the first nucleation peak and the coalescence one. In particular, it can be used to evaluate these peaks as a function of N and the temperature T.

In the top panel of Fig.5.10, we compare the force-extension curves obtained through the

exact zipper model with the ones delivered by the stationary phase method. Observe that while this approximation, stated in Eqs.(5.53), is finer as N grows, our results show the possibility of a good approximation of just the nucleation peak already for small values of N (we used $N = 10$ in Fig.5.10, top panel). Also, the approximation correctly reproduces the last downward peak, corresponding to the coalescence of the remaining folded regions to the fully unfolded phase. The most important result, quite evident in this framework, is the dependence of the Maxwell (propagation) force on the temperature, through the parameter $\tilde{\beta}$. We observe that for the represented case with $\alpha < 1$ (softening) as $\tilde{\beta}$ decreases (*e.g.* temperature increases), the value of the propagation force f_M decreases, also affecting the height and the width of the nucleation and coalescence peaks with an entropic stabilization of the unfolded phase.

In the bottom panel of Fig.5.10, we observe that, when the number of units N increases and the thermodynamic limit is approached, the mechanical response of the system in the Helmholtz ensemble (see Eq.(5.53)) approaches the Gibbs behavior, where there is a force plateau without nucleation and coalescence force peaks. In particular, we notice that by means of the stationary phase method (when $N \to \infty$), the typical saw-tooth path of the isometric condition disappears whereas only the first and the last peaks remain, as expected from a macroscopic point of view. We remark that, in experiments and simulations of phase transformations in nanowires or other nanostructures, it is possible to observe only the first nucleation peak, while the last one is rarely attained because of the breaking of the specimen or because of the boundary effects induced by the grips of the traction device.

Given the importance of the first nucleation force peak, we now look for an explicit expression of its magnitude. Consider Eq.(5.53) and observe that in the region of the first peak only the term $e^{\Delta g_0 N}$ is relevant, being $e^{\Delta g_1 N}$ negligible. Then, we can write a reduced form of Eq.(5.53), as follows

$$\langle \tilde{f} \rangle = \tilde{k} \frac{\sqrt{\tilde{k}} \mathcal{C}_N \, e^{-\frac{\tilde{\beta}\tilde{k}}{2} N \mathrm{y}^2} \left(\mathrm{y} + \frac{\tilde{f}_M}{\tilde{k}} \right) + \tilde{f}_M}{\sqrt{\tilde{k}} \mathcal{C}_N \, e^{-\frac{\tilde{\beta}\tilde{k}}{2} N \mathrm{y}^2} + 1}, \tag{5.57}$$

where we introduced the change of variable $\mathrm{y} = \bar{\lambda} - 1 - \frac{\tilde{f}_M}{\tilde{k}}$. Now, let us consider as reference for the force its Maxwell value, so as to obtain

$$\langle \tilde{f} \rangle - \tilde{f}_M = \tilde{k} \mathrm{y} \frac{\sqrt{\tilde{k}} \mathcal{C}_N \, e^{-\frac{\tilde{\beta}\tilde{k}}{2} N \mathrm{y}^2}}{\sqrt{\tilde{k}} \mathcal{C}_N e^{-\frac{\tilde{\beta}\tilde{k}}{2} N \mathrm{y}^2} + 1}. \tag{5.58}$$

We search for the stationary point of Eq.(5.58) by derivation, easily obtaining

$$\left(\frac{\tilde{\beta}\tilde{k}}{2} N \mathrm{y}^2 - \frac{1}{2} \right) e^{\frac{\tilde{\beta}\tilde{k}}{2} N \mathrm{y}^2 - \frac{1}{2}} = \frac{\mathcal{C}_N}{2} \sqrt{\frac{\tilde{k}}{e}}, \tag{5.59}$$

which is a Lambert equation of the form $\mathrm{w} e^{\mathrm{w}} = \mathrm{s}$, solved by $\mathrm{w} = \mathrm{W}_0(\mathrm{s})$, where W_0 is the Lambert function (more precisely, W_0 is the principal branch of the Lambert function) [322, 323]. Thus, we may write

$$\frac{\tilde{\beta}\tilde{k}}{2} N \mathrm{y}^2 - \frac{1}{2} = \mathrm{W}_0 \left(\frac{\mathcal{C}_N}{2} \sqrt{\frac{\tilde{k}}{e}} \right). \tag{5.60}$$

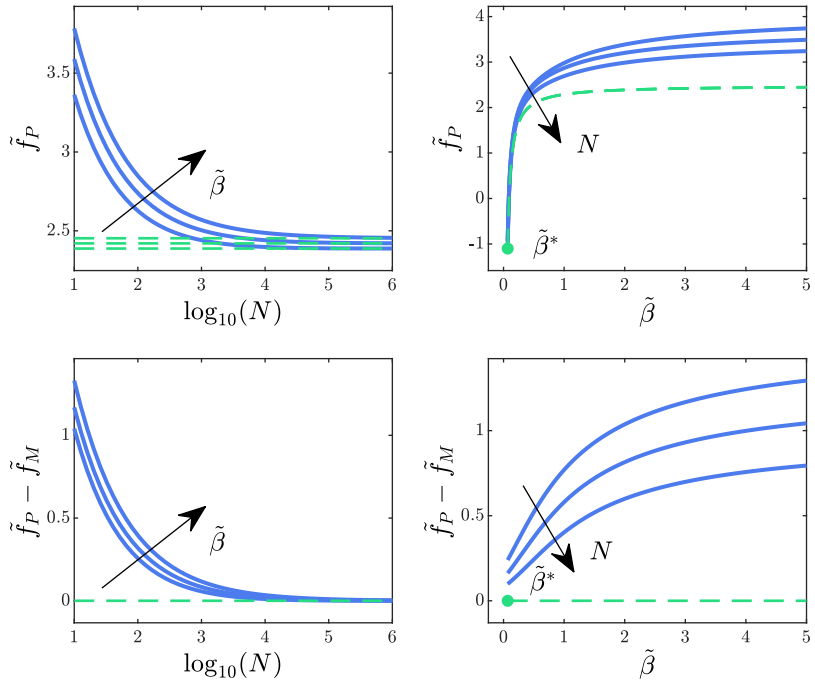

Figure 5.11: Behavior of the nucleation force peak as a function of the number N of units of the chain and of $\tilde{\beta}$. First row: $\tilde{f}_P$ versus $\log_{10}(N)$, parametrized by $\tilde{\beta} = \{2,3,6\}$, and $\tilde{f}_P$ versus $\tilde{\beta}$, parametrized by $N = \{10,15,25\}$. The green dashed lines correspond to $\tilde{f}_M$, and $\tilde{\beta}^*$ is the critical value corresponding to $\tilde{f}_F$ (floor force with $\alpha < 1$). Second row: $\tilde{f}_P - \tilde{f}_M$ versus $\log_{10}(N)$, parametrized by $\tilde{\beta} = \{2,3,6\}$, and $\tilde{f}_P - \tilde{f}_M$ versus $\tilde{\beta}$, parametrized by $N = \{10,15,25\}$. Here, the green dashed lines correspond to zero. We adopted the parameters $\tilde{k} = 6$, $\tilde{h} = 2$, $\tilde{Q}(-1) = 0$, $\tilde{Q}(+1) = \Delta\tilde{E} = 6$, and $\chi = 3$. The arrows indicate the direction in which $\tilde{\beta}$ and N increase.

Eventually, by using Eq.(5.60) in Eq.(5.58) we get

$$\tilde{f}_P - \tilde{f}_M = \frac{\tilde{k}}{\sqrt{\frac{\tilde{\beta}\tilde{k}}{2}N}} \frac{\mathrm{W}_0\left(\frac{\mathcal{C}_N}{2}\sqrt{\frac{\tilde{k}}{e}}\right)}{\sqrt{\frac{1}{2}+\mathrm{W}_0\left(\frac{\mathcal{C}_N}{2}\sqrt{\frac{\tilde{k}}{e}}\right)}}, \tag{5.61}$$

where $\tilde{f}_P$ is the value of the nucleation force peak. It is worth remarking that Eq.(5.61) gives the explicit dependence of the force peak on both $\tilde{\beta}$ and the number of units of the chain N.

In the first row of Fig.5.11, we study the nucleation peak with respect to N (parametrized by $\tilde{\beta}$) and with respect to $\tilde{\beta}$ (parametrized by N). Similarly, in the second row, we show the plots of $\tilde{f}_P - \tilde{f}_M$. The trend can be summarized by stating that $\tilde{f}_P - \tilde{f}_M$ increases for increasing values of $\tilde{\beta}$ and decreases for increasing values of N. Moreover, $\tilde{f}_P$ converges to $\tilde{f}_M$ in the thermodynamic limit.

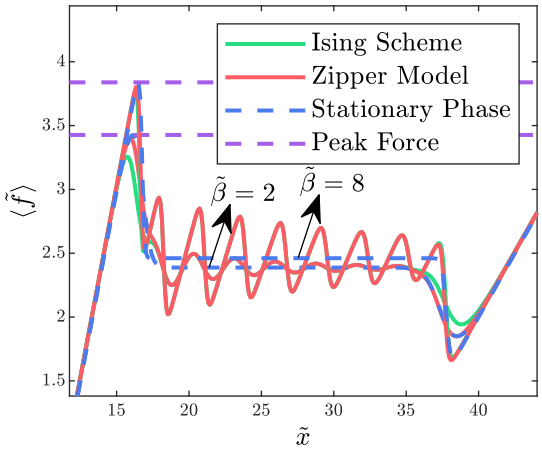

Figure 5.12: Comparison of the force-extension relation observed within the Helmholtz ensemble and obtained with (i) the Ising scheme, (ii) the zipper model, and (iii) the stationary phase approximation. Also, the amplitude of the first nucleation peak calculated by Eq.(5.61) is shown. Adopted parameters: $N = 10$, $\tilde{k} = 6$, $\tilde{h} = 2$, $\tilde{Q}(-1) = 0$, $\tilde{Q}(+1) = \Delta\tilde{E} = 30$, $\chi = 3$, $\tilde{\beta} = \{2, 8\}$.

The consistency of the approaches presented in this work can be appreciated by observing Fig.5.12. Here, we compare the force-extension relation evaluated within the Helmholtz ensemble and obtained with (i) the complete Ising scheme discussed in Section 5.2.2, (ii) the simplified zipper model introduced in Section 5.4.2, and (iii) the stationary phase approximation given in Eq.(5.53). Moreover, we also show the amplitude of the first peak calculated by Eq.(5.61). This plot proves that, for a sufficiently large value of N and with the hypothesis of strong ferromagnetic interactions (large values of $\tilde{\beta}$), the three frameworks give the same results and hence the hypothesis introduced are consistent with the problem under investigation.

5.6 Applications to the tensile behavior of nanowires

While, as pointed out earlier, our model can be applied to different multistable systems with softening or hardening effects (*i.e.* with different stiffness of the different phases) and non-local

interactions, we here focus our attention on the specific application to phase transition in metallic nanowires. We can show the ability of the model to predict the main physical phenomena observed during the phase transition at variable temperatures. Single-crystalline metal nanowires with nanometric cross-section can exhibit a pseudo-elastic behavior characterized by very large elongations which can be up to 50% of the original length [230–233]. This behavior, which is exceptional compared to all other shape memory alloys, is due to a reversible lattice reorientation process with twin boundary propagation between two differently oriented face-centered cubic (FCC) crystalline structures. This behavior is typical of Copper (Cu) and Nickel (Ni), where we can identify the two following configurations: the original one named $< 110 > / \{111\}$ with axis $< 110 >$ and surfaces $\{111\}$, and the deformed one named $< 001 > / \{100\}$ with axis $< 001 >$ and surfaces $\{100\}$, as shown *e.g.* in Figs.2 and 3 of Ref.[230].

To compare the behavior with our one-dimensional system, let s be the area on the cross-section pertaining to a single longitudinal chain of atoms in the nanowire crystal structure. Let then M be the average number of atoms in the cross-section so that the total area is given by $S = Ms$. Similarly, we use ℓ to indicate roughly the lattice constant of the crystal structure, and hence $L = N\ell$ is the total nanowire length, being N the number of atoms in the longitudinal direction. Accordingly, SL is the total volume of the system, MN is the total number of atoms, $s\ell$ is the average volume pertaining to one atom, and one can observe also that $s \simeq \ell^2$ and $s\ell \simeq \ell^3$.

It is important to remark that both the Maxwell force in Eqs.(5.30) and the force-extension relation in Eq.(5.53), have been obtained for a single chain of units (here atoms) and therefore the continuous parameters must be introduced as follows. We define

$$E_f = \frac{k_0 \ell}{s} \text{ [GPa]}, \quad E_u = \frac{h_0 \chi \ell}{s} \text{ [GPa]}, \tag{5.62}$$

the Young moduli of the folded (f) and unfolded (u) phases, respectively. Accordingly, k_0 and h_0 are the elastic constants of the two crystals in the harmonic limit. Moreover, the jump energy between the two configurations can be written as $\Delta E = s\ell \Delta e$ where Δe [J/m^3] is the energy density difference between the two crystal states. In addition, the Ising energy can be rewritten as $J = \Lambda\, s$, where Λ [J/m^2] is the surface energy density of the twin boundary separating original and deformed crystals. We remark that the parameters Δe and Λ may depend on the total area S when elastic surface effects are relevant, as in the case of metallic nanowires. Further, the longitudinal (normal) stress is defined by $\sigma = \langle f \rangle / s$, with $\langle f \rangle$ given in Eq.(5.53) if we consider the stationary phase approximation. The strain is defined as $\bar{\varepsilon} = \frac{x - N\ell}{N\ell}$, and therefore we have $\bar{\varepsilon} = \bar{\lambda} - 1$.

We use the introduced continuous quantities to rewrite previous expressions, for the purpose of mimicking the tensile behavior of one-dimensional structures. Indeed, Eqs.(5.30) and (5.28) can be rewritten as

$$\frac{1}{2} \log \left(\frac{E_f}{E_u} \chi \right) + \beta s \ell \left[\sigma_M (\chi - 1) + \frac{1}{2} \sigma_M^2 \left(\frac{\chi}{E_u} - \frac{1}{E_f} \right) - \Delta e \right] = 0, \tag{5.63}$$

that is used to obtain the temperature-dependent Maxwell stress σ_M. We observe that, due to the hypothesis of homogeneity in the cross-section, the specific response of the wire coincides with that of a longitudinal chain of atoms. Correspondingly, the nucleation stress can be defined, using Eq.(5.61) as follows

$$\sigma_P - \sigma_M = \sqrt{\frac{2E_f}{\beta s \ell N}} \frac{\mathrm{W}_0(C)}{\sqrt{\frac{1}{2} + \mathrm{W}_0(C)}}, \tag{5.64}$$

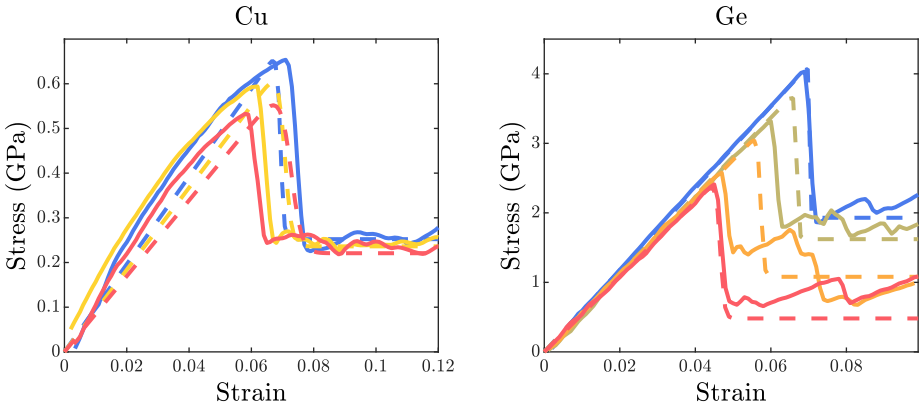

Figure 5.13: Comparison of the stress-strain curves obtained with molecular dynamic simulations (solid lines) and through our theoretical approach (dashed lines) for Cu nanowires (1.96 nm $\times$ 1.96 nm) in the left panel and Ge nanowires (radius of 1.8 Å) in the right panel. In the left panel, we used the temperatures T=100 K (blue lines), T=200 K (yellow lines), and T=300 K (red lines). In the right panel, we used the temperatures T=100 K (blue lines), T=200 K (green lines), T=300 K (yellow lines), and T=400 K (red lines).

where $C = \frac{\mathcal{C}_N}{2}\sqrt{\frac{\tilde{k}}{e}}$ is, by using (5.56), given by

$$C = \frac{2e^{2\beta\Lambda s}-1}{2}\left[\chi - 1 + \sigma_M\left(\frac{\chi}{E_u} - \frac{1}{E_f}\right)\right]\sqrt{\frac{\beta s \ell E_f}{2eN}}. \tag{5.65}$$

Moreover, by recalling the definition of $\beta = 1/(K_B T)$, we introduce also the the parameterizations

$$\Delta e = \gamma \frac{K_B T_0}{s\ell}, \qquad \Lambda = \tilde{\beta}_o \frac{K_B T_0}{s} \tag{5.66}$$

to obtain the two values of the characteristic energies. Here, we use the reference temperature $T_0 = 300$ K.

In Ref.[230] a series of molecular dynamics simulations have been performed to obtain the stress-strain behavior of Cu nanowires at different temperatures and under quasi-static tensile deformation, which is compatible with our equilibrium statistical mechanics approach. The simulations are based on the embedded-atom-method interatomic potential for Cu [230], and the uniaxial displacement-controlled loading strategy is applied coherently with our Helmholtz ensemble. The stress-strain behaviors of this Cu nanowire (1.96 nm $\times$ 1.96 nm section) at temperatures of 100, 200, and 300 K is compared with our model in Fig.5.13, left panel. The theoretical results are based on the stationary phase approximation stated in Eq.(5.53). As one can see, the model is able to reproduce the magnitude of both the nucleation stress and the Maxwell stress plateau. In Table 5.1, one can find the temperature-dependent Young moduli we adopted to reproduce the simulations of Ref.[230]. Moreover, we adopt the following parameters: $N = 206$, $\ell = 0.14$ nm, $s = \ell^2$ and $\chi = 4.4$. By introducing the parameterizations in Eq.(5.66), we obtained the adimensional values $\gamma = 7.7$ and $\tilde{\beta}_0 = 6.8$. We remark that since $\tilde{\beta}_0$, representing our adimensional parameter $\tilde{\beta}$ for the higher value of the temperatures, is sufficiently larger than 1, the use of the zipper model, simplified by the stationary phase method, is justified. Moreover, the propagation of a single twin boundary is confirmed by the simulations in Ref.[230].

Young modulus	Value
$E_f(T = 100\text{K})$	122 GPa
$E_f(T = 200\text{K})$	114 GPa
$E_f(T = 300\text{K})$	105 GPa
$E_u(T = 100\text{K})$	10 GPa
$E_u(T = 200\text{K})$	11 GPa
$E_u(T = 300\text{K})$	12 GPa

Table 5.1: Mechanical parameters used to reproduce the molecular dynamics simulations on a Cu nanowire of Ref.[230].

Young modulus	Value
$E_f(T = 100\text{K})$	588 GPa
$E_f(T = 200\text{K})$	561 GPa
$E_f(T = 300\text{K})$	552 GPa
$E_f(T = 400\text{K})$	540 GPa
$E_u(T = 100\text{K})$	23 GPa
$E_u(T = 200\text{K})$	43 GPa
$E_u(T = 300\text{K})$	63 GPa
$E_u(T = 400\text{K})$	83 GPa

Table 5.2: Mechanical parameters used to reproduce the molecular dynamics simulations on a Ge ultra-thin nanowire of Ref.[234].

We also propose a second example for the application of our model to ultrathin semiconductor Germanium (Ge) nanowires that have been recently studied due to their peculiar properties. Here, we compare our results with molecular dynamics simulations of the helix Ge nanowire with a radius of 1.8 Å(see Fig.1 in Ref.[234]). The stress-strain curves have been obtained for temperatures of $100, 200, 300$, and 400 K [234]. The simulations for germanium were based on the Stillinger-Weber potential, coupled with the Nosé-Hoover thermostat to impose the system temperature. In Fig. 5.13, right panel, we show the comparison of the simulations with our model, and we observe that the nucleation and Maxwell stresses are in fairly good agreement. Unfortunately, the numerical stress plateaus are rather noisy because they correspond to a single simulation (without averaging) and the amorphous phase is strongly fluctuating. Anyway, the temperature-dependent behavior of such plateaus is clearly visible. The helical structure is perfectly ordered initially (see Fig.1 in Ref.[234]), and shows a transition to an amorphous structure (see Fig.5 in Ref.[234]) following a transition process that begins with a stress peak, namely the nucleation stress. After this nucleation, the unfolded region evolves 'smoothly' into the one-atom chain structure. In our theoretical formulation, we used the parameters listed in Table 5.2 corresponding to the data in Ref. [234]. Moreover, we adopted the parameters: $N = 5562$, $\ell = 0.208$ nm, $s = \ell^2$ and $\chi = 3.36$. In particular, by introducing the parameterizations in Eq.(5.66), we obtained the adimensional values $\gamma = 2.3$ and $\tilde{\beta}_0 = 25.3$ (or $\tilde{\beta} = 19$ in the case of highest temperature $T = 400K$) so that the assumption of the zipper model is widely justified.

To summarize our results, we considered systems where two possible configurations exist here. In the first application, they correspond to two different crystal structures whereas in the second example to a regular helical structure and an irregular amorphous structure. It is worth noticing that the model based on statistical mechanics here developed is able to reproduce the

complex behavior of these systems. It is important to highlight that in our model there is no crystallographic or morphological information on the three-dimensional structures, instead, the particular microstructures are embedded in the elastic and energetic properties of the system. Thus the model captures the main physical behavior in terms of nucleation and propagation stress and their dependence on temperature, without exploiting the microstructural details. Nevertheless, the generality of the model allows its application to different systems ranging from material science to cooperative biological structures. Of course, if it is necessary to take into account crystallographic details, structural anisotropies, twin-boundary geometries, and other morphological features, then it is necessary to turn to another class of models that are specifically adapted to the problem at hand, *e.g.* the model in Ref.[230] for the pseudo-elasticity of metallic nanowires. On the other hand, the possibility of deducing explicit equations of the temperature dependence of the nucleation and propagation stress, depending on parameters with a clear physical interpretation, represents in our opinion the main advantage of the proposed model both in the perspectives of interpreting the transition behavior of biological materials and phase transition alloys and in the field of new material design.

5.7 Conclusions

In this work, we elaborated some models, with different levels of complexity, to describe the temperature-dependent behavior of one-dimensional non-local non-convex systems. The paradigmatic system under investigation is composed of a sequence of units, exhibiting a bistable behavior described by a two-state potential energy, in interaction with each other. On the one hand, this scheme is able to represent the specific feature of several macromolecules of biological origin (mainly proteins). In this case, the non-convexity (bistability) describes the possible switching of each domain of the macromolecule between its folded and unfolded states. In addition, the non-locality, introduced by means of the Ising scheme, depicts the cooperativity observed in most of the biological structures. On the other hand, the proposed model is equally able to represent the phase transformations in materials. The two states of the bistable behavior represent in this case two microstructures of the solid material, corresponding *e.g.* to two crystal structures or to austenitic and martensitic phases. This enables the study of pseudo-elasticity and shape memory effects in solid systems such as whiskers, nanowires, or nanocomposites. For these systems, the Ising interaction scheme reproduces the energy cost of creating an interface between the two different states of matter due to the absence of kinematic compatibility. Our model then describes in a prototypical way the origin of the nucleation, propagation, and, possibly, coalescence phenomena and their possible dependence on temperature when small dimensions are considered as in the case of nanowires so that entropic contributions can compete with bulk elastic energy terms.

Indeed, in the proposed approach, the thermal effects are carefully considered by introducing the statistical mechanics' analysis of the problem, based on the method of the spin variables. This allows us to develop a complete thermodynamic framework of the transformation processes in systems with non-locality and non-convexity. The first proposed approach is the most refined and implements the complexity of the system in its entire generality, without simplifying assumptions. The system is constituted by a chain of bistable elements interacting through an Ising scheme. We can study both the Gibbs (isotensional) and the Helmholtz (isometric) ensembles of the statistical mechanics by evaluating the pertinent partition functions in closed form. These results are valid for both the ferromagnetic (positive Ising interaction) and antiferromagnetic cases (negative Ising interaction). However, in this work, we mainly focus on ferromagnetic behavior. In this model, each unit can freely assume one of the two admitted states, depending on the system

temperature and on the mechanical actions applied to the system. The number of interfaces between folded and unfolded regions is therefore free to vary and represents a measure of the entropic effects on the system. Hence, we can observe an increase in the number of interfaces with increasing temperature for a ferromagnetic system. The important point is that for strongly ferromagnetic systems (with a high energetic cost of interface generation), which are the most common in practical applications, only one interface is observed between the two different states and it propagates along the chain when the traction or elongation are applied to the system. In addition to the interface propagation phenomenon, in the isometric Helmholtz case, we can also observe an initial upward peak of force, representing the nucleation of the new unfolded phase, and a final downward peak of force, representing the coalescence of the folded phase into the unfolded one. An important feature of this system is that the force plateau, describing the interface propagation within the chain is in general temperature dependent for both isotensional and isometric boundary conditions. The origin of this dependence lies in the difference between the elastic constants of the unfolded and folded phases. In fact, when these elastic constants are equal, the force plateau becomes independent of temperature and known results from the literature are retrieved.

Since the thermodynamic limit analysis is extremely complex for the exact Ising model (in particular, for the isometric case), and since the important case for applications is the strongly ferromagnetic one, we have introduced the zipper model where we consider only one interface propagating along the system. This assumption makes the calculation of the partition function much simpler in both the Gibbs and the Helmholtz ensembles. The thermodynamic limit for the Gibbs ensemble can be analyzed straightforwardly and the results are perfectly coherent with the exact Ising model studied previously. In particular, the temperature-dependent behavior of the force plateau is confirmed also by means of this zipper approach.

The investigation of the thermodynamic limit concerning the zipper model under isometric condition, *i.e.* within the Helmholtz ensemble, represents the third approach of this work. This analysis is based on the stationary phase method and it is useful to obtain three important results: (i) a simplified expression of the force-extension relation under isometric conditions valid for very long and strongly ferromagnetic chains (which perfectly describes the nucleation, propagation, and coalescence phenomena), (ii) an explicit expression for the amplitude of the first force peak (based on the Lambert function), representing the nucleation of unfolded units, and (iii) a rigorous demonstration of the equivalence of the Gibbs and Helmholtz ensembles for the zipper model (nucleation and coalescence peaks disappear as length increases). These results, based on the stationary phase approximation, properly describe the transformation processes in one-dimensional objects (macromolecules or solid nanowires) in terms of thermal fluctuations and mechanical actions applied to the system. Some examples of quantitative comparisons are shown for the microstructural evolution in metallic and semiconductor nanowires.

Although this work could be generalized and expanded in many ways, we mention here only two future perspectives of some interest. The first neglected aspect represents the real microstructure of the considered metastable states. This point can be improved by introducing the main properties of the real molecular structures of the two phases of the system. The second aspect concerns the fact that we have carried out the entire discussion at thermodynamic equilibrium and therefore under static or quasi-static conditions. The dynamics could be introduced by taking into account the non-equilibrium statistical mechanics and, in particular, the Langevin and/or Fokker-Planck methodologies. Both issues will be addressed in future developments.

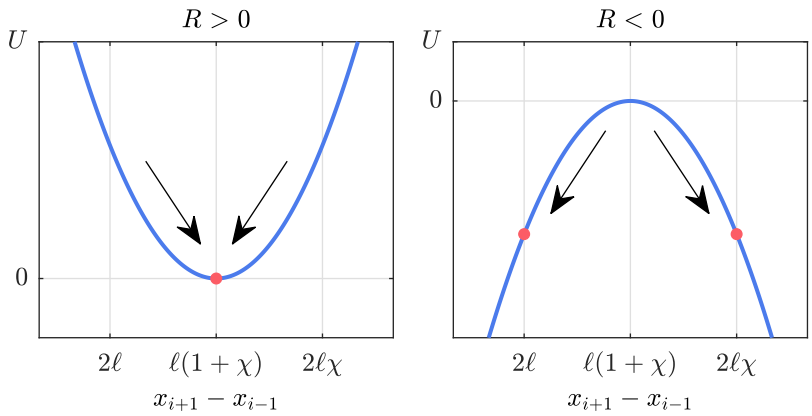

Figure 5.14: Potential energy U of a linear spring representing an arbitrary NNN element. The two cases correspond to the antiferromagnetic ($R>0$) and ferromagnetic ($R<0$) behaviors of the chain with the NNN linear elastic elements.

5.8 Appendix

5.8.1 Non-local behavior: relation between the next to nearest neighbor (NNN) interaction strategy and the Ising scheme

The non-local interactions in discrete elastic chains are typically introduced through next to nearest neighbor (NNN) elastic elements [24, 165]. Under specific hypotheses, we prove here that the scheme with the NNN elements can be reconducted to a typical Ising model, widely adopted in previous studies on similar topics [102, 295]. To begin with, we consider a chain of bistable units with additional NNN linear springs to model non-local effects [165]. The Hamiltonian reads

$$\begin{aligned} H = &\sum_{i=1}^{N} \left\{ Q(S_i) + \frac{K(S_i)\ell^2}{2} \left[\lambda_i - \lambda_0(S_i)\right]^2 \right\} \\ &+ \sum_{i=1}^{N-1} \frac{R\ell^2}{2} \left[\lambda_{i+1} + \lambda_i - \lambda_0(-1) - \lambda_0(+1)\right]^2, \end{aligned} \tag{5.67}$$

where R is the elastic constant of the NNN springs, and the other quantities are defined in Section 5.2. In particular, we name here H_0 the energy corresponding to the bistable nearest neighbor (NN) elements and H_I the energy of the NNN linear springs, such that $H = H_0 + H_I$. We assume that the equilibrium length of the NNN elements is fixed at $L(-1) + L(+1) = (1+\chi)\ell$, and we introduce two different behaviors: an antiferromagnetic one when $R>0$, and a ferromagnetic one when $R<0$. In the former case ($R>0$), two adjacent units entail a lower energy if they are in two different states (folded and unfolded) while, in the latter one ($R<0$), two adjacent units result in a lower energy if they are in the same state (either both folded or both unfolded), as shown in Fig.5.14.

Supposing that the elastic constants k and αk are sufficiently large, the Hamiltonian H_I can be simplified by assuming that the lengths of the units can be approximated with the equilibrium lengths of the explored wells. Then, by using the relations $\lambda_{i+1} \simeq \lambda_0(S_{i+1})$ and $\lambda_i \simeq \lambda_0(S_i)$, we

get

$$\lambda_{i+1}+\lambda_i \simeq \lambda_0(S_{i+1})+\lambda_0(S_i) = -\frac{S_{i+1}}{2}(1-\chi)-\frac{S_i}{2}(1-\chi)+(1+\chi). \tag{5.68}$$

Thus, the interaction Hamiltonian becomes

$$\begin{aligned} H_I &\simeq \sum_{i=1}^{N-1}\frac{R\ell^2}{2}\left[-\frac{(1-\chi)}{2}(S_{i+1}+S_i)\right]^2 \\ &= \frac{R}{4}\ell^2(1-\chi)^2(N-1) - J\sum_{i=1}^{N-1} S_{i+1}S_i, \end{aligned} \tag{5.69}$$

where

$$J = -\frac{R}{4}\ell^2(1-\chi)^2. \tag{5.70}$$

This proves that we can approximate the behavior of the chain with the NNN elements by means of a classical Ising chain. We observe that when $J>0$ ($R<0$) we are in a ferromagnetic case, and when $J<0$ ($R>0$) in the antiferromagnetic one. For this reason, in this work, we adopted the overall Hamiltonian given by Eq.(5.4), where we neglected the irrelevant constant in H_I.

5.8.2 Partition function for the Gibbs ensemble

For the Gibbs ensemble, using Eq.(5.5), the partition function can be evaluated as

$$\begin{aligned} Z_G(\tilde{f}) &= \ell^N \sum_{\{S_i\}} \int_{\mathbb{R}^N} e^{-\tilde{\beta}(\tilde{H}-\tilde{f}\sum_{i=1}^N \lambda_i)} \mathrm{d}\lambda_1 \ldots \mathrm{d}\lambda_N \\ &= \ell^N \sum_{\{S_i\}} e^{-\tilde{\beta}\left(\sum_{i=1}^N \tilde{Q}(S_i) - \sum_{i=1}^{N-1} S_i S_{i+1}\right)} \\ &\quad \times \int_{\mathbb{R}^N} e^{\tilde{\beta}\sum_{i=1}^N \left[\frac{\tilde{K}(S_i)}{2}(\lambda_i-\lambda_0(S_i))^2 - \tilde{f}\lambda_i\right]} \mathrm{d}\lambda_1 \ldots \mathrm{d}\lambda_N, \end{aligned} \tag{5.71}$$

where $\tilde{f}$ is the dimensionless force applied to the last unit of the chain. Each sum on S_i ($i=1,\ldots,N$) must be interpreted as a sum over the values $+1$ and -1. By a Gaussian integration, we obtain

$$Z_G(\tilde{f}) = \ell^N \sum_{\{S_i\}} e^{\tilde{\beta}\sum_{i=1}^{N-1} S_i S_{i+1}} \prod_{i=1}^N \sqrt{\frac{2\pi}{\tilde{\beta}\tilde{K}(S_i)}} e^{\tilde{\beta}\left(\frac{\tilde{f}^2}{2\tilde{K}(S_i)} + \lambda_0(S_i)\tilde{f} - \tilde{Q}(S_i)\right)}. \tag{5.72}$$

We can define

$$c(S_i) = \sqrt{\frac{2\pi}{\tilde{\beta}\tilde{K}(S_i)}} e^{\tilde{\beta}\left(\frac{\tilde{f}^2}{2\tilde{K}(S_i)} + \lambda_0(S_i)\tilde{f} - \tilde{Q}(S_i)\right)}, \tag{5.73}$$

so that we obtain

$$Z_G(\tilde{f}) = \ell^N \sum_{\{S_i\}} \sqrt{c(S_1)} \left[\prod_{i=1}^{N-1} e^{\tilde{\beta}S_i S_{i+1}} \sqrt{c(S_i)c(S_{i+1})}\right] \sqrt{c(S_N)}. \tag{5.74}$$

In order to explicitly evaluate the summation we can use the transfer matrix method [302]. We obtain

$$Z_G(\tilde{f}) = \boldsymbol{w}^\intercal \boldsymbol{T}^{N-1} \boldsymbol{w}, \tag{5.75}$$

where we have defined the transfer matrix $\boldsymbol{T}$ and the vector $\boldsymbol{w}$ (taking care of the boundary conditions) as follows

$$\boldsymbol{T} = \begin{pmatrix} e^{\tilde{\beta}} c_- & e^{-\tilde{\beta}} \sqrt{c_+ c_-} \\ e^{-\tilde{\beta}} \sqrt{c_+ c_-} & e^{\tilde{\beta}} c_+ \end{pmatrix}, \tag{5.76}$$

$$\boldsymbol{w} = \begin{pmatrix} \sqrt{c_-} \\ \sqrt{c_+} \end{pmatrix}, \tag{5.77}$$

with, see Eq.(5.73),

$$c_+ \triangleq c(+1), \quad c_- \triangleq c(-1). \tag{5.78}$$

By using the standard matrix functions theory [324, 325], we have

$$\boldsymbol{T}^{N-1} = \frac{\hat{\lambda}_1^{N-1} - \hat{\lambda}_2^{N-1}}{\hat{\lambda}_1 - \hat{\lambda}_2} \boldsymbol{T} + \frac{\hat{\lambda}_1 \hat{\lambda}_2^{N-1} - \hat{\lambda}_1^{N-1} \hat{\lambda}_2}{\hat{\lambda}_1 - \hat{\lambda}_2} \boldsymbol{I}, \tag{5.79}$$

where $\boldsymbol{I}$ is the 2×2 identity matrix and $\hat{\lambda}_{1,2}$ are the eigenvalues of $\boldsymbol{T}$, namely

$$\begin{aligned} \hat{\lambda}_{1,2} &= \frac{e^{\tilde{\beta}}}{2} \left[c_+ + c_- \pm \sqrt{(c_+ - c_-)^2 + 4 c_+ c_- e^{-4\tilde{\beta}}} \right] \\ &= \frac{e^{\tilde{\beta}}}{2} \left(c_+ + c_- \pm \sqrt{\Delta} \right). \end{aligned} \tag{5.80}$$

In Eq.(5.80), $\hat{\lambda}_1$ ($\hat{\lambda}_2$) corresponds to the $+$ ($-$) sign and we have also defined

$$\Delta = (c_+ - c_-)^2 + 4 c_+ c_- e^{-4\tilde{\beta}}. \tag{5.81}$$

By substituting $\hat{\lambda}_{1,2}$ into Eq.(5.75) and Eq.(5.79), we get the partition function given in Eq. (5.8).

5.8.3 Partition function for the Helmholtz ensemble

We consider here the case with fixed x_N (isometric condition), described by the Helmholtz ensemble, and evaluate the canonical partition function $Z_H(x_N)$. The partition functions in the Gibbs and Helmholtz ensembles are linked by a Laplace transform [98]

$$Z_G(f) = \int_{-\infty}^{+\infty} Z_H(x_N) \, e^{\beta f x_N} \, \mathrm{d}x_N. \tag{5.82}$$

Thus, one can write $Z_H(x_N)$, using the change of variable $f \to -i\omega/\beta$, as an inverse Fourier transform in the complex plane

$$Z_H(x_N) = \frac{1}{2\pi} \int_{-\infty}^{+\infty} Z_G \left(-\frac{i\omega}{\beta} \right) e^{i\omega x_N} \, \mathrm{d}\omega. \tag{5.83}$$

To simplify the notation and perform the calculation we define

$$\delta_{1,2} = e^{-\tilde{\beta}}\,\hat{\lambda}_{1,2} = \frac{1}{2}\left(c_+ + c_- \pm \sqrt{\Delta}\right). \tag{5.84}$$

Thus, the Gibbs partition function can be written as

$$Z_G(\tilde{f}) = \frac{(\ell e^{\tilde{\beta}})^N}{2\cosh\tilde{\beta}}\left[\delta_1^N\left(1 + e^{-2\tilde{\beta}}\frac{\delta_1+\delta_2}{\delta_1-\delta_2}\right) + \delta_2^N\left(1 - e^{-2\tilde{\beta}}\frac{\delta_1+\delta_2}{\delta_1-\delta_2}\right)\right]. \tag{5.85}$$

By using the Newton binomial rule to expand the powers δ_1^N and δ_2^N, we find

$$\begin{aligned} Z_G(\tilde{f}) = \left(\frac{\ell e^{\tilde{\beta}}}{2}\right)^N \frac{1}{2\cosh\tilde{\beta}}\Bigg\{&\sum_{k=0}^{N}\binom{N}{k}(c_+ + c_-)^{N-k}\Delta^{\frac{k}{2}}\left[1 + (-1)^k\right] \\ &+ \sum_{k=0}^{N}\binom{N}{k}(c_+ + c_-)^{N-k+1}e^{-2\tilde{\beta}}\Delta^{\frac{k-1}{2}}\left[1 - (-1)^k\right]\Bigg\}. \end{aligned} \tag{5.86}$$

Here, we can separate the even and odds terms as follows

$$\sum_{k=0}^{N} a_k = \sum_{k=0}^{\left[\frac{N}{2}\right]} a_{2k} + \sum_{k=0}^{\left[\frac{N-1}{2}\right]} a_{2k+1}, \tag{5.87}$$

where the square brackets in the sums stand for the floor function defined as $[x] = \max\{n \in \mathbb{Z} | n \leq x\}$. Then, we get

$$\begin{aligned} Z_G(\tilde{f}) = \frac{(\ell e^{\tilde{\beta}})^N}{2^N\cosh\tilde{\beta}}\Bigg\{&\sum_{k=0}^{\left[\frac{N}{2}\right]}\binom{N}{2k}(c_+ + c_-)^{N-2k}\Delta^k \\ &+ e^{-2\tilde{\beta}}\sum_{k=0}^{\left[\frac{N-1}{2}\right]}\binom{N}{2k+1}(c_+ + c_-)^{N-2k}\Delta^k\Bigg\}. \end{aligned} \tag{5.88}$$

We can further develop the powers Δ^k and $(c_+ + c_-)^{N-2j}$ through the Newton binomial rule, obtaining

$$\begin{aligned} Z_G(\tilde{f}) = \frac{(\ell e^{\tilde{\beta}})^N}{2^N\cosh\tilde{\beta}}\Bigg\{&\sum_{k=0}^{\left[\frac{N}{2}\right]}\sum_{j=0}^{k}\sum_{s=0}^{N-2j}\binom{N}{2k}\binom{k}{j}\binom{N-2j}{s} \\ &\times c_-^{N-j-s}c_+^{j+s}(-1)^j 4^j\left(1 - e^{-4\tilde{\beta}}\right)^j \\ &+ e^{-2\tilde{\beta}}\sum_{k=0}^{\left[\frac{N-1}{2}\right]}\sum_{j=0}^{k}\sum_{s=0}^{N-2j}\binom{N}{2k+1}\binom{k}{j}\binom{N-2j}{s} \\ &\times c_-^{N-j-s}c_+^{j+s}(-1)^j 4^j\left(1 - e^{-4\tilde{\beta}}\right)^j\Bigg\}. \end{aligned} \tag{5.89}$$

Finally, Eq. (5.83) can be evaluated, yielding the canonical partition function within the Helmholtz ensemble given in Eqs.(5.14) and (5.15).

5.8.4 Asymptotic force-extension relation for the zipper model under isometric condition

Let us then introduce the average chain stretch $\bar{\lambda} = \frac{x_N}{\ell N}$, prescribed to the chain under isometric conditions. By using Eqs.(5.16) and (5.52), we obtain the force-extension relation in the form

$$\langle \tilde{f} \rangle = \frac{(F_0 G_0 + F_N G_N)\left(1 - e^{-2\tilde{\beta}}\right) + e^{-2\tilde{\beta}} \sum_{\xi=0}^{N} F(\xi) G(\xi)}{(F_0 + F_N)\left(1 - e^{-2\tilde{\beta}}\right) + e^{-2\tilde{\beta}} \sum_{\xi=0}^{N} F(\xi)}, \tag{5.90}$$

where we introduced the following functions

$$G(\xi) = \hat{k}\left(\frac{\xi}{N}\right) \frac{(N-\xi)(\bar{\lambda}-1) + \xi(\bar{\lambda}-\chi)}{N}, \tag{5.91}$$

$$F(\xi) = \frac{\exp\left\{-\tilde{\beta}\left[\hat{k}\left(\frac{\xi}{N}\right) \frac{[(N-\xi)(\bar{\lambda}-1)+\xi(\bar{\lambda}-\chi)]^2}{2N} + \Delta\tilde{E}\xi\right]\right\}}{\sqrt{N\alpha^{\xi}/\hat{k}\left(\frac{\xi}{N}\right)}}, \tag{5.92}$$

we defined the rescaled global stiffness of the system (with $0 \leq t \leq 1$)

$$\hat{k}(t) = \left(\frac{1-t}{\tilde{k}} + \frac{t}{\alpha\tilde{k}}\right)^{-1}, \tag{5.93}$$

and we used the compact notations $F_0 = F(0), G_0 = G(0), F_N = F(N), G_N = G(N)$. Let us now consider the behavior in the thermodynamical limit $N \to \infty$. By following the approach suggested in Refs.[1, 93] to obtain explicit analytical results, not only for the stress plateau but also for the stress peak, we may consider the Euler-MacLaurin (EM) approximation for a given function ϕ

$$\sum_{\xi=0}^{N} \phi(\xi) \simeq \int_0^N \phi(\xi)\mathrm{d}\xi + \frac{\phi(0)+\phi(N)}{2}, \tag{5.94}$$

where higher-order terms of the EM approximation would lead to more detailed, but analytically cumbersome results. Thus, from Eq.(5.90) we get

$$\langle \tilde{f} \rangle = \frac{(F_0 G_0 + F_N G_N)\left(1 - \frac{e^{-2\tilde{\beta}}}{2}\right) + e^{-2\tilde{\beta}} \int_0^N F(\xi) G(\xi)\mathrm{d}\xi}{(F_0 + F_N)\left(1 - \frac{e^{-2\tilde{\beta}}}{2}\right) + e^{-2\tilde{\beta}} \int_0^N F(\xi)\mathrm{d}\xi}. \tag{5.95}$$

To simplify the calculation, we may rewrite the integrals as

$$\int_0^N F(\xi)\mathrm{d}\xi = \sqrt{N} \int_0^1 e^{Ng(\eta)} \sqrt{\hat{k}(\eta)}\mathrm{d}\eta, \tag{5.96}$$

$$\int_0^N F(\xi) G(\xi)\mathrm{d}\xi = \sqrt{N} \int_0^1 e^{Ng(\eta)} \sqrt{\hat{k}(\eta)} f(\eta)\mathrm{d}\eta, \tag{5.97}$$

where we introduced the phase fraction $\eta = \xi/N$ and the auxiliary functions

$$g(\eta) = \frac{\eta}{2}\log\frac{1}{\alpha} - \tilde{\beta}\left(\eta\Delta\tilde{E} + \hat{k}(\eta)\frac{[(1-\eta)(\bar{\lambda}-1)+\eta(\bar{\lambda}-\chi)]^2}{2}\right), \tag{5.98}$$

$$f(\eta) = \hat{k}(\eta)\left[(1-\eta)(\bar{\lambda}-1)+\eta(\bar{\lambda}-\chi)\right]. \tag{5.99}$$

Now, we use the following general results [326, 327].

Let

$$I(x) = \int_a^b e^{x\mathcal{G}(t)}\mathcal{F}(t)\mathrm{d}t, \tag{5.100}$$

then, we have

1. Suppose $\mathcal{F}$ is bounded and continuous on (a,b), and $\mathcal{F}(a)\mathcal{F}(b) \neq 0$. Suppose also that $\mathcal{G}$ is strictly monotone and differentiable and that $\frac{\mathcal{F}(a)}{\mathcal{G}'(a)}$ and $\frac{\mathcal{F}(b)}{\mathcal{G}'(b)}$ both exist as finite reals, defined as limits if either endpoint is infinite. Assume also that the integral in Eq.(5.100) exists for all $x > 0$. Then, we have that

$$I(x) \underset{x\to\infty}{\simeq} \frac{1}{x}\frac{\mathcal{F}(b)}{\mathcal{G}'(b)}e^{x\mathcal{G}(b)} - \frac{1}{x}\frac{\mathcal{F}(a)}{\mathcal{G}'(a)}e^{x\mathcal{G}(a)}. \tag{5.101}$$

2. Suppose $\mathcal{F}$ is bounded and continuous on (a,b), that $\mathcal{G}$ has unique maximum at some c in the open interval (a,b), $\mathcal{G}$ is differentiable in some neighborhood of c, $\mathcal{G}''(c)$ exists and is $\mathcal{G}''(c) < 0$, and that $\mathcal{F}(c) \neq 0$. Then, we have that

$$I(x) \underset{x\to\infty}{\simeq} \frac{\sqrt{2\pi}\mathcal{F}(c)e^{x\mathcal{G}(c)}}{\sqrt{-x\mathcal{G}''(c)}}. \tag{5.102}$$

We use the results in Eqs.(5.101) and (5.102) to analyze the behavior of the integrals defined in Eqs.(5.96) and (5.97). First, by using Eq.(5.98), we obtain

$$\begin{aligned}\frac{\partial g}{\partial\eta} = {} & \tilde{\beta}\hat{k}(\eta)\left[(1-\eta)(\bar{\lambda}-1)+\eta(\bar{\lambda}-\chi)\right](\chi-1) - \tilde{\beta}\Delta\tilde{E} + \frac{1}{2}\log\frac{1}{\alpha} \\ & + \frac{\tilde{\beta}[\hat{k}(\eta)]^2}{2}[(1-\eta)(\bar{\lambda}-1)+\eta(\bar{\lambda}-\chi)]^2\left(\frac{1}{\alpha\tilde{k}} - \frac{1}{\tilde{k}}\right).\end{aligned} \tag{5.103}$$

Solving $\frac{\partial g}{\partial\eta} = 0$, we obtain the solution η_0 that represents the stationary point to be computed. Thus, following the definition in Eq.(5.99), we also introduce the value

$$\tilde{f}_0 = \tilde{f}(\eta_0) = \hat{k}(\eta_0)\left[(1-\eta_0)(\bar{\lambda}-1)+\eta_0(\bar{\lambda}-\chi)\right]. \tag{5.104}$$

We observe that the equation $\frac{\partial g}{\partial\eta} = 0$ can be written in terms of $\tilde{f}_0$ as

$$\frac{1}{2}\log\left(\frac{1}{\alpha}\right) - \tilde{\beta}\left[\Delta\tilde{E} - (\chi-1)\tilde{f}_0 - \left(\frac{1}{\alpha}-1\right)\frac{\tilde{f}_0^2}{2\tilde{k}}\right] = 0, \tag{5.105}$$

that coincides with Eq.(5.30) (*i.e.* with $\delta = 0$). Thus, we identify $\tilde{f}_0$ with the Maxwell force $\tilde{f}_M$. Now, we can use Eq.(5.102) (stationary phase theorem) to simplify Eqs.(5.96) and (5.97) only if

$0 < \eta_0 < 1$ (the stationary point must be within the integration interval). For $\eta_0 = 0$, we have $\tilde{f}_0 = (\bar{\lambda} - 1)\tilde{k}$, and for $\eta_0 = 1$, we have $\tilde{f}_0 = (\bar{\lambda} - \chi)\alpha\tilde{k}$, as given by Eq.(5.104). Hence, the interval $0 < \eta_0 < 1$ is equivalent to $1 + \frac{\tilde{f}_0}{\tilde{k}} < \bar{\lambda} < \chi + \frac{\tilde{f}_0}{\alpha\tilde{k}}$, which corresponds to the force plateau region between the two elastic branches. Therefore, only in the plateau interval, we do have a stationary point and we can approximate Eqs.(5.96) and (5.97) with Eq.(5.102). The application of the stationary phase method is further justified by the relation $g''(\eta_0) < 0$, simply proved by a direct evaluation

$$g''(\eta_0) = -\tilde{\beta}\hat{k}(\eta_0)\left[\left(\chi + \frac{\tilde{f}_0}{\alpha\tilde{k}}\right) - \left(1 + \frac{\tilde{f}_0}{\tilde{k}}\right)\right]^2 < 0. \tag{5.106}$$

Note that from now on, we use the notation $\tilde{f}_M$ for the quantity $\tilde{f}_0$, to be consistent with previous Sections. We obtain from Eq.(5.95) the expression

$$\langle \tilde{f} \rangle = \frac{\mathcal{C}_N \left[e^{\Delta g_0 N} (\bar{\lambda} - 1)\tilde{k}^{\frac{1}{2}} + e^{\Delta g_1 N} (\bar{\lambda} - \chi)(\alpha\tilde{k})^{\frac{3}{2}} \right] + \tilde{f}_M}{\mathcal{C}_N \left[\sqrt{\tilde{k}}\, e^{\Delta g_0 N} + \sqrt{\alpha\tilde{k}}\, e^{\Delta g_1 N} \right] + 1}, \tag{5.107}$$

where

$$\Delta g_0 = g(0) - g(\eta_0) = -\frac{\tilde{\beta}\tilde{k}}{2}\left[\bar{\lambda} - \left(1 + \frac{\tilde{f}_M}{\tilde{k}}\right)\right]^2, \tag{5.108}$$

$$\Delta g_1 = g(1) - g(\eta_0) = -\frac{\tilde{\beta}\alpha\tilde{k}}{2}\left[\bar{\lambda} - \left(\chi + \frac{\tilde{f}_M}{\alpha\tilde{k}}\right)\right]^2, \tag{5.109}$$

$$\mathcal{C}_N = \frac{2\, e^{2\tilde{\beta}} - 1}{2}\sqrt{\frac{\tilde{\beta}}{2\pi N}}\left[\chi + \frac{\tilde{f}_M}{\alpha\tilde{k}} - \left(1 + \frac{\tilde{f}_M}{\tilde{k}}\right)\right]. \tag{5.110}$$

This is the main result given in Eqs.(5.53)-(5.56) of the main text. Considering that $\Delta g(0) < 0$ and $\Delta g(1) < 0$ (since $g(\eta_0)$ is the maximum value of $g(\eta)$ in the interval $0 < \eta < 1$), we may prove that in the thermodynamic limit

$$\lim_{N \to \infty} \langle \tilde{f} \rangle = \tilde{f}_M, \tag{5.111}$$

which is valid for $1 + \frac{\tilde{f}_M}{\tilde{k}} < \bar{\lambda} < \chi + \frac{\tilde{f}_M}{\alpha\tilde{k}}$, and meaning that the Maxwell force is the same for both the Helmholtz and Gibbs ensembles, proving their equivalence for the zipper model.

In order to conclude the analysis, we have to simplify Eq.(5.95) also for the external regions, *i.e.* for $\bar{\lambda} < 1 + \frac{\tilde{f}_M}{\tilde{k}}$ and $\bar{\lambda} > \chi + \frac{\tilde{f}_M}{\alpha\tilde{k}}$. Hence, we suppose that the critical point η_0 is external to the interval $(0, 1)$. We can have either $\eta_0 < 0$ or $\eta_0 > 1$. In these cases, the asymptotic behavior of the integrals in Eqs.(5.96) and (5.97) is described by Eq.(5.101). Then, Eq.(5.95) assumes the form

$$\langle \tilde{f} \rangle = \frac{e^{Ng(0)}\tilde{k}^{\frac{3}{2}}(\bar{\lambda} - 1) + e^{Ng(1)}(\alpha\tilde{k})^{\frac{3}{2}}(\bar{\lambda} - \chi) + \frac{2}{2e^{2\tilde{\beta}} - 1}\mathcal{A}}{e^{Ng(0)}\sqrt{\tilde{k}} + e^{Ng(1)}\sqrt{\alpha\tilde{k}} + \frac{2}{2e^{2\tilde{\beta}} - 1}\mathcal{B}}, \tag{5.112}$$

where

$$\mathcal{A} = \frac{(\alpha\tilde{k})^{\frac{3}{2}}}{g'(1)} e^{Ng(1)}(\bar{\lambda} - \chi) - \frac{\tilde{k}^{\frac{3}{2}}}{g'(0)} e^{Ng(0)}(\bar{\lambda} - 1), \tag{5.113}$$

$$\mathcal{B} = \frac{\sqrt{\alpha\tilde{k}}}{g'(1)} e^{Ng(1)} - \frac{\sqrt{\tilde{k}}}{g'(0)} e^{Ng(0)}. \tag{5.114}$$

Now, by using Eq.(5.105), we determine the quantity $g(1) - g(0)$ that eventually reads

$$g(1) - g(0) = \frac{\tilde{\beta}\tilde{k}}{2} \left[\left(\bar{\lambda} - 1 - \frac{\tilde{f}_M}{\tilde{k}} \right)^2 - \alpha \left(\bar{\lambda} - \chi - \frac{\tilde{f}_M}{\alpha\tilde{k}} \right)^2 \right]. \tag{5.115}$$

Accordingly, in the limit of $N \to \infty$, we obtain

$$g(1) - g(0) \begin{cases} > 0 \quad \text{if} \quad \bar{\lambda} > \chi + \dfrac{\tilde{f}_M}{\alpha\tilde{k}} \Rightarrow \langle \tilde{f} \rangle = \alpha\tilde{k}(\bar{\lambda} - \chi), \\ < 0 \quad \text{if} \quad \bar{\lambda} < 1 + \dfrac{\tilde{f}_M}{\tilde{k}} \Rightarrow \langle \tilde{f} \rangle = \tilde{k}(\bar{\lambda} - 1), \end{cases} \tag{5.116}$$

a result representing the elastic branches in the external regions, corresponding to the fully folded (left) and fully unfolded (right) phases. This completes the proof of the equivalence of the ensembles in the thermodynamic limit for the zipper model.

Chapter 6

Thermal effect on brittle fracture and brittle-to-ductile transition

6.1 Introduction

The mechanical degradation of materials typically results from the insurgence of cracks, from their geometric arrangement and interactions, and, finally, from temperature. The classical Griffith energetic approach in fracture mechanics deduces that under the same homogeneous stress σ, a single slit crack with half-length L grows if $\sigma > \sqrt{2\gamma_s E'/(\pi L)}$, while if $\sigma < \sqrt{2\gamma_s E'/(\pi L)}$, it remains stable [119, 328]. Here, E' is the equivalent elastic modulus, equal to the Young modulus E in plane stress condition, and equal to $E/(1-\nu^2)$ in plane strain condition, where ν is the Poisson ratio of the material. Moreover, γ_s is the surface energy density, that is, the energy expended to debond a unit-length crack. This stability criterion measures an energy competition between the free surface energy created by the fracture and the elastic energy stored in the deformable solid. The latter has been evaluated within the linear elasticity theory by Inglis [329] and Kolosoff [330] and used by Griffith to develop his criterion. The ingenious approach proposed by Griffith in his celebrated criterion has been largely and successfully tested in glass and other brittle materials containing cracks of controlled length [331, 332], and also validated by atomistic simulations in ideal mono-crystalline systems [333, 334]. Its main limiting hypothesis is that the overall fracture energy coincides with the surface energy, *i.e.* with the energy needed to break the bonds between the two crack faces. Since Griffith's theory fails to apply to ductile materials (where fracture energy is much higher than the only surface energy [335, 336]) it was generalized by Irwin to include plastic dissipation [120, 121]. More advanced models for ductile fracture, taking into account an explicit description of the 'cohesive zone' where the plastic processes localize, have then been proposed by Dugdale and Barenblatt [134, 135]. The theoretical relationship between Griffith's theory, its Irwin modification, and the Dugdale-Barenblatt models was initially studied by Willis [337] and further investigated by Rice through the concept of J-integral [338]. In addition to the single fracture study, an important topic in linear elastic fracture mechanics is represented by the collective degradation mechanism induced by populations of cracks that interact depending on their geometric arrangement [199, 200, 339–347]. Due to the wide scientific and technological interest, the theoretical and experimental studies of fracture phenomena have been extremely extensive. Therefore, its history is long and complicated and, here, we refer the reader to the relevant literature [348–352]. We simply mention that current advanced researches concern the

traction-separation relation in cohesive models [353, 354], the instability in dynamic fracture [148, 355], and the variational approach to fracture [356, 357]. Computational techniques for cracks propagation include the phase field method and the dual-horizon peridynamics formulation [358–361]. Other efficient numerical techniques to study fracture propagation in dynamic regime with viscosity and/or thermal coupling are based on the finite elements method [362–364].

Previously described investigations are predominantly based on deterministic assumptions and theories. Of course, also statistical approaches have been widely applied to rupture phenomena [365–370], and among others those based on the so-called fiber bundle model are particularly significant [371–374]. Importantly, the statistical analysis plays a crucial role in understanding the effect of disorder in failure processes and other micromechanical problems [136–147]. Despite the wide diffusion of statistical techniques, the approaches that allow studying the effects of thermal fluctuations on the fracture are rather limited [149, 375–382]. In particular, the temperature dependence of crack stability criteria has not been studied explicitly. For this reason, we propose here two paradigmatic models able to evaluate the effects of thermal fluctuations on the quasi-static brittle fracture and on the brittle-to-ductile transition. These approaches make it possible to study how fracture stability is influenced by temperature changes and to determine the transition temperature between brittle and ductile behaviors. The proposed fracture models are based on equilibrium statistical mechanics and they are implemented by means of the spin variable approach, useful to deal with arbitrarily non-convex potential energies [91]. This method has been largely applied to several situations including the physics of muscles [74, 75], the folding of macromolecules [92, 94, 95, 102, 164], the adhesion or peeling processes [1, 93], the phase transformations in solids [2, 165], and the stick-slip on rigid substrate [166]. This technique complements the more classical methods used to study the behavior of physical systems with multiple stable and metastable states [27, 53–55]. In the context of fracture, the prototypical models here proposed are discrete and based on quasi-one-dimensional lattices composed of breakable and unbreakable bonds. While the unbreakable springs serve to distribute the forces in the system, thus describing material elastic energy, the breakable springs are useful in mimicking the fracture propagation. It is important to note in this context that the role of discreteness in fracture models has already been highlighted in different studies [383–386].

In the first model proposed here (elasto-fragile model), developed to describe temperature effects in brittle fracture, each breakable spring can be in one of two states, intact or broken, depending on its extension. Conversely, in the second proposed model (softening-fracture model), useful to describe temperature effects in brittle-to-ductile transitions, each breakable spring can be in one of three states, intact, softened, or broken, depending again on the spring extension. In our model, the softened state represents an intermediate configuration where the elastic constant of the spring is smaller than that of the intact spring, but it is still not zero as instead assumed for the broken configuration. This intermediate state represents here the counterpart of the material behavior of the cohesive zone introduced in the Dugdale-Barenblatt model, having also the role of introducing an internal length scale. Both proposed models are approached by calculating the exact partition function, by an approximation obtained for large values of the number N of breakable springs, and, finally by the analysis of the thermodynamic limit. This multifaceted treatment allows us to state that both models exhibit a critical behavior with an associated phase transition, whose mechanical implications are thoroughly discussed. In our opinion, the results are particularly useful for the interpretation of failure processes in micro- and nano-systems, where the effect of temperature is typically studied experimentally and through molecular dynamics simulations [122–133]. We want to emphasize that our models, being discrete and addressed to the study of thermal fluctuations, neglect important aspects related to the distribution of elastic fields around the fracture. This is consistent with the fact that they are not developed to replace classical models of continuum mechanics but rather to provide new elements to improve and

complement them.

This Chapter is structured as follows. In Section 6.2, we introduce the first model for the brittle fracture and we apply the tools of statistical mechanics to eventually obtain exact results. Then, in Section 6.3, we obtain an approximate analytic solution for systems with a large number N of breakable springs, and in Section 6.4, we study the thermodynamic limit with $N \to \infty$. This allows for a generalization of Griffith's criterion that takes temperature into account by means of critical behavior. Concerning the model with the softening mechanism, we introduce its structure and we elaborate its formalism in Section 6.5. Further, we obtain its asymptotic behavior for large values of N in Section 6.6, and we study the thermodynamic limit with $N \to \infty$ in Section 6.7. Here we obtain the closed-form expression for the brittle-to-ductile transition temperature and describe the corresponding complex critical scenario.

6.2 Elasto-fragile model

We introduce here a discrete model that helps us to better understand the effect of thermal fluctuations on the brittle fracture processes in solid materials. As shown in Fig.6.1, the model consists of a network of springs with different elastic constants arranged in a quasi-one-dimensional lattice, aimed at reproducing a mode I fracture geometry [346]. Based on symmetry assumptions, we reduce the scheme in Fig.6.1(a) to the one in Fig.6.1(b). The structure in Fig.6.1(b) connects a fixed substrate, at $y = 0$, with a rigid top layer that can be placed at different heights $y = Y$ (isometric conditions within the Helmholtz ensemble). More in detail, see Fig.6.1(b), this structure is composed of a series of $N+1$ springs, with elastic constant k, linked together to form a horizontal chain (colored in purple). The left end-side of the chain, at $i = 0$, is attached to the bottom fixed substrate at $y = 0$ while the other end, located at $i = N + 1$, is attached to the top layer at $y = Y$. The inner points of the chain, identified by $i = 1, \ldots, N$, are individually linked to the top layer through N springs with elastic constant l (colored in yellow), mimicking the elasticity of the upper half plane. Moreover, the first ones ($i = 1, \ldots, \eta$), are linked to the bottom layer through η breakable springs (intact in blue, broken in red). We assume that it exists an elongation threshold Y_M after which the potential energy for a breakable spring is constant and the resulting elastic force is zero (broken state), see Fig.6.2. The behavior of a single breakable spring corresponds to an elastic constant h when its elongation y_i does not exceed the threshold Y_M (blue continuous curve in Fig.6.2). When $|y_i| > Y_M$ the potential energy is constant and then the resulting force is zero (red continuous lines in Fig.6.2).

We remark that we adopted here simple piecewise linear constitutive equations for the springs of the system. We wish to mention that several important results have been obtained for the crack propagation in nonlinear materials described by power-law stress-strain behavior [387–389]. However, from one side it is difficult to combine the thermal analysis with nonlinear materials, and from the other side, the nonlinear phenomena are rather limited in nanoscopic systems [124, 125]. It is also worth mentioning that due to the discrete quasi-one-dimensional structure of our model, it is not possible to find here the results concerning the stress singularities at the crack tip and the calculation of the corresponding stress intensity factor (this is true for both the elasto-fragile model and the softening-fracture model) [343, 346].

We analyze the fracture behavior of the proposed model in the framework of equilibrium statistical mechanics, introducing a temperature T of an embedding thermal bath. As previously anticipated, we investigate its behavior by adopting isometric conditions corresponding to the Helmholtz ensemble [98, 109, 390]. We make the assumption that, during the system extension (*i.e.*, increasing Y), the system is composed of a segment with ξ intact elements on the left side of the system, and of a segment with $\eta - \xi$ broken elements on the right. As a result, the

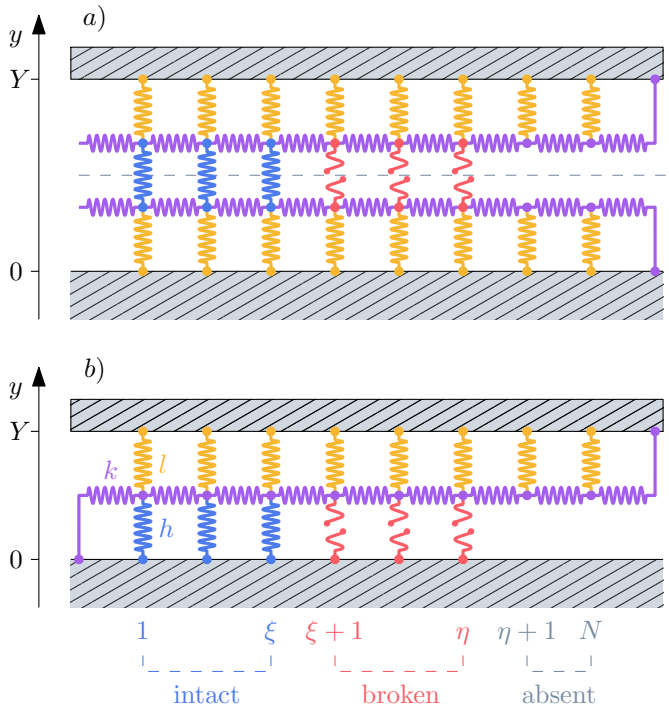

Figure 6.1: Panel (a): scheme of a crack propagating within an arbitrary crystal lattice. Panel (b): reduced scheme of the elasto-fragile model, based on symmetry assumption. The central chain (colored in purple) is composed of $N+1$ linear elastic springs of elastic constant k. The nodes of this chain are connected to the top layer of the system (at $y=Y$) with N linear elastic springs of elastic constant l (colored in yellow). Moreover, the first η nodes ($i=1,\dots,\eta$) are also linked to the bottom layer (at $y=0$) through η breakable springs of elastic constant h (intact in blue, broken in red). We underline that the first node ($i=0$) and the last one ($i=N+1$) are anchored to the bottom and the top layer, respectively. Hence, the first and the last shear springs fix the direction of the crack propagation from the right to the left of the system.

system evolution is characterized by the propagation of a single interface between intact and broken springs, regulated by the assigned traction conditions and by the temperature. This hypothesis (known as the single domain wall assumption) simplifies the calculations and makes it possible to analytically derive the partition function and, thus, the important macroscopic physical quantities. The same hypothesis is considered in the classical continuum fracture models recalled in the introduction. The configurations previously described can be summarized by the relation $1 \leq \xi \leq \eta \leq N$, where ξ represents the domain wall or interface position. We remark that the last $N-\eta$ sites of the chain are always considered disconnected from the bottom layer in order to simulate a possible existing initial fractured domain. This is coherent with the assumption of an initial crack extension in the classical Griffith criterion, which is the milestone of the linear elastic fracture mechanics [119, 328].

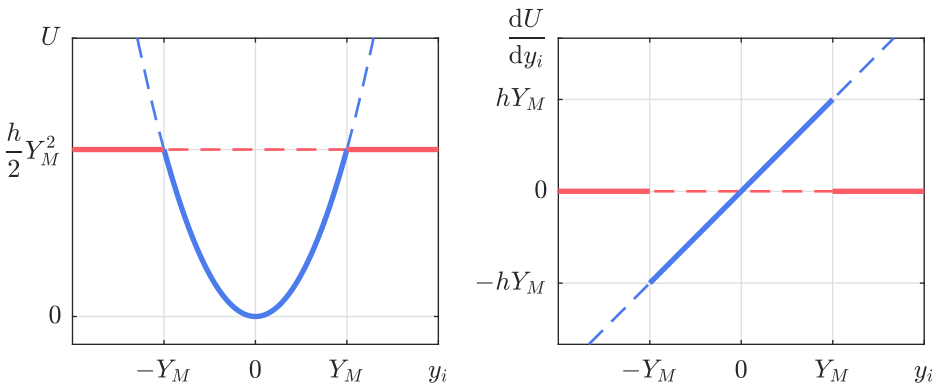

Figure 6.2: Potential energy of a single breakable spring with elastic constant h (continuous red and blue curve on the left) and corresponding force (continuous red and blue curve on the right). The quantity Y_M is the elongation after which the spring breaks, resulting in a force equal to zero. The dashed curves correspond to the spin approximations energy profile.

Based on previous key premises, the total energy of the system is

$$\begin{aligned}\Phi_H(y_1,...,y_N,\xi) = &\sum_{i=0}^{N}\frac{k}{2}(y_{i+1}-y_i)^2+\sum_{i=1}^{N}\frac{l}{2}(Y-y_i)^2\\ &+\sum_{i=1}^{\xi}\frac{h}{2}y_i^2+\sum_{i=\xi+1}^{\eta}\frac{h}{2}Y_M^2,\end{aligned} \tag{6.1}$$

with the boundary conditions $y_0 = 0$ and $y_{N+1} = Y$. Here, the variables y_i represent the vertical coordinates of the lattice points while ξ assigns the discrete interface position. Observe that the first addend of Eq.(6.1), proportional to the elastic constant k, is the energetic contribution of the shear unbreakable springs. We remark that the use of the shear springs with elastic constant k is an approximation valid under the small deformation assumption (in our models the central nodes can only move vertically). The second addend, proportional to the elastic constant l, is the contribution of the vertical unbreakable springs that connect the upper layer to the inner lattice points. Finally, the energetic contribution proportional to the elastic constant h, regarding the breakable springs, is split into two addends: the first one corresponds to the unbroken springs (going from $i = 1$ to $i = \xi$) and the second one corresponds to the broken ones (from $i = \xi + 1$ to $i = \eta$). Again, the assumption of linear elastic springs, as typical in linear elastic fracture mechanics, allows for a proper description of fracture effects under the hypothesis of small strains. Such a simplification is crucial for the following analytical treatment. The energy contribution associated with broken bonds corresponds to the surface energy of the two exposed sides of the fracture, originally introduced by Griffith in the overall energy balance and eventually yielding his classical stability criterion [119].

The energy in Eq.(6.1) can be rewritten as

$$\begin{aligned}\Phi_H = \frac{k}{2}\left[\sum_{i=1}^{N}\left(2+\frac{l}{k}\right)y_i^2 + \sum_{i=1}^{\xi}\frac{h}{k}y_i^2 - \sum_{i=1}^{N-1}y_{i+1}y_i - \sum_{i=1}^{N-1}y_i y_{i+1}\right] \\ + kY\left[-\sum_{i=1}^{N}\frac{l}{k}y_i - y_N\right] + \frac{1}{2}kY^2 + \frac{1}{2}lNY^2 + \frac{1}{2}hY_M^2(\eta-\xi).\end{aligned} \tag{6.2}$$

We can introduce the following N-component vectors

$$\mathbf{y}^{\mathsf{T}} = \begin{pmatrix} y_1 & y_2 & \dots & y_N \end{pmatrix} \in \mathbb{R}^N, \tag{6.3}$$

$$\mathbf{v}^{\mathsf{T}} = \begin{pmatrix} \beta & \dots & \beta & 1+\beta \end{pmatrix} \in \mathbb{R}^N, \tag{6.4}$$

and the tridiagonal matrix

$$\mathcal{A} = \begin{pmatrix} a_1 & -1 & 0 & \cdots & 0 \\ -1 & \ddots & \ddots & \ddots & \vdots \\ 0 & \ddots & \ddots & \ddots & 0 \\ \vdots & \ddots & \ddots & \ddots & -1 \\ 0 & \cdots & 0 & -1 & a_N \end{pmatrix}, \tag{6.5}$$

where the diagonal components a_i are defined as follows

$$a_i = \begin{cases} 2+\alpha & \text{if } 1 \le i \le \xi, \\ 2+\beta & \text{if } \xi+1 \le i \le N, \end{cases} \tag{6.6}$$

with

$$\alpha = \frac{l+h}{k}, \quad \beta = \frac{l}{k}, \tag{6.7}$$

measuring extension versus shear springs stiffness of the lattice. Adopting the matrix $\mathcal{A}$ and the vectors $\mathbf{y}$ and $\mathbf{v}$, we can write Eq.(6.2) as

$$\Phi_H = \frac{1}{2}k\mathbf{y}^{\mathsf{T}}\mathcal{A}\mathbf{y} - kY\mathbf{v}^{\mathsf{T}}\mathbf{y} + \frac{1}{2}kY^2 + \frac{1}{2}lNY^2 + \frac{1}{2}hY_M^2(\eta-\xi). \tag{6.8}$$

This new compact expression is more suitable to evaluate the partition function of the system, defined by

$$Z_H(Y) = \sum_{\xi=0}^{\eta}\int_{\mathbb{R}^N} e^{-\frac{\Phi_H}{K_B T}}\,\mathrm{d}y_1 \dots \mathrm{d}y_N. \tag{6.9}$$

Here, we have integrated the continuous coordinates y_i and we have summed over the discrete or spin variable ξ identifying the interface position. We have

$$Z_H(Y) = \sum_{\xi=0}^{\eta}\exp\left\{-\frac{kY^2}{2K_BT} - \frac{lNY^2}{2K_BT} - \frac{hY_M^2(\eta-\xi)}{2K_BT}\right\}\mathcal{I}_\xi, \tag{6.10}$$

where

$$\mathcal{I}_\xi = \int_{\mathbb{R}^N}\exp\left\{-\frac{k}{2K_BT}\mathbf{y}^{\mathsf{T}}\mathcal{A}\mathbf{y} + \frac{kY}{K_BT}\mathbf{v}^{\mathsf{T}}\mathbf{y}\right\}\mathrm{d}y_1 \dots \mathrm{d}y_N. \tag{6.11}$$

By using the classical Gaussian integral,

$$\int_{\mathbb{R}^N} e^{-\mathbf{y}^\mathsf{T}\mathcal{M}\mathbf{y}+\mathbf{w}^\mathsf{T}\mathbf{y}}\mathrm{d}y_1\dots\mathrm{d}y_N = \sqrt{\frac{\pi^N}{\det\mathcal{M}}}e^{\frac{1}{4}\mathbf{w}^\mathsf{T}\mathcal{M}^{-1}\mathbf{w}}, \tag{6.12}$$

which is valid for a positive definite symmetric matrix $\mathcal{M}$ (as can be shown for the tridiagonal matrix $\mathcal{A}$) and for any vector $\mathbf{w}$, we get

$$\mathcal{I}_\xi = \sqrt{\frac{(2\pi K_B T)^N}{k^N \det\mathcal{A}}}\exp\left\{\frac{kY^2}{2K_BT}\mathbf{v}^\mathsf{T}\mathcal{A}^{-1}\mathbf{v}\right\}. \tag{6.13}$$

Thus, the partition function can be written as

$$\begin{aligned} Z_H(Y) = \sum_{\xi=0}^{\eta}&\exp\left\{-\frac{kY^2}{2K_BT}-\frac{lNY^2}{2K_BT}-\frac{hY_M^2(\eta-\xi)}{2K_BT}\right\} \\ &\times\sqrt{\frac{(2\pi K_BT)^N}{k^N\det\mathcal{A}}}\exp\left\{\frac{kY^2}{2K_BT}\mathbf{v}^\mathsf{T}\mathcal{A}^{-1}\mathbf{v}\right\}. \end{aligned} \tag{6.14}$$

Since $\mathcal{A}$ depends on ξ, see Eqs.(6.5) and (6.6), both $\mathcal{A}^{-1}$ and $\det\mathcal{A}$ depend on ξ in the sum of Eq.(6.14). In Appendix 6.9.1, we discuss an efficient method to determine $\mathcal{A}^{-1}$ and $\det\mathcal{A}$ for a tridiagonal matrix. This method will be used to obtain asymptotic expressions, useful to study the system behavior for large values of N (and for the thermodynamic limit). Introducing the quantity

$$q = 1+\beta N - \mathbf{v}^\mathsf{T}\mathcal{A}^{-1}\mathbf{v}, \tag{6.15}$$

we can write the partition function in the form

$$Z_H(Y) = \sum_{\xi=0}^{\eta}\sqrt{\frac{(2\pi K_BT)^N}{k^N\det\mathcal{A}}}\exp\left\{\left[\frac{-hY_M^2(\eta-\xi)-kY^2q}{2K_BT}\right]\right\}. \tag{6.16}$$

We can now evaluate the expected values of macroscopic quantities. For example, the expectation value of the force applied to the system is [98, 109, 390]

$$\langle f\rangle = -K_BT\frac{1}{Z_H}\frac{\partial Z_H}{\partial Y}, \tag{6.17}$$

resulting in

$$\langle f\rangle = \frac{\sum_{\xi=0}^{\eta}(\det\mathcal{A})^{-\frac{1}{2}}\exp\left\{\frac{-hY_M^2(\eta-\xi)-kY^2q}{2K_BT}\right\}q}{\sum_{\xi=0}^{\eta}(\det\mathcal{A})^{-\frac{1}{2}}\exp\left\{\frac{-hY_M^2(\eta-\xi)-kY^2q}{2K_BT}\right\}}kY. \tag{6.18}$$

This expression gives a physical interpretation to the expectation value $\langle q\rangle$ of the variable q. Since $\langle f\rangle = k\langle q\rangle Y$, the quantity $k\langle q\rangle$ represents the effective stiffness $\langle f\rangle/Y$ of the system. Using a similar analysis, it is possible to obtain the average value of the number of unbroken bonds,

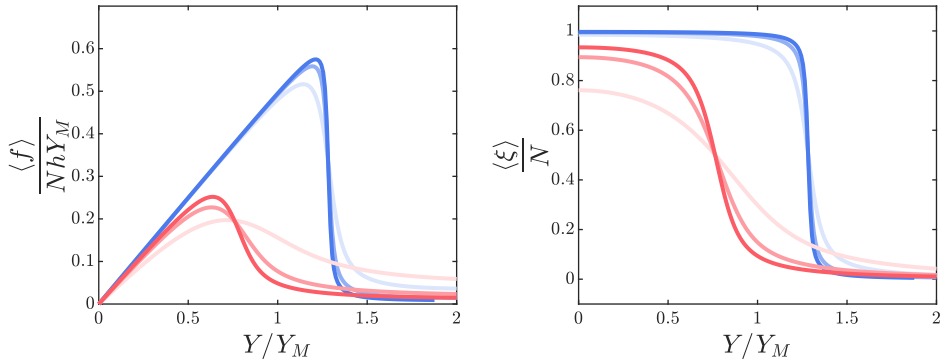

Figure 6.3: Behavior of the brittle-fracture model with a variable number of units ($N = \{50, 125, 200\}$ from faded to vivid curves) and a variable thermal to elastic energy ratio $K_BT/(hY_M^2) = \{0.5, 2\}$ (blue and red curves, respectively). The dimensionless quantities $\langle f\rangle/(NhY_M)$ and $\langle \xi\rangle/N$ are represented versus the dimensionless parameter Y/Y_M, where, in both cases, $l/h = k/h = 1$. We also fixed $\eta = N$, which means there are no missing or broken elements in the initial configuration.

which is given by

$$\langle \xi\rangle = \frac{\sum_{\xi=0}^{\eta} (\det \mathcal{A})^{-\frac{1}{2}} \exp\left\{\frac{-hY_M^2(\eta-\xi)-kY^2q}{2K_BT}\right\}\xi}{\sum_{\xi=0}^{\eta} (\det \mathcal{A})^{-\frac{1}{2}} \exp\left\{\frac{-hY_M^2(\eta-\xi)-kY^2q}{2K_BT}\right\}}. \tag{6.19}$$

In Fig.6.3, we show the main effects on the fracture behavior of both temperature T and discreteness parameter N. The main effect that can be observed is related to temperature, which is able to shift the value of the extension corresponding to the fracture of the system. In particular, we may observe that, as typically experimentally observed, the higher the temperature, the lower the force and the extension required to induce fracture. The model then predicts a thermally activated fracture phenomenon. As described in the following, in the thermodynamic limit (*i.e.*, for $N \to \infty$), this behavior can be theoretically interpreted as a phase transition. We can observe now (see Fig.6.3) that, as the discreteness parameter N increases, the force-displacement curves become sharper, increasing the brittleness of the system. In summary, the model exhibits a temperature-dependent brittle behavior, which can be thoroughly described by analytic expressions for large values of N, obtained in the following Section.

6.3 Asymptotic behavior of the elasto-fragile model

Eqs.(6.18) and (6.19) determine the expected value of $\langle f\rangle$, the force applied to the system, and the average value $\langle \xi\rangle$ of the number of intact bonds as functions of both the assigned displacement Y and of the temperature T. Here, to give a clearer physical interpretation of such results, we obtain analytical approximated relations, effective in the case of large values of N. In particular, for large values of N, we have (see Appendix 6.9.2)

$$q \simeq \frac{lh}{l+h}\frac{\xi}{k} + \epsilon, \tag{6.20}$$

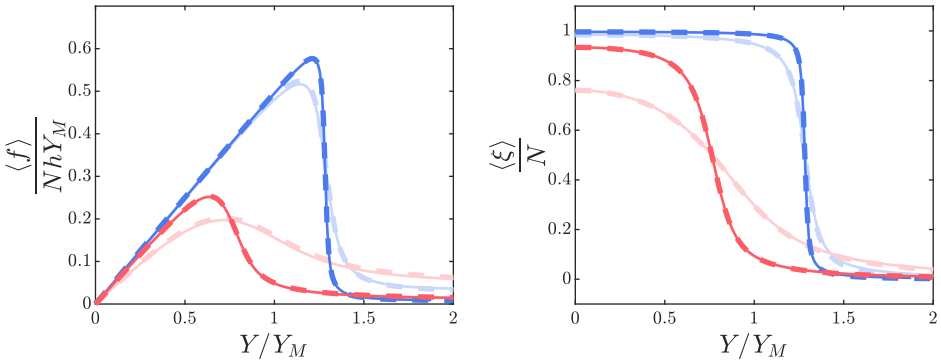

Figure 6.4: Comparison between the approximated quantities given by Eqs.(6.28) and (6.31) (dashed lines) and the corresponding exact results in Eqs.(6.18) and (6.19) (continuous lines) for $\langle f \rangle/(NhY_M)$ and $\langle \xi \rangle/N$ versus the dimensionless extension Y/Y_M. The thermal to elastic energy ratio $K_BT/(hY_M^2)$ is set to 0.5 (blue curves) and 2 (red curves). The total number of units is set to $N = 50$ (faded curves) and to $N = 200$ (vivid curves). The dimensionless quantities are set to $l/h = 1$ and $k/h = 1$. We also considered $\eta = N$.

where

$$\epsilon = \frac{\sqrt{\beta^2 + 4\beta} - \beta}{2} > 0 \tag{6.21}$$

and

$$\det \mathcal{A} \simeq \tau_\alpha^\xi \tau_\beta^{N-\xi}, \tag{6.22}$$

with

$$\tau_s = \frac{2 + s + \sqrt{s^2 + 4s}}{2}, \quad s = \alpha, \beta. \tag{6.23}$$

By using Eq.(6.18), we obtain the following asymptotic expression of the force-extension relation

$$\langle f \rangle \simeq \frac{\sum_{\xi=0}^{\eta} \exp\left\{ -\frac{\xi}{2} \log \delta + \frac{hY_M^2 \xi}{2K_BT} - \frac{Y^2}{2K_BT} \frac{lh}{l+h} \xi \right\} q}{\sum_{\xi=0}^{\eta} \exp\left\{ -\frac{\xi}{2} \log \delta + \frac{hY_M^2 \xi}{2K_BT} - \frac{Y^2}{2K_BT} \frac{lh}{l+h} \xi \right\}} kY, \tag{6.24}$$

where we introduced $\delta = \tau_\alpha/\tau_\beta$. After defining

$$z = \exp\left\{ -\frac{1}{2} \log \delta + \frac{hY_M^2}{2K_BT} - \frac{Y^2}{2K_BT} \frac{lh}{l+h} \right\}, \tag{6.25}$$

and adopting similar considerations for the quantity $\langle \xi \rangle$, we may easily deduce

$$\langle f \rangle \simeq \left(k\epsilon + \frac{lh}{l+h} \frac{\sum_{\xi=0}^{\eta} \xi z^\xi}{\sum_{\xi=0}^{\eta} z^\xi} \right) Y, \tag{6.26}$$

$$\langle \xi \rangle \simeq \frac{\sum_{\xi=0}^{\eta} \xi z^\xi}{\sum_{\xi=0}^{\eta} z^\xi}, \tag{6.27}$$

for large values of N. Combining Eqs.(6.26) and (6.27), we find

$$\langle f\rangle \simeq \left(k\epsilon + \frac{lh}{l+h}\langle\xi\rangle\right) Y. \tag{6.28}$$

So, if we calculate the expectation value of intact elements $\langle\xi\rangle$, we also deduce the force-extension relation $\langle f\rangle$-Y. To do this in explicit form, we have to evaluate the sums that appear in the expression of $\langle\xi\rangle$, *i.e.*

$$\sum_{\xi=0}^{\eta} \xi z^{\xi} = \frac{z\left[1-(\eta+1)z^{\eta}+\eta z^{\eta+1}\right]}{(1-z)^2}, \tag{6.29}$$

$$\sum_{\xi=0}^{\eta} z^{\xi} = \frac{1-z^{\eta+1}}{1-z}, \tag{6.30}$$

where we adopted the variable z defined in Eq.(6.25). To conclude, we write

$$\langle\xi\rangle \simeq \frac{1-(\eta+1)z^{\eta}+\eta z^{\eta+1}}{1-z^{\eta+1}}\frac{z}{1-z}, \tag{6.31}$$

These results represent the approximated expressions for the response of the system under isometric conditions for large values of N. As shown in Fig.6.4 (for $\eta = N$), we can observe that the approximations given in Eqs.(6.28) and (6.31) (dashed lines in the figure) are in perfect agreement with the exact results (continuous lines), previously obtained in Eqs.(6.18) and (6.19). We remark that the agreement is very good for different temperatures and for different (large) values of N. These approximated results are particularly useful to study the thermodynamic limit or, equivalently, to study the limiting case for $N \to \infty$, as discussed below.

6.4 Thermodynamic limit of the elasto-fragile model

We perform now the limit for $N \to \infty$. Since previous asymptotic results in Eqs.(6.28) and (6.31) depend on powers of z, we study the inequality $z > 1$. To verify this condition we need to set the argument of the exponential in Eq.(6.25) larger than zero, obtaining the following condition on Y

$$|Y| \leq \sqrt{\frac{l+h}{lh}\left[hY_M^2 - K_B T \log\delta\right]} \triangleq Y_s, \tag{6.32}$$

where we introduced the critical extension Y_s, the physical interpretation of which will be given below. We also define a critical temperature T_c for the system through the condition $hY_M^2 - K_B T_c \ln\delta = 0$ (see Eq.(6.32)) that, once solved for T_c, gives

$$T_c = \frac{hY_M^2}{K_B \log\left(\dfrac{2+\frac{l+h}{k}+\sqrt{\left(\frac{l+h}{k}\right)^2+4\frac{l+h}{k}}}{2+\frac{l}{k}+\sqrt{\left(\frac{l}{k}\right)^2+4\frac{l}{k}}}\right)}, \tag{6.33}$$

where we used $\delta = \tau_\alpha/\tau_\beta$. This is a specific value of the temperature, depending on the main material parameters of the system, which corresponds to a phase transition, as discussed below.

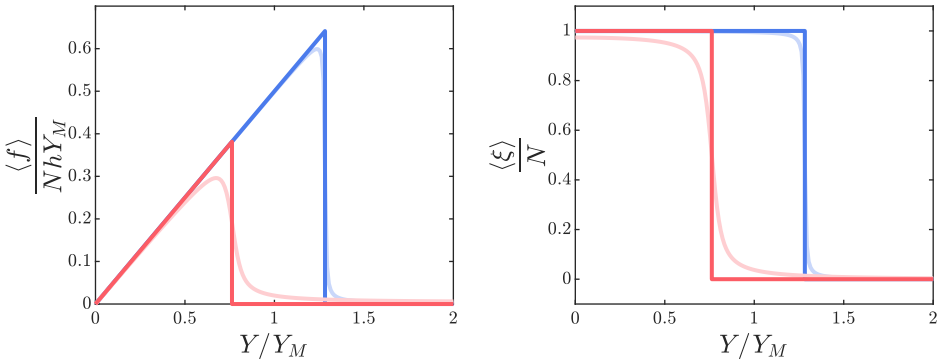

Figure 6.5: Comparison between the thermodynamic limit obtained for $N \to \infty$ (red and blue curves) and the approximations obtained with large values of N (soft colors). We plotted $\langle f\rangle/(NhY_M)$ and $\langle \xi\rangle/N$ versus the dimensionless extension Y/Y_M. The thermal to elastic energy ratio is set to $K_BT/(hY_M^2) = 0.5$ (in blue) and to $K_BT/(hY_M^2) = 2$ (in red) while the total number of units for the large N approximation is set to $N = 500$. The dimensionless quantities are set to $l/h = 1$ and $k/h = 1$. Moreover, we adopted $\eta = N$ corresponding to $\phi = 0$.

For the moment, we can write

$$z > 1 \iff |Y| \leq \sqrt{\frac{l+h}{l} Y_M^2 \left(1 - \frac{T}{T_c}\right)} \triangleq Y_s \tag{6.34}$$

so that $Y_s = 0$ when $T = T_c$.

We first analyze the limit for $N \to \infty$ of the average fraction of intact elements

$$\begin{aligned} \frac{\langle \xi\rangle}{N} &= \frac{1-(\eta+1)z^\eta+\eta z^{\eta+1}}{1-z^{\eta+1}} \frac{z}{1-z} \frac{1}{N} \\ &= \frac{1-z^{\eta+1}+(\eta+1)(z^{\eta+1}-z^\eta)}{1-z^{\eta+1}} \frac{z}{1-z} \frac{1}{N} \\ &= \left(\frac{1}{N} + \frac{\eta+1}{N} \frac{1-z}{z-z^{-\eta}}\right) \frac{z}{1-z}. \end{aligned} \tag{6.35}$$

Now, we consider $\eta = N - M$, where $M = \phi N$ is the number of initially absent breakable springs (initial fractured domain). Here, ϕ is the percentage of initially absent breakable springs over the total number N of elements. The fraction of intact elements is determined as follows

$$\lim_{N\to\infty} \frac{\langle \xi\rangle}{N} = \begin{cases} 1-\phi & \text{if } z > 1 \text{ or } |Y| < Y_s, \\ 0 & \text{if } z < 1 \text{ or } |Y| > Y_s. \end{cases} \tag{6.36}$$

This means that all elements are broken simultaneously (brittle fracture) when $Y = Y_s$.

For the stress $\langle f\rangle/N$ (density of force over the number of bonds), we get

$$\lim_{N\to\infty} \frac{\langle f\rangle}{N} = \begin{cases} \frac{lh}{l+h}(1-\phi)Y & \text{if } z > 1 \text{ or } |Y| < Y_s, \\ 0 & \text{if } z < 1 \text{ or } |Y| > Y_s. \end{cases} \tag{6.37}$$

Thus (see Fig.6.5), after an initial linear behavior, the stress collapses to zero at the extension

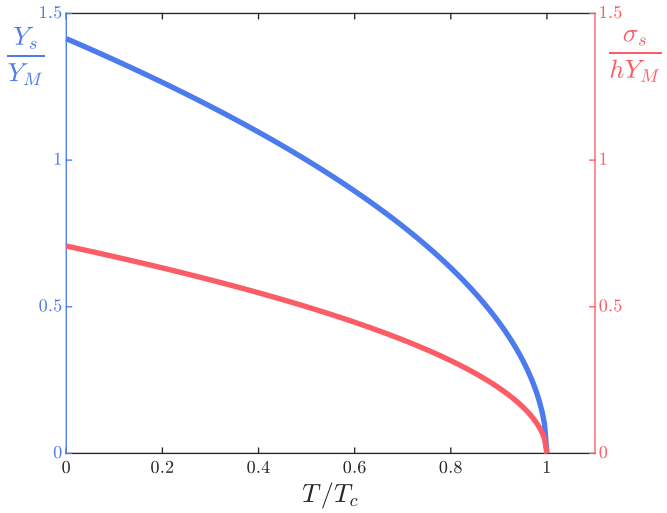

Figure 6.6: Fracture extension Y_s/Y_M (in blue) and fracture strength $\sigma_s/(hY_M)$ (in red) versus the reduced temperature T/T_c. All quantities are written in dimensionless form. We can observe that both quantities present a critical behavior corresponding to a phase transition for $T = T_c$. We adopted $l/h = 1$, $k/h = 1$, and $\phi = 0$.

threshold Y_s. Together with the extension threshold Y_s, we can therefore introduce the stress threshold σ_s as follows

$$Y_s = Y_M \sqrt{\frac{l+h}{l}\left(1 - \frac{T}{T_c}\right)}, \tag{6.38}$$

$$\sigma_s = hY_M(1-\phi)\sqrt{\frac{l}{l+h}\left(1 - \frac{T}{T_c}\right)}. \tag{6.39}$$

In other words, σ_s is the value of $\langle f \rangle/N$ in correspondence of $Y = Y_s$. We can say that Y_s is the fracture extension while σ_s is the fracture strength inducing the breaking process.

The behavior of the system is shown in Fig.6.5, where the dimensionless quantities $\langle f \rangle/(NhY_M)$ and $\langle \xi \rangle/N$ are represented versus the dimensionless extension Y/Y_M. We compared here the response for a large value of N and the thermodynamic limit. In this limit, the breaking is fully brittle with temperature-dependent fracture extension and stress. Thus, as typical in collective phenomena of complex systems, although each breakable spring has a temperature-independent breakage threshold, the overall system exhibits a temperature-dependent fracture point due to the interactions between the springs and the thermal bath. In particular, the system undergoes a phase transition for $T = T_c$, with both fracture extension and stress decreasing to zero at $T = T_c$ when the system breaks without any external mechanical actions. This is described in Fig.6.6, where we plot the dimensionless fracture extension Y_s/Y_M and the dimensionless fracture strength $\sigma_s/(hY_M)$ versus the temperature ratio T/T_c. This critical behavior corresponds to a classical second-order phase transition. We also remark that Eq.(6.39) represents an extension of the Griffith criterion of the linear elastic fracture mechanics, accounting for the additional effects of temperature. From Fig.6.2, we see that the energy necessary to break an element is given by $hY_M^2/2$ and then the Griffith surface energy density γ_s is proportional to $hY_M^2/2$. Equivalently, Y_M is proportional to $\sqrt{\gamma_s}$ and therefore it is easily seen that the fracture strength given in

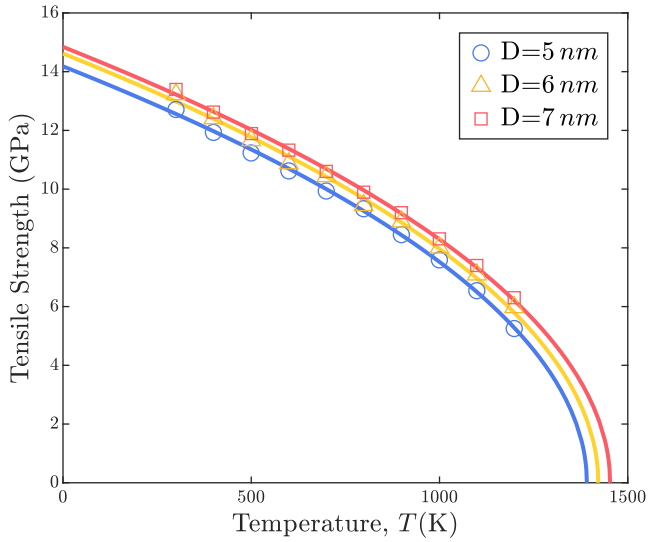

Figure 6.7: Tensile strength of [110]-oriented silicon nanowires as a function of temperature for wires with different diameters: comparison between molecular dynamics simulations results [125] (symbols) and our theory given by Eq.(6.39) (continuous lines). The parameters used are reported in the main text.

Eq.(6.39) is proportional to $\sqrt{\gamma_s}$, exactly as in Griffith's criterion [119]. Moreover, at a constant temperature, it is well seen that the breaking strength decreases if ϕ increases, which is exactly what Griffith's criterion states [119]. This means that, if the initial system is degraded, a smaller force is required to continue its mechanical degradation. Of course, our version is quantitatively different from the original one because of the simplified geometry we used. In particular, we do not consider the exact elastic energy distributed over the deformed continuum due to fracture. Our model, however, introduces thermal effects in brittle fracture and, in particular, shows the phase transition at the critical temperature T_c given in Eq.(6.33).

To show the effectiveness of the obtained results, we analyze the temperature-dependent fracture behavior of [110]-oriented silicon nanowires [125]. In Fig.6.7, we compare the theoretical fracture force given by Eq.(6.39) with the molecular dynamics results discussed in Ref.[125]. We observe that the theory well predicts the brittle fracture behavior of the nanowires both temperature- and diameter-wise (see Fig.4(b) of Ref.[125]). In the figure the theoretical force in Eq.(6.39) has been divided by the area S pertaining to each breakable spring in order to obtain the stress $\sigma = \langle f \rangle / (N\mathsf{S}) = \sigma_s/\mathsf{S}$. The strain has been determined as $\varepsilon = Y/\ell$, where ℓ is the characteristic length scale induced by the crystal structure. For all curves we adopted the parameters $Y_M = 1.78 \times 10^{-11}$m, $\mathsf{S} = 2.27 \times 10^{-21}$m^2, $\ell = 1.82 \times 10^{-10}$m, $k = 88.4$N/m, and $K_B = 1.38 \times 10^{-23}$J/K. Moreover, for the blue curve ($D = 5$nm) we used $l = 9.07$N/m and $h = 2.00$N/m; for the yellow curve ($D = 6$nm) we used $l = 9.54$N/m and $h = 2.05$N/m; for the red curve ($D = 7$nm) we used $l = 9.94$N/m and $h = 2.08$N/m. While most of the geometrical parameters were available in the original paper dealing with molecular dynamics simulations, the other physical parameters (in particular the elastic constants), were fitted to correctly reproduce the results. The elastic constants take effective values pertinent to the springs of our lattices and therefore cannot be directly obtained from the data available in the above papers. Interestingly, all the obtained (fitted) values are reasonable and consistent with the underlying physics of the system. In particular, the fact that h and l increase with the diameter is consistent with the results

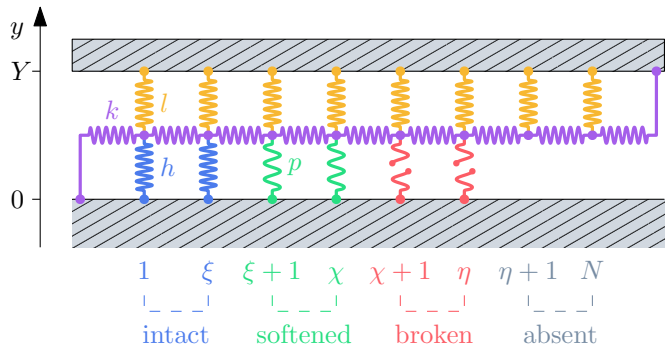

Figure 6.8: Scheme of the fracture model with the softening mechanism. The central chain (colored in purple) is composed of $N+1$ linear springs with elastic constant k. The nodes of this chain are connected to the top layer (at $y=Y$) by N springs with elastic constant l (colored in yellow). The first η nodes ($i=1,\dots,\eta$) are also linked to the bottom layer (at $y=0$) by η softenable and breakable springs with elastic constant h when intact (colored in blue), or p when softened (colored in green). The broken elements are represented in red. We remark that the first node ($i=0$) and the last one ($i=N+1$) are anchored to the bottom and the top layers, respectively.

of Ref.[125], providing evidence that the nanowires Young modulus E increases with the diameter (scale effect). This coherence is also quantitative since in our case we have $E=\ell/[(1/l+1/h)\mathsf{S}]$, which assumes the values 130GPa, 135GPa, and 138GPa, for the three diameters 5nm, 6nm, and 7nm, in agreement with Fig.4(a) of Ref.[125]. The good agreement between theory and simulations makes us confident in the applicability of our theory to micro- and nanoscopic systems.

6.5 Softening-Fracture model

The previous model, useful to describe brittle fracture, is further generalized here to introduce a material ductile behavior of the elements possibly resulting in a brittle-to-ductile transition. Specifically, in the same spirit of the Dugdale-Barenblatt model [134, 135], we introduce a cohesive zone between the elastic and fractured domains of the breakable springs, characterized by two different states before the broken configuration, depending on their extension y_i (see Fig.6.8). More precisely, each breakable spring presents an elastic constant h when its extension is less than the softening point Y_p, and a lower elastic constant $p<h$ for larger extensions until the breaking point corresponding to the extension Y_b is attained and the link is broken (see Fig.6.9). As we can see, each breakable element behaves as a spring of elastic constant h when $-Y_p \le y_i \le Y_p$. Then, the spring is softened with an elastic constant $p<h$ when $Y_p \le |y_i| \le Y_b$. After the breaking point Y_b, the potential energy is constant and therefore the resulting force is zero. Thus, the potential energy of a breakable spring is

$$U(y_i)=\begin{cases}\frac{1}{2}hy_i^2 & \text{if } |y_i|\le Y_p,\\ \frac{1}{2}py_i^2+\Delta E & \text{if } Y_p\le|y_i|\le Y_b,\\ \frac{1}{2}pY_b^2+\Delta E & \text{if } |y_i|\ge Y_b.\end{cases} \tag{6.40}$$

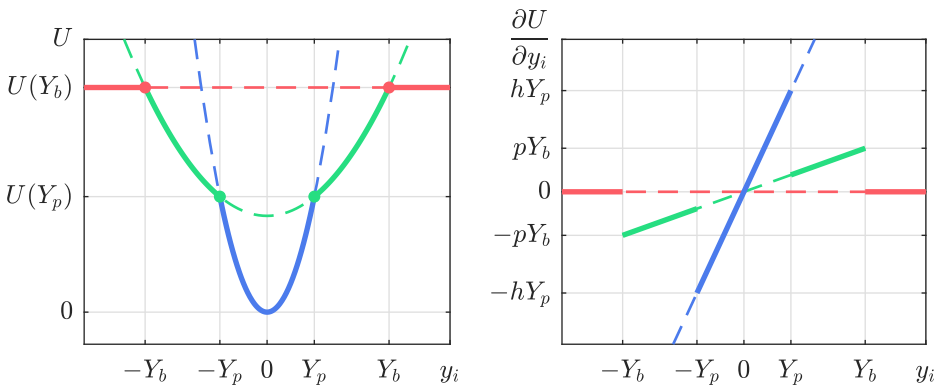

Figure 6.9: Potential energy of a single softenable and breakable spring of elastic constants h and p (continuous curve on the left) and corresponding force (continuous curve on the right). We see that Y_p is the elongation after which the spring is weakened, and Y_b is the elongation after which the spring is broken. The dashed curves correspond to the spin approximation energy landscape.

Given the two elastic moduli h and p (with $p < h$) and the energy gap $\Delta E > 0$, we obtain the softening point

$$Y_p = \sqrt{\frac{2\Delta E}{h-p}}, \tag{6.41}$$

which must always satisfy the condition $Y_p < Y_b$. Thus $\Delta E + pY_p^2/2 = hY_p^2/2$ is the energy necessary to weaken one breakable element of the system, and $\Delta E + pY_b^2/2 = hY_p^2/2 + p(Y_b^2 - Y_p^2)/2$ is the energy necessary to break the element. This reproduces in the discrete context considered here the Irwin generalization of Griffith's criterion [120, 121].

The total energy $\Phi_H(y_1, \ldots, y_N, \xi, \chi)$ of the system is

$$\begin{aligned}\Phi_H = &\sum_{i=0}^{N} \frac{k}{2}(y_{i+1} - y_i)^2 + \sum_{i=1}^{N} \frac{l}{2}(Y - y_i)^2 + \sum_{i=1}^{\xi} \frac{h}{2} y_i^2 \\ &+ \sum_{i=\xi+1}^{\chi} \left(\frac{p}{2} y_i^2 + \Delta E\right) + \sum_{i=\chi+1}^{\eta} \left(\frac{p}{2} Y_b^2 + \Delta E\right).\end{aligned} \tag{6.42}$$

Here we introduced the position ξ of the interface between intact and softened elements, the position χ of the interface between softened and fully broken elements, and, finally, the position η of the interface between fully broken and initially absent elements. The value of η corresponds to the initial state of the system and is therefore fixed. The two interfaces at ξ and χ can move as a function of temperature and mechanical actions in the system. The aim of this section is to study the (quasi-static) evolution of these interfaces determining the fracture propagation phenomenon. The region between ξ and χ, characterized by softened elements, identifies the cohesive zone of the rupture phenomenon. When the cohesive zone is absent or negligible, the fracture is brittle; on the other hand, when the cohesive zone is not negligible, the fracture becomes ductile. Therefore, as we show in the following, this model allows describing the brittle-to-ductile transitions. As in Section 6.2, we remark that the use of the shear springs with elastic constant k is an approximation valid under the small deformation assumption (in our models the central nodes can only move vertically).

We can rewrite Eq.(6.42) as

$$\begin{aligned}\Phi_H = \frac{k}{2}\left[\sum_{i=1}^{N}\left(2+\frac{l}{k}\right)y_i^2 + \sum_{i=1}^{\xi}\frac{h}{k}y_i^2 + \sum_{i=\xi+1}^{\chi}\frac{p}{k}y_i^2 - 2\sum_{i=1}^{N-1}y_{i+1}y_i\right] \\ + kY\left[-\sum_{i=1}^{N}\frac{l}{k}y_i - y_N\right] + \frac{1}{2}kY^2 + \frac{1}{2}lNY^2 \\ + \left(\frac{p}{2}Y_b^2 + \Delta E\right)(\eta-\chi) + (\chi-\xi)\Delta E.\end{aligned} \tag{6.43}$$

As before, to simplify the mathematical structure of the energy function, we introduce the vectors in Eqs.(6.3) and (6.4), and the tridiagonal matrix in Eq.(6.5), where the diagonal elements a_i are now defined as follows

$$a_i = \begin{cases} 2+\alpha & \text{if } 1 \le i \le \xi, \\ 2+\gamma & \text{if } \xi+1 \le i \le \chi, \\ 2+\beta & \text{if } \chi+1 \le i \le N, \end{cases} \tag{6.44}$$

with the parameters

$$\alpha = \frac{l+h}{k}, \quad \beta = \frac{l}{k}, \quad \gamma = \frac{l+p}{k}, \tag{6.45}$$

satisfying the condition $\beta < \gamma < \alpha$. By introducing the matrix $\mathcal{A}$ and the vectors $\mathbf{y}$ and $\mathbf{v}$, we are able to write the total energy as

$$\Phi_H = \frac{k}{2}\mathbf{y}^{\mathsf{T}}\mathcal{A}\mathbf{y} - kY\mathbf{v}^{\mathsf{T}}\mathbf{y} + \frac{k}{2}Y^2 + \frac{l}{2}NY^2 + \frac{p}{2}Y_b^2(\eta-\chi) + (\eta-\xi)\Delta E. \tag{6.46}$$

We suppose to embed the system in a thermal bath at temperature T and, assuming to be not far from the thermodynamic equilibrium, we can evaluate the partition function

$$Z_H(Y) = \sum_{\chi=0}^{\eta}\sum_{\xi=0}^{\chi}\int_{\mathbb{R}^N} e^{-\frac{\Phi_H}{K_BT}}\,\mathrm{d}y_1\ldots\mathrm{d}y_N. \tag{6.47}$$

By using Eq.(6.46), it can be evaluated as

$$Z_H(Y) = \sum_{\chi=0}^{\eta}\sum_{\xi=0}^{\chi}\mathcal{I}_{\xi,\chi}e^{\lambda_{\xi,\chi}}, \tag{6.48}$$

where

$$\lambda_{\xi,\chi} = -\frac{kY^2}{2K_BT} - \frac{lNY^2}{2K_BT} - \frac{\Delta E}{K_BT}(\eta-\xi) - \frac{pY_b^2}{2K_BT}(\eta-\chi), \tag{6.49}$$

and

$$\mathcal{I}_{\xi,\chi} = \int_{\mathbb{R}^N}\exp\left\{-\frac{k}{2K_BT}\mathbf{y}^{\mathsf{T}}\mathcal{A}\mathbf{y} + \frac{kY}{K_BT}\mathbf{v}^{\mathsf{T}}\mathbf{y}\right\}\mathrm{d}y_1\ldots\mathrm{d}y_N. \tag{6.50}$$

Using Eq.(6.12) we get

$$\mathcal{I}_{\xi,\chi} = \sqrt{\frac{(2\pi K_BT)^N}{k^N\det\mathcal{A}}}\exp\left\{\frac{kY^2}{2K_BT}\mathbf{v}^{\mathsf{T}}\mathcal{A}^{-1}\mathbf{v}\right\}. \tag{6.51}$$

Summing up, we obtain the partition function as

$$Z_H(Y) = \sum_{\chi=0}^{\eta}\sum_{\xi=0}^{\chi}\sqrt{\frac{(2\pi K_B T)^N}{k^N \det\mathcal{A}}}e^{-\frac{kY^2}{2K_BT}\left(1+\beta N-\mathbf{v}^{\mathsf{T}}\mathcal{A}^{-1}\mathbf{v}\right)} \times \exp\left\{-\frac{\Delta E}{K_B T}(\eta-\xi)-\frac{pY_b^2}{2K_BT}(\eta-\chi)\right\}. \tag{6.52}$$

In this case, by using Eq.(6.17), we get that the expected value of the applied force is

$$\langle f\rangle = \frac{\sum_{\chi=0}^{\eta}\sum_{\xi=0}^{\chi}(\det\mathcal{A})^{-\frac{1}{2}}\exp\left\{\frac{2\Delta E\xi+pY_b^2\chi-kY^2q}{2K_BT}\right\}q}{\sum_{\chi=0}^{\eta}\sum_{\xi=0}^{\chi}(\det\mathcal{A})^{-\frac{1}{2}}\exp\left\{\frac{2\Delta E\xi+pY_b^2\chi-kY^2q}{2K_BT}\right\}}kY, \tag{6.53}$$

where we used the definition of q in Eq.(6.15). This is the expression for the average value of the force necessary to impose the extension Y to the system. Similarly, we obtain the interfaces positions

$$\langle\xi\rangle = \frac{\sum_{\chi=0}^{\eta}\sum_{\xi=0}^{\chi}(\det\mathcal{A})^{-\frac{1}{2}}\exp\left\{\frac{2\Delta E\xi+pY_b^2\chi-kY^2q}{2K_BT}\right\}\xi}{\sum_{\chi=0}^{\eta}\sum_{\xi=0}^{\chi}(\det\mathcal{A})^{-\frac{1}{2}}\exp\left\{\frac{2\Delta E\xi+pY_b^2\chi-kY^2q}{2K_BT}\right\}}, \tag{6.54}$$

$$\langle\chi\rangle = \frac{\sum_{\chi=0}^{\eta}\sum_{\xi=0}^{\chi}(\det\mathcal{A})^{-\frac{1}{2}}\exp\left\{\frac{2\Delta E\xi+pY_b^2\chi-kY^2q}{2K_BT}\right\}\chi}{\sum_{\chi=0}^{\eta}\sum_{\xi=0}^{\chi}(\det\mathcal{A})^{-\frac{1}{2}}\exp\left\{\frac{2\Delta E\xi+pY_b^2\chi-kY^2q}{2K_BT}\right\}}. \tag{6.55}$$

These results allow us to fully describe the fracture behavior for a ductile material. In particular, based on Eqs.(6.54) and (6.55), we are able to determine when the fracture is brittle, without the region of softened elements, or when the fracture is ductile, *i.e.*, with a non-negligible fraction of softened elements, representing the cohesive region.

We mentioned the Dugdale and Barenblatt models since historically they are the most important approaches to introduce a process zone in fracture phenomena. It is useful to remember that the original Dugdale model has been developed for plane strain conditions. Other approaches have been developed successively to consider plane stress conditions [391, 392]. However, our model is composed of a quasi-one-dimensional lattice of springs that does not allow access to realistic elastic fields in the structure. Hence, it is difficult to quantitatively compare our results with elastic models in both plane stress and plane strain. Moreover, the Dugdale model does not account for hardening phenomena, such as our approach, which is completely linear. In spite of these limitations, the Dugdale model has been generalized for strain-hardening materials [393, 394]. It is also important to remember that the process zone in real situations extends beyond the fracture growth plane, a point neglected in both Dugdale's original model and ours. In real fractures, the actual deformation is represented by a complicated three-dimensional field, completely disregarded in our one-dimensional analysis. To conclude, the purpose of our models

is not to improve aspects related to continuous elastic fields but rather to introduce the effects of temperature into a simplified model. With this in mind, our approaches are not created to replace classical ones but only to inform them of how temperature acts in fracture phenomena.

It is also important to discuss the physical meaning of the softened state of breakable springs. The ductility in metallic materials is related to a population of dislocations originated by the moving crack, generating a damaged zone near the crack tip with degraded elastic properties [395–398]. Since we do not have the possibility to consider realistic dislocations in our model, we introduced the weakened state for the breakable springs, corresponding to the degraded elastic properties of the damaged zone. In the realistic case, the brittle-to-ductile transition is controlled by the competition between continuing the fracture (as in the brittle case) or using an amount of energy to generate dislocations that degrade the material. In our model, we have similar competition between the intact/broken switching (brittle regime) and the intact/softened switching (ductile regime). This competition is strongly influenced by temperature and our model explains this effect in detail. Besides metals, a similar damaged zone, describing the physical state of the material between the intact and the fully broken conditions, has been also observed in different systems including concrete [399], soft materials [400, 401], polymeric networks [86, 402], bones [403].

6.6 Asymptotic behavior of the softening-fracture model

Once again to obtain clearer analytic results, we consider the behavior of systems with large values of N. We have (see Appendix 6.9.2)

$$q \simeq \beta^2 \left(\frac{\xi}{\gamma} - \frac{\xi}{\alpha} - \frac{\chi}{\gamma} + \frac{\chi}{\beta} \right) + \epsilon, \tag{6.56}$$

where ϵ is given in Eq.(6.21), and

$$\frac{\log \det \mathcal{A}}{N} \simeq \log \tau_\beta + \frac{\xi}{N} \log \frac{\tau_\alpha}{\tau_\gamma} + \frac{\chi}{N} \log \frac{\tau_\gamma}{\tau_\beta}, \tag{6.57}$$

where τ_α, τ_β and τ_γ are given in Eq.(6.23), for $s = \alpha, \beta, \gamma$. Thus, we can write the expressions for the average force and the average interface positions as follows

$$\langle f \rangle \simeq \frac{\sum_{\chi=0}^{\eta} \sum_{\xi=0}^{\chi} \left[\beta^2 \left(\frac{\xi}{\gamma} - \frac{\xi}{\alpha} - \frac{\chi}{\gamma} + \frac{\chi}{\beta} \right) + \epsilon \right] e^{q_\xi \xi + q_\chi \chi}}{\sum_{\chi=0}^{\eta} \sum_{\xi=0}^{\chi} e^{q_\xi \xi + q_\chi \chi}} kY, \tag{6.58}$$

$$\langle \xi \rangle \simeq \frac{\sum_{\chi=0}^{\eta} \sum_{\xi=0}^{\chi} \xi e^{q_\xi \xi + q_\chi \chi}}{\sum_{\chi=0}^{\eta} \sum_{\xi=0}^{\chi} e^{q_\xi \xi + q_\chi \chi}}, \tag{6.59}$$

$$\langle \chi \rangle \simeq \frac{\sum_{\chi=0}^{\eta} \sum_{\xi=0}^{\chi} \chi e^{q_\xi \xi + q_\chi \chi}}{\sum_{\chi=0}^{\eta} \sum_{\xi=0}^{\chi} e^{q_\xi \xi + q_\chi \chi}}, \tag{6.60}$$

where we introduced the quantities

$$q_\xi = -\frac{1}{2}\log\frac{\tau_\alpha}{\tau_\gamma} - \frac{kY^2\beta^2}{2K_BT}\left(\frac{1}{\gamma}-\frac{1}{\alpha}\right) + \frac{\Delta E}{K_BT}, \tag{6.61}$$

$$q_\chi = -\frac{1}{2}\log\frac{\tau_\gamma}{\tau_\beta} - \frac{kY^2\beta^2}{2K_BT}\left(\frac{1}{\beta}-\frac{1}{\gamma}\right) + \frac{pY_b^2}{2K_BT}. \tag{6.62}$$

Using the expressions for $\langle\xi\rangle$ and $\langle\chi\rangle$, we can rewrite $\langle f\rangle$ in the simpler form

$$\langle f\rangle \simeq \left[\epsilon + \beta^2\left(\frac{1}{\gamma}-\frac{1}{\alpha}\right)\langle\xi\rangle + \beta^2\left(\frac{1}{\beta}-\frac{1}{\gamma}\right)\langle\chi\rangle\right] kY. \tag{6.63}$$

Hence, once we know the expected values $\langle\xi\rangle$ and $\langle\chi\rangle$ of the interfaces positions, we also know the force required to impose the extension Y. To simplify the notation, we introduce

$$w = e^{q_\xi}, \quad z = e^{q_\chi}. \tag{6.64}$$

By Eqs.(6.59) and (6.60), using Eqs.(6.29) and (6.30),after long but straightforward calculations, we obtain

$$\langle\xi\rangle = \frac{N_\xi}{D}, \quad \langle\chi\rangle = \frac{N_\chi}{D}, \tag{6.65}$$

where, for the sake of readability, we introduced

$$\begin{aligned} N_\xi = \frac{w}{1-w}\Bigg\{ & \frac{1-z^{\eta+1}}{1-z} - \frac{1-(wz)^{\eta+1}}{1-wz} \\ & - \frac{(1-w)wz}{(1-wz)^2}\left[1-(wz)^\eta(1+\eta)+\eta(wz)^{\eta+1}\right]\Bigg\}, \end{aligned} \tag{6.66}$$

$$\begin{aligned} N_\chi = {} & \frac{z}{(1-z)^2}\left[1-z^\eta(1+\eta)+\eta z^{\eta+1}\right] \\ & - \frac{w^2 z}{(1-wz)^2}\left[1-(wz)^\eta(1+\eta)+\eta(wz)^{\eta+1}\right], \end{aligned} \tag{6.67}$$

$$D = \frac{1-z^{\eta+1}}{1-z} - w\frac{1-(wz)^{\eta+1}}{1-wz}. \tag{6.68}$$

These results approximate the behavior of the fracture process in the presence of the softening phenomenon for large values of N. In particular, we can determine the limit for $N\to\infty$ of the main observables, in order to provide a precise physical interpretation of the brittle-to-ductile transition. The obtained expressions depend on w^η, z^η, and $(wz)^\eta$ and, since in our model $\eta = N(1-\phi)$ where ϕ is the fraction of initially absent breakable springs, they present an exponent going to infinity when $N\to\infty$. We know that when $N\to\infty$, a generic power x^N tends to infinity if $x>1$ and tends to zero if $|x|<1$, hence we study the three inequalities $w>1$, $z>1$ and $wz>1$, which will be useful to better understand the system behavior. These inequalities are equivalent to studying the positive character of their exponents q_ξ, q_χ, and $q_\xi+q_\chi$.

We start by setting the exponent of w larger than zero

$$q_\xi = -\frac{1}{2}\log\frac{\tau_\alpha}{\tau_\gamma} - \frac{kY^2\beta^2}{2K_BT}\left(\frac{1}{\gamma}-\frac{1}{\alpha}\right) + \frac{\Delta E}{K_BT} > 0. \tag{6.69}$$

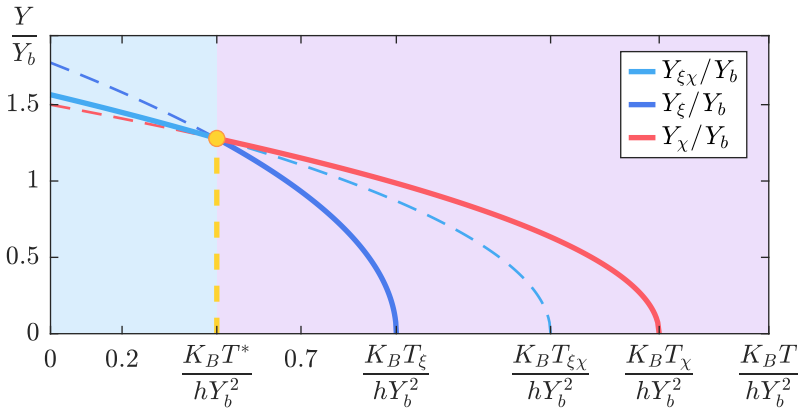

Figure 6.10: Behavior of the three dimensionless extension thresholds Y_ξ/Y_b, Y_χ/Y_b and $Y_{\xi\chi}/Y_b$ versus the dimensionless temperature $K_BT/(hY_b^2)$ of the system. From the physical point of view, $Y_{\xi\chi}$ describes the brittle fracture below the transition temperature T^* (light blue shaded area on the left), and the couple (Y_ξ, Y_χ) describes the ductile fracture above the temperature T^* (pink shaded area on the right). The three curves Y_ξ/Y_b, Y_χ/Y_b and $Y_{\xi\chi}/Y_b$ versus $K_BT/(hY_b^2)$ intersect at the bifurcation point (yellow), characterized by T^*. We adopted the parameters $\alpha = 7/5$, $\beta = 2/5$, $\gamma = 9/10$, and $\Delta E/(hY_b^2) = 1/10$.

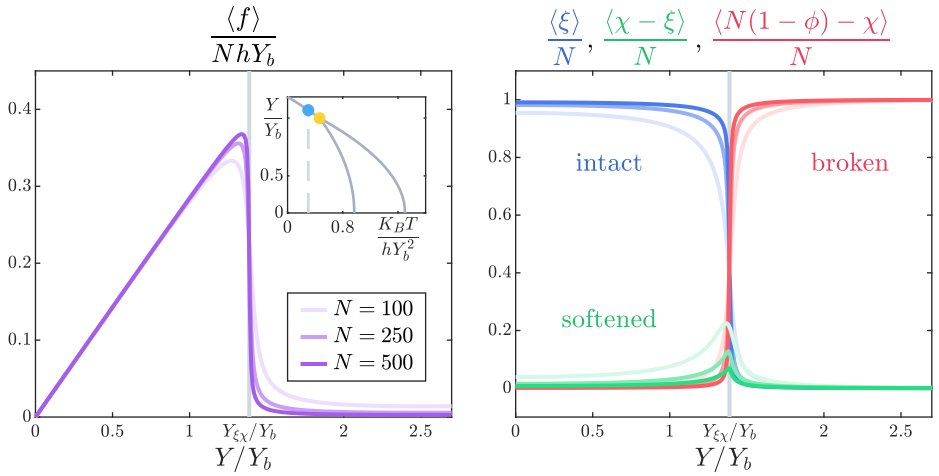

Figure 6.11: Brittle response of the fracture phenomenon ($0 < T < T^*$). Left panel: dimensionless force versus dimensionless extension for different values of N. Right panel: fraction of intact, softened and broken elements for different values of N. Inset: same plot as Fig.6.10, where the temperature used here is indicated (light blue point). Here, the yellow point represents the bifurcation shown in Fig.6.10. We adopted the parameters $\alpha = 7/5$, $\beta = 2/5$, $\gamma = 9/10$, $\Delta E/(hY_b^2) = 1/10$, $\phi = 0$ (*i.e.*, $\eta = N$), and $K_BT/(hY_b^2) = 3/10$.

In terms of Y, this inequality gives

$$|Y| < \sqrt{\frac{1}{k\beta^2\left(\frac{1}{\gamma}-\frac{1}{\alpha}\right)}\left[(h-p)Y_p^2 - K_B T \log\frac{\tau_\alpha}{\tau_\gamma}\right]} \triangleq Y_\xi, \tag{6.70}$$

where we introduced a first extension threshold Y_ξ. We observe that $k\beta^2\left(\frac{1}{\gamma}-\frac{1}{\alpha}\right)$ is always positive because $p<h$ by definition and, then, the argument of the square root is positive when the temperature T is smaller than the critical temperature T_ξ defined as

$$T_\xi = \frac{(h-p)Y_p^2}{K_B \log\frac{\tau_\alpha}{\tau_\gamma}}. \tag{6.71}$$

The meaning of Y_ξ and T_ξ will be clarified later. By setting the exponent of z greater than zero, we define the inequality

$$q_\chi = -\frac{1}{2}\log\frac{\tau_\gamma}{\tau_\beta} - \frac{kY^2\beta^2}{2K_B T}\left(\frac{1}{\beta}-\frac{1}{\gamma}\right) + \frac{pY_b^2}{2K_B T} > 0. \tag{6.72}$$

It can be solved with respect to Y, eventually giving the result

$$|Y| < \sqrt{\frac{1}{k\beta^2\left(\frac{1}{\beta}-\frac{1}{\gamma}\right)}\left[pY_b^2 - K_B T \log\frac{\tau_\gamma}{\tau_\beta}\right]} \triangleq Y_\chi, \tag{6.73}$$

where we introduced a second extension threshold Y_χ. As before, the quantity $k\beta^2\left(\frac{1}{\beta}-\frac{1}{\gamma}\right)$ is always positive, and therefore the whole square root argument is positive for values of the temperature below the critical temperature T_χ defined as

$$T_\chi = \frac{pY_b^2}{K_B \log\frac{\tau_\gamma}{\tau_\beta}}. \tag{6.74}$$

As before, Y_χ and T_χ will be physically interpreted in the following. Finally, we set the exponent of wz greater than zero, which corresponds to $q_\xi + q_\chi > 0$. We obtain the inequality

$$|Y| < \sqrt{\frac{1}{k\beta^2\left(\frac{1}{\beta}-\frac{1}{\alpha}\right)}\left[pY_b^2 + (h-p)Y_p^2 - K_B T \log\frac{\tau_\alpha}{\tau_\beta}\right]} \triangleq Y_{\xi\chi}, \tag{6.75}$$

where we introduced a third extension threshold $Y_{\xi\chi}$. Being $k\beta^2\left(\frac{1}{\beta}-\frac{1}{\alpha}\right)$ always positive, the square root has a positive argument when $T < T_{\xi\chi}$, where

$$T_{\xi\chi} = \frac{pY_b^2 + (h-p)Y_p^2}{K_B \log\frac{\tau_\alpha}{\tau_\beta}}. \tag{6.76}$$

Again, we will discuss soon the physical meaning of $Y_{\xi\chi}$ and $T_{\xi\chi}$. Summarizing these results, we

can write

$$\begin{cases} w > 1 \\ q_\xi > 0 \end{cases} \iff |Y| < \sqrt{\frac{(l+p)(l+h)Y_p^2}{l^2}\left(1-\frac{T}{T_\xi}\right)}, \tag{6.77}$$

$$\begin{cases} z > 1 \\ q_\chi > 0 \end{cases} \iff |Y| < \sqrt{\frac{(l+p)Y_b^2}{l}\left(1-\frac{T}{T_\chi}\right)}, \tag{6.78}$$

$$\begin{cases} wz > 1 \\ q_\xi + q_\chi > 0 \end{cases} \iff |Y| < \sqrt{\frac{pY_b^2+(h-p)Y_p^2}{\frac{lh}{l+h}}\left(1-\frac{T}{T_{\xi\chi}}\right)}, \tag{6.79}$$

where we used the definition for the critical temperatures T_ξ, T_χ and $T_{\xi\chi}$ previously introduced.

The three dimensionless extension thresholds Y_ξ/Y_b, Y_χ/Y_b and $Y_{\xi\chi}/Y_b$ are plotted versus the dimensionless temperature $K_BT/(hY_b^2)$ in Fig.6.10. We can already anticipate that brittle or ductile behavior depends on the sign of $Y_\chi - Y_\xi$. Indeed, we have a brittle fracture if $Y_\chi < Y_\xi$ (light blue shaded area in Fig.6.10), and a ductile fracture if $Y_\chi > Y_\xi$ (pink shaded area in Fig.6.10). In the first brittle case, the rupture occurs for $Y = Y_{\xi\chi}$. In the second ductile case, the softening occurs for $Y = Y_\xi$ and rupture for $Y = Y_\chi$. We observe therefore that exists a brittle-to-ductile transition temperature T^* that separates the brittle behavior from the ductile one (see the yellow point in Fig.6.10). This temperature is defined by equating Y_ξ and Y_χ, as follows

$$\sqrt{\frac{(h-p)Y_p^2}{k\beta^2\left(\frac{1}{\gamma}-\frac{1}{\alpha}\right)}\left(1-\frac{T^*}{T_\xi}\right)} = \sqrt{\frac{pY_b^2}{k\beta^2\left(\frac{1}{\beta}-\frac{1}{\gamma}\right)}\left(1-\frac{T^*}{T_\chi}\right)}. \tag{6.80}$$

When solved, this equation gives the value of T^* as

$$\frac{K_BT^*}{hY_b^2} = \frac{\left(\frac{1}{\alpha-\beta}\right)\left[\alpha\left(\frac{Y_p}{Y_b}\right)^2-\beta\right]}{\left(\frac{\alpha}{\alpha-\gamma}\right)\log\frac{\tau_\alpha}{\tau_\gamma}-\left(\frac{\beta}{\gamma-\beta}\right)\log\frac{\tau_\gamma}{\tau_\beta}}. \tag{6.81}$$

Interestingly, this quantity can be also explicitly written in terms of the elastic constants of the system

$$T^* = \frac{(l+h)Y_p^2 - lY_b^2}{K_B\left(\frac{l+h}{h-p}\log\frac{\tau_\alpha}{\tau_\gamma}-\frac{l}{p}\log\frac{\tau_\gamma}{\tau_\beta}\right)}. \tag{6.82}$$

To justify the introduction of all these quantities and notations, we use now Eqs.(6.63) and (6.65) to observe the behavior of the system with different values of N and temperature T. In particular, we consider Fig.6.10 and we show the system behavior for three values of the temperature belonging to the regions $0 < T < T^*$ (brittle response, Fig.6.11), $T^* < T < T_\xi$ (ductile response, Fig.6.12), and $T_\xi < T < T_\chi$ (over-ductile response, Fig.6.13). We do not consider values of the temperature larger than T_χ since, in this case, all elements are broken due to only thermal effects, without the application of mechanical actions.

In Fig.6.11, we can find the dimensionless force given by Eq.(6.63) in the first panel, and the three quantities $\langle\xi\rangle/N$, $\langle\chi-\xi\rangle/N$ and $\langle N(1-\phi)-\chi\rangle/N$ representing the fraction of intact, softened and broken elements, calculated through Eqs.(6.65), respectively, in the second panel. For simplicity, we always considered $\phi = 0$. Note that the dimensionless force is divided by N so as to be consistent with the definition of mechanical stress. We can see that, with a temperature

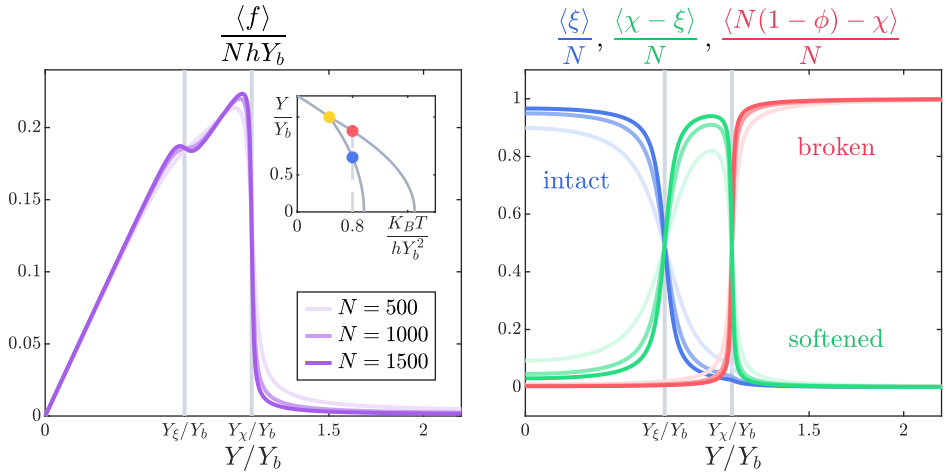

Figure 6.12: Ductile response of the fracture phenomenon ($T^* < T < T_\xi$). Left panel: dimensionless force versus dimensionless extension for different values of N. Right panel: fraction of intact, softened, and broken elements for different values of N. Inset: same plot as Fig.6.10, where the temperature used here is indicated (blue and red points). Here, the yellow point represents the bifurcation shown in Fig.6.10. We adopted the parameters $\alpha = 7/5$, $\beta = 2/5$, $\gamma = 9/10$, $\Delta E/(hY_b^2) = 1/10$, $\phi = 0$ (*i.e.*, $\eta = N$), and $K_BT/(hY_b^2) = 4/5$.

in the range $0 < T < T^*$, the force drops to zero in correspondence to the extension threshold $Y_{\xi\chi}$, describing the simultaneous rupture of all elements. Indeed, it can be seen in the second panel that the elements change almost completely from intact to broken state, with a fraction of softened elements that is negligible. The response becomes increasingly sharp as the value of N increases. In particular, the fraction of softened elements decreases to zero for N growing. A direct transition from intact to broken elements without an intermediate phase is therefore observed. This confirms that the response is brittle for $T < T^*$ and the rupture of the system occur in this case at the applied extension $Y_{\xi\chi}$.

In Fig.6.12, we represent the same functions for a temperature in the range $T^* < T < T_\xi$. In this case, we observe an almost simultaneous transition of all breakable elements from the intact to the softened state at the extension Y_ξ and a subsequent transition from the softened to the broken state at the threshold Y_χ. This behavior reproduces a ductile fracture, and the intermediate phase, characterized by the softened elements, mimics the cohesive phase of the fracture phenomenon. Also, in the force-extension diagram, we see a first peak in correspondence to the softening of the elements, and a second peak describing the actual rupture. This curve is sharper for high values of N and smoother for low values. The comparison of Figs.6.11 and 6.12 shows the transition from a brittle to a ductile fracture as temperature increases, T^* being the threshold temperature between the two regimes. This transition is described by the bifurcation at T^* exhibited in Fig.6.10 (see the yellow point), which gives rise to the intermediate region with softened elements.

To complete the picture of the system behavior, we also show in Fig.6.13 the extreme situation when the temperature is in the range $T_\xi < T < T_\chi$ (over-ductile response). Since the temperature is larger than T_ξ, at the beginning of the traction almost all elements are already in the softened state even without an applied mechanical action. As a result, we can observe only one transition between the softened state and the broken state at the extension threshold Y_χ. Consequently, in this temperature range, we observe a brittle transition between thermally-softened and broken

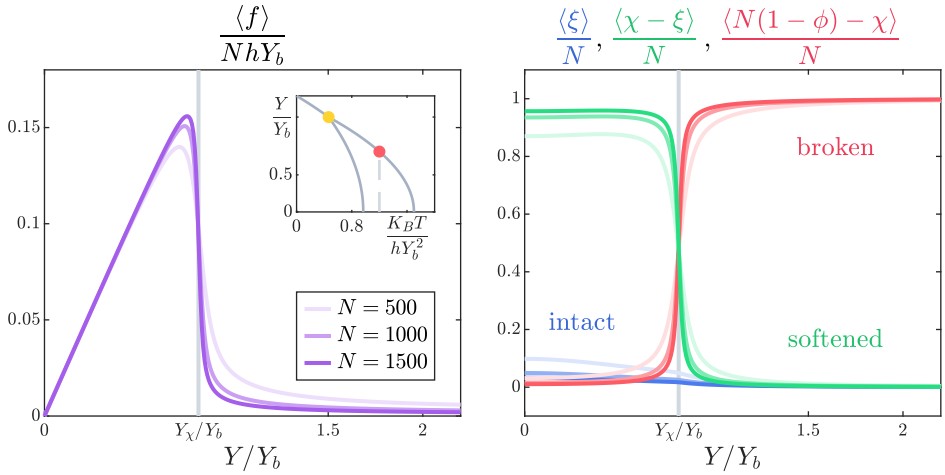

Figure 6.13: Over-ductile response of the fracture phenomenon ($T_\xi < T < T_\chi$). Left panel: dimensionless force versus dimensionless extension for different values of N. Right panel: fraction of intact, softened, and broken elements for different values of N. Inset: same plot as Fig.6.10, where the temperature used here is indicated (the red point). Here, the yellow point represents the bifurcation shown in Fig.6.10. We adopted the parameters $\alpha = 7/5$, $\beta = 2/5$, $\gamma = 9/10$, $\Delta E/(hY_b^2) = 1/10$, $\phi = 0$ (*i.e.*, $\eta = N$), and $K_BT/(hY_b^2) = 6/5$.

elements. Since this response is observed only after the classical ductile behavior, we called it an over-ductile response.

To better visualize the transitions between the different fracture regimes, we show in Fig.6.14 some force-extension curves corresponding to different temperatures, spanning over brittle, ductile, and over-ductile regimes. It is interesting to remark that, within the ductile fracture, the shape of the force-extension curve is smoother in correspondence to the system softening/breaking since the cohesive phase is able to absorb an amount of energy before the final rupture. We also note that, within the ductile regime, the softening stress is higher than the failure stress for lower temperatures and conversely the softening stress becomes lower than the failure stress for higher temperatures. This point will be further discussed below. It is important to underline that all curves seen in Figs.6.11, 6.12, 6.13, and 6.14 have been obtained through Eqs.(6.63) and (6.65) with a large, but finite value of N. In the following, we also describe the thermodynamic limit $N \to \infty$.

What has been described so far represents the modeling of brittle-to-ductile transition induced by thermal fluctuations. Our model also allows us to describe a parametric brittle-to-ductile transition, *i.e.*, intrinsic to the structure of the system. This means that there can be systems that exhibit only brittle or ductile behavior, regardless of temperature. On the one hand, an example of an always brittle system is shown in Fig.6.15, left panel, where we represent the three dimensionless extension thresholds Y_ξ/Y_b, Y_χ/Y_b and $Y_{\xi\chi}/Y_b$ versus the dimensionless temperature $K_BT/(hY_b^2)$. We can see that $Y_\chi < Y_{\xi\chi} < Y_\xi$ for any value of the temperature. This means that there is no temperature high enough to induce a ductile fracture ($T^* > T_\xi$). On the other hand, an example of an always ductile system is shown in Fig.6.15, right panel. In this case, $Y_\chi > Y_{\xi\chi} > Y_\xi$ for any value of the temperature so that there is no temperature low enough to induce a brittle fracture ($T^* < 0$). These two situations describe materials that are always brittle or always ductile, regardless of the considered temperature.

To conclude, we obtained two types of brittle-to-ductile transitions: a *thermal* transition,

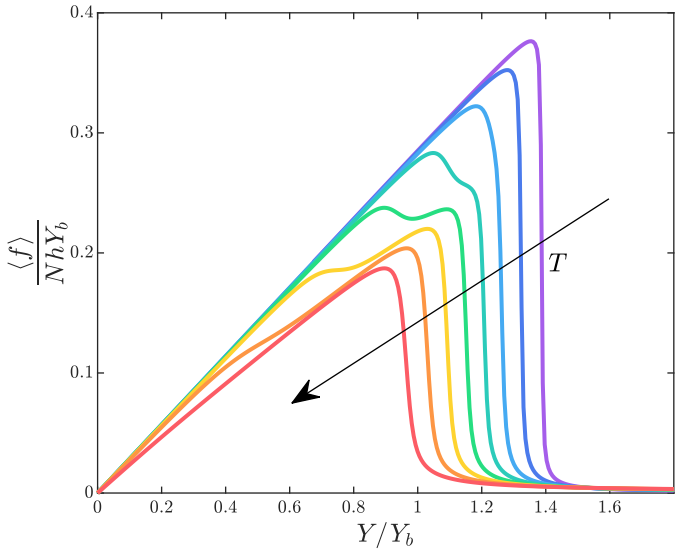

Figure 6.14: Dimensionless force versus dimensionless extension for different values of the thermal to elastic energy ratio $K_BT/(hY_b^2) = \{0.3, 0.4, 0.5, 0.6, 0.7, 0.8, 0.9, 1\}$ (from purple to red curves). We observe that the behavior of the model changes from brittle, at low values of temperature, ductile for intermediate temperatures, to over ductile at high temperatures. We adopted the parameters $N = 1000$, $\alpha = 7/5$, $\beta = 2/5$, $\gamma = 9/10$, $\phi = 0$, and $\Delta E/(hY_b^2) = 1/10$.

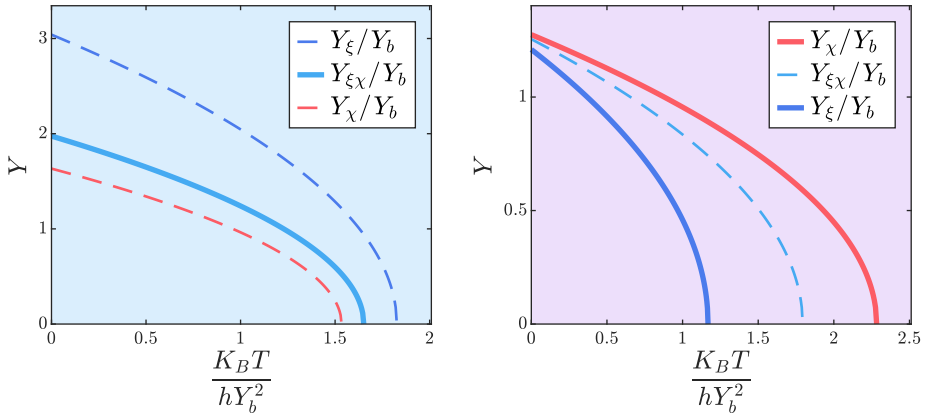

Figure 6.15: Behavior of the dimensionless extension thresholds Y_ξ/Y_b, Y_χ/Y_b and $Y_{\xi\chi}/Y_b$ versus the dimensionless temperature $K_BT/(hY_b^2)$ for a system always brittle (left panel), and for a system always ductile (right panel). In the left panel we have $Y_\chi < Y_{\xi\chi} < Y_\xi$ and we adopted the parameters $\alpha = 13/10$, $\beta = 3/10$, $\gamma = 4/5$, and $\Delta E/(hY_b^2) = 1/5$. In the right panel we have $Y_\chi > Y_{\xi\chi} > Y_\xi$ and we adopted the parameters $\alpha = 9/5$, $\beta = 4/5$, $\gamma = 13/10$, and $\Delta E/(hY_b^2) = 1/10$.

induced by the effects of thermal fluctuations, and a *parametric* transition, induced by the values of the elastic parameters. It is worth pointing out that this rather rich fracture behavior has been obtained based on a minimal system depending on the competition between elastic, entropic, and fracture energy terms, regulated by the temperature and material parameters.

6.7 Thermodynamic limit of the softening-fracture model

To give an even clearer physical description, we deduce here analytic results in the thermodynamical limit, $N \to \infty$. We start the analysis by examining the average value of the number of intact, softened, and broken elements of the system. If we consider the brittle behavior, with $0 < T < T^*$, the thermodynamic limit gives

$$\lim_{N\to\infty} \frac{\langle \xi \rangle}{N} = \begin{cases} 1-\phi & \text{if } Y < Y_{\xi\chi}, \\ 0 & \text{if } Y > Y_{\xi\chi}, \end{cases} \tag{6.83}$$

$$\lim_{N\to\infty} \frac{\langle \chi - \xi \rangle}{N} = 0 \quad \forall\, Y, \tag{6.84}$$

$$\lim_{N\to\infty} \frac{\langle N(1-\phi) - \chi \rangle}{N} = \begin{cases} 0 & \text{if } Y < Y_{\xi\chi}, \\ 1-\phi & \text{if } Y > Y_{\xi\chi}. \end{cases} \tag{6.85}$$

In this case, we observe a direct transition between intact and broken elements without going through the softened state. However, if we take into account the ductile behavior with $T^* < T < T_\xi$, we obtain for $N \to \infty$

$$\lim_{N\to\infty} \frac{\langle \xi \rangle}{N} = \begin{cases} 1-\phi & \text{if } Y < Y_{\xi}, \\ 0 & \text{if } Y > Y_{\xi}, \end{cases} \tag{6.86}$$

$$\lim_{N\to\infty} \frac{\langle \chi - \xi \rangle}{N} = \begin{cases} 0 & \text{if } Y < Y_{\xi}, \\ 1-\phi & \text{if } Y_\xi < Y < Y_\chi, \\ 0 & \text{if } Y > Y_{\chi}, \end{cases} \tag{6.87}$$

$$\lim_{N\to\infty} \frac{\langle N(1-\phi) - \chi \rangle}{N} = \begin{cases} 0 & \text{if } Y < Y_{\chi}, \\ 1-\phi & \text{if } Y > Y_{\chi}. \end{cases} \tag{6.88}$$

In this case, we observe the emergence of a region with softened elements, corresponding to the cohesive zone. Finally, the over-ductile regime, characterized by $T_\xi < T < T_\chi$, for $N \to \infty$ leads to

$$\lim_{N\to\infty} \frac{\langle \xi \rangle}{N} = 0 \quad \forall\, Y, \tag{6.89}$$

$$\lim_{N\to\infty} \frac{\langle \chi - \xi \rangle}{N} = \begin{cases} 1-\phi & \text{if } Y < Y_{\chi}, \\ 0 & \text{if } Y > Y_{\chi}, \end{cases} \tag{6.90}$$

$$\lim_{N\to\infty} \frac{\langle N(1-\phi) - \chi \rangle}{N} = \begin{cases} 0 & \text{if } Y < Y_{\chi}, \\ 1-\phi & \text{if } Y > Y_{\chi}. \end{cases} \tag{6.91}$$

In this regime, all elements are initially softened and therefore the single transition corresponds to their complete breaking.

Concerning the expected value of the force, from Eq.(6.63), we can write

$$\lim_{N\to\infty}\frac{\langle f\rangle}{N}=\left[\beta^2\left(\frac{1}{\gamma}-\frac{1}{\alpha}\right)\frac{\langle\xi\rangle}{N}+\beta^2\left(\frac{1}{\beta}-\frac{1}{\gamma}\right)\frac{\langle\chi\rangle}{N}\right]kY, \tag{6.92}$$

where we can substitute the values of $\langle\xi\rangle/N$ and $\langle\chi\rangle/N$ pertinent to each fracture regime. We remark that in Eq.(6.92), we have canceled out the first term shown in Eq.(6.63) since $N\to\infty$. For the brittle behavior ($0<T<T^*$), we have

$$\lim_{N\to\infty}\frac{\langle f\rangle}{N}=\begin{cases}\beta^2(1-\phi)\left(\frac{1}{\beta}-\frac{1}{\alpha}\right)kY & \text{if } Y<Y_{\xi\chi},\\ 0 & \text{if } Y>Y_{\xi\chi}.\end{cases} \tag{6.93}$$

For the ductile behavior ($T^*<T<T_\xi$), we have

$$\lim_{N\to\infty}\frac{\langle f\rangle}{N}=\begin{cases}\beta^2(1-\phi)\left(\frac{1}{\beta}-\frac{1}{\alpha}\right)kY & \text{if } Y<Y_{\xi},\\ \beta^2(1-\phi)\left(\frac{1}{\beta}-\frac{1}{\gamma}\right)kY & \text{if } Y_\xi<Y<Y_\chi,\\ 0 & \text{if } Y>Y_\chi.\end{cases} \tag{6.94}$$

Finally, for the over-ductile behavior ($T_\xi<T<T_\chi$), we get

$$\lim_{N\to\infty}\frac{\langle f\rangle}{N}=\begin{cases}\beta^2(1-\phi)\left(\frac{1}{\beta}-\frac{1}{\gamma}\right)kY & \text{if } Y<Y_{\chi},\\ 0 & \text{if } Y>Y_{\chi}.\end{cases} \tag{6.95}$$

The thermodynamic limit behavior ($N\to\infty$) of the intact, softened, and broken elements together with the value of the stress $\langle f\rangle/N$ is exhibited in Fig.6.16, where all the three fracture regimes brittle, ductile and over-ductile are considered. We remark that the resulting overall picture is coherent with the plots in Figs.6.11, 6.12, 6.13, where the same quantities were represented for large, but finite values of N.

These results allow us to identify the values of stress corresponding to behavioral transitions. In the brittle regime ($0<T<T^*$) we identify the fracture or breaking stress corresponding to $\sigma_B=\lim_{N\to\infty}\langle f\rangle/N$, for $Y=Y_{\xi\chi}$, which assumes the value

$$\begin{aligned}\sigma_B&=(1-\phi)\sqrt{k\beta^2\left(\frac{1}{\beta}-\frac{1}{\alpha}\right)\left[pY_b^2+(h-p)Y_p^2\right]\left(1-\frac{T}{T_{\xi\chi}}\right)}\\&=(1-\phi)\sqrt{\frac{lh}{l+h}\left[pY_b^2+(h-p)Y_p^2\right]\left(1-\frac{T}{T_{\xi\chi}}\right)},\end{aligned} \tag{6.96}$$

depending on the critical temperature $T_{\xi\chi}$ (see fourth row, first panel, of Fig.6.16). In the ductile regime ($T^*<T<T_\xi$), we have a first transition coinciding with the softening of all elements. It represents the beginning of the plastic regime. Two different values of stress describe this transition: the upper yield strength $\sigma_S^+=\lim_{N\to\infty}\langle f\rangle/N$ (for $Y=Y_\xi^-$, *i.e.* on the left of Y_ξ),

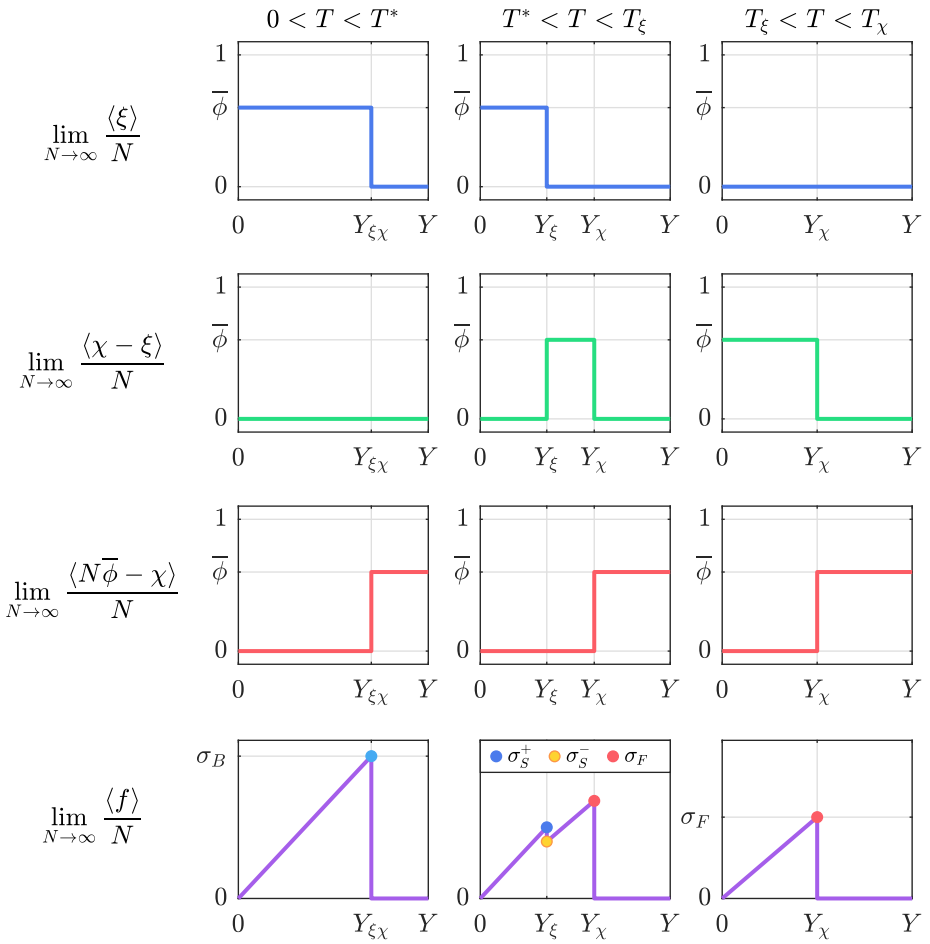

Figure 6.16: Response of the system in the thermodynamic limit within the three temperature regimes $0 < T < T^*$ (brittle, first column), $T^* < T < T_\xi$ (ductile, second column), and $T_\xi < T < T_\chi$ (over-ductile, third column). We plotted the average number of intact, softened, and broken elements, and the stress $\langle f \rangle / N$, for $N \to \infty$. To compact the notation, we defined $\bar{\phi} = 1 - \phi$, and we introduced the characteristic stresses σ_B, σ_S^+, σ_S^-, and σ_F, as defined in Eqs.(6.96), (6.97), (6.98) and (6.100).

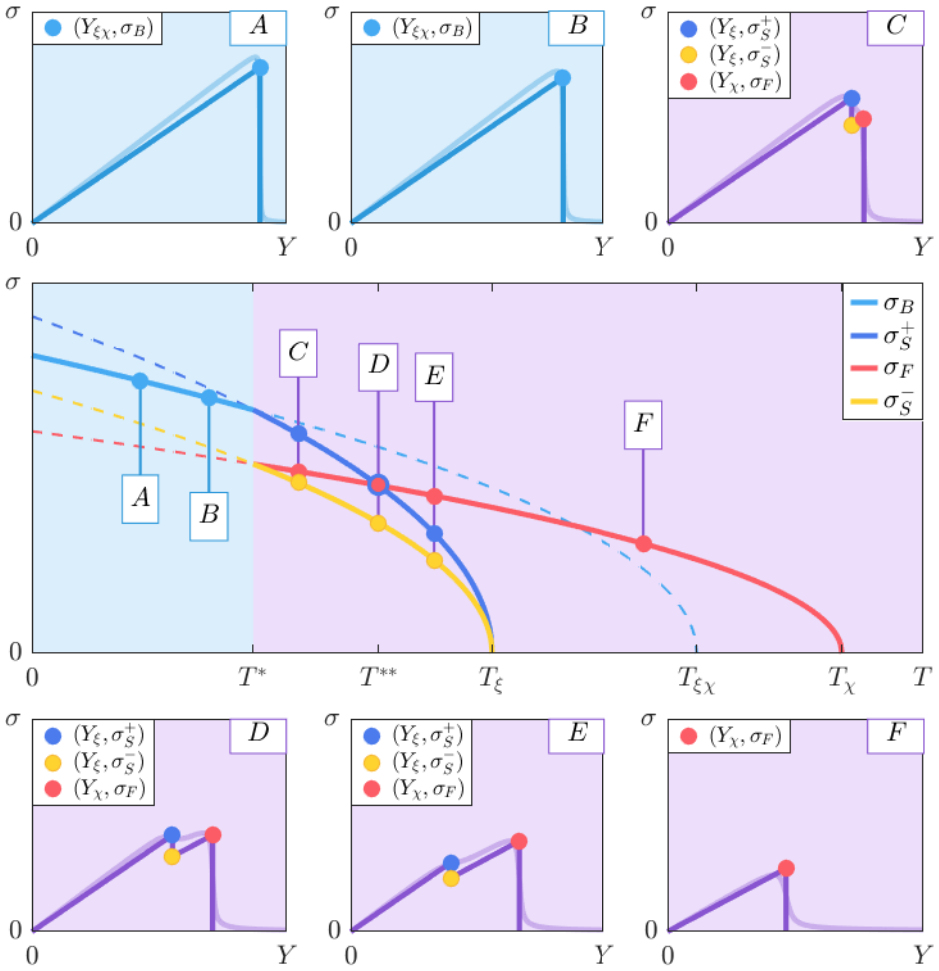

Figure 6.17: Behavior of the characteristic stresses σ_B, σ_S^+, σ_S^-, and σ_F versus the temperature T, as defined in Eqs.(6.96), (6.97), (6.98) and (6.100) with $\phi = 0$. Moreover, some stress-extension curves are plotted in correspondence with the following values of the temperature: A) $0 < T < T^*$; B) $T = (T^*)^-$ (on the left of T^*); C) $T = (T^*)^+$ (on the right of T^*); D) $T = T^{**}$; E) $T^{**} < T < T_\xi$; F) $T_\xi < T < T_\chi$. While the temperature T^* indicates the switching between brittle and ductile behavior, see Eq.(6.82), the temperature T^{**} corresponds to $\sigma_S^+ = \sigma_F$, see Eq.(6.101). In panels A), B), C), D), E), and F) we also show the stress-extension response for $N = 1000$ (soft colors).

and the lower yield strength $\sigma_S^- = \lim_{N\to\infty}\langle f\rangle/N$ (for $Y = Y_\xi^+$, *i.e.* on the right of Y_ξ), given by

$$\begin{aligned}\sigma_S^+ &= (1-\phi)\sqrt{k\beta^2\frac{\left(\frac{1}{\beta}-\frac{1}{\alpha}\right)^2}{\frac{1}{\gamma}-\frac{1}{\alpha}}(h-p)Y_p^2\left(1-\frac{T}{T_\xi}\right)}\\ &= (1-\phi)\sqrt{h^2\frac{l+p}{l+h}Y_p^2\left(1-\frac{T}{T_\xi}\right)},\end{aligned} \tag{6.97}$$

$$\begin{aligned}\sigma_S^- &= (1-\phi)\sqrt{k\beta^2\frac{\left(\frac{1}{\beta}-\frac{1}{\gamma}\right)^2}{\frac{1}{\gamma}-\frac{1}{\alpha}}(h-p)Y_p^2\left(1-\frac{T}{T_\xi}\right)}\\ &= (1-\phi)\sqrt{p^2\frac{l+h}{l+p}Y_p^2\left(1-\frac{T}{T_\xi}\right)},\end{aligned} \tag{6.98}$$

which depend on the critical temperature T_ξ (see fourth row, second panel, of Fig.6.16). These two values are useful to calculate the stress jump corresponding to the softening mechanism (yielding) within the ductile regime

$$\sigma_S^+ - \sigma_S^- = (1-\phi)Y_p\frac{l(h-p)}{\sqrt{(l+h)(l+p)}}\sqrt{1-\frac{T}{T_\xi}}, \tag{6.99}$$

which is always positive since $h > p$. Still in the ductile regime ($T^* < T < T_\xi$), we observe the second transition describing the complete failure of all the elements for a stress $\sigma_F = \lim_{N\to\infty}\langle f\rangle/N$, for $Y = Y_\chi$, assuming the value

$$\begin{aligned}\sigma_F &= (1-\phi)\sqrt{k\left(\frac{1}{\beta}-\frac{1}{\gamma}\right)p\left(1-\frac{T}{T_\chi}\right)}\beta Y_b\\ &= (1-\phi)\sqrt{\frac{l}{l+p}\left(1-\frac{T}{T_\chi}\right)}pY_b^2,\end{aligned} \tag{6.100}$$

depending on the critical temperature T_χ (see fourth row, second panel, of Fig.6.16). In the over-ductile regime ($T_\xi < T < T_\chi$), the complete breaking of the system occurs at the same stress σ_F given in Eq.(6.100) and shown in the fourth row, third panel, of Fig.6.16.

The behavior of these transition stresses is summarized in Fig.6.17, where they are plotted versus the temperature T. In addition, different stress-extension curves are shown at different temperatures of interest. In the first two cases, A) and B), we observe a brittle behavior characterized by the breaking of the system when the stress reaches the value σ_B and the extension the value $Y_{\xi\chi}$. While case B) corresponds to a temperature slightly smaller than T^* (brittle), case C) represents a temperature slightly larger than T^*, being therefore in the ductile region. We see here both the softening transition at Y_ξ and the failure transition at Y_χ. In this case C), the stresses satisfy the relationship $\sigma_S^- < \sigma_F < \sigma_S^+$, and then the softening peak (upper yield strength) is larger than the failure peak. We can now continue to increase the temperature until $\sigma_S^- < \sigma_F = \sigma_S^+$, that is, until the softening peak is equal to the failure peak. This condition

is fulfilled in the panel D) of Fig.6.17, and it corresponds to the temperature T^{**}, defined as

$$T^{**} = \frac{\frac{h^2}{l+h}Y_p^2 - \frac{p^2 l}{(p+l)^2}Y_b^2}{K_B\left[\frac{h^2}{(l+h)(h-p)}\log\frac{\tau_\alpha}{\tau_\gamma} - \frac{pl}{(p+l)^2}\log\frac{\tau_\gamma}{\tau_\beta}\right]}. \tag{6.101}$$

In the stress-temperature plot, this temperature value T^{**} represents the intersection of the two curves σ_F and σ_S^+ versus T. Increasing the temperature further, we enter the region $T^{**} < T < T_\xi$ (once again ductile), represented in the panel E), where the failure peak is larger than the softening peak (upper yield strength), $\sigma_S^- < \sigma_S^+ < \sigma_F$. Finally, for values of temperature in the range $T_\xi < T < T_\chi$, we are in the over-ductile regime and the softening peak disappears, remaining only the failure peak σ_F for the overall system, as shown in panel F) of Fig.6.17. In panels A), B), C), D), E), and F) of Fig.6.17 we also represent the stress-extension response for a finite (large) value of N in order to show the good agreement between the approximated expressions and the thermodynamic limit.

As a conclusion to this discussion, we would like to point out that the strength (rupture stress) of the system as a function of temperature is finally represented by a discontinuous curve formed by the branch σ_B for $0 < T < T^*$ (brittle) and by the branch σ_F for $T^* < T < T_\chi$ (ductile), as one can see in the panel $\sigma - T$ of Fig.6.17. This discontinuity can be easily explained by observing that the brittle-to-ductile transition involves the phenomenon of softening and thus the synchronized lowering of the elastic constant of all breakable elements. Since we are applying a stretching to the system controlled by the extension, the reduction of the overall elastic constant produces a consequent reduction in stress (which is therefore discontinuous). We further remark that the strength (σ_B or σ_F, depending on the temperature) is proportional to the factor $1-\phi$, which represents the fraction of initially present elements (ϕ is in fact the fraction of initially absent elements). This is reminiscent of the Griffith criterion, stating that the stress at fracture is lower if the initial crack opening is larger [119]. In our case, the initial crack opening is proportional to ϕ and, therefore, the Griffith criterion is respected. However, we add here the temperature-dependent nature of this criterion, which is described by the classical term $\sqrt{1-\frac{T}{T_{\xi\chi}}}$ in σ_B, or $\sqrt{1-\frac{T}{T_\chi}}$ in σ_F, which represents the critical behavior eventually resulting in a genuine phase transition.

The brittle-to-ductile transition has been observed in GaN nanowires through molecular dynamics simulations [124], and Fig.6.18 shows the comparison with our theoretical results. We considered a GaN nanowire oriented in the direction [0001], with a diameter of 1.92 nm and a length of 6.12 nm, as reported in Fig.2(d) of Ref.[124]. The lateral facets of this system are oriented along the $\{11\bar{2}0\}$ side planes, as shown in Fig.1(b) of Ref.[124]. In Fig.6.18, the blue curves represent the brittle behavior whereas the red ones describe the ductile behavior. We remark that Eqs.(6.93) and (6.94) define a relation $\langle f\rangle/N = \mathcal{F}(Y)$ where $\mathcal{F}$ is a given function. We have to introduce the real stress $\sigma = \langle f\rangle/(N\mathsf{S})$, where S is the area pertaining to each breakable spring, and the real strain $\varepsilon = Y/\ell$, where ℓ is the characteristic lengthscale induced by the crystal structure. The stress-strain relation can be therefore written as $\sigma = \mathcal{F}(\varepsilon\ell)/\mathsf{S}$, where $\mathcal{F}$ is the relationship defined by Eqs.(6.93) and (6.94). In Fig.6.18, we adopted the parameters $h = 3.77$N/m, $p = 0.234$N/m, $l = 0.725$N/m, $k = 2.00$N/m, $\Delta E = 11.0\times10^{-21}$J, $Y_b = 17.8\times10^{-11}$m, $\mathsf{S} = 22.7\times10^{-22}$m^2, $\ell = 12.1\times10^{-12}$m, and $K_B = 1.38\times10^{-23}$J/K. As before, most of the geometrical parameters were available in the original paper dealing with molecular dynamics simulations, and the others were fitted to correctly reproduce the results. We then plotted the stress-strain curves for the two temperatures $T = 300$K (brittle behavior) and $T = 1800$K (ductile behavior). It is interesting to note that the structural parameters used in our

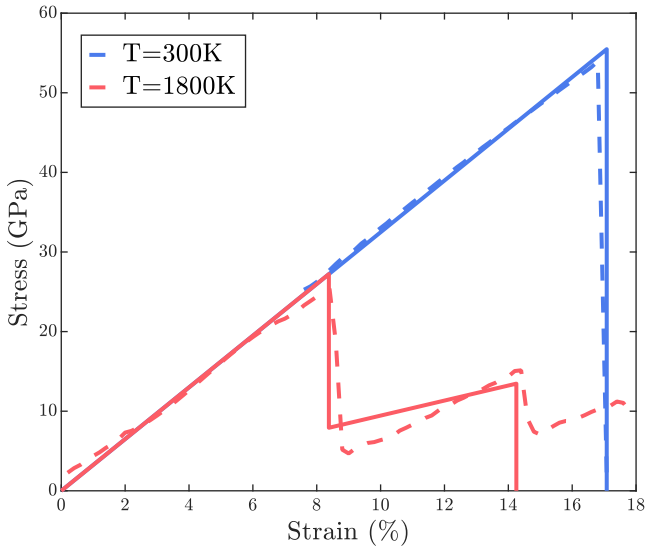

Figure 6.18: Tensile stress-strain curves for a GaN nanowire oriented in the direction [0001] (diameter of 1.92 nm, length of 6.12 nm). The lateral facets are oriented along the $\{11\bar{2}0\}$ side planes. Comparison between molecular dynamics simulations results [124] (dashed lines) and our theory given by Eqs.(6.93) and (6.94) (continuous lines). The parameters used are reported in the main text.

model are able to predict the correct brittle-to-ductile transition as obtained through molecular dynamics simulations. Moreover, also the upper and lower yield stresses of the ductile behavior are in quite good agreement with simulations. We remark that in our model there is a single softening process and therefore we can see only one failure peak after the softening peak in the stress-strain relation. As discussed in the conclusions, the model could be generalized with more softening steps to describe real damage such as that of the nanowires studied here.

6.8 Conclusions

We proposed and studied two prototypical models able to describe temperature effects in fracture processes. The first is aimed at explaining the temperature-dependent behavior of brittle systems, and the second is aimed at showing the complex damage processes occurring in the presence of ductile breakable links with a possibility of a brittle-to-ductile transition regulated by thermal effects. Both models are based on a simple lattice structure built through unbreakable and breakable springs. The system is confined between two layers, one fixed and one movable, and is designed in such a way that lifting the top layer results in a force experienced by the system, being able to generate fracture propagation. This structure is supposed to be embedded into a thermal bath at a fixed temperature. Hence, the models are developed within the equilibrium statistical mechanics formalism. The difference between the two models lies in the behavior at the rupture of the breakable springs. In the first model for brittle fracture, each breakable spring can be in two states, namely elastic or broken, depending on the extension applied to the element itself. The state transition occurs through the absorption of an amount of energy that corresponds to the typical surface energy of the Griffith criterion [119]. In the second model, each breakable spring can be in three different states representing the elastic, softened, and broken

regimes. The intermediate softened state is introduced to reproduce the possible ductile regime of the fracture process. In this case, we have a 'yielding' point between the elastic and the ductile regimes, followed by a final failure point corresponding to fracture. The transition between intact and softened states occurs after the yielding energy is absorbed, and the transition between softened and broken occurs through the absorption of another amount of energy corresponding to fracture. Thus, in both models the energy balance is similar to what is typically assumed in linear elastic fracture mechanics since Griffith's and Irwin's pioneering works [119–121], with the fracture phenomenon regulated by elastic, damage and fracture (surface) energy. However, including thermal fluctuations sensibly modifies the results and adds important features to the system description.

As for the model for brittle fracture, we obtain a temperature-dependent fracture stress and a corresponding fracture strain, representing a 'genuine' phase transition. Thus, we obtain a critical temperature at which both fracture stress and fracture strain are zero and therefore the material is always broken for supercritical temperatures. Interestingly, the obtained temperature-dependent strength is in good agreement with several experiments and molecular dynamics simulations as demonstrated previously. It is interesting to note that although breakable springs have a temperature-independent breaking behavior, the overall system exhibits a breaking point that is highly dependent on temperature. This is a typical case of a complex system with collective behavior, giving rise to a critical phenomenon. We argue that this effect is relevant in the case of weak links, such as hydrogen bonds in biological materials, or in rubber, where the elasticity has an entropic character, or in small-size metallic or semiconductor systems, such as the considered nanowires [122–133].

The model with ductile breakable elements exhibits an even richer behavior. In this case, it is the full response of the system that is temperature dependent. Indeed, we have demonstrated the existence of a brittle-to-ductile transition temperature T^* (whose expression is obtained in closed form) that regulates the behavior of the fracture process. On the one hand, for temperatures lower than T^*, we observe a brittle behavior characterized by a direct transition of the springs from the elastic to the broken state, without passing through the intermediate softened state. On the other hand, for temperatures higher than T^*, we see that, as the extension applied to the system increases, first the springs soften (yielding point), and then they switch from the softened to the broken state (failure point). The intermediate softened region reproduces in this discrete context the cohesive zone of the classical Dugdale-Barenblatt model of the ductile fracture [134, 135]. Of course, both yielding and failure points depend on temperature and are again characterized by phase transitions. In fact, importantly, we are not only able to calculate the brittle-to-ductile transition temperature, but also to predict the critical behavior of the upper and lower yield strengths, and the thermal properties of the fracture strength. Our model is also able to predict the existence of a special fracture regime, here called over-ductile, in which the temperature is high enough to damage all elements without mechanical action. In this situation, as the extension of the system increases, we observe the only transition from the softened to the broken regime.

From the methodological point of view, to elaborate the closed form expression of the partition function in both proposed models, we adopted specific techniques particularly suitable for calculating the determinant and inverse of tridiagonal matrices [96, 97]. These approaches allow the derivation of exact solutions as shown in Appendix 6.9.1, but also asymptotic approximations as discussed in Appendix 6.9.2. Although these mathematical developments are relegated to the appendices, they are of crucial importance for obtaining the physical results of fracture processes.

We point out that even if the models here presented clarify fundamental aspects of thermally activated rupture phenomena, they should be generalized to take into account the complex reality of these processes. We want to mention here at least four points that partially limit the

applicability of these models to real situations. The first issue concerns the spatial homogeneity of the adopted models. We have always considered all springs of discrete systems to have the same mechanical behavior (in terms of elastic constants, failure thresholds, etc.). In reality, this is true only for perfect monocrystalline structures that are quite rare. It would be interesting to study these phenomena in disordered systems that, on the one hand, are more similar to several real structures, and on the other hand, may generate even more interesting critical behaviors typical of complex systems with quenched disorder [136, 138–147]. The second point to be explored is the kinetic of rupture processes. Here we have considered only quasi-static phenomena studied by means of equilibrium statistical mechanics. In real experiments, traction can be applied at different tensile velocities, and the response obviously depends on these traction rates [148, 149]. To model these phenomena one would have to adopt out-of-equilibrium statistical mechanics and then base the analysis on Langevin or Fokker-Planck methodologies [100, 101, 150, 151]. To conclude, the third point that could be improved concerns the fact that the softening process is restricted to a single step of reduction of the elastic constant of the breakable springs. In order to be more adherent to the physical reality of the yielding process one would have to imagine a series of steps where several reductions of the elastic constant take place progressively. In this sense, the yielding point would be implemented through a multi-softening process, more similar to what happens in real nonlinear materials. The fourth and final point concerns the too-simple geometry of our model, which should be improved (with 2D or 3D lattices) in order to be able to represent real elastic fields to be compared with models from continuum mechanics.

6.9 Appendix

6.9.1 Exact results for tridiagonal matrices

Since the matrix $\mathcal{A}$ defined in Eq.(6.5) is tridiagonal, we can analytically evaluate the inverse $\mathcal{A}^{-1}$ and the determinant $\det\mathcal{A}$ [96, 97]. We consider a generic tridiagonal matrix $\mathcal{M}$, and we define its elements as $\mathcal{M}_{i,i} = b_i$ (main diagonal), $\mathcal{M}_{i,i-1} = a_i$ (lower diagonal), and $\mathcal{M}_{i,i+1} = c_i$ (upper diagonal). All other elements are zero. We can introduce the quantities θ_i by means of the following recurrence relation

$$\begin{cases} \theta_i = b_i\theta_{i-1} - a_i c_{i-1}\theta_{i-2}, \\ \theta_{-1} = 0, \theta_0 = 1, i = 1, 2, \ldots, N, \end{cases} \tag{6.102}$$

where, in particular, $\theta_N = \det\mathcal{M}$. Furthermore, it is possible to define the quantities ϕ_i through the recurrence formula

$$\begin{cases} \phi_i = b_i\phi_{i+1} - c_i a_{i+1}\phi_{i+2}, \\ \phi_{N+2} = 0, \phi_{N+1} = 1, i = N, N-1, \ldots, 1, \end{cases} \tag{6.103}$$

where $\phi_1 = \theta_N = \det \mathcal{M}$. These definitions can be used to determine the elements of the inverse matrix $\mathcal{M}^{-1}$ [96, 97], as follows

$$(\mathcal{M}^{-1})_{i,j} = \begin{cases} \dfrac{(-1)^{i+j} c_i c_{i+1} \dots c_{j-1} \theta_{i-1} \phi_{j+1}}{\theta_N}, & \text{if } i < j, \\ \dfrac{\theta_{i-1}\phi_{i+1}}{\theta_N}, & \text{if } i = j, \\ \dfrac{(-1)^{i+j} a_{j+1} a_{j+2} \dots a_i \theta_{j-1} \phi_{i+1}}{\theta_N}, & \text{if } i > j. \end{cases} \tag{6.104}$$

By considering our particular case, the elements in the main diagonal of $\mathcal{A}$ are defined as $a_i = 2+\alpha$ for $1 \leq i \leq \xi$, and $a_i = 2+\beta$ for $\xi+1 \leq i \leq N$. Moreover, we have that $\mathcal{A}_{i,i+1} = \mathcal{A}_{i+1,i} = -1$ for the upper and lower diagonals. For this special situation, θ_i and ϕ_i are defined by the rules

$$\begin{cases} \theta_i = a_i \theta_{i-1} - \theta_{i-2}, \\ \theta_{-1} = 0, \theta_0 = 1, i = 1, 2, \dots, N, \end{cases} \tag{6.105}$$

and

$$\begin{cases} \phi_i = a_i \phi_{i+1} - \phi_{i+2}, \\ \phi_{N+2} = 0, \phi_{N+1} = 1, i = N, N-1, \dots, 1. \end{cases} \tag{6.106}$$

Consequently, the elements of the inverse matrix $\mathcal{A}^{-1}$ are given by

$$(\mathcal{A}^{-1})_{i,j} = \begin{cases} \dfrac{\theta_{i-1}\phi_{j+1}}{\theta_N}, & \text{if } i < j, \\ \dfrac{\theta_{i-1}\phi_{i+1}}{\theta_N}, & \text{if } i = j, \\ \dfrac{\theta_{j-1}\phi_{i+1}}{\theta_N}, & \text{if } i > j. \end{cases} \tag{6.107}$$

Hence, we need to find θ_i and ϕ_i in order to obtain the inverse matrix elements. We start by evaluating θ_i for $i \leq \xi$. In this case, $a_i = 2+\alpha$, and Eq.(6.105) becomes

$$\theta_i = (2+\alpha)\theta_{i-1} - \theta_{i-2}. \tag{6.108}$$

To find a solution, we substitute $\theta_i = \lambda^i$ in the last equation, and we obtain a second-degree algebraic equation with solutions

$$\lambda_{1,2} = \frac{2+\alpha \pm \sqrt{\alpha^2 - 4\alpha}}{2}. \tag{6.109}$$

Then, a generic solution for θ_i, with $i \leq \xi$, is given by the following linear combination

$$\theta_i = A \left(\frac{2+\alpha+\sqrt{\Delta_\alpha}}{2} \right)^i + B \left(\frac{2+\alpha-\sqrt{\Delta_\alpha}}{2} \right)^i, \tag{6.110}$$

where we introduced $\Delta_\alpha = \alpha^2 + 4\alpha$. We can obtain the two coefficients A and B by the initial conditions in Eq.(6.105). We obtain

$$A = \frac{2+\alpha+\sqrt{\Delta_\alpha}}{2\sqrt{\Delta_\alpha}}, \quad B = -\frac{2+\alpha-\sqrt{\Delta_\alpha}}{2\sqrt{\Delta_\alpha}}. \tag{6.111}$$

Therefore, the final solution for θ_i, when $i \leq \xi$, is

$$\theta_i = \mathcal{G}(\alpha, i+1), \tag{6.112}$$

where we introduced the function

$$\mathcal{G}(\gamma, z) = \frac{1}{\sqrt{\Delta_\gamma}} \left[\left(\frac{2+\gamma+\sqrt{\Delta_\gamma}}{2} \right)^z - \left(\frac{2+\gamma-\sqrt{\Delta_\gamma}}{2} \right)^z \right], \tag{6.113}$$

with $\Delta_\gamma = \gamma^2 + 4\gamma$. If we introduce the parameters τ_γ and ρ_γ as follows

$$\tau_\gamma = \frac{2+\gamma+\sqrt{\Delta_\gamma}}{2}, \quad \rho_\gamma = \frac{2+\gamma-\sqrt{\Delta_\gamma}}{2}, \tag{6.114}$$

the function $\mathcal{G}(\gamma, z)$ can be written as

$$\mathcal{G}(\gamma, z) = \frac{1}{\sqrt{\Delta_\gamma}} \left(\tau_\gamma^z - \rho_\gamma^z \right). \tag{6.115}$$

We note that

$$\tau_\gamma - \rho_\gamma = \sqrt{\Delta_\gamma}, \quad \rho_\gamma \tau_\gamma = 1. \tag{6.116}$$

Now, we evaluate θ_i when $i \geq \xi + 1$. In this case, $a_i = 2 + \beta$ and Eq.(6.105) becomes

$$\theta_i = (2+\beta)\theta_{i-1} - \theta_{i-2}. \tag{6.117}$$

As before, we find that the general solution is given by the linear combination

$$\theta_i = C \left(\frac{2+\beta+\sqrt{\Delta_\beta}}{2} \right)^i + D \left(\frac{2+\beta-\sqrt{\Delta_\beta}}{2} \right)^i, \tag{6.118}$$

where $\Delta_\beta = \beta^2 + 4\beta$. To find the coefficients C and D, we exploit the initial conditions $\theta_\xi = \mathcal{G}(\alpha, \xi+1)$ and $\theta_{\xi-1} = \mathcal{G}(\alpha, \xi)$. Straightforward calculations lead to the solution for θ_i, when $i \geq \xi + 1$, in the form

$$\theta_i = \mathcal{G}(\beta, i-\xi+1)\mathcal{G}(\alpha, \xi+1) - \mathcal{G}(\beta, i-\xi)\mathcal{G}(\alpha, \xi), \tag{6.119}$$

where we used the function defined in Eq.(6.113). We consider Eq.(6.106) and we proceed with the evaluation of ϕ_i. We start with the case where $i \geq \xi + 1$. In this condition, the recurrent equation becomes

$$\phi_i = (2+\beta)\phi_{i+1} - \phi_{i+2}, \tag{6.120}$$

which must be combined with the initial conditions in Eq.(6.106). Eventually, we obtain ϕ_i for $i \geq \xi + 1$ in the form

$$\phi_i = -\mathcal{G}(\beta, i-N-2). \tag{6.121}$$

We can find ϕ_i when $i \leq \xi$ by using the two conditions $\phi_{\xi+1} = -\mathcal{G}(\beta, \xi - N - 1) = \mathcal{G}(\beta, N + 1 - \xi)$ and $\phi_{\xi+2} = -\mathcal{G}(\beta, \xi - N) = \mathcal{G}(\beta, N - \xi)$. After straightforward calculations, we get for $i \leq \xi$

$$\begin{aligned} \phi_i = \mathcal{G}(\beta, N + 1 - \xi)\mathcal{G}(\alpha, \xi + 2 - i) \\ - \mathcal{G}(\beta, N - \xi)\mathcal{G}(\alpha, \xi + 1 - i). \end{aligned} \tag{6.122}$$

The obtained values of θ_i and ϕ_i allow the calculation of $\mathcal{A}^{-1}$ and $\det \mathcal{A}$, useful to implement the determination of the partition function in Eq.(6.16) and the quantities in Eqs.(6.18) and (6.19). Moreover, these results are useful to develop some asymptotic expressions in Appendix 6.9.2.

6.9.2 Asymptotic analysis

Considering the brittle model with a large number N of units, it is possible to derive approximations to simplify the partition function and the main average quantities. More specifically, we can find approximations for $\mathbf{v}^\mathsf{T}\mathcal{A}^{-1}\mathbf{v}$ and for $\det \mathcal{A}$. We start our analysis by expanding the first quadratic form as follows

$$\begin{aligned} \mathbf{v}^\mathsf{T}\mathcal{A}^{-1}\mathbf{v} &= \sum_{i=1}^{N}\sum_{j=1}^{N} v_i (\mathcal{A}^{-1})_{i,j} v_j \\ &= \sum_{i=1}^{N}\sum_{j=1}^{N} (\beta + \delta_{i,N})(\mathcal{A}^{-1})_{i,j}(\beta + \delta_{j,N}) \\ &= \beta^2 \sum_{i=1}^{N}\sum_{j=1}^{N} (\mathcal{A}^{-1})_{i,j} + 2\beta \sum_{i=1}^{N} (\mathcal{A}^{-1})_{i,N} + (\mathcal{A}^{-1})_{N,N} \\ &= \beta^2 S_2(\xi) + 2\beta S_1(\xi) + S_0(\xi), \end{aligned} \tag{6.123}$$

where we introduced $S_2(\xi)$ as the sum over all the elements of the inverse matrix, $S_1(\xi)$ as the sum over all the elements of the N-th column of the inverse matrix, and $S_0(\xi)$ as the element (N, N) of the inverse matrix. We observe that these three quantities are in general function of ξ.

Exploiting the symmetry of the inverse matrix $\mathcal{A}^{-1}$, we write $S_2(\xi)$ as

$$S_2(\xi) = \sum_{i=1}^{N} (\mathcal{A}^{-1})_{i,i} + 2 \sum_{i=1}^{N-1} \sum_{j=i+1}^{N} (\mathcal{A}^{-1})_{i,j}. \tag{6.124}$$

The evaluation of $S_2(\xi)$ for a matrix $\mathcal{A}$ that shows heterogeneous diagonal elements a_i ($\xi \neq \{0, N\}$) can be done but is not straightforward. Fortunately, it is possible to observe that, in the limit of large N, the form of $S_2(\xi)$ is a linear combination of the two values $S_2(0)$ and $S_2(N)$, each corresponding to a matrix with homogeneous diagonal. In fact, when $\xi = 0$, the diagonal components of $\mathcal{A}$ are all equal to $2 + \beta$, and when $\xi = N$, the diagonal components of $\mathcal{A}$ are all equal to $2 + \alpha$.

With the help of the left panel of Fig.6.19, we can observe that, as N increases, the form of $S_2(\xi)$ numerically obtained through Eq.(6.107) (blue curves), approach the straight line joining $S_2(0)$ and $S_2(N)$ (red dashed line). To improve the approximation, we observe that in the linear solution for $S_2(\xi)$ we could also add a zeroth order term (with respect to N), represented by an additional small quantity $C(\xi)$, possibly dependent on ξ, but independent of N.

Now, we analytically evaluate $S_2(0)$. By means of this value, it is also easy to obtain $S_2(N)$

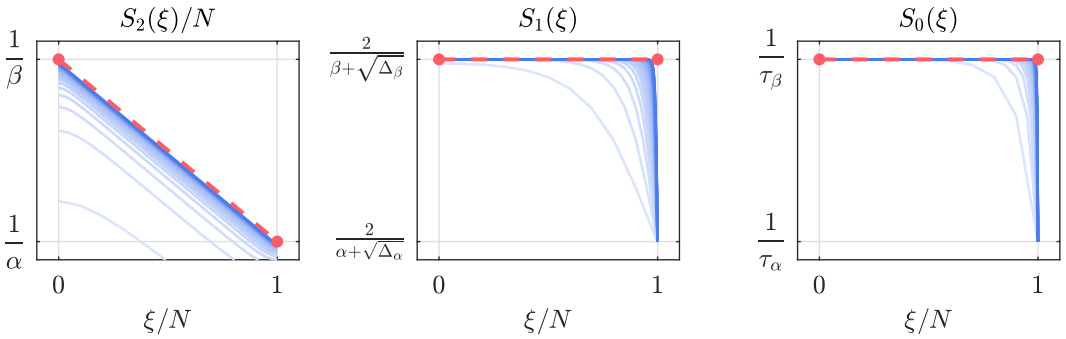

Figure 6.19: The quantities $S_2(\xi)/N$, $S_1(\xi)$ and $S_0(\xi)$ are obtained using Usmani relations (blue curves) for different values of $N = \{10, \ldots, 300\}$ (with a step of 10). We observe that, as N increases, the quantities approach their relative approximations obtained for large N (red dashed lines).

simply by substituting β with α. When $\xi = 0$, we have from Appendix 6.9.1

$$\theta_i = \mathcal{G}(\beta, i+1), \tag{6.125}$$
$$\phi_i = \mathcal{G}(\beta, N+2-i), \tag{6.126}$$

where $i = 1, \ldots, N$. In addition, Eq.(6.107) gives

$$(\mathcal{A}^{-1})_{i,j} = \begin{cases} \dfrac{\mathcal{G}(\beta,i)\mathcal{G}(\beta,N+1-j)}{\mathcal{G}(\beta,N+1)}, & \text{if } i < j, \\ \dfrac{\mathcal{G}(\beta,i)\mathcal{G}(\beta,N+1-i)}{\mathcal{G}(\beta,N+1)}, & \text{if } i = j, \\ \dfrac{\mathcal{G}(\beta,j)\mathcal{G}(\beta,N+1-i)}{\mathcal{G}(\beta,N+1)}, & \text{if } i > j. \end{cases} \tag{6.127}$$

We can therefore write $S_2(0)$ as

$$\begin{aligned} S_2(0) = &\sum_{i=1}^{N} \frac{\mathcal{G}(\beta,i)\mathcal{G}(\beta,N+1-i)}{\mathcal{G}(\beta,N+1)} \\ &+ 2\sum_{i=1}^{N-1}\sum_{j=i+1}^{N} \frac{\mathcal{G}(\beta,i)\mathcal{G}(\beta,N+1-j)}{\mathcal{G}(\beta,N+1)}. \end{aligned} \tag{6.128}$$

Using the definition of $\mathcal{G}(\gamma, z)$ in Eq.(6.113), and the properties of τ_γ and ρ_γ introduced in

Eq.(6.116), we get

$$S_2(0) = \Bigg\{ 2(N-1)\left(\frac{\tau_\beta^{N+1}}{\tau_\beta - 1} - \frac{\tau_\beta^{-N}}{\tau_\beta - 1}\right) + \frac{2\tau_\beta^{2-N} - 2\tau_\beta^{N}}{\tau_\beta^2 - 1} + N(\tau_\beta^{N+1} + \tau_\beta^{-N-1}) + \frac{2\tau_\beta}{(\tau_\beta^2 - 1)}(\tau_\beta^{-N} - \tau_\beta^{N}) + \frac{2 + 2\tau_\beta}{(\tau_\beta - 1)^2}(1 + \tau_\beta - \tau_\beta^{N} - \tau_\beta^{1-N}) \Bigg\} \frac{(\tau_\beta^{N+1} - \tau_\beta^{-N-1})^{-1}}{\sqrt{\Delta_\beta}}, \tag{6.129}$$

where we used several times the geometric sum. The expression for $S_2(0)$ given in Eq.(6.129) is not transparent but, in the limit of large N, it can be approximated by

$$S_2(0) \simeq \frac{N}{\beta} - \frac{\sqrt{\beta^2 + 4\beta} - \beta}{\beta^2} = \frac{N}{\beta} + C(0), \tag{6.130}$$

where

$$C(0) = -\frac{\sqrt{\beta^2 + 4\beta} - \beta}{\beta^2}. \tag{6.131}$$

This term represents the zeroth order correction (with respect to N), previously discussed. When $\xi = N$, we can obtain the result by simply substituting β with α, eventually obtaining

$$S_2(N) \simeq \frac{N}{\alpha} - \frac{\sqrt{\alpha^2 + 4\alpha} - \alpha}{\alpha^2} = \frac{N}{\alpha} + C(N), \tag{6.132}$$

where

$$C(N) = -\frac{\sqrt{\alpha^2 + 4\alpha} - \alpha}{\alpha^2}. \tag{6.133}$$

Finally, we can write the general approximation for $S_2(\xi)$ in the limit of large N as

$$S_2(\xi) \sim \frac{N}{\beta} + \left(\frac{N}{\alpha} - \frac{N}{\beta}\right)\frac{\xi}{N} + C(\xi), \quad \text{if } \alpha, \beta \neq 0, \tag{6.134}$$

where $C(0)$ is given in Eq.(6.131), $C(N)$ is given in Eq.(6.133), and $C(\xi)$ assumes a constant value for $\xi \in \{1, \ldots, N-1\}$ (for large N), which is always in the range between $C(0)$ and $C(N)$. We do not determine here this value since is not relevant to our analysis. Indeed, although the zeroth order term of $S_2(\xi)$ is represented by three different values of the constant depending on ξ, in the application to the fracture problem we adopt the value $C(0)$ in all calculations. It is not difficult to realize that this is the only value playing a role in our model since it describes the behavior of the system when $\xi = 0$, *i.e.* when all the breakable springs are fractured. In this condition, only one spring links together the two layers of the system and the constant $C(0)$ is able to describe the exact stiffness of the resulting spring network. The other values $C(\xi)$, for $\xi \neq 0$, are negligible when $N \to \infty$.

The approach used to find the approximation of $S_2(\xi)$ for large N, can be also applied for $S_1(\xi)$ and $S_0(\xi)$. Concerning $S_1(\xi)$, as shown in the center panel of Fig.6.19, its value numerically obtained with Eq.(6.107) approaches the constant value $S_1(0)$ as N increases. This value is therefore the approximation of $S_1(\xi)$ for large N. Through previous definitions, we can write

$S_1(0)$ as

$$S_1(0) = \sum_{i=1}^{N} (\mathcal{A}^{-1})_{i,N} = \sum_{i=1}^{N} \frac{\theta_{i-1}}{\theta_N} = \sum_{i=1}^{N} \frac{\mathcal{G}(\beta, i)}{\mathcal{G}(\beta, N+1)}, \tag{6.135}$$

which, in the limit of large N, leads to

$$S_1(\xi) \simeq S_1(0) \simeq \frac{2}{\beta + \sqrt{\Delta_\beta}}. \tag{6.136}$$

We can observe that the exact values of $S_0(\xi)$ approach the constant value $S_0(0)$ for large N, as one can see in the right panel of Fig.6.19. We have the exact expression

$$S_0(0) = (\mathcal{A}^{-1})_{N,N} = \frac{\theta_{N-1}}{\theta_N}, \tag{6.137}$$

which, in the limit of large N, gives

$$S_0(\xi) \simeq S_0(0) \simeq \frac{1}{\tau_\beta} = \frac{2}{2 + \beta + \sqrt{\beta^2 + 4\beta}}, \tag{6.138}$$

as shown in the right panel of Fig.6.19. Now we determine the value of the quadratic form in Eq.(6.123), for large N, as

$$\begin{aligned} \mathbf{v}^\mathsf{T} \mathcal{A}^{-1} \mathbf{v} \simeq \beta^2 \left[\frac{N}{\beta} + \left(\frac{1}{\alpha} - \frac{1}{\beta} \right) \xi + C(0) \right] \\ + 2\beta \left(\frac{2}{\beta + \sqrt{\beta^2 + 4\beta}} \right) + \left(\frac{2}{2 + \beta + \sqrt{\beta^2 + 4\beta}} \right). \end{aligned} \tag{6.139}$$

To conclude, we recall the definition of q, stated in Eq.(6.15), and we get

$$q = 1 + \beta N - \mathbf{v}^\mathsf{T} \mathcal{A}^{-1} \mathbf{v} \sim \frac{lh}{l+h} \frac{\xi}{k} + \epsilon, \tag{6.140}$$

where we introduced

$$\epsilon = \frac{\sqrt{\beta^2 + 4\beta} - \beta}{2}. \tag{6.141}$$

Finally, Eqs.(6.140) and (6.141) prove Eqs.(6.20) and (6.21) of the main text.

To complete this part, we study the approximation of $\det \mathcal{A}$ for large values of N. Thanks to Usmani theory [96, 97], we have

$$\det \mathcal{A} = \theta_N. \tag{6.142}$$

Adopting the results of Appendix 6.9.1, it is possible to evaluate the determinant of $\mathcal{A}$ for different $\xi = 0, \ldots, N$. The results can be found in Fig.6.20, from which we realize that the value of $\log(\det \mathcal{A})/N$ is approximated by a straight line that links together the values of $\log \det \mathcal{A}/N$ when $\xi = 0$, and when $\xi = N$, in the limit of large N. It is simple to prove that for $\xi = 0$ we have $\log \theta_N / N \simeq \log \tau_\beta$ when $N \to \infty$, and similarly for $\xi = N$ we have $\log \theta_N / N \simeq \log \tau_\alpha$ when $N \to \infty$. The equation that gives the value of $\log \det \mathcal{A}/N$, in the limit of large N, is therefore obtained as

$$\frac{\log \det \mathcal{A}}{N} = \frac{\log \theta_N}{N} \simeq \log \tau_\beta + \frac{\xi}{N} \log \frac{\tau_\alpha}{\tau_\beta}. \tag{6.143}$$

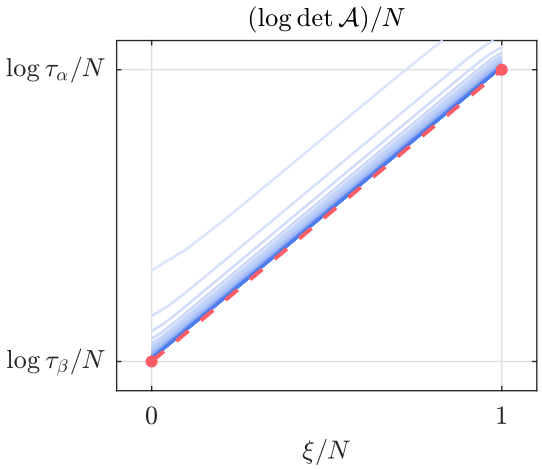

Figure 6.20: The quantity $\log\det\mathcal{A}/N$ is obtained using Usmani relations (blue curves) for different values of $N=\{10,\dots,300\}$ (with steps of 10). We observe that, as N increases, $\log\det\mathcal{A}/N$ approaches its approximation for large N (red dashed line).

Equivalently, we can write

$$\det\mathcal{A}\simeq\tau_\alpha^{\xi}\tau_\beta^{N-\xi}, \tag{6.144}$$

which proves Eq.(6.22) of the main text.

We discuss now the same results for the model with the softening mechanism. In this case, the quadratic form $\mathbf{v}^{\mathsf{T}}\mathcal{A}^{-1}\mathbf{v}$, can be written as in Eq.(6.123)

$$\mathbf{v}^{\mathsf{T}}\mathcal{A}^{-1}\mathbf{v}=\beta^2 S_2(\xi,\chi)+2\beta S_1(\xi,\chi)+S_0(\xi,\chi), \tag{6.145}$$

where S_2, S_1 and S_0 depends now on both interface positions ξ and χ. We start by analyzing the behavior of S_2. Since $S_2(0,0)\simeq N/\beta$, $S_2(0,N)\simeq N/\gamma$ and $S_2(N,N)\simeq N/\alpha$, we get for large values of N the following expression

$$S_2(\xi,\chi)\simeq\frac{N}{\beta}+\left(\frac{N}{\alpha}-\frac{N}{\gamma}\right)\frac{\xi}{N}+\left(\frac{N}{\gamma}-\frac{N}{\beta}\right)\frac{\chi}{N}+C, \tag{6.146}$$

where considerations similar to the previous ones confirm that the zeroth order term C assumes the same value in Eq.(6.131). Similarly, we can prove that, for large values of N, the quantities S_1 and S_0 assume the same values obtained for the purely brittle fracture model, *i.e.*

$$S_1(\xi,\chi)\simeq\frac{2}{\beta+\sqrt{\beta^2+4\beta}}, \tag{6.147}$$

$$S_0(\xi,\chi)\simeq\frac{2}{2+\beta+\sqrt{\beta^2+4\beta}}, \tag{6.148}$$

which are independent of ξ andχ. Adopting these approximations in the expression for q, we obtain for $N\to\infty$

$$q\simeq\beta^2\left(\frac{\xi}{\gamma}-\frac{\xi}{\alpha}-\frac{\chi}{\gamma}+\frac{\chi}{\beta}\right)+\epsilon, \tag{6.149}$$

where ϵ is given by

$$\epsilon = \frac{\sqrt{\beta^2 + 4\beta} - \beta}{2}. \tag{6.150}$$

This result corresponds to Eq.(6.56) of the main text. Finally, we can also find an approximated expression for $\det \mathcal{A}(\xi, \chi)$ that now depends on both ξ and χ. Since previous approximation for $\log\det \mathcal{A}(\xi)$ was a linear function of ξ linking the values obtained for the two homogeneous matrices at $\xi = 0$ and $\xi = N$, we can now assume that the approximation for $\log\det \mathcal{A}(\xi, \chi)$ is a linear function in ξ and χ passing through the three points identified by $(\xi, \chi) = (0,0), (N,0)$ and (N,N). Hence, we assume that

$$\frac{\log\det \mathcal{A}}{N} \simeq a + b\xi + c\chi, \tag{6.151}$$

where a, b and c are coefficients, which can be found with the assumptions $a = \log\tau_\beta$, $a + cN = \log\tau_\gamma$, and $a + cN + bN = \log\tau_\alpha$, with

$$\tau_\alpha = \frac{2 + \alpha + \sqrt{\alpha^2 + 4\alpha}}{2}, \tag{6.152}$$

$$\tau_\beta = \frac{2 + \beta + \sqrt{\beta^2 + 4\beta}}{2}, \tag{6.153}$$

$$\tau_\gamma = \frac{2 + \gamma + \sqrt{\gamma^2 + 4\gamma}}{2}. \tag{6.154}$$

These values satisfy the relation $\tau_\beta < \tau_\gamma < \tau_\alpha$. To conclude, we obtain the relation

$$\frac{\log\det \mathcal{A}}{N} \simeq \log\tau_\beta + \frac{\xi}{N}\log\frac{\tau_\alpha}{\tau_\gamma} + \frac{\chi}{N}\log\frac{\tau_\gamma}{\tau_\beta}, \tag{6.155}$$

which corresponds to Eq.(6.57) of the main text.

Chapter 7

Conclusion and perspectives

The work presented in this manuscript provides the study of different microinstability scenarios using statistical mechanics and micromechanics principles by the use of the spin variable approach within the Gibbs and Helmholtz ensembles. At the beginning of the manuscript, we present the current state of the art and the motivation for our research (Chapter 1). The spin variable approach and its use within the different statistical ensembles is briefly introduced in Chapter 2.

In the third Chapter, we discuss a previously developed model to describe the cohesion/decohesion process related to a film deposited on a substrate, paying particular attention to the thermal effects. We analyzed this process both under the Gibbs (prescribed force) and Helmholtz (prescribed extension) ensembles. To tackle the problem, we combined the method based on the spin variables with a refined analysis of the properties of some tridiagonal matrices, characterizing the system under investigation. Eventually, for both statistical ensembles, we obtained explicit results giving the force-extension relation, the average number of broken units, and the average extension of all the elements of the chain as functions of the temperature and of the external mechanical action (a force for the Gibbs ensemble and an extension for the Helmholtz one). These results were obtained in a first moment for an arbitrary number N of elements of the chain and then in the thermodynamic limit, where $N \to \infty$. The thermodynamic limit allowed proving that, in the case of an infinite number of units for a chain, the peeling of the film from the substrate takes place at a given critical force, which is temperature-dependent. Furthermore, the origin of the temperature-dependent peeling force is explained through the observation of a phase transition taking place at a given critical temperature able to fully detach the film from the substrate. The relation for the temperature-dependant force has been tested against experimental data concerning the unzipping process for RNA and DNA hairpins, eventually obtaining a good agreement with the data.

While the presented model is interesting since leads to a fully analytic approach able to explain the emergence of the phase transition and the nonequivalence of the ensembles, it could be generalized to take into consideration more complex situations. For instance, the spin variable methodology, here employed to calculate the partition functions, is limited to the study of equilibrium thermodynamics. It could be interesting to generalize it to the dynamic regime, where the rate constants between the intact and broken states of the units of the system play an important role.

In the following Chapter, we expanded the previous cohesion/decohesion model taking into account the possible softening of the bonds involved in the decohesion phenomena. The new softening mechanism for each unit of the chain was modeled by means of three different operating

regions: a first linear region corresponding to an intact element (small deformation), a second region corresponding to the softened element with a reduced stiffness (intermediate deformation), and a last region corresponding to a broken element (large deformation). In both the Gibbs and the Helmholtz ensembles, we obtained a temperature-dependent decohesion force, which physically represents the strength of the system, for a chain composed of a number N of elements. Also, the number of broken and softened elements has been determined as a function of the temperature and of the external mechanical action for both statistical ensembles. To better understand the meaning of these results, we analyzed the system behavior under the hypothesis of thermodynamic limit $N \to \infty$. The analysis of the thermodynamic limit case delivers a clear explanation of the temperature-dependent strength in terms of phase transitions able to give a rigorous explanation of the relationship between strength and temperature in systems where a complex transition in the breaking mechanism occurs (here represented by the bonds softening).

Possible generalizations of the theory may include the dynamic behavior of cohesion/decohesion processes, or the multi-state softening *i.e.* composed of several steps with different stiffness (described by several domain walls in the chain).

After introducing these two models to describe the adhesion and decohesion phenomena present in micro and nanoscale structures, we changed subject and applied the same theoretical techniques to two different types of physical phenomena, firstly to the phase transformation and then to the crack propagation. In Chapter 5, we elaborated some models to describe the temperature-dependent behavior of one-dimensional non-local non-convex systems obtaining the tools to represent the specific feature of several macromolecules of biological origin (*e.g.* proteins) and nanowire with pseudo elasticity. In this case, the bistability of the units of the system under investigation described the possible switching of each domain between its 'folded' and 'unfolded' states. In addition to this, through the Ising scheme, we introduced the non-locality behavior that depicts the cooperativity observed in most of the biological structures and in materials science. As done for previous modelization, the thermal effects were carefully considered by introducing the statistical mechanics' analysis, and a complete thermodynamic framework of the transformation processes in systems with non-locality and non-convexity was obtained. For system with strong Ising interaction (*i.e.*, strongly ferromagnetic systems), which are the most common in practical applications, only one interface was observed between the two different states and it propagates along the chain when a force or an elongation were applied to the system. In the isometric Helmholtz case, we could also observe an initial upward peak of force, representing the nucleation of the new unfolded phase, and a final downward peak of force, representing the coalescence of the folded phase into the unfolded one. An important feature of this system is that the force plateau, describing the interface propagation within the chain is in general temperature dependent for both isotensional and isometric boundary conditions. We have then introduced the zipper model where we consider only one interface propagating along the system that made the calculation of the partition function much simpler in both the Gibbs and the Helmholtz ensembles. The investigation of the thermodynamic limit concerning the zipper model under isometric condition, *i.e.* within the Helmholtz ensemble, closed the Chapter. With this last hypothesis, we obtained results that properly describe the transformation processes in one-dimensional objects (macromolecules or solid nanowires) in terms of thermal fluctuations and mechanical actions applied to the system.

The first neglected aspect of this part represents the real molecular architecture of the considered metastable states. This point can be improved by introducing the main properties of the real molecular structures of the two phases of the system, for example in molecular dynamics simulations. The second aspect concerns the fact that we have carried out the entire discussion at thermodynamic equilibrium and therefore under static or quasi-static conditions. The dynamics could be introduced by taking into account the non-equilibrium statistical mechanics and, in

particular, by the Langevin and/or Fokker-Planck methodologies.

In Chapter 6th, we proposed and studied two prototypical models able to describe temperature effects in fracture processes. The first was aimed at explaining the temperature-dependent behavior of brittle systems, and the second was aimed at showing the complex damage processes occurring in the presence of ductile breakable links with a possibility of a brittle-to-ductile transition regulated by thermal effects. In the first brittle model, each breakable spring could be in two states, namely elastic or broken, depending on the extension applied to the element itself, and in the second model, each breakable spring could be in three different states representing the elastic, softened, and broken regimes. In both models, the energy balance is similar to what is typically assumed in linear elastic fracture mechanics since Griffith's and Irwin's pioneering works, with the fracture phenomenon regulated by elastic, damage, and fracture (surface) energy. However, including thermal fluctuations sensibly modified the results and added important features to the system description.

We point out that even if the models here presented clarify fundamental aspects of thermally activated rupture phenomena, they should be generalized to take into account the complex reality of these processes. Recalling some of the points that partially limit the applicability of these models to real situations, we mention the spatial homogeneity of the adopted models since we have always considered all springs of discrete systems to have the same mechanical behavior (in terms of elastic constants, failure thresholds, etc.). In reality, this is true only for perfect monocrystalline structures that are quite rare. It would be interesting to study these phenomena in disordered systems that, on the one hand, are more similar to several real structures, and on the other hand, may generate even more interesting critical behaviors typical of complex systems with quenched disorder. The second point to be explored is the kinetic of rupture processes. Here we have considered only quasi-static phenomena studied by means of equilibrium statistical mechanics. In real experiments, traction can be applied at different tensile velocities, and the response obviously depends on these traction rates. To model these phenomena one would have to adopt out-of-equilibrium statistical mechanics and then base the analysis on Langevin or Fokker-Planck methodologies. To conclude, the third point that could be improved concerns the fact that the softening process is restricted to a single step of reduction of the elastic constant of the breakable springs. In order to be more adherent to the physical reality of the yielding process one would have to imagine a series of steps where several reductions of the elastic constant take place progressively. In this sense, the yielding point would be implemented through a multi-softening process, more similar to what happens in real nonlinear materials. The fourth and final point concerns the too-simple geometry of our model, which should be improved (with 2D or 3D lattices) in order to be able to represent real elastic fields to be compared with models from continuum mechanics.

Bibliography

[1] Andrea Cannizzo, Giuseppe Florio, Giuseppe Puglisi, and Stefano Giordano. "Temperature controlled decohesion regimes of an elastic chain adhering to a fixed substrate by softening and breakable bonds". In: *Journal of Physics A: Mathematical and Theoretical* 54.44 (2021), p. 445001. DOI: 10.1088/1751-8121/ac2a07.

[2] Andrea Cannizzo, Luca Bellino, Giuseppe Florio, Giuseppe Puglisi, and Stefano Giordano. "Thermal control of nucleation and propagation transition stresses in discrete lattices with non-local interactions and non-convex energy". In: *The European Physical Journal Plus* 137.5 (2022), p. 569. DOI: 10.1140/epjp/s13360-022-02790-9.

[3] Andrea Cannizzo and Stefano Giordano. "Thermal effects on fracture and the brittle-to-ductile transition". In: *Phys. Rev. E* 107 (3 Mar. 2023), p. 035001. DOI: 10.1103/PhysRevE.107.035001.

[4] Pierre-Philippe Cortet, Matteo Ciccotti, and Loïc Vanel. "Imaging the stick–slip peeling of an adhesive tape under a constant load". In: *Journal of Statistical Mechanics: Theory and Experiment* 2007.3 (2007), P03005. DOI: 10.1088/1742-5468/2007/03/P03005.

[5] S. Xia, L. Ponson, G. Ravichandran, and K. Bhattacharya. "Toughening and Asymmetry in Peeling of Heterogeneous Adhesives". In: *Physical Review Letters* 108.19 (2012), p. 196101. DOI: 10.1103/PhysRevLett.108.196101.

[6] Marie-Julie Dalbe, Pierre-Philippe Cortet, Matteo Ciccotti, Loïc Vanel, and Stéphane Santucci. "Multiscale Stick-Slip Dynamics of Adhesive Tape Peeling". In: *Physical Review Letters* 115.12 (2015), p. 128301. DOI: 10.1103/PhysRevLett.115.128301.

[7] F. Maddalena, D. Percivale, G. Puglisi, and L. Truskinovsky. "Mechanics of reversible unzipping". In: *Continuum Mechanics and Thermodynamics* 21.4 (2009), p. 251. DOI: 10.1007/s00161-009-0108-2.

[8] G. Puglisi and L. Truskinovsky. "Cohesion-decohesion asymmetry in geckos". In: *Physical Review E* 87.3 (2013), p. 032714. DOI: 10.1103/PhysRevE.87.032714.

[9] Saurabh Das, Sathya Chary, Jing Yu, John Tamelier, Kimberly L. Turner, and Jacob N. Israelachvili. "JKR Theory for the Stick–Slip Peeling and Adhesion Hysteresis of Gecko Mimetic Patterned Surfaces with a Smooth Glass Surface". In: *Langmuir* 29.48 (2013), pp. 15006–15012. DOI: 10.1021/la403420f.

[10] Jin Qian, Ji Lin, Guang-Kui Xu, Yuan Lin, and Huajian Gao. "Thermally assisted peeling of an elastic strip in adhesion with a substrate via molecular bonds". In: *Journal of the Mechanics and Physics of Solids* 101 (2017), pp. 197–208. DOI: 10.1016/j.jmps.2017.01.007.

[11] Ahmad Rafsanjani, Abdolhamid Akbarzadeh, and Damiano Pasini. "Snapping Mechanical Metamaterials under Tension". In: *Advanced Materials* 27.39 (2015), pp. 5931–5935. DOI: 10.1002/adma.201502809.

[12] Neel Nadkarni, Andres F. Arrieta, Christopher Chong, Dennis M. Kochmann, and Chiara Daraio. "Unidirectional Transition Waves in Bistable Lattices". In: *Physical Review Letters* 116.24 (2016), p. 244501. DOI: 10.1103/PhysRevLett.116.244501.

[13] Michael J. Frazier and Dennis M. Kochmann. "Band gap transmission in periodic bistable mechanical systems". In: *Journal of Sound and Vibration* 388 (2017), pp. 315–326. DOI: 10.1016/j.jsv.2016.10.041.

[14] Shmuel Katz and Sefi Givli. "Solitary waves in a bistable lattice". In: *Extreme Mechanics Letters* 22 (2018), pp. 106–111. DOI: 10.1016/j.eml.2018.06.003.

[15] Shmuel Katz and Sefi Givli. "Solitary waves in a nonintegrable chain with double-well potentials". In: *Physical Review E* 100.3 (2019), p. 032209. DOI: 10.1103/PhysRevE.100.032209.

[16] Myungwon Hwang and Andres F. Arrieta. "Input-Independent Energy Harvesting in Bistable Lattices from Transition Waves". In: *Scientific Reports* 8.1 (2018), p. 3630. DOI: 10.1038/s41598-018-22003-7.

[17] R. L. Harne, M. E. Schoemaker, B. E. Dussault, and K. W. Wang. "Wave heave energy conversion using modular multistability". In: *Applied Energy* 130 (2014), pp. 148–156. DOI: 10.1016/j.apenergy.2014.05.038.

[18] R. L. Harne, M. E. Schoemaker, and K. W. Wang. "Multistable chain for ocean wave vibration energy harvesting: Active and Passive Smart Structures and Integrated Systems 2014". In: *Active and Passive Smart Structures and Integrated Systems 2014*. Proceedings of SPIE - The International Society for Optical Engineering (2014). DOI: 10.1117/12.2044267.

[19] J. L. Ericksen. "Equilibrium of bars". In: *Journal of Elasticity* 5.3 (1975), pp. 191–201. DOI: 10.1007/BF00126984.

[20] Ingo Müller and Piero Villaggio. "A model for an elastic-plastic body". In: *Archive for Rational Mechanics and Analysis* 65 (1977), pp. 25–46. DOI: 10.1007/BF00289355.

[21] B. Fedelich and G. Zanzotto. "Hysteresis in discrete systems of possibly interacting elements with a double-well energy". In: *Journal of Nonlinear Science* 2.3 (1992), pp. 319–342. DOI: 10.1007/BF01208928.

[22] Lev Truskinovsky and Anna Vainchtein. "The origin of nucleation peak in transformational plasticity". In: *Journal of the Mechanics and Physics of Solids* 52.6 (2004), pp. 1421–1446. DOI: 10.1016/j.jmps.2003.09.034.

[23] G. Puglisi and L. Truskinovsky. "Thermodynamics of rate-independent plasticity". In: *Journal of the Mechanics and Physics of Solids* 53.3 (2005), pp. 655–679. DOI: 10.1016/j.jmps.2004.08.004.

[24] G. Puglisi. "Hysteresis in multi-stable lattices with non-local interactions". In: *Journal of the Mechanics and Physics of Solids* 54.10 (2006), pp. 2060–2088. DOI: 10.1016/j.jmps.2006.04.006.

[25] Yalchin R. Efendiev and Lev Truskinovsky. "Thermalization of a driven bi-stable FPU chain". In: *Continuum Mechanics and Thermodynamics* 22.6 (2010), pp. 679–698. DOI: 10.1007/s00161-010-0166-5.

[26] Alexander Mielke and Lev Truskinovsky. “From Discrete Visco-Elasticity to Continuum Rate-Independent Plasticity: Rigorous Results”. In: *Archive for Rational Mechanics and Analysis* 203.2 (2012), pp. 577–619. DOI: 10.1007/s00205-011-0460-9.

[27] Itamar Benichou and Sefi Givli. “Structures undergoing discrete phase transformation”. In: *Journal of the Mechanics and Physics of Solids* 61.1 (2013), pp. 94–113. DOI: 10.1016/j.jmps.2012.08.009.

[28] M. Caruel, J. -M. Allain, and L. Truskinovsky. “Mechanics of collective unfolding”. In: *Journal of the Mechanics and Physics of Solids* 76 (2015), pp. 237–259. DOI: 10.1016/j.jmps.2014.11.010.

[29] M. Caruel and L. Truskinovsky. “Bi-stability resistant to fluctuations”. In: *Journal of the Mechanics and Physics of Solids* 109 (2017), pp. 117–141. DOI: 10.1016/j.jmps.2017.08.007.

[30] Robin L. Blumberg Selinger, Zhen-Gang Wang, William M. Gelbart, and Avinoam Ben-Shaul. “Statistical-thermodynamic approach to fracture”. In: *Physical Review A* 43.8 (1991), pp. 4396–4400. DOI: 10.1103/PhysRevA.43.4396.

[31] H. Borja da Rocha and L. Truskinovsky. “Equilibrium unzipping at finite temperature”. In: *Archive of Applied Mechanics* 89.3 (2019), pp. 535–544. DOI: 10.1007/s00419-018-1485-4.

[32] Hudson Borja da Rocha and Lev Truskinovsky. “Rigidity-Controlled Crossover: From Spinodal to Critical Failure”. In: *Physical Review Letters* 124.1 (2020), p. 015501. DOI: 10.1103/PhysRevLett.124.015501.

[33] S. S. Brenner. “Mechanical Behavior of Sapphire Whiskers at Elevated Temperatures”. In: *Journal of Applied Physics* 33.1 (1962), pp. 33–39. DOI: 10.1063/1.1728523.

[34] Easo P. George, Dierk Raabe, and Robert O. Ritchie. “High-entropy alloys”. In: *Nature Reviews Materials* 4.8 (2019), pp. 515–534. DOI: 10.1038/s41578-019-0121-4.

[35] D. B. Miracle and O. N. Senkov. “A critical review of high entropy alloys and related concepts”. In: *Acta Materialia* 122 (2017), pp. 448–511. DOI: 10.1016/j.actamat.2016.08.081.

[36] B. Cantor, I. T. H. Chang, P. Knight, and A. J. B. Vincent. “Microstructural development in equiatomic multicomponent alloys”. In: *Materials Science and Engineering: A* 375-377 (2004), pp. 213–218. DOI: 10.1016/j.msea.2003.10.257.

[37] F. Otto, A. Dlouhý, Ch. Somsen, H. Bei, G. Eggeler, and E. P. George. “The influences of temperature and microstructure on the tensile properties of a CoCrFeMnNi high-entropy alloy”. In: *Acta Materialia* 61.15 (2013), pp. 5743–5755. DOI: 10.1016/j.actamat.2013.06.018.

[38] A. Gali and E. P. George. “Tensile properties of high- and medium-entropy alloys”. In: *Intermetallics* 39 (2013), pp. 74–78. DOI: 10.1016/j.intermet.2013.03.018.

[39] Jianping Gao, W. D. Luedtke, D. Gourdon, M. Ruths, J. N. Israelachvili, and Uzi Landman. “Frictional Forces and Amontons’ Law: From the Molecular to the Macroscopic Scale”. In: *The Journal of Physical Chemistry B* 108.11 (2004), pp. 3410–3425. DOI: 10.1021/jp0363621.

[40] Michael Urbakh, Joseph Klafter, Delphine Gourdon, and Jacob Israelachvili. “The nonlinear nature of friction”. In: *Nature* 430.6999 (2004), pp. 525–528. DOI: 10.1038/nature02750.

[41] Andrea Vanossi, Nicola Manini, Michael Urbakh, Stefano Zapperi, and Erio Tosatti. "Colloquium: Modeling friction: From nanoscale to mesoscale". In: *Reviews of Modern Physics* 85.2 (2013), pp. 529–552. DOI: 10.1103/RevModPhys.85.529.

[42] A. I. Vakis, V. A. Yastrebov, J. Scheibert, L. Nicola, D. Dini, C. Minfray, A. Almqvist, M. Paggi, S. Lee, G. Limbert, J. F. Molinari, G. Anciaux, R. Aghababaei, S. Echeverri Restrepo, A. Papangelo, A. Cammarata, P. Nicolini, C. Putignano, G. Carbone, S. Stupkiewicz, J. Lengiewicz, G. Costagliola, F. Bosia, R. Guarino, N. M. Pugno, M. H. Müser, and M. Ciavarella. "Modeling and simulation in tribology across scales: An overview". In: *Tribology International* 125 (2018), pp. 169–199. DOI: 10.1016/j.triboint.2018.02.005.

[43] Markus Ternes, Christopher P. Lutz, Cyrus F. Hirjibehedin, Franz J. Giessibl, and Andreas J. Heinrich. "The force needed to move an atom on a surface". In: *Science (New York, N.Y.)* 319.5866 (2008), pp. 1066–1069. DOI: 10.1126/science.1150288.

[44] Izabela Szlufarska, Michael Chandross, and Robert W. Carpick. "Recent advances in single-asperity nanotribology". In: *Journal of Physics D: Applied Physics* 41.12 (2008), p. 123001. DOI: 10.1088/0022-3727/41/12/123001.

[45] Yifei Mo, Kevin T. Turner, and Izabela Szlufarska. "Friction laws at the nanoscale". In: *Nature* 457.7233 (2009), pp. 1116–1119. DOI: 10.1038/nature07748.

[46] Sergey Yu. Krylov and Joost W. M. Frenken. "The physics of atomic-scale friction: Basic considerations and open questions". In: *physica status solidi (b)* 251.4 (2014), pp. 711–736. DOI: 10.1002/pssb.201350154.

[47] N. Manini, G. Mistura, G. Paolicelli, E. Tosatti, and A. Vanossi. "Current trends in the physics of nanoscale friction". In: *Advances in Physics: X* 2.3 (2017), pp. 569–590. DOI: 10.1080/23746149.2017.1330123.

[48] Valentin L. Popov. *Contact Mechanics and Friction: Physical Principles and Applications*. Springer Berlin, Heidelberg, 2010. 362 pp.

[49] C. Storm and P. C. Nelson. "Theory of high-force DNA stretching and overstretching". In: *Physical Review E* 67.5 (2003), p. 051906. DOI: 10.1103/PhysRevE.67.051906.

[50] Toni Hoffmann and Lorna Dougan. "Single molecule force spectroscopy using polyproteins". In: *Chemical Society Reviews* 41.14 (2012), pp. 4781–4796. DOI: 10.1039/C2CS35033E.

[51] Olga K. Dudko. "Decoding the mechanical fingerprints of biomolecules". In: *Quarterly Reviews of Biophysics* 49 (2016), e3. DOI: 10.1017/S0033583515000220.

[52] Megan L. Hughes and Lorna Dougan. "The physics of pulling polyproteins: a review of single molecule force spectroscopy using the AFM to study protein unfolding". In: *Reports on Progress in Physics* 79.7 (2016), p. 076601. DOI: 10.1088/0034-4885/79/7/076601.

[53] A. Prados, A. Carpio, and L. L. Bonilla. "Sawtooth patterns in force-extension curves of biomolecules: An equilibrium-statistical-mechanics theory". In: *Physical Review E* 88.1 (2013), p. 012704. DOI: 10.1103/PhysRevE.88.012704.

[54] L. L. Bonilla, A. Carpio, and A. Prados. "Theory of force-extension curves for modular proteins and DNA hairpins". In: *Physical Review E* 91.5 (2015), p. 052712. DOI: 10.1103/PhysRevE.91.052712.

[55] D. De Tommasi, N. Millardi, G. Puglisi, and G. Saccomandi. "An energetic model for macromolecules unfolding in stretching experiments". In: *Journal of The Royal Society Interface* 10.88 (2013), p. 20130651. DOI: 10.1098/rsif.2013.0651.

[56] Fabio Manca, Stefano Giordano, Pier Luca Palla, Fabrizio Cleri, and Luciano Colombo. "Response to "Comment on 'Elasticity of flexible and semiflexible polymers with extensible bonds in the Gibbs and Helmholtz ensembles"' [J. Chem. Phys. 138, 157101 (2013)]". In: *The Journal of Chemical Physics* 138.15 (2013), p. 157102. DOI: 10.1063/1.4801656.

[57] Tomas Bleha and Peter Cifra. "Energy/entropy partition of force at DNA stretching". In: *Biopolymers* 113.5 (2022), e23487. DOI: 10.1002/bip.23487.

[58] Tomáš Bleha and Peter Cifra. "Stretching and compression of DNA by external forces under nanochannel confinement". In: *Soft Matter* 14.7 (2018), pp. 1247–1259. DOI: 10.1039/C7SM02413D.

[59] George I. Bell. "Models for the Specific Adhesion of Cells to Cells". In: *Science* 200.4342 (1978), pp. 618–627. DOI: 10.1126/science.347575.

[60] G. I. Bell, M. Dembo, and P. Bongrand. "Cell adhesion. Competition between nonspecific repulsion and specific bonding". In: *Biophysical Journal* 45.6 (1984), pp. 1051–1064. DOI: 10.1016/S0006-3495(84)84252-6.

[61] Barry M. Gumbiner. "Cell Adhesion: The Molecular Basis of Tissue Architecture and Morphogenesis". In: *Cell* 84.3 (1996), pp. 345–357. DOI: 10.1016/S0092-8674(00)81279-9.

[62] T. Erdmann and U. S. Schwarz. "Impact of receptor-ligand distance on adhesion cluster stability". In: *The European Physical Journal E* 22.2 (2007), pp. 123–137. DOI: 10.1140/epje/e2007-00019-8.

[63] Huajian Gao, Jin Qian, and Bin Chen. "Probing mechanical principles of focal contacts in cell–matrix adhesion with a coupled stochastic–elastic modelling framework". In: *Journal of The Royal Society Interface* 8.62 (2011), pp. 1217–1232. DOI: 10.1098/rsif.2011.0157.

[64] Ulrich S. Schwarz and Samuel A. Safran. "Physics of adherent cells". In: *Reviews of Modern Physics* 85.3 (2013), pp. 1327–1381. DOI: 10.1103/RevModPhys.85.1327.

[65] Jan Liphardt, Bibiana Onoa, Steven B. Smith, Ignacio Tinoco, and Carlos Bustamante. "Reversible Unfolding of Single RNA Molecules by Mechanical Force". In: *Science* 292.5517 (2001), pp. 733–737. DOI: 10.1126/science.1058498.

[66] Olga K. Dudko, Jérôme Mathé, Attila Szabo, Amit Meller, and Gerhard Hummer. "Extracting Kinetics from Single-Molecule Force Spectroscopy: Nanopore Unzipping of DNA Hairpins". In: *Biophysical Journal* 92.12 (2007), pp. 4188–4195. DOI: 10.1529/biophysj.106.102855.

[67] Jérôme Mathé, Hasina Visram, Virgile Viasnoff, Yitzhak Rabin, and Amit Meller. "Nanopore Unzipping of Individual DNA Hairpin Molecules". In: *Biophysical Journal* 87.5 (2004), pp. 3205–3212. DOI: 10.1529/biophysj.104.047274.

[68] Michael T Woodside, Cuauhtémoc García-García, and Steven M Block. "Folding and unfolding single RNA molecules under tension". In: *Current opinion in chemical biology* 12.6 (2008), pp. 640–646. DOI: 10.1016/j.cbpa.2008.08.011.

[69] Maria Manosas, Joan Camunas-Soler, Vincent Croquette, and Felix Ritort. "Single molecule high-throughput footprinting of small and large DNA ligands". In: *Nature Communications* 8.1 (2017), p. 304. DOI: 10.1038/s41467-017-00379-w.

[70] A. F Huxley and R. M. Simmons. "Proposed Mechanism of Force Generation in Striated Muscle". In: *Nature* 233.5321 (1971), pp. 533–538. DOI: 10.1038/233533a0.

[71] Terrell L. Hill. "Theory of Muscular Contraction Extended to Groups of Actin Sites". In: *Proceedings of the National Academy of Sciences* 70.10 (1973), pp. 2732–2736. DOI: 10.1073/pnas.70.10.2732.

[72] M. Epstein and W. Herzog. *Theoretical models of skeletal muscle: biological and mathematical considerations*. OCLC: 37879071. Chichester ; New York: Wiley, 1998. 238 pp.

[73] M. Caruel, J.-M. Allain, and L. Truskinovsky. "Muscle as a Metamaterial Operating Near a Critical Point". In: *Physical Review Letters* 110.24 (2013), p. 248103. DOI: 10.1103/PhysRevLett.110.248103.

[74] M. Caruel and L. Truskinovsky. "Statistical mechanics of the Huxley-Simmons model". In: *Physical Review E* 93.6 (2016), p. 062407. DOI: 10.1103/PhysRevE.93.062407.

[75] M. Caruel and L. Truskinovsky. "Physics of muscle contraction". In: *Reports on Progress in Physics* 81.3 (2018), p. 036602. DOI: 10.1088/1361-6633/aa7b9e.

[76] Matthieu Caruel, Philippe Moireau, and Dominique Chapelle. "Stochastic modeling of chemical–mechanical coupling in striated muscles". In: *Biomechanics and Modeling in Mechanobiology* 18.3 (2019), pp. 563–587. DOI: 10.1007/s10237-018-1102-z.

[77] M. Peyrard and A. R. Bishop. "Statistical mechanics of a nonlinear model for DNA denaturation". In: *Physical Review Letters* 62.23 (1989), pp. 2755–2758. DOI: 10.1103/PhysRevLett.62.2755.

[78] Nikos Theodorakopoulos, Michel Peyrard, and Robert S. MacKay. "Nonlinear Structures and Thermodynamic Instabilities in a One-Dimensional Lattice System". In: *Physical Review Letters* 93.25 (2004), p. 258101. DOI: 10.1103/PhysRevLett.93.258101.

[79] Paolo Grinza and Alessandro Mossa. "Topological Origin of the Phase Transition in a Model of DNA Denaturation". In: *Physical Review Letters* 92.15 (2004), p. 158102. DOI: 10.1103/PhysRevLett.92.158102.

[80] Michel Peyrard. "Nonlinear dynamics and statistical physics of DNA". In: *Nonlinearity* 17.2 (2004), R1. DOI: 10.1088/0951-7715/17/2/R01.

[81] Vassili Ivanov, Yan Zeng, and Giovanni Zocchi. "Statistical mechanics of base stacking and pairing in DNA melting". In: *Physical Review E* 70.5 (2004), p. 051907. DOI: 10.1103/PhysRevE.70.051907.

[82] John Palmeri, Manoel Manghi, and Nicolas Destainville. "Thermal denaturation of fluctuating finite DNA chains: The role of bending rigidity in bubble nucleation". In: *Physical Review E* 77.1 (2008), p. 011913. DOI: 10.1103/PhysRevE.77.011913.

[83] Ana Elisa Bergues Pupo, Fernando Falo, and Alessandro Fiasconaro. "DNA overstretching transition induced by melting in a dynamical mesoscopic model". In: *The Journal of Chemical Physics* 139.9 (2013), p. 095101. DOI: 10.1063/1.4819263.

[84] Grégoire Perret, Thomas Lacornerie, Fabio Manca, Stefano Giordano, Momoko Kumemura, Nicolas Lafitte, Laurent Jalabert, Mehmet C. Tarhan, Eric F. Lartigau, Fabrizio Cleri, Hiroyuki Fujita, and Dominique Collard. "Real-time mechanical characterization of DNA degradation under therapeutic X-rays and its theoretical modeling". In: *Microsystems & Nanoengineering* 2.1 (2016), pp. 1–9. DOI: 10.1038/micronano.2016.62.

[85] Grégoire Perret, Thomas Lacornerie, Fabio Manca, Stefano Giordano, Momoko Kumemura, Nicolas Lafitte, Laurent Jalabert, Mehmet C. Tarhan, Eric F. Lartigau, Fabrizio Cleri, Hiroyuki Fujita, and Dominique Collard. "Mesure de la dégradation bio-mécanique d'une fibre d'ADN sous l'effet des rayons X thérapeutiques". In: *médecine/sciences* 33.12 (2017), pp. 1026–1029. DOI: 10.1051/medsci/20173312003.

[86] Michael R. Buche and Meredith N. Silberstein. "Chain breaking in the statistical mechanical constitutive theory of polymer networks". In: *Journal of the Mechanics and Physics of Solids* 156 (2021), p. 104593. DOI: 10.1016/j.jmps.2021.104593.

[87] Volker Bormuth, Vladimir Varga, Jonathon Howard, and Erik Schäffer. "Protein Friction Limits Diffusive and Directed Movements of Kinesin Motors on Microtubules". In: *Science* 325.5942 (2009), pp. 870–873. DOI: 10.1126/science.1174923.

[88] R. Sahli, G. Pallares, C. Ducottet, I. E. Ben Ali, S. Al Akhrass, M. Guibert, and J. Scheibert. "Evolution of real contact area under shear and the value of static friction of soft materials". In: *Proceedings of the National Academy of Sciences* 115.3 (2018), pp. 471–476. DOI: 10.1073/pnas.1706434115.

[89] Pierre Sens. "Stick–slip model for actin-driven cell protrusions, cell polarization, and crawling". In: *Proceedings of the National Academy of Sciences* 117.40 (2020), pp. 24670–24678. DOI: 10.1073/pnas.2011785117.

[90] Evangelos Liamas, Simon D. Connell, Shivaprakash N. Ramakrishna, and Anwesha Sarkar. "Probing the frictional properties of soft materials at the nanoscale". In: *Nanoscale* 12.4 (2020), pp. 2292–2308. DOI: 10.1039/C9NR07084B.

[91] Stefano Giordano. "Spin variable approach for the statistical mechanics of folding and unfolding chains". In: *Soft Matter* 13.38 (2017), pp. 6877–6893. DOI: 10.1039/C7SM00882A.

[92] Manon Benedito and Stefano Giordano. "Thermodynamics of small systems with conformational transitions: The case of two-state freely jointed chains with extensible units". In: *The Journal of Chemical Physics* 149.5 (2018), p. 054901. DOI: 10.1063/1.5026386.

[93] Giuseppe Florio, Giuseppe Puglisi, and Stefano Giordano. "Role of temperature in the decohesion of an elastic chain tethered to a substrate by onsite breakable links". In: *Physical Review Research* 2.3 (2020), p. 033227. DOI: 10.1103/PhysRevResearch.2.033227.

[94] G. Florio and G. Puglisi. "Unveiling the influence of device stiffness in single macromolecule unfolding". In: *Scientific Reports* 9.1 (2019), p. 4997. DOI: 10.1038/s41598-019-41330-x.

[95] Luca Bellino, Giuseppe Florio, and Giuseppe Puglisi. "The influence of device handles in single-molecule experiments". In: *Soft Matter* 15.43 (2019), pp. 8680–8690. DOI: 10.1039/C9SM01376H.

[96] R. A. Usmani. "Inversion of a Tridiagonal Jacobi Matrix". In: *Linear Algebra and Its Applications* 212/213 (1994), p. 413.

[97] R. A. Usmani. "Inversion of Jacobi's tridiagonal matrix". en. In: *Computers & Mathematics with Applications* 27.8 (Apr. 1994), pp. 59–66. DOI: 10.1016/0898-1221(94)90066-3.

[98] J.H. Weiner. *Statistical Mechanics of Elasticity*. New York: John Wiley & Sons, Inc., 1983.

[99] H. A. Kramers. "Brownian motion in a field of force and the diffusion model of chemical reactions". In: *Physica* 7.4 (1940), pp. 284–304. DOI: 10.1016/S0031-8914(40)90098-2.

[100] Itamar Benichou and Sefi Givli. "Rate Dependent Response of Nanoscale Structures Having a Multiwell Energy Landscape". In: *Physical Review Letters* 114.9 (2015), p. 095504. DOI: 10.1103/PhysRevLett.114.095504.

[101] Itamar Benichou, Yaojun Zhang, Olga K. Dudko, and Sefi Givli. "The rate dependent response of a bistable chain at finite temperature". In: *Journal of the Mechanics and Physics of Solids* 95 (2016), pp. 44–63. DOI: 10.1016/j.jmps.2016.05.001.

[102] Manon Benedito and Stefano Giordano. "Isotensional and isometric force-extension response of chains with bistable units and Ising interactions". In: *Physical Review E* 98.5 (2018), p. 052146. DOI: 10.1103/PhysRevE.98.052146.

[103] Manon Benedito and Stefano Giordano. "Unfolding pathway and its identifiability in heterogeneous chains of bistable units". In: *Physics Letters A* 384.5 (2020), p. 126124. DOI: 10.1016/j.physleta.2019.126124.

[104] J. H. Gibbs and E. A. DiMarzio. "Statistical Mechanics of Helix-Coil Transitions in Biological Macromolecules". In: *The Journal of Chemical Physics* 30.1 (1959), pp. 271–282. DOI: 10.1063/1.1729886.

[105] D. M. Crothers, Neville R. Kallenbach, and B. H. Zimm. "The melting transition of low-molecular-weight DNA: Theory and experiment". In: *Journal of Molecular Biology* 11.4 (1965), pp. 802–820. DOI: 10.1016/S0022-2836(65)80037-7.

[106] C. Kittel. "Phase Transition of a Molecular Zipper". In: *American Journal of Physics* 37.9 (1969), pp. 917–920. DOI: 10.1119/1.1975930.

[107] K. Nishinari, S. Koide, P. A. Williams, and G. O. Phillips. "A zipper model approach to the thermoreversible gel-sol transition". In: *Journal de Physique* 51.16 (1990), pp. 1759–1768. DOI: 10.1051/jphys:0199000510160175900.

[108] Roland G. Winkler. "Equivalence of statistical ensembles in stretching single flexible polymers". In: *Soft Matter* 6.24 (2010), pp. 6183–6191. DOI: 10.1039/C0SM00488J.

[109] Fabio Manca, Stefano Giordano, Pier Luca Palla, Rinaldo Zucca, Fabrizio Cleri, and Luciano Colombo. "Elasticity of flexible and semiflexible polymers with extensible bonds in the Gibbs and Helmholtz ensembles". In: *The Journal of Chemical Physics* 136.15 (2012), p. 154906. DOI: 10.1063/1.4704607.

[110] Fabio Manca, Stefano Giordano, Pier Luca Palla, Fabrizio Cleri, and Luciano Colombo. "Two-state theory of single-molecule stretching experiments". In: *Physical Review E* 87.3 (2013), p. 032705. DOI: 10.1103/PhysRevE.87.032705.

[111] Fabio Manca, Stefano Giordano, Pier Luca Palla, and Fabrizio Cleri. "On the equivalence of thermodynamics ensembles for flexible polymer chains". In: *Physica A: Statistical Mechanics and its Applications* 395 (2014), pp. 154–170. DOI: 10.1016/j.physa.2013.10.042.

[112] Stefano Giordano. "Helmholtz and Gibbs ensembles, thermodynamic limit and bistability in polymer lattice models". In: *Continuum Mechanics and Thermodynamics* 30.3 (2018), pp. 459–483. DOI: 10.1007/s00161-017-0615-5.

[113] A. M. Skvortsov, L. I. Klushin, and F. a. M. Leermakers. "Negative compressibility and nonequivalence of two statistical ensembles in the escape transition of a polymer chain". In: *The Journal of Chemical Physics* 126.2 (2007), p. 024905. DOI: 10.1063/1.2406075.

[114] D. I. Dimitrov, L. I. Klushin, A. Skvortsov, A. Milchev, and K. Binder. "The escape transition of a polymer: A unique case of non-equivalence between statistical ensembles". In: *The European Physical Journal E* 29.1 (2009), pp. 9–25. DOI: 10.1140/epje/i2008-10442-0.

[115] Alexander M. Skvortsov, Leonid I. Klushin, Alexey A. Polotsky, and Kurt Binder. "Mechanical desorption of a single chain: Unusual aspects of phase coexistence at a first-order transition". In: *Physical Review E* 85.3 (2012), p. 031803. DOI: 10.1103/PhysRevE.85.031803.

[116] Sandipan Dutta and Panayotis Benetatos. "Inequivalence of fixed-force and fixed-extension statistical ensembles for a flexible polymer tethered to a planar substrate". In: *Soft Matter* 14.33 (2018), pp. 6857–6866. DOI: 10.1039/C8SM01321G.

[117] Sandipan Dutta and Panayotis Benetatos. "Statistical ensemble inequivalence for flexible polymers under confinement in various geometries". In: *Soft Matter* 16.8 (2019), pp. 2114–2127. DOI: 10.1039/C9SM02246E.

[118] Geunho Noh and Panayotis Benetatos. “Tensile elasticity of a freely jointed chain with reversible hinges”. In: *Soft Matter* 17.12 (2021), pp. 3333–3345. DOI: 10.1039/D1SM00053E.

[119] Alan Arnold Griffith and Geoffrey Ingram Taylor. “VI. The phenomena of rupture and flow in solids”. In: *Philosophical Transactions of the Royal Society of London. Series A, Containing Papers of a Mathematical or Physical Character* 221.582 (1921), pp. 163–198. DOI: 10.1098/rsta.1921.0006.

[120] G. R. Irwin. “Analysis of Stresses and Strains Near the End of a Crack Traversing a Plate”. In: *Journal of Applied Mechanics* 24.3 (1957), pp. 361–364. DOI: 10.1115/1.4011547.

[121] G. R. Irwin. “Fracture”. In: *Encyclopaedia of Physics*. Vol. 6. Elasticity and Plasticity. Berlin: Springer, 1958, pp. 551–590.

[122] D. J. Dijkstra, J. C. M. Torfs, and A. J. Pennings. “Temperature-dependent fracture mechanisms in ultra-high strength polyethylene fibers”. en. In: *Colloid and Polymer Science* 267.10 (Oct. 1989), pp. 866–875. DOI: 10.1007/BF01410334.

[123] K. Kang and W. Cai. “Brittle and ductile fracture of semiconductor nanowires – molecular dynamics simulations”. In: *Philosophical Magazine* 87.14-15 (May 2007), pp. 2169–2189. DOI: 10.1080/14786430701222739.

[124] Zhiguo Wang, Xiaotao Zu, Li Yang, Fei Gao, and William J. Weber. “Atomistic simulations of the size, orientation, and temperature dependence of tensile behavior in GaN nanowires”. In: *Physical Review B* 76.4 (2007), p. 045310. DOI: 10.1103/PhysRevB.76.045310.

[125] Keonwook Kang and Wei Cai. “Size and temperature effects on the fracture mechanisms of silicon nanowires: Molecular dynamics simulations”. In: *International Journal of Plasticity*. Special Issue In Honor of David L. McDowell 26.9 (2010), pp. 1387–1401. DOI: 10.1016/j.ijplas.2010.02.001.

[126] Zhaoxuan Wu, Yong-Wei Zhang, Mark H. Jhon, Huajian Gao, and David J. Srolovitz. “Nanowire Failure: Long = Brittle and Short = Ductile”. In: *Nano Letters* 12.2 (Feb. 2012), pp. 910–914. DOI: 10.1021/nl203980u.

[127] Jiangwei Wang, Frederic Sansoz, Jianyu Huang, Yi Liu, Shouheng Sun, Ze Zhang, and Scott X. Mao. “Near-ideal theoretical strength in gold nanowires containing angstrom scale twins”. en. In: *Nature Communications* 4.1 (Apr. 2013), p. 1742. DOI: 10.1038/ncomms2768.

[128] J. Ast, J. J. Schwiedrzik, J. Wehrs, D. Frey, M. N. Polyakov, J. Michler, and X. Maeder. “The brittle-ductile transition of tungsten single crystals at the micro-scale”. en. In: *Materials & Design* 152 (Aug. 2018), pp. 168–180. DOI: 10.1016/j.matdes.2018.04.009.

[129] Md Adnan Mahathir Munshi, Sourajit Majumder, Mohammad Motalab, and Sourav Saha. “Insights into the mechanical properties and fracture mechanism of Cadmium Telluride nanowire”. en. In: *Materials Research Express* 6.10 (Aug. 2019), p. 105083. DOI: 10.1088/2053-1591/ab3ba1.

[130] Guangming Cheng, Yin Zhang, Tzu-Hsuan Chang, Qunfeng Liu, Lin Chen, Wei D. Lu, Ting Zhu, and Yong Zhu. “In Situ Nano-thermomechanical Experiment Reveals Brittle to Ductile Transition in Silicon Nanowires”. In: *Nano Letters* 19.8 (Aug. 2019), pp. 5327–5334. DOI: 10.1021/acs.nanolett.9b01789.

[131] G. Puglisi and G. Saccomandi. “Multi-scale modelling of rubber-like materials and soft tissues: an appraisal”. In: *Proceedings of the Royal Society A: Mathematical, Physical and Engineering Sciences* 472.2187 (Mar. 2016), p. 20160060. DOI: 10.1098/rspa.2016.0060.

[132] Giuseppe Florio, Nicola M. Pugno, Markus J. Buehler, and Giuseppe Puglisi. "A coarse-grained mechanical model for folding and unfolding of tropoelastin with possible mutations". en. In: *Acta Biomaterialia* 134 (Oct. 2021), pp. 477–489. DOI: 10.1016/j.actbio.2021.07.032.

[133] Giuseppe Florio and Giuseppe Puglisi. "A predictive model for the thermomechanical melting transition of double stranded DNA". en. In: *Acta Biomaterialia* 157 (Feb. 2023), pp. 225–235. DOI: 10.1016/j.actbio.2022.11.046.

[134] D. S. Dugdale. "Yielding of steel sheets containing slits". en. In: *Journal of the Mechanics and Physics of Solids* 8.2 (May 1960), pp. 100–104. DOI: 10.1016/0022-5096(60)90013-2.

[135] G. I. Barenblatt. "The Mathematical Theory of Equilibrium Cracks in Brittle Fracture". en. In: *Advances in Applied Mechanics*. Ed. by H. L. Dryden, Th. von Kármán, G. Kuerti, F. H. van den Dungen, and L. Howarth. Vol. 7. Elsevier, Jan. 1962, pp. 55–129. DOI: 10.1016/S0065-2156(08)70121-2.

[136] J. C. Charmet, Stéphane Roux, and Etienne Guyon. *Disorder and Fracture*. en. Google-Books-ID: eSzyWAGWMn4C. Springer Science & Business Media, 1990.

[137] Francisco-José Pérez-Reche, Lev Truskinovsky, and Giovanni Zanzotto. "Driving-Induced Crossover: From Classical Criticality to Self-Organized Criticality". In: *Physical Review Letters* 101.23 (Dec. 2008), p. 230601. DOI: 10.1103/PhysRevLett.101.230601.

[138] Giorgio Parisi, Itamar Procaccia, Corrado Rainone, and Murari Singh. "Shear bands as manifestation of a criticality in yielding amorphous solids". In: *Proceedings of the National Academy of Sciences* 114.22 (May 2017), pp. 5577–5582. DOI: 10.1073/pnas.1700075114.

[139] Laurent Ponson and Nadjime Pindra. "Crack propagation through disordered materials as a depinning transition: A critical test of the theory". In: *Physical Review E* 95.5 (May 2017), p. 053004. DOI: 10.1103/PhysRevE.95.053004.

[140] Gianni Niccolini, Alessio Rubino, and Alberto Carpinteri. "Dimensional transitions in creeping materials due to nonlinearity and microstructural disorder". en. In: *Chaos, Solitons & Fractals* 141 (Dec. 2020), p. 110345. DOI: 10.1016/j.chaos.2020.110345.

[141] Santanu Sinha, Subhadeep Roy, and Alex Hansen. "Phase transitions and correlations in fracture processes where disorder and stress compete". In: *Physical Review Research* 2.4 (Oct. 2020), p. 043108. DOI: 10.1103/PhysRevResearch.2.043108.

[142] Mathias Lebihain, Laurent Ponson, Djimédo Kondo, and Jean-Baptiste Leblond. "Effective toughness of disordered brittle solids: A homogenization framework". en. In: *Journal of the Mechanics and Physics of Solids* 153 (Aug. 2021), p. 104463. DOI: 10.1016/j.jmps.2021.104463.

[143] Hudson Borja da Rocha and Lev Truskinovsky. "Mean field fracture in disordered solids: Statistics of fluctuations". en. In: *Journal of the Mechanics and Physics of Solids* 158 (Jan. 2022), p. 104646. DOI: 10.1016/j.jmps.2021.104646.

[144] Michel Tsamados, Anne Tanguy, Chay Goldenberg, and Jean-Louis Barrat. "Local elasticity map and plasticity in a model Lennard-Jones glass". In: *Physical Review E* 80.2 (Aug. 2009), p. 026112. DOI: 10.1103/PhysRevE.80.026112.

[145] A. Tanguy, F. Leonforte, and J. -L. Barrat. "Plastic response of a 2D Lennard-Jones amorphous solid: Detailed analysis of the local rearrangements at very slow strain rate". en. In: *The European Physical Journal E* 20.3 (July 2006), pp. 355–364.

[146] A. Tanguy, B. Mantisi, and M. Tsamados. "Vibrational modes as a predictor for plasticity in a model glass". en. In: *Europhysics Letters* 90.1 (Apr. 2010), p. 16004. DOI: 10.1209/0295-5075/90/16004.

[147] F. Léonforte, A. Tanguy, J. P. Wittmer, and J.-L. Barrat. "Inhomogeneous Elastic Response of Silica Glass". In: *Physical Review Letters* 97.5 (July 2006), p. 055501. DOI: 10.1103/PhysRevLett.97.055501.

[148] Chih-Hung Chen, Eran Bouchbinder, and Alain Karma. "Instability in dynamic fracture and the failure of the classical theory of cracks". en. In: *Nature Physics* 13.12 (Dec. 2017), pp. 1186–1190. DOI: 10.1038/nphys4237.

[149] Tom Vincent-Dospital, Renaud Toussaint, Stéphane Santucci, Loïc Vanel, Daniel Bonamy, Lamine Hattali, Alain Cochard, Eirik G. Flekkøy, and Knut Jørgen Måløy. "How heat controls fracture: the thermodynamics of creeping and avalanching cracks". en. In: *Soft Matter* 16.41 (Oct. 2020), pp. 9590–9602. DOI: 10.1039/D0SM01062F.

[150] Hannes Risken. *The Fokker-Planck Equation: Methods of Solution and Applications*. en. Google-Books-ID: dXvpCAAAQBAJ. Springer Science & Business Media, Dec. 2012.

[151] William Coffey, Yu P. Kalmykov, and J. T. Waldron. *The Langevin Equation: With Applications to Stochastic Problems in Physics, Chemistry, and Electrical Engineering*. en. Google-Books-ID: dFBZMLJsQ5gC. World Scientific, 2004.

[152] Christopher H. Scholz. "Earthquakes and friction laws". In: *Nature* 391.6662 (1998), pp. 37–42. DOI: 10.1038/34097.

[153] Chris Marone. "The effect of loading rate on static friction and the rate of fault healing during the earthquake cycle". In: *Nature* 391.6662 (1998), pp. 69–72. DOI: 10.1038/34157.

[154] Eric G. Daub and Jean M. Carlson. "Friction, Fracture, and Earthquakes". In: *Annual Review of Condensed Matter Physics* 1.1 (2010), pp. 397–418. DOI: 10.1146/annurev-conmatphys-070909-104025.

[155] David Amitrano, Jean-Robert Grasso, and Didier Hantz. "From diffuse to localised damage through elastic interaction". In: *Geophysical Research Letters* 26.14 (1999), pp. 2109–2112. DOI: 10.1029/1999GL900388.

[156] Eric Gerde and M. Marder. "Friction and fracture". In: *Nature* 413.6853 (2001), pp. 285–288. DOI: 10.1038/35095018.

[157] O. Kresse and L. Truskinovsky. "Lattice friction for crystalline defects: from dislocations to cracks". In: *Journal of the Mechanics and Physics of Solids* 52.11 (2004), pp. 2521–2543. DOI: 10.1016/j.jmps.2004.04.011.

[158] F. Gimbert, D. Amitrano, and J. Weiss. "Crossover from quasi-static to dense flow regime in compressed frictional granular media". In: *Europhysics Letters* 104.4 (2013), p. 46001. DOI: 10.1209/0295-5075/104/46001.

[159] Paolo Biscari, Marco Fabrizio Urbano, Anna Zanzottera, and Giovanni Zanzotto. "Intermittency in Crystal Plasticity Informed by Lattice Symmetry". In: *Journal of Elasticity* 123.1 (2016), pp. 85–96. DOI: 10.1007/s10659-015-9548-z.

[160] Kamran Karimi, David Amitrano, and Jérôme Weiss. "From plastic flow to brittle fracture: Role of microscopic friction in amorphous solids". In: *Physical Review E* 100.1 (2019), p. 012908. DOI: 10.1103/PhysRevE.100.012908.

[161] N. Gorbushin, G. Mishuris, and L. Truskinovsky. "Frictionless Motion of Lattice Defects". In: *Physical Review Letters* 125.19 (2020), p. 195502. DOI: 10.1103/PhysRevLett.125.195502.

[162] Manon Benedito, Fabio Manca, and Stefano Giordano. "Full Statistics of Conjugated Thermodynamic Ensembles in Chains of Bistable Units". In: *Inventions* 4.1 (2019), p. 19. DOI: 10.3390/inventions4010019.

[163] Manon Benedito, Fabio Manca, Pier Luca Palla, and Stefano Giordano. "Rate-dependent force–extension models for single-molecule force spectroscopy experiments". In: *Physical Biology* 17.5 (2020), p. 056002. DOI: 10.1088/1478-3975/ab97a8.

[164] Romain Jorge Do Marco and Stefano Giordano. "Thermodynamics of Extra-Toughness and Hidden-Length in Polymeric Materials with Sacrificial Bonds". In: *Applied Mechanics* 3.3 (2022), pp. 935–955. DOI: 10.3390/applmech3030053.

[165] Luca Bellino, Giuseppe Florio, Stefano Giordano, and Giuseppe Puglisi. "On the competition between interface energy and temperature in phase transition phenomena". In: *Applications in Engineering Science* 2 (2020), p. 100009. DOI: 10.1016/j.apples.2020.100009.

[166] Stefano Giordano. "Statistical mechanics of rate-independent stick-slip on a corrugated surface composed of parabolic wells". In: *Continuum Mechanics and Thermodynamics* 34.5 (2022), pp. 1343–1372. DOI: 10.1007/s00161-022-01129-0.

[167] Michael R. Buche and Meredith N. Silberstein. "Statistical mechanical constitutive theory of polymer networks: The inextricable links between distribution, behavior, and ensemble". In: *Physical Review E* 102.1 (2020), p. 012501. DOI: 10.1103/PhysRevE.102.012501.

[168] T. R. Strick, M.-N. Dessinges, G. Charvin, N. H. Dekker, J.-F. Allemand, D. Bensimon, and V. Croquette. "Stretching of macromolecules and proteins". In: *Reports on Progress in Physics* 66.1 (2002), p. 1. DOI: 10.1088/0034-4885/66/1/201.

[169] F. Ritort. "Single-molecule experiments in biological physics: methods and applications". In: *Journal of Physics: Condensed Matter* 18.32 (2006), R531. DOI: 10.1088/0953-8984/18/32/R01.

[170] Fabrizio Cleri. "Microscopic mechanics of biomolecules in living cells". In: *Scientific Modeling and Simulation SMNS* 15.1 (2008), pp. 339–362. DOI: 10.1007/s10820-008-9104-2.

[171] Keir C. Neuman and Attila Nagy. "Single-molecule force spectroscopy: optical tweezers, magnetic tweezers and atomic force microscopy". In: *Nature Methods* 5.6 (2008), pp. 491–505. DOI: 10.1038/nmeth.1218.

[172] Sanjay Kumar and Mai Suan Li. "Biomolecules under mechanical force". In: *Physics Reports* 486.1 (2010), pp. 1–74. DOI: 10.1016/j.physrep.2009.11.001.

[173] Soumit S. Mandal. "Force Spectroscopy on Single Molecules of Life". In: *ACS Omega* 5.20 (2020), pp. 11271–11278. DOI: 10.1021/acsomega.0c00814.

[174] Annamaria Zaltron, Michele Merano, Giampaolo Mistura, Cinzia Sada, and Flavio Seno. "Optical tweezers in single-molecule experiments". In: *The European Physical Journal Plus* 135.11 (2020), p. 896. DOI: 10.1140/epjp/s13360-020-00907-6.

[175] Iwijn De Vlaminck and Cees Dekker. "Recent advances in magnetic tweezers". In: *Annual Review of Biophysics* 41 (2012), pp. 453–472. DOI: 10.1146/annurev-biophys-122311-100544.

[176] A. Ashkin. "Atomic-Beam Deflection by Resonance-Radiation Pressure". In: *Physical Review Letters* 25.19 (1970), pp. 1321–1324. DOI: 10.1103/PhysRevLett.25.1321.

[177] A. Ashkin. "Acceleration and Trapping of Particles by Radiation Pressure". In: *Physical Review Letters* 24.4 (1970), pp. 156–159. DOI: 10.1103/PhysRevLett.24.156.

[178] A. Ashkin, J. M. Dziedzic, J. E. Bjorkholm, and Steven Chu. "Observation of a single-beam gradient force optical trap for dielectric particles". In: *Optics Letters* 11.5 (1986), pp. 288–290. DOI: 10.1364/OL.11.000288.

[179] Jan Gieseler, Juan Ruben Gomez-Solano, Alessandro Magazzù, Isaac Pérez Castillo, Laura Pérez García, Marta Gironella-Torrent, Xavier Viader-Godoy, Felix Ritort, Giuseppe Pesce, Alejandro V. Arzola, Karen Volke-Sepúlveda, and Giovanni Volpe. "Optical tweezers — from calibration to applications: a tutorial". In: *Advances in Optics and Photonics* 13.1 (2021), pp. 74–241. DOI: 10.1364/AOP.394888.

[180] F. H. C. Crick and A. F. W. Hughes. "The physical properties of cytoplasm: A study by means of the magnetic particle method Part I. Experimental". In: *Experimental Cell Research* 1.1 (1950), pp. 37–80. DOI: 10.1016/0014-4827(50)90048-6.

[181] P A Valberg and D F Albertini. "Cytoplasmic motions, rheology, and structure probed by a novel magnetic particle method." In: *Journal of Cell Biology* 101.1 (1985), pp. 130–140. DOI: 10.1083/jcb.101.1.130.

[182] P. A. Valberg and H. A. Feldman. "Magnetic particle motions within living cells. Measurement of cytoplasmic viscosity and motile activity". In: *Biophysical Journal* 52.4 (1987), pp. 551–561. DOI: 10.1016/S0006-3495(87)83244-7.

[183] Steven B. Smith, Laura Finzi, and Carlos Bustamante. "Direct Mechanical Measurements of the Elasticity of Single DNA Molecules by Using Magnetic Beads". In: *Science* 258.5085 (1992), pp. 1122–1126. DOI: 10.1126/science.1439819.

[184] T. R. Strick, J. F. Allemand, D. Bensimon, A. Bensimon, and V. Croquette. "The elasticity of a single supercoiled DNA molecule". In: *Science (New York, N.Y.)* 271.5257 (1996), pp. 1835–1837. DOI: 10.1126/science.271.5257.1835.

[185] Thomas E Fisher, Andres F Oberhauser, Mariano Carrion-Vazquez, Piotr E Marszalek, and Julio M Fernandez. "The study of protein mechanics with the atomic force microscope". In: *Trends in Biochemical Sciences* 24.10 (1999), pp. 379–384. DOI: 10.1016/S0968-0004(99)01453-X.

[186] G. Binnig, C. F. Quate, and Ch. Gerber. "Atomic Force Microscope". In: *Physical Review Letters* 56.9 (1986), pp. 930–933. DOI: 10.1103/PhysRevLett.56.930.

[187] Felix Rico, Laura Gonzalez, Ignacio Casuso, Manel Puig-Vidal, and Simon Scheuring. "High-speed force spectroscopy unfolds titin at the velocity of molecular dynamics simulations". In: *Science (New York, N.Y.)* 342.6159 (2013), pp. 741–743. DOI: 10.1126/science.1239764.

[188] Frédéric Eghiaian, Felix Rico, Adai Colom, Ignacio Casuso, and Simon Scheuring. "High-speed atomic force microscopy: Imaging and force spectroscopy". In: *FEBS Letters* 588.19 (2014), pp. 3631–3638. DOI: 10.1016/j.febslet.2014.06.028.

[189] Claire Valotteau, Fidan Sumbul, and Felix Rico. "High-speed force spectroscopy: microsecond force measurements using ultrashort cantilevers". In: *Biophysical Reviews* 11.5 (2019), pp. 689–699. DOI: 10.1007/s12551-019-00585-4.

[190] Felix Rico, Andreas Russek, Laura González, Helmut Grubmüller, and Simon Scheuring. "Heterogeneous and rate-dependent streptavidin–biotin unbinding revealed by high-speed force spectroscopy and atomistic simulations". In: *Proceedings of the National Academy of Sciences* 116.14 (2019), pp. 6594–6601. DOI: 10.1073/pnas.1816909116.

[191] Frauke Gräter, Jianhua Shen, Hualiang Jiang, Mathias Gautel, and Helmut Grubmüller. "Mechanically Induced Titin Kinase Activation Studied by Force-Probe Molecular Dynamics Simulations". In: *Biophysical Journal* 88.2 (2005), pp. 790–804. DOI: 10.1529/biophysj.104.052423.

[192] Eric H. Lee, Jen Hsin, Marcos Sotomayor, Gemma Comellas, and Klaus Schulten. "Discovery Through the Computational Microscope". In: *Structure* 17.10 (2009), pp. 1295–1306. DOI: 10.1016/j.str.2009.09.001.

[193] P. Rai-Choudhury. *MEMS and MOEMS Technology and Applications*. SPIE, 2000.

[194] Albert Folch. *Introduction to BioMEMS*. CRC Press, 2016. DOI: 10.1201/b12263.

[195] Chi-Han Chiou and Gwo-Bin Lee. "A micromachined DNA manipulation platform for the stretching and rotation of a single DNA molecule*". In: *Journal of Micromechanics and Microengineering* 15.1 (2005), p. 109. DOI: 10.1088/0960-1317/15/1/017.

[196] Fangfang Ren, Yingbo Zu, Kartik Kumar Rajagopalan, and Shengnian Wang. "Regulation of DNA conformations and dynamics in flows with hybrid field microfluidics". In: *Biomicrofluidics* 6.4 (2012), p. 044103. DOI: 10.1063/1.4762852.

[197] Mehmet C. Tarhan, Nicolas Lafitte, Yannick Tauran, Laurent Jalabert, Momoko Kumemura, Grégoire Perret, Beomjoon Kim, Anthony W. Coleman, Hiroyuki Fujita, and Dominique Collard. "A rapid and practical technique for real-time monitoring of biomolecular interactions using mechanical responses of macromolecules". In: *Scientific Reports* 6.1 (2016), p. 28001. DOI: 10.1038/srep28001.

[198] Christophe Yamahata, Dominique Collard, Bernard Legrand, Tetsuya Takekawa, Momoko Kumemura, Gen Hashiguchi, and Hiroyuki Fujita. "Silicon Nanotweezers With Subnanometer Resolution for the Micromanipulation of Biomolecules". In: *Journal of Microelectromechanical Systems* 17.3 (2008), pp. 623–631. DOI: 10.1109/JMEMS.2008.922080.

[199] Fabio Manca, Stefano Giordano, Pier Luca Palla, and Fabrizio Cleri. "Scaling Shift in Multicracked Fiber Bundles". In: *Physical Review Letters* 113.25 (2014), p. 255501. DOI: 10.1103/PhysRevLett.113.255501.

[200] Fabio Manca, Stefano Giordano, Pier Luca Palla, and Fabrizio Cleri. "Stochastic mechanical degradation of multi-cracked fiber bundles with elastic and viscous interactions". In: *The European Physical Journal E* 38.5 (2015), p. 44. DOI: 10.1140/epje/i2015-15044-1.

[201] Rita Salánki, Csaba Hős, Norbert Orgovan, Beatrix Péter, Noémi Sándor, Zsuzsa Bajtay, Anna Erdei, Robert Horvath, and Bálint Szabó. "Single Cell Adhesion Assay Using Computer Controlled Micropipette". In: *PLOS ONE* 9.10 (2014), e111450. DOI: 10.1371/journal.pone.0111450.

[202] Patricia M. Davidson, Gregory R. Fedorchak, Solenne Mondésert-Deveraux, Emily S. Bell, Philipp Isermann, Denis Aubry, Rachele Allena, and Jan Lammerding. "High-throughput microfluidic micropipette aspiration device to probe time-scale dependent nuclear mechanics in intact cells". In: *Lab on a Chip* 19.21 (2019), pp. 3652–3663. DOI: 10.1039/C9LC00444K.

[203] Neophytos Christodoulou and Paris A. Skourides. "Distinct spatiotemporal contribution of morphogenetic events and mechanical tissue coupling during Xenopus neural tube closure". In: *Development (Cambridge, England)* 149.13 (2022), dev200358. DOI: 10.1242/dev.200358.

[204] alemnis. *TENSILE TESTING*. 2023.

[205] J. D. Watson and F. H. C. Crick. "Molecular Structure of Nucleic Acids: A Structure for Deoxyribose Nucleic Acid". In: *Nature* 171.4356 (1953), pp. 737–738. DOI: 10.1038/171737a0.

[206] J. F. Marko and E. D. Siggia. "Bending and twisting elasticity of DNA". In: *Macromolecules* 27.4 (1995), pp. 981–988. DOI: 10.1021/ma00082a015.

[207] C. Bustamante, J. F. Marko, E. D. Siggia, and S. Smith. "Entropic Elasticity of λ-Phage DNA". In: *Science* 265.5178 (1994), pp. 1599–1600. DOI: 10.1126/science.8079175.

[208] Olli Punkkinen, Per Lyngs Hansen, Ling Miao, and Ilpo Vattulainen. "DNA Overstretching Transition: Ionic Strength Effects". In: *Biophysical Journal* 89.2 (2005), pp. 967–978. DOI: 10.1529/biophysj.105.063099.

[209] Jay R. Wenner, Mark C. Williams, Ioulia Rouzina, and Victor A. Bloomfield. "Salt dependence of the elasticity and overstretching transition of single DNA molecules". In: *Biophysical Journal* 82.6 (2002), pp. 3160–3169. DOI: 10.1016/S0006-3495(02)75658-0.

[210] Kirstin A. Walther, Jasna Brujić, Hongbin Li, and Julio M. Fernández. "Sub-Angstrom Conformational Changes of a Single Molecule Captured by AFM Variance Analysis". In: *Biophysical Journal* 90.10 (2006), pp. 3806–3812. DOI: 10.1529/biophysj.105.076224.

[211] Jan Lipfert, Jacob W. J. Kerssemakers, Tessa Jager, and Nynke H. Dekker. "Magnetic torque tweezers: measuring torsional stiffness in DNA and RecA-DNA filaments". In: *Nature Methods* 7.12 (2010), pp. 977–980. DOI: 10.1038/nmeth.1520.

[212] Jan Lipfert, Matthew Wiggin, Jacob W. J. Kerssemakers, Francesco Pedaci, and Nynke H. Dekker. "Freely orbiting magnetic tweezers to directly monitor changes in the twist of nucleic acids". In: *Nature Communications* 2.1 (2011), p. 439. DOI: 10.1038/ncomms1450.

[213] Stefanos K. Nomidis, Franziska Kriegel, Willem Vanderlinden, Jan Lipfert, and Enrico Carlon. "Twist-Bend Coupling and the Torsional Response of Double-Stranded DNA". In: *Physical Review Letters* 118.21 (2017), p. 217801. DOI: 10.1103/PhysRevLett.118.217801.

[214] Stefanos K. Nomidis, Enrico Skoruppa, Enrico Carlon, and John F. Marko. "Twist-bend coupling and the statistical mechanics of the twistable wormlike-chain model of DNA: Perturbation theory and beyond". In: *Physical Review E* 99.3 (2019), p. 032414. DOI: 10.1103/PhysRevE.99.032414.

[215] Steven B. Smith, Yujia Cui, and Carlos Bustamante. "Overstretching B-DNA: The Elastic Response of Individual Double-Stranded and Single-Stranded DNA Molecules". In: *Science* 271.5250 (1996), pp. 795–799. DOI: 10.1126/science.271.5250.795.

[216] I. Rouzina and V. A. Bloomfield. "Force-induced melting of the DNA double helix. 2. Effect of solution conditions". In: *Biophysical Journal* 80.2 (2001), pp. 894–900. DOI: 10.1016/S0006-3495(01)76068-7.

[217] I. Rouzina and V. A. Bloomfield. "Force-induced melting of the DNA double helix 1. Thermodynamic analysis". In: *Biophysical Journal* 80.2 (2001), pp. 882–893. DOI: 10.1016/S0006-3495(01)76067-5.

[218] Simona Cocco, Jie Yan, Jean-Francois Léger, Didier Chatenay, and John F. Marko. "Overstretching and force-driven strand separation of double-helix DNA". In: *Physical Review E* 70.1 (2004), p. 011910. DOI: 10.1103/PhysRevE.70.011910.

[219] Niklas Bosaeus, Afaf H. El-Sagheer, Tom Brown, Steven B. Smith, Björn Åkerman, Carlos Bustamante, and Bengt Nordén. "Tension induces a base-paired overstretched DNA conformation". In: *Proceedings of the National Academy of Sciences* 109.38 (2012), pp. 15179–15184. DOI: 10.1073/pnas.1213172109.

[220] Manoel Manghi, Nicolas Destainville, and John Palmeri. "Mesoscopic models for DNA stretching under force: New results and comparison with experiments". In: *The European Physical Journal E* 35.10 (2012), p. 110. DOI: 10.1140/epje/i2012-12110-2.

[221] Matthias Rief, Filipp Oesterhelt, Berthold Heymann, and Hermann E. Gaub. "Single Molecule Force Spectroscopy on Polysaccharides by Atomic Force Microscopy". In: *Science* 275.5304 (1997), pp. 1295–1297. DOI: 10.1126/science.275.5304.1295.

[222] Matthias Rief, Julio M. Fernandez, and Hermann E. Gaub. "Elastically Coupled Two-Level Systems as a Model for Biopolymer Extensibility". In: *Physical Review Letters* 81.21 (1998), pp. 4764–4767. DOI: 10.1103/PhysRevLett.81.4764.

[223] Junpeng Wang, Tatiana B. Kouznetsova, Roman Boulatov, and Stephen L. Craig. "Mechanical gating of a mechanochemical reaction cascade". In: *Nature Communications* 7.1 (2016), p. 13433. DOI: 10.1038/ncomms13433.

[224] Matthias Rief, Mathias Gautel, Filipp Oesterhelt, Julio M. Fernandez, and Hermann E. Gaub. "Reversible Unfolding of Individual Titin Immunoglobulin Domains by AFM". In: *Science* 276.5315 (1997), pp. 1109–1112. DOI: 10.1126/science.276.5315.1109.

[225] Andres F. Oberhauser, Piotr E. Marszalek, Harold P. Erickson, and Julio M. Fernandez. "The molecular elasticity of the extracellular matrix protein tenascin". In: *Nature* 393.6681 (1998), pp. 181–185. DOI: 10.1038/30270.

[226] Matthias Rief, Jaime Pascual, Matti Saraste, and Hermann E Gaub. "Single molecule force spectroscopy of spectrin repeats: low unfolding forces in helix bundles11Edited by W. Baumeister". In: *Journal of Molecular Biology* 286.2 (1999), pp. 553–561. DOI: 10.1006/jmbi.1998.2466.

[227] W. Mason. "The Lüders' Lines on Mild Steel". en. In: *Proceedings of the Physical Society of London* 23.1 (Dec. 1910), p. 305. DOI: 10.1088/1478-7814/23/1/331.

[228] Ahmet Yilmaz. "The Portevin–Le Chatelier effect: a review of experimental findings". In: *Science and Technology of Advanced Materials* 12.6 (Dec. 2011), p. 063001. DOI: 10.1088/1468-6996/12/6/063001.

[229] A. A. Shibkov, A. E. Zolotov, M. A. Zheltov, and A. A. Denisov. "Morphological diagram of Savart-Masson bands of macrolocalized deformation". en. In: *Crystallography Reports* 57.1 (Jan. 2012), pp. 105–111. DOI: 10.1134/S1063774511030308.

[230] Wuwei Liang, David J. Srolovitz, and Min Zhou. "A micromechanical continuum model for the tensile behavior of shape memory metal nanowires". In: *Journal of the Mechanics and Physics of Solids* 55.8 (2007), pp. 1729–1761. DOI: 10.1016/j.jmps.2007.01.001.

[231] Wuwei Liang and Min Zhou. "Atomistic simulations reveal shape memory of fcc metal nanowires". In: *Physical Review B* 73.11 (2006), p. 115409. DOI: 10.1103/PhysRevB.73.115409.

[232] X. Guo, W. Liang, and M. Zhou. "Mechanism for the Pseudoelastic Behavior of FCC Shape Memory Nanowires". In: *Experimental Mechanics* 49.2 (2009), pp. 183–190. DOI: 10.1007/s11340-008-9173-x.

[233] Fei Ma, Ke-Wei Xu, and Paul K. Chu. "Surface-induced structural transformation in nanowires". In: *Materials Science and Engineering R: Reports* 74.6 (2013), pp. 173–209. DOI: 10.1016/j.mser.2013.05.001.

[234] Po-Yu Yang, Shin-Pon Ju, Zhu-Min Lai, Jin-Yuan Hsieh, and Jenn-Sen Lin. "The mechanical properties and thermal stability of ultrathin germanium nanowires". In: *RSC Advances* 6.107 (2016), pp. 105713–105722. DOI: 10.1039/C6RA21841E.

[235] Xuan Cao, Ehsan Ban, Brendon M. Baker, Yuan Lin, Jason A. Burdick, Christopher S. Chen, and Vivek B. Shenoy. "Multiscale model predicts increasing focal adhesion size with decreasing stiffness in fibrous matrices". In: *Proceedings of the National Academy of Sciences of the United States of America* 114.23 (2017), E4549–E4555. DOI: 10.1073/pnas.1620486114.

[236] Wenyan Xie, Xi Wei, Heemin Kang, Hong Jiang, Zhiqin Chu, Yuan Lin, Yong Hou, and Qiang Wei. "Static and Dynamic: Evolving Biomaterial Mechanical Properties to Control Cellular Mechanotransduction". en. In: *Advanced Science* 10.9 (2023), p. 2204594. DOI: 10.1002/advs.202204594.

[237] Pakorn Kanchanawong and David A. Calderwood. "Organization, dynamics and mechanoregulation of integrin-mediated cell–ECM adhesions". en. In: *Nature Reviews Molecular Cell Biology* 24.2 (Feb. 2023), pp. 142–161. DOI: 10.1038/s41580-022-00531-5.

[238] George S. Hussey, Jenna L. Dziki, and Stephen F. Badylak. "Extracellular matrix-based materials for regenerative medicine". en. In: *Nature Reviews Materials* 3.7 (July 2018), pp. 159–173. DOI: 10.1038/s41578-018-0023-x.

[239] Huixun Du, Juliet M. Bartleson, Sergei Butenko, Valentina Alonso, Wendy F. Liu, Daniel A. Winer, and Manish J. Butte. "Tuning immunity through tissue mechanotransduction". en. In: *Nature Reviews Immunology* 23.3 (Mar. 2023), pp. 174–188. DOI: 10.1038/s41577-022-00761-w.

[240] Alexander Fuhrmann and Adam J. Engler. "The Cytoskeleton Regulates Cell Attachment Strength". In: *Biophysical Journal* 109.1 (2015), pp. 57–65. DOI: 10.1016/j.bpj.2015.06.003.

[241] Manoel Manghi and Nicolas Destainville. "Physics of base-pairing dynamics in DNA". In: *Physics Reports*. Physics of base-pairing dynamics in DNA 631 (2016), pp. 1–41. DOI: 10.1016/j.physrep.2016.04.001.

[242] Richard Villey, Costantino Creton, Pierre-Philippe Cortet, Marie-Julie Dalbe, Thomas Jet, Baudouin Saintyves, Stéphane Santucci, Loïc Vanel, David J. Yarusso, and Matteo Ciccotti. "Rate-dependent elastic hysteresis during the peeling of pressure sensitive adhesives". In: *Soft Matter* 11.17 (2015), pp. 3480–3491. DOI: 10.1039/C5SM00260E.

[243] H. Zhao and N. R. Aluru. "Temperature and strain-rate dependent fracture strength of graphene". In: *Journal of Applied Physics* 108.6 (2010), p. 064321. DOI: 10.1063/1.3488620.

[244] P. M. McGuiggan, A. Chiche, J. J. Filliben, and D. J. Yarusso. "Peel of an adhesive tape from a temperature-gradient surface". en. In: *International Journal of Adhesion and Adhesives*. Peel testing 28.4 (June 2008), pp. 185–191. DOI: 10.1016/j.ijadhadh.2007.05.004.

[245] Zhilong Peng, Cong Wang, Lei Chen, and Shaohua Chen. "Peeling behavior of a viscoelastic thin-film on a rigid substrate". en. In: *International Journal of Solids and Structures* 51.25 (Dec. 2014), pp. 4596–4603. DOI: 10.1016/j.ijsolstr.2014.10.011.

[246] S. Murray, C. Hillman, and M. Pecht. "Environmental aging and deadhesion of siloxane-polyimide-epoxy adhesive". In: *IEEE Transactions on Components and Packaging Technologies* 26.3 (Sept. 2003), pp. 524–531. DOI: 10.1109/TCAPT.2003.817642.

[247] F. Bosia, S. Colella, V. Mattoli, B. Mazzolai, and N. M. Pugno. "Hierarchical multiple peeling simulations". en. In: *RSC Advances* 4.48 (June 2014), pp. 25447–25452. DOI: 10.1039/C4RA03459G.

[248] Sara Iliafar, Dmitri Vezenov, and Anand Jagota. "Brownian Dynamics Simulation of Peeling a Strongly-Adsorbed Polymer Molecule from a Frictionless Substrate". In: *Langmuir* 29.5 (Feb. 2013), pp. 1435–1445. DOI: 10.1021/la304361f.

[249] I.S. Gradshteyn and I.M. Ryzhik. *Table of integrals, series, and products*. Academic Press, 1965.

[250] Milton Abramowitz and Irene A. Stegun. *Handbook of Mathematical Functions: With Formulas, Graphs, and Mathematical Tables*. en. Google-Books-ID: MtU8uP7XMvoC. Courier Corporation, Jan. 1965.

[251] Changbong Hyeon and D. Thirumalai. "Mechanical unfolding of RNA hairpins". In: *Proceedings of the National Academy of Sciences* 102.19 (2005), pp. 6789–6794. DOI: 10.1073/pnas.0408314102.

[252] Garima Mishra, Debaprasad Giri, M. S. Li, and Sanjay Kumar. "Role of loop entropy in the force induced melting of DNA hairpin". In: *The Journal of Chemical Physics* 135.3 (2011), p. 035102. DOI: 10.1063/1.3609970.

[253] William Stephenson, Sean Keller, Rachel Santiago, James E. Albrecht, Papa Nii Asare-Okai, Scott A. Tenenbaum, Michael Zuker, and Pan T. X. Li. "Combining temperature and force to study folding of an RNA hairpin". In: *Physical Chemistry Chemical Physics* 16.3 (2013), pp. 906–917. DOI: 10.1039/C3CP52042K.

[254] Sara De Lorenzo, Marco Ribezzi-Crivellari, J. Ricardo Arias-Gonzalez, Steven B. Smith, and Felix Ritort. "A Temperature-Jump Optical Trap for Single-Molecule Manipulation". In: *Biophysical Journal* 108.12 (2015), pp. 2854–2864. DOI: 10.1016/j.bpj.2015.05.017.

[255] Xiaofang Wang, Hyun Jeong Lim, and Ahjeong Son. "Characterization of denaturation and renaturation of DNA for DNA hybridization". In: *Environmental Health and Toxicology* 29 (2014), e2014007. DOI: 10.5620/eht.2014.29.e2014007.

[256] R. B. Wallace, J. Shaffer, R. F. Murphy, J. Bonner, T. Hirose, and K. Itakura. "Hybridization of synthetic oligodeoxyribonucleotides to phi chi 174 DNA: the effect of single base pair mismatch". In: *Nucleic Acids Research* 6.11 (1979), pp. 3543–3557. DOI: 10.1093/nar/6.11.3543.

[257] J. Marmur and P. Doty. "Determination of the base composition of deoxyribonucleic acid from its thermal denaturation temperature". In: *Journal of Molecular Biology* 5.1 (1962), pp. 109–118. DOI: 10.1016/S0022-2836(62)80066-7.

[258] John F. Marko and Simona Cocco. "The micromechanics of DNA". In: *Physics World* 16.3 (2003), p. 37. DOI: 10.1088/2058-7058/16/3/40.

[259] Lei Bao, Xi Zhang, Ya-Zhou Shi, Yuan-Yan Wu, and Zhi-Jie Tan. "Understanding the Relative Flexibility of RNA and DNA Duplexes: Stretching and Twist-Stretch Coupling". In: *Biophysical Journal* 112.6 (2017), pp. 1094–1104. DOI: 10.1016/j.bpj.2017.02.022.

[260] Alberto Marin-Gonzalez, J. G. Vilhena, Ruben Perez, and Fernando Moreno-Herrero. "Understanding the mechanical response of double-stranded DNA and RNA under constant stretching forces using all-atom molecular dynamics". In: *Proceedings of the National Academy of Sciences* 114.27 (2017), pp. 7049–7054. DOI: 10.1073/pnas.1705642114.

[261] D. Marenduzzo, Somendra M. Bhattacharjee, A. Maritan, E. Orlandini, and F. Seno. "Dynamical Scaling of the DNA Unzipping Transition". In: *Physical Review Letters* 88.2 (Dec. 2001), p. 028102. DOI: 10.1103/PhysRevLett.88.028102.

[262] D. Marenduzzo, A. Maritan, E. Orlandini, F. Seno, and A. Trovato. "Phase diagrams for DNA denaturation under stretching forces". en. In: *Journal of Statistical Mechanics: Theory and Experiment* 2009.04 (Apr. 2009), p. L04001. DOI: 10.1088/1742-5468/2009/04/L04001.

[263] E. Orlandini and S. G. Whittington. "Statistical mechanics of polymers subject to a force". en. In: *Journal of Physics A: Mathematical and Theoretical* 49.34 (July 2016), p. 343001. DOI: 10.1088/1751-8113/49/34/343001.

[264] E. Orlandini, M. C. Tesi, and S. G. Whittington. "Adsorption of a directed polymer subject to an elongational force". en. In: *Journal of Physics A: Mathematical and General* 37.5 (Jan. 2004), p. 1535. DOI: 10.1088/0305-4470/37/5/005.

[265] E. Orlandini and S. G. Whittington. "Pulling a polymer at an interface: directed walk models". en. In: *Journal of Physics A: Mathematical and General* 37.20 (May 2004), p. 5305. DOI: 10.1088/0305-4470/37/20/004.

[266] G. K. Iliev, E. Orlandini, and S. G. Whittington. "Polymers undergoing inhomogeneous adsorption: exact results and Monte Carlo simulations". en. In: *Journal of Physics A: Mathematical and Theoretical* 44.40 (Sept. 2011), p. 405004. DOI: 10.1088/1751-8113/44/40/405004.

[267] E. Orlandini and S. G. Whittington. "Adsorbing polymers subject to an elongational force: the effect of pulling direction". en. In: *Journal of Physics A: Mathematical and Theoretical* 43.48 (Nov. 2010), p. 485005. DOI: 10.1088/1751-8113/43/48/485005.

[268] G. K. Iliev, E. Orlandini, and S. G. Whittington. "Directed walk models of adsorbing semi-flexible polymers subject to an elongational force". en. In: *Journal of Physics A: Mathematical and Theoretical* 43.31 (July 2010), p. 315202. DOI: 10.1088/1751-8113/43/31/315202.

[269] G. K. Iliev, E. Orlandini, and S. G. Whittington. "Pulling polymers adsorbed on a striped surface". en. In: *Journal of Physics A: Mathematical and Theoretical* 46.5 (Jan. 2013), p. 055001. DOI: 10.1088/1751-8113/46/5/055001.

[270] E. J. Janse van Rensburg and S. G. Whittington. "Adsorbed self-avoiding walks subject to a force". en. In: *Journal of Physics A: Mathematical and Theoretical* 46.43 (Oct. 2013), p. 435003. DOI: 10.1088/1751-8113/46/43/435003.

[271] E. J. Janse van Rensburg and S. G. Whittington. "Self-avoiding walks subject to a force". en. In: *Journal of Physics A: Mathematical and Theoretical* 49.11 (Feb. 2016), 11LT01. DOI: 10.1088/1751-8113/49/11/11LT01.

[272] E. J. Janse van Rensburg and S. G. Whittington. "Self-avoiding walks adsorbed at a surface and subject to a force*". en. In: *Journal of Physics A: Mathematical and Theoretical* 49.24 (May 2016), p. 244001. DOI: 10.1088/1751-8113/49/24/244001.

[273] Gianpietro Del Piero and Lev Truskinovsky. "Macro- and micro-cracking in one-dimensional elasticity". en. In: *International Journal of Solids and Structures* 38.6 (Feb. 2001), pp. 1135–1148. DOI: 10.1016/S0020-7683(00)00078-0.

[274] K. Matsushige, S. V. Radcliffe, and E. Baer. "The pressure and temperature effects on brittle-to-ductile transition in PS and PMMA". en. In: *Journal of Applied Polymer Science* 20.7 (1976), pp. 1853–1866. DOI: 10.1002/app.1976.070200714.

[275] Elizabeth A. Shank, Ciro Cecconi, Jesse W. Dill, Susan Marqusee, and Carlos Bustamante. "The folding cooperativity of a protein is controlled by its chain topology". en. In: *Nature* 465.7298 (June 2010), pp. 637–640. DOI: 10.1038/nature09021.

[276] Ramachandra M. Bhaskara and Narayanaswamy Srinivasan. “Stability of domain structures in multi-domain proteins”. en. In: *Scientific Reports* 1.1 (July 2011), p. 40. DOI: 10.1038/srep00040.

[277] Pilkee Kim, Minh Sang Nguyen, Ojin Kwon, Young-Jin Kim, and Yong-Jin Yoon. “Phase-dependent dynamic potential of magnetically coupled two-degree-of-freedom bistable energy harvester”. en. In: *Scientific Reports* 6.1 (Sept. 2016), p. 34411. DOI: 10.1038/srep34411.

[278] Christopher A. Hunter and Harry L. Anderson. “What is Cooperativity?” In: *Angewandte Chemie International Edition* 48.41 (2009), pp. 7488–7499. DOI: 10.1002/anie.200902490.

[279] François Kimmig and Matthieu Caruel. “Hierarchical modeling of force generation in cardiac muscle”. en. In: *Biomechanics and Modeling in Mechanobiology* 19.6 (Dec. 2020), pp. 2567–2601. DOI: 10.1007/s10237-020-01357-w.

[280] Bolei Deng, Pai Wang, Vincent Tournat, and Katia Bertoldi. “Nonlinear transition waves in free-standing bistable chains”. en. In: *Journal of the Mechanics and Physics of Solids*. The Davide Bigoni 60th Anniversary Issue 136 (Mar. 2020), p. 103661. DOI: 10.1016/j.jmps.2019.07.004.

[281] J. M. Ball and R. D. James. “Fine Phase Mixtures as Minimizers of Energy”. en. In: *Analysis and Continuum Mechanics: A Collection of Papers Dedicated to J. Serrin on His Sixtieth Birthday*. Ed. by Stuart S. Antman, Haïm Brezis, Bernard D. Coleman, Martin Feinberg, John A. Nohel, and William P. Ziemer. Berlin, Heidelberg: Springer, 1989, pp. 647–686. DOI: 10.1007/978-3-642-83743-2_36.

[282] Lev Truskinovsky and Giovanni Zanzotto. “Ericksen’s bar revisited : Energy wiggles”. In: *Journal of the Mechanics and Physics of Solids* 44.8 (1996), pp. 1371–1408. DOI: 10.1016/0022-5096(96)00020-8.

[283] Stefan Müller. “Variational models for microstructure and phase transitions”. en. In: *Calculus of Variations and Geometric Evolution Problems: Lectures given at the 2nd Session of the Centro Internazionale Matematico Estivo (C.I.M.E.) held in Cetraro, Italy, June 15–22, 1996*. Ed. by Fabrice Bethuel, Gerhard Huisken, Stefan Müller, Klaus Steffen, Stefan Hildebrandt, and Michael Struwe. Lecture Notes in Mathematics. Berlin, Heidelberg: Springer, 1999, pp. 85–210. DOI: 10.1007/BFb0092670.

[284] J. A. Shaw and S. Kyriakides. “On the nucleation and propagation of phase transformation fronts in a NiTi alloy”. In: *Acta Materialia* 45.2 (1997), pp. 683–700. DOI: 10.1016/S1359-6454(96)00189-9.

[285] R. Abeyaratne, C. Chu, and R. D. James. “Kinetics of materials with wiggly energies: Theory and application to the evolution of twinning microstructures in a Cu-Al-Ni shape memory alloy”. In: *Philosophical Magazine A* 73.2 (1996), pp. 457–497. DOI: 10.1080/01418619608244394.

[286] N. Triantafyllidis and S. Bardenhagen. “On higher order gradient continuum theories in 1-D nonlinear elasticity. Derivation from and comparison to the corresponding discrete models”. en. In: *Journal of Elasticity* 33.3 (Dec. 1993), pp. 259–293. DOI: 10.1007/BF00043251.

[287] Bernard D. Coleman. “Necking and drawing in polymeric fibers under tension”. en. In: *Archive for Rational Mechanics and Analysis* 83.2 (June 1983), pp. 115–137. DOI: 10.1007/BF00282158.

[288] Xiaofeng Ren and Lev Truskinovsky. “Finite Scale Microstructures in Nonlocal Elasticity”. en. In: *Journal of elasticity and the physical science of solids* 59.1 (June 2000), pp. 319–355. DOI: 10.1023/A:1011003321453.

[289] G. Puglisi and L. Truskinovsky. “Mechanics of a discrete chain with bi-stable elements”. en. In: *Journal of the Mechanics and Physics of Solids* 48.1 (Jan. 2000), pp. 1–27. DOI: 10.1016/S0022-5096(99)00006-X.

[290] G. Puglisi. “Nucleation and phase propagation in a multistable lattice with weak nonlocal interactions”. en. In: *Continuum Mechanics and Thermodynamics* 19.5 (Oct. 2007), pp. 299–319. DOI: 10.1007/s00161-007-0056-7.

[291] A. Duval, M. Haboussi, and T. Ben Zineb. “Modelling of localization and propagation of phase transformation in superelastic SMA by a gradient nonlocal approach”. In: *International Journal of Solids and Structures* 48.13 (2011), pp. 1879–1893. DOI: 10.1016/j.ijsolstr.2011.02.019.

[292] Roberto Alessi and Davide Bernardini. “Analysis of localization phenomena in Shape Memory Alloys bars by a variational approach”. In: *International Journal of Solids and Structures* 73-74 (2015), pp. 113–133. DOI: 10.1016/j.ijsolstr.2015.06.021.

[293] Zilong Song. “Analytical study on phase transition of shape memory alloy wire under uniaxial tension”. In: *International Journal of Engineering Science* 152 (2020), p. 103295. DOI: 10.1016/j.ijengsci.2020.103295.

[294] Douglas B. Staple, Stephen H. Payne, Andrew L. C. Reddin, and Hans Jürgen Kreuzer. “Stretching and unfolding of multidomain biopolymers: a statistical mechanics theory of titin”. en. In: *Physical Biology* 6.2 (July 2009), p. 025005. DOI: 10.1088/1478-3975/6/2/025005.

[295] Dmitrii E. Makarov. “A Theoretical Model for the Mechanical Unfolding of Repeat Proteins”. en. In: *Biophysical Journal* 96.6 (Mar. 2009), pp. 2160–2167. DOI: 10.1016/j.bpj.2008.12.3899.

[296] M. Ruiz-García, L. L. Bonilla, and A. Prados. “STM-driven transition from rippled to buckled graphene in a spin-membrane model”. In: *Physical Review B* 94.20 (Nov. 2016), p. 205404. DOI: 10.1103/PhysRevB.94.205404.

[297] M. Ruiz-Garcia, L. L. Bonilla, and A. Prados. “Bifurcation analysis and phase diagram of a spin-string model with buckled states”. In: *Physical Review E* 96.6 (Dec. 2017), p. 062147. DOI: 10.1103/PhysRevE.96.062147.

[298] J. K. Schoelz, P. Xu, V. Meunier, P. Kumar, M. Neek-Amal, P. M. Thibado, and F. M. Peeters. “Graphene ripples as a realization of a two-dimensional Ising model: A scanning tunneling microscope study”. In: *Physical Review B* 91.4 (Jan. 2015), p. 045413. DOI: 10.1103/PhysRevB.91.045413.

[299] Suraj Shankar and David R. Nelson. “Thermalized buckling of isotropically compressed thin sheets”. In: *Physical Review E* 104.5 (Nov. 2021), p. 054141. DOI: 10.1103/PhysRevE.104.054141.

[300] Paul Z. Hanakata, Abigail Plummer, and David R. Nelson. “Anomalous Thermal Expansion in Ising-like Puckered Sheets”. In: *Physical Review Letters* 128.7 (Feb. 2022), p. 075902. DOI: 10.1103/PhysRevLett.128.075902.

[301] Dilip Kondepudi and Ilya Prigogine. *Modern Thermodynamics: From Heat Engines to Dissipative Structures*. en. Google-Books-ID: SPU8BQAAQBAJ. John Wiley & Sons, Nov. 2014.

[302] Rodney J. Baxter. *Exactly Solved Models in Statistical Mechanics*. en. Google-Books-ID: G3owDULfBuEC. Courier Corporation, Jan. 2007.

[303] J. A Shaw and S Kyriakides. “Initiation and propagation of localized deformation in elasto-plastic strips under uniaxial tension”. en. In: *International Journal of Plasticity* 13.10 (Dec. 1997), pp. 837–871. DOI: 10.1016/S0749-6419(97)00062-4.

[304] R. Nogueira de Codes, O. S. Hopperstad, O. Engler, O.-G. Lademo, J. D. Embury, and A. Benallal. “Spatial and Temporal Characteristics of Propagating Deformation Bands in AA5182 Alloy at Room Temperature”. en. In: *Metallurgical and Materials Transactions A* 42.11 (Nov. 2011), pp. 3358–3369. DOI: 10.1007/s11661-011-0749-1.

[305] Rainer Schwab and Volker Ruff. “On the nature of the yield point phenomenon”. en. In: *Acta Materialia* 61.5 (Mar. 2013), pp. 1798–1808. DOI: 10.1016/j.actamat.2012.12.003.

[306] Julian F. Hallai and Stelios Kyriakides. “Underlying material response for Lüders-like instabilities”. en. In: *International Journal of Plasticity* 47 (Aug. 2013), pp. 1–12. DOI: 10.1016/j.ijplas.2012.12.002.

[307] Hanlin Gu, Lars Bumke, Christoph Chluba, Eckhard Quandt, and Richard D. James. “Phase engineering and supercompatibility of shape memory alloys”. en. In: *Materials Today* 21.3 (Apr. 2018), pp. 265–277. DOI: 10.1016/j.mattod.2017.10.002.

[308] Saeid Pourbabak, Andrey Orekhov, Vahid Samaee, Bert Verlinden, Jan Van Humbeeck, and Dominique Schryvers. “In-Situ TEM Stress Induced Martensitic Transformation in Ni50.8Ti49.2 Microwires”. en. In: *Shape Memory and Superelasticity* 5.2 (June 2019), pp. 154–162. DOI: 10.1007/s40830-019-00217-6.

[309] Harold S. Park. “Stress-Induced Martensitic Phase Transformation in Intermetallic Nickel Aluminum Nanowires”. In: *Nano Letters* 6.5 (May 2006), pp. 958–962. DOI: 10.1021/nl060024p.

[310] Jingui Yu, Qiaoxin Zhang, and Zhufeng Yue. “Tensile mechanical properties of Ni3Al nanowires at intermediate temperature”. en. In: *RSC Advances* 4.40 (May 2014), pp. 20789–20796. DOI: 10.1039/C4RA01431F.

[311] Reza Mirzaeifar, Ken Gall, Ting Zhu, Arash Yavari, and Reginald DesRoches. “Structural transformations in NiTi shape memory alloy nanowires”. In: *Journal of Applied Physics* 115.19 (May 2014), p. 194307. DOI: 10.1063/1.4876715.

[312] Na-Young Park, Ho-Seok Nam, Pil-Ryung Cha, and Seung-Cheol Lee. “Size-dependent transition of the deformation behavior of Au nanowires”. en. In: *Nano Research* 8.3 (Mar. 2015), pp. 941–947. DOI: 10.1007/s12274-014-0575-z.

[313] Lili Li and Ming Han. “Molecular dynamics simulations on tensile behaviors of single-crystal bcc Fe nanowire: effects of strain rates and thermal environment”. en. In: *Applied Physics A* 123.6 (May 2017), p. 450. DOI: 10.1007/s00339-017-1062-7.

[314] Reza Rezaei and Chuang Deng. “Pseudoelasticity and shape memory effects in cylindrical FCC metal nanowires”. en. In: *Acta Materialia* 132 (June 2017), pp. 49–56. DOI: 10.1016/j.actamat.2017.04.039.

[315] Seyedeh Mohadeseh Taheri Mousavi, Haofei Zhou, Guijin Zou, and Huajian Gao. “Transition from source- to stress-controlled plasticity in nanotwinned materials below a softening temperature”. en. In: *npj Computational Materials* 5.1 (Jan. 2019), pp. 1–7. DOI: 10.1038/s41524-018-0140-5.

[316] Hui Cao, Zhiyuan Rui, and Fuqian Yang. “Mechanical properties of Cu nanowires: Effects of cross-sectional area and temperature”. en. In: *Materials Science and Engineering: A* 791 (July 2020), p. 139644. DOI: 10.1016/j.msea.2020.139644.

[317] Jiacheng Zhang, Mao Zhang, Lei Deng, Junsong Jin, Pan Gong, and Xinyun Wang. "Mechanical behavior of tetragonal zirconia nanopillars subjected to uniaxial loading: A molecular dynamics study". en. In: *Mechanics of Materials* 151 (Dec. 2020), p. 103666. DOI: 10.1016/j.mechmat.2020.103666.

[318] I. Müller and S. Seelecke. "Thermodynamic aspects of shape memory alloys". en. In: *Mathematical and Computer Modelling* 34.12 (Dec. 2001), pp. 1307–1355. DOI: 10.1016/S0895-7177(01)00134-0.

[319] A. Tanguy and T. Vettorel. "From weak to strong pinning I: A finite size study". en. In: *The European Physical Journal B - Condensed Matter and Complex Systems* 38.1 (Mar. 2004), pp. 71–82. DOI: 10.1140/epjb/e2004-00101-6.

[320] Anne Tanguy, Matthieu Gounelle, and Stéphane Roux. "From individual to collective pinning: Effect of long-range elastic interactions". In: *Physical Review E* 58.2 (Aug. 1998), pp. 1577–1590. DOI: 10.1103/PhysRevE.58.1577.

[321] S. Ramos and A. Tanguy. "Pinning-depinning of the contact line on nanorough surfaces". en. In: *The European Physical Journal E* 19.4 (Apr. 2006), pp. 433–440. DOI: 10.1140/epje/i2005-10056-0.

[322] J. H. Lambert. "Observationes Variae in Mathesin Puram". In: *Acta Helvetica Physico-Mathematico-Anatomico-Botanico-Medica*. Vol. 3. Basileae: Acta Helvetica, 1758.

[323] R. M. Corless, G. H. Gonnet, D. E. G. Hare, D. J. Jeffrey, and D. E. Knuth. "On the LambertW function". en. In: *Advances in Computational Mathematics* 5.1 (Dec. 1996), pp. 329–359. DOI: 10.1007/BF02124750.

[324] George Weiss. "The Theory of Matrices. vol. 1 and vol. 2. F. R. Gantmacher. Chelsea Publishing Company, New York 68, 1959. vol. 1: x + 374 pp. vol. 2: x + 277 pp. $6 each." In: *Science* 131.3408 (Apr. 1960), pp. 1216–1216. DOI: 10.1126/science.131.3408.1216.b.

[325] Peter Lancaster and Miron Tismenetsky. *The Theory of Matrices: With Applications*. en. Google-Books-ID: 2c011Aptsa8C. Academic Press, May 1985.

[326] Mark J. Ablowitz and A. S. Fokas. *Complex Variables: Introduction and Applications*. en. Google-Books-ID: SFqbV3i3hO0C. Cambridge University Press, Apr. 2003.

[327] Karl W. Breitung. *Asymptotic Approximations for Probability Integrals*. en. Google-Books-ID: EXB6CwAAQBAJ. Springer, Nov. 2006.

[328] Nicola M. Pugno. "The centenary of Griffith's theory". en. In: *Matter* 4.12 (Dec. 2021), pp. 3811–3813. DOI: 10.1016/j.matt.2021.11.002.

[329] C. E. Inglis. "Stresses in a plate due to the presence of cracks and sharp corners". In: *Transactions of the Institution of Naval Architects*. Vol. 54. Trans. I.N.A., 1913, pp. 219–230.

[330] G. Kolossoff. "Über einige Eigenschaften des ebenen Problems der Elastizitätstheorie". In: *Zeitschr. für Math. u. Phys.* 62 (1914).

[331] Brian Lawn. *Fracture of Brittle Solids*. 2nd ed. Cambridge Solid State Science Series. Cambridge: Cambridge University Press, 1993. DOI: 10.1017/CBO9780511623127.

[332] Andreas Öchsner. *Continuum Damage and Fracture Mechanics*. en. Google-Books-ID: W5vDCgAAQBAJ. Springer, Oct. 2015.

[333] A. Mattoni, L. Colombo, and F. Cleri. "Atomic Scale Origin of Crack Resistance in Brittle Fracture". In: *Physical Review Letters* 95.11 (Sept. 2005), p. 115501. DOI: 10.1103/PhysRevLett.95.115501.

[334] Hongwei Bao, Yuhong Huang, Zhi Yang, Yunjin Sun, Yu Bai, Yaping Miao, Paul K. Chu, Kewei Xu, and Fei Ma. "Molecular Dynamics Simulation of Nanocrack Propagation in Single-Layer MoS2 Nanosheets". In: *The Journal of Physical Chemistry C* 122.2 (Jan. 2018), pp. 1351–1360. DOI: 10.1021/acs.jpcc.7b10094.

[335] E. Orowan. "Fracture and strength of solids". en. In: *Reports on Progress in Physics* 12.1 (Jan. 1949), p. 185. DOI: 10.1088/0034-4885/12/1/309.

[336] Egon Orowan. *Energy criteria of fracture*. Tech. rep. Cambridge, Massachusetts: Massachusetts Inst of Tech Cambridge Dept of Mechanical Engineering, 1954.

[337] J. R. Willis. "A comparison of the fracture criteria of griffith and barenblatt". en. In: *Journal of the Mechanics and Physics of Solids* 15.3 (May 1967), pp. 151–162. DOI: 10.1016/0022-5096(67)90029-4.

[338] J. R. Rice. "A Path Independent Integral and the Approximate Analysis of Strain Concentration by Notches and Cracks". In: *Journal of Applied Mechanics* 35.2 (June 1968), pp. 379–386. DOI: 10.1115/1.3601206.

[339] Mark Kachanov. "Effective Elastic Properties of Cracked Solids: Critical Review of Some Basic Concepts". In: *Applied Mechanics Reviews* 45.8 (Aug. 1992), pp. 304–335. DOI: 10.1115/1.3119761.

[340] Mark Kachanov. "Elastic Solids with Many Cracks and Related Problems". en. In: *Advances in Applied Mechanics*. Ed. by John W. Hutchinson and Theodore Y. Wu. Vol. 30. Elsevier, Jan. 1993, pp. 259–445. DOI: 10.1016/S0065-2156(08)70176-5.

[341] Stefano Giordano and Luciano Colombo. "Effects of the orientational distribution of cracks in isotropic solids". en. In: *Engineering Fracture Mechanics* 74.13 (Sept. 2007), pp. 1983–2003. DOI: 10.1016/j.engfracmech.2006.10.006.

[342] Stefano Giordano and Luciano Colombo. "Effects of the Orientational Distribution of Cracks in Solids". In: *Physical Review Letters* 98.5 (Jan. 2007), p. 055503. DOI: 10.1103/PhysRevLett.98.055503.

[343] Stefano Giordano and Luciano Colombo. "Local elastic fields around cracks and their stress density of states". In: *Physical Review B* 76.17 (Nov. 2007), p. 174120. DOI: 10.1103/PhysRevB.76.174120.

[344] Stefano Giordano and Luciano Colombo. "Elastic properties of solids containing elliptic cracks". In: *Physical Review B* 77.5 (Feb. 2008), p. 054106. DOI: 10.1103/PhysRevB.77.054106.

[345] L. Dormieux and D. Kondo. "Stress-based estimates and bounds of effective elastic properties: The case of cracked media with unilateral effects". en. In: *Computational Materials Science* 46.1 (July 2009), pp. 173–179. DOI: 10.1016/j.commatsci.2009.02.027.

[346] Stefano Giordano, Alessandro Mattoni, Luciano Colombo, et al. "Brittle Fracture: From elasticity theory to atomistic simulations". In: *Reviews in Computational Chemistry* 27 (2011), p. 1.

[347] Luc Dormieux and Djimedo Kondo. *Micromechanics of Fracture and Damage*. en. Google-Books-ID: yi3fCwAAQBAJ. John Wiley & Sons, Mar. 2016.

[348] K. B. Broberg. "Critical review of some theories in fracture mechanics". en. In: *International Journal of Fracture Mechanics* 4.1 (Mar. 1968), pp. 11–19. DOI: 10.1007/BF00189139.

[349] Genady P. Cherepanov, Alexander S. Balankin, and Vera S. Ivanova. "Fractal fracture mechanics—A review". en. In: *Engineering Fracture Mechanics* 51.6 (Aug. 1995), pp. 997–1033. DOI: 10.1016/0013-7944(94)00323-A.

[350] K. Bertram Broberg. *Cracks and Fracture*. en. Google-Books-ID: P79Fk7l5Nn0C. Elsevier, Feb. 1999.

[351] Dietmar Gross. "Some Remarks on the History of Fracture Mechanics". en. In: *The History of Theoretical, Material and Computational Mechanics - Mathematics Meets Mechanics and Engineering*. Ed. by Erwin Stein. Lecture Notes in Applied Mathematics and Mechanics. Berlin, Heidelberg: Springer, 2014, pp. 195–209. DOI: 10.1007/978-3-642-39905-3_12.

[352] F Erdogan. "Fracture mechanics". en. In: *International Journal of Solids and Structures* 37.1 (Jan. 2000), pp. 171–183. DOI: 10.1016/S0020-7683(99)00086-4.

[353] Kyoungsoo Park and Glaucio H. Paulino. "Cohesive Zone Models: A Critical Review of Traction-Separation Relationships Across Fracture Surfaces". In: *Applied Mechanics Reviews* 64.060802 (Feb. 2013). DOI: 10.1115/1.4023110.

[354] Sanjida Ferdousi, Qiyi Chen, Mehrzad Soltani, Jiadeng Zhu, Pengfei Cao, Wonbong Choi, Rigoberto Advincula, and Yijie Jiang. "Characterize traction–separation relation and interfacial imperfections by data-driven machine learning models". en. In: *Scientific Reports* 11.1 (July 2021), p. 14330. DOI: 10.1038/s41598-021-93852-y.

[355] J. Fineberg and M. Marder. "Instability in dynamic fracture". en. In: *Physics Reports* 313.1 (May 1999), pp. 1–108. DOI: 10.1016/S0370-1573(98)00085-4.

[356] Blaise Bourdin, Gilles A. Francfort, and Jean-Jacques Marigo. "The Variational Approach to Fracture". en. In: *Journal of Elasticity* 91.1 (Apr. 2008), pp. 5–148. DOI: 10.1007/s10659-007-9107-3.

[357] A. Mesgarnejad, B. Bourdin, and M. M. Khonsari. "Validation simulations for the variational approach to fracture". en. In: *Computer Methods in Applied Mechanics and Engineering* 290 (June 2015), pp. 420–437. DOI: 10.1016/j.cma.2014.10.052.

[358] Christian Miehe, Martina Hofacker, and Fabian Welschinger. "A phase field model for rate-independent crack propagation: Robust algorithmic implementation based on operator splits". en. In: *Computer Methods in Applied Mechanics and Engineering* 199.45 (Nov. 2010), pp. 2765–2778. DOI: 10.1016/j.cma.2010.04.011.

[359] H. L. Ren, X. Y. Zhuang, C. Anitescu, and T. Rabczuk. "An explicit phase field method for brittle dynamic fracture". en. In: *Computers & Structures* 217 (June 2019), pp. 45–56. DOI: 10.1016/j.compstruc.2019.03.005.

[360] Abigail Agwai, Ibrahim Guven, and Erdogan Madenci. "Predicting crack propagation with peridynamics: a comparative study". en. In: *International Journal of Fracture* 171.1 (Sept. 2011), pp. 65–78. DOI: 10.1007/s10704-011-9628-4.

[361] Huilong Ren, Xiaoying Zhuang, Yongchang Cai, and Timon Rabczuk. "Dual-horizon peridynamics". en. In: *International Journal for Numerical Methods in Engineering* 108.12 (2016), pp. 1451–1476. DOI: 10.1002/nme.5257.

[362] Timo Saksala, Delphine Brancherie, Isaac Harari, and Adnan Ibrahimbegovic. "Combined continuum damage-embedded discontinuity model for explicit dynamic fracture analyses of quasi-brittle materials". In: *International Journal for Numerical Methods in Engineering* 101.3 (2015), pp. 230–250. DOI: https://doi.org/10.1002/nme.4814. eprint: https://onlinelibrary.wiley.com/doi/pdf/10.1002/nme.4814.

[363] Van-Minh Ngo, Adnan Ibrahimbegović, and Delphine Brancherie. "Model for localized failure with thermo-plastic coupling: Theoretical formulation and ED-FEM implementation". In: *Computers & Structures* 127 (2013). Special Issue IASS-IACM-2012, pp. 2–18. DOI: https://doi.org/10.1016/j.compstruc.2012.12.013.

[364] T. Saksala, D. Brancherie, and A. Ibrahimbegovic. "Numerical modeling of dynamic rock fracture with a combined 3D continuum viscodamage-embedded discontinuity model". In: *International Journal for Numerical and Analytical Methods in Geomechanics* 40.9 (2016), pp. 1339–1357. DOI: https://doi.org/10.1002/nag.2492. eprint: https://onlinelibrary.wiley.com/doi/pdf/10.1002/nag.2492.

[365] L. Truskinovsky. "Fracture as a phase transition". In: *Contemporary Research in Mechanics and Mathematics of Materials*. Ericksen's Symposium. Barcelona: CIMNE, 1996, pp. 322–332.

[366] Stefano Zapperi, Purusattam Ray, H. Eugene Stanley, and Alessandro Vespignani. "First-Order Transition in the Breakdown of Disordered Media". In: *Physical Review Letters* 78.8 (Feb. 1997), pp. 1408–1411. DOI: 10.1103/PhysRevLett.78.1408.

[367] Y. Moreno, J. B. Gómez, and A. F. Pacheco. "Fracture and Second-Order Phase Transitions". In: *Physical Review Letters* 85.14 (Oct. 2000), pp. 2865–2868. DOI: 10.1103/PhysRevLett.85.2865.

[368] Mikko J. Alava, Phani K. V. V. Nukala, and Stefano Zapperi. "Statistical models of fracture". In: *Advances in Physics* 55.3-4 (May 2006), pp. 349–476. DOI: 10.1080/00018730300741518.

[369] Hikaru Kawamura, Takahiro Hatano, Naoyuki Kato, Soumyajyoti Biswas, and Bikas K. Chakrabarti. "Statistical physics of fracture, friction, and earthquakes". In: *Reviews of Modern Physics* 84.2 (May 2012), pp. 839–884. DOI: 10.1103/RevModPhys.84.839.

[370] Knut S. Gjerden, Arne Stormo, and Alex Hansen. "Universality Classes in Constrained Crack Growth". In: *Physical Review Letters* 111.13 (Sept. 2013), p. 135502. DOI: 10.1103/PhysRevLett.111.135502.

[371] D. Sornette. "Elasticity and failure of a set of elements loaded in parallel". en. In: *Journal of Physics A: Mathematical and General* 22.6 (Mar. 1989), p. L243. DOI: 10.1088/0305-4470/22/6/010.

[372] D. Gary Harlow and S. Leigh Phoenix. "Approximations for the strength distribution and size effect in an idealized lattice model of material breakdown". en. In: *Journal of the Mechanics and Physics of Solids* 39.2 (Jan. 1991), pp. 173–200. DOI: 10.1016/0022-5096(91)90002-6.

[373] Srutarshi Pradhan, Alex Hansen, and Bikas K. Chakrabarti. "Failure processes in elastic fiber bundles". In: *Reviews of Modern Physics* 82.1 (Mar. 2010), pp. 499–555. DOI: 10.1103/RevModPhys.82.499.

[374] Kornél Kovács, Raul Cruz Hidalgo, Ignacio Pagonabarraga, and Ferenc Kun. "Brittle-to-ductile transition in a fiber bundle with strong heterogeneity". In: *Physical Review E* 87.4 (Apr. 2013), p. 042816. DOI: 10.1103/PhysRevE.87.042816.

[375] M. Ausloos. "Phase transition theory approach to fracture of materials". en. In: *Solid State Communications* 59.6 (Aug. 1986), pp. 401–404. DOI: 10.1016/0038-1098(86)90572-7.

[376] AK Khitrin. "Brittle fracture as a phase transition". In: *Fizika Tverdogo Tela* 30.10 (1988), pp. 3024–3029.

[377] M. Marder. “Statistical mechanics of cracks”. In: *Physical Review E* 54.4 (Oct. 1996), pp. 3442–3454. DOI: 10.1103/PhysRevE.54.3442.

[378] M. Ortiz. “Plastic Yielding as a Phase Transition”. In: *Journal of Applied Mechanics* 66.2 (Oct. 1999), pp. 289–298. DOI: 10.1115/1.2791048.

[379] S. Santucci, L. Vanel, A. Guarino, R. Scorretti, and S. Ciliberto. “Thermal activation of rupture and slow crack growth in a model of homogeneous brittle materials”. en. In: *Europhysics Letters* 62.3 (May 2003), p. 320. DOI: 10.1209/epl/i2003-00398-1.

[380] A. Guarino, L. Vanel, R. Scorretti, and S. Ciliberto. “The cooperative effect of load and disorder in thermally activated rupture of a two-dimensional random fuse network”. en. In: *Journal of Statistical Mechanics: Theory and Experiment* 2006.06 (June 2006), P06020. DOI: 10.1088/1742-5468/2006/06/P06020.

[381] A. Guarino and S. Ciliberto. “Thermally activated fracture of porous media”. en. In: *The European Physical Journal B* 83.2 (Sept. 2011), p. 215. DOI: 10.1140/epjb/e2011-10977-4.

[382] Tom Vincent-Dospital, Renaud Toussaint, Alain Cochard, Knut Jørgen Måløy, and Eirik G. Flekkøy. “Thermal weakening of cracks and brittle-ductile transition of matter: A phase model”. In: *Physical Review Materials* 4.2 (Feb. 2020), p. 023604. DOI: 10.1103/PhysRevMaterials.4.023604.

[383] Nicola M. Pugno † and Rodney S. Ruoff ‡. “Quantized fracture mechanics”. In: *Philosophical Magazine* 84.27 (Sept. 2004), pp. 2829–2845. DOI: 10.1080/14786430412331280382.

[384] Mariella Ippolito, Alessandro Mattoni, Luciano Colombo, and Nicola Pugno. “Role of lattice discreteness on brittle fracture: Atomistic simulations versus analytical models”. In: *Physical Review B* 73.10 (Mar. 2006), p. 104111. DOI: 10.1103/PhysRevB.73.104111.

[385] Mariella Ippolito, Alessandro Mattoni, Nicola Pugno, and Luciano Colombo. “Failure strength of brittle materials containing nanovoids”. In: *Physical Review B* 75.22 (June 2007), p. 224110. DOI: 10.1103/PhysRevB.75.224110.

[386] Nicola Pugno, Alberto Carpinteri, Mariella Ippolito, Alessandro Mattoni, and Luciano Colombo. “Atomistic fracture: QFM vs. MD”. en. In: *Engineering Fracture Mechanics*. Critical Distance Theories of Fracture 75.7 (May 2008), pp. 1794–1803. DOI: 10.1016/j.engfracmech.2007.01.028.

[387] J. W. Hutchinson. “Singular behaviour at the end of a tensile crack in a hardening material”. en. In: *Journal of the Mechanics and Physics of Solids* 16.1 (Jan. 1968), pp. 13–31. DOI: 10.1016/0022-5096(68)90014-8.

[388] J. R. Rice and G. F. Rosengren. “Plane strain deformation near a crack tip in a power-law hardening material”. en. In: *Journal of the Mechanics and Physics of Solids* 16.1 (Jan. 1968), pp. 1–12. DOI: 10.1016/0022-5096(68)90013-6.

[389] Alberto Carpinteri and Marco Paggi. “Asymptotic analysis in Linear Elasticity: From the pioneering studies by Wieghardt and Irwin until today”. en. In: *Engineering Fracture Mechanics* 76.12 (Aug. 2009), pp. 1771–1784. DOI: 10.1016/j.engfracmech.2009.03.012.

[390] Josiah Willard Gibbs. *Elementary Principles In Statistical Mechanics*. Charles Scribner’s Sons, 1902. 236 pp.

[391] G. T Hahn and A. R Rosenfield. “Local yielding and extension of a crack under plane stress”. en. In: *Acta Metallurgica* 13.3 (Mar. 1965), pp. 293–306. DOI: 10.1016/0001-6160(65)90206-3.

[392] Li Jia. “A Dugdale–Barenblatt Model for a Plane Stress Semi-Infinite Crack under Mixed Mode Concentrated Forces”. en. In: *International Journal of Fracture* 88.2 (Nov. 1997), pp. 153–166. DOI: 10.1023/A:1007449126431.

[393] X. G. Chen, X. R. Wu, and M. G. Yan. “Dugdale model for strain hardening materials”. en. In: *Engineering Fracture Mechanics* 41.6 (Apr. 1992), pp. 843–871. DOI: 10.1016/0013-7944(92)90236-8.

[394] Andrzej Neimitz. “Modification of Dugdale model to include the work hardening and in- and out-of-plane constraints”. en. In: *Engineering Fracture Mechanics* 71.11 (July 2004), pp. 1585–1600. DOI: 10.1016/S0013-7944(03)00212-1.

[395] James R. Rice and Robb Thomson. “Ductile versus brittle behaviour of crystals”. In: *The Philosophical Magazine: A Journal of Theoretical Experimental and Applied Physics* 29.1 (Jan. 1974), pp. 73–97. DOI: 10.1080/14786437408213555.

[396] Robb Thomson. “Physics of Fracture”. en. In: *Solid State Physics*. Ed. by Henry Ehrenreich and David Turnbull. Vol. 39. Academic Press, Jan. 1986, pp. 1–129. DOI: 10.1016/S0081-1947(08)60368-9.

[397] James R. Rice. “Dislocation nucleation from a crack tip: An analysis based on the Peierls concept”. en. In: *Journal of the Mechanics and Physics of Solids* 40.2 (Jan. 1992), pp. 239–271. DOI: 10.1016/S0022-5096(05)80012-2.

[398] R. P. Thompson and W. J. Clegg. “Predicting whether a material is ductile or brittle”. en. In: *Current Opinion in Solid State and Materials Science* 22.3 (June 2018), pp. 100–108. DOI: 10.1016/j.cossms.2018.04.001.

[399] X. -Z. Hu and F. H. Wittmann. “Fracture energy and fracture process zone”. en. In: *Materials and Structures* 25.6 (July 1992), pp. 319–326. DOI: 10.1007/BF02472590.

[400] Costantino Creton and Matteo Ciccotti. “Fracture and adhesion of soft materials: a review”. en. In: *Reports on Progress in Physics* 79.4 (Mar. 2016), p. 046601. DOI: 10.1088/0034-4885/79/4/046601.

[401] F. Trentadue, D. De Tommasi, and G. Puglisi. “A predictive micromechanically-based model for damage and permanent deformations in copolymer sutures”. en. In: *Journal of the Mechanical Behavior of Biomedical Materials* 115 (Mar. 2021), p. 104277. DOI: 10.1016/j.jmbbm.2020.104277.

[402] Firas Awaja, Shengnan Zhang, Manoj Tripathi, Anton Nikiforov, and Nicola Pugno. “Cracks, microcracks and fracture in polymer structures: Formation, detection, autonomic repair”. en. In: *Progress in Materials Science* 83 (Oct. 2016), pp. 536–573. DOI: 10.1016/j.pmatsci.2016.07.007.

[403] Helmut Kirchner. “Ductility and brittleness of bone”. en. In: *International Journal of Fracture* 139.3 (June 2006), pp. 509–516. DOI: 10.1007/s10704-006-0050-2.

Statistical mechanics and thermodynamics of adhesion, phase transformations, and fracture in micro- and nano-systems

Abstract

Micro-instability and multi-stability phenomena play a key role in various mechanical and physical systems, both artificial and biological. As such, their understanding is addressed in a wide field of studies, with many practical and theoretical applications. The modeling of the temperature effect on micro-instabilities, appearing in different artificial and biological phenomena, allows the validation of the statistical mechanics for small systems, through the comparison with experimental data obtained using force spectroscopy and micromecanical testing, thus providing useful insights on the responses induced by applied forces or elongations. These analyses are particularly important in the study of all the systems that present two (or more) metastable states such as the adhesion/deadhesion processes, the phase transformations (*e.g.* the folding/unfolding and pseudo-elastic phenomena) and the cracks and fractures propagation in nano- and micro-scale systems. As examples, the temperature strongly influences the phase transoformation features of pseudo-elastic nanowires used as actuators and sensors in nanotechnology, or modifies the adhesion properties of metastatic cells in cancer invasion processes. The force-extension or stress-strain response is one of the main useful features to understand the effects of micro-instabilities and, in order to be analytically obtained, one needs to evaluate the system partition function, which is the essential tool of the statistical mechanics. Hence, the complex potential energy landscape of the problem under investigation is approximated using the spin variables technique, intoducing a discrete quantity able to identify the different potential energy wells. The first part of this thesis addresses the state of the art, the open problems, the motivations and the description of the adopted methodologies. The following part shows how commonly different physical phenomena can be studied by the same modelling approach.

Keywords: microinstabilities, phase transformations, statistical mechanics, material science, fracture, crack propagation, attachment, detachment, biophysics, ising model

---

Mécanique statistique et thermodynamique de l'adhésion, des transformations de phase et de la rupture dans les micro et nanosystèmes

Résumé

Les phénomènes de micro-instabilité et de multi-stabilité jouent un rôle clé dans divers systèmes mécaniques et physiques, tant artificiels que biologiques. Leur compréhension fait donc l'objet d'un vaste champ d'études, avec de nombreuses applications pratiques et théoriques. La modélisation de l'effet de la température sur les micro-instabilités, apparaissant dans différents phénomènes artificiels et biologiques, permet la validation de la mécanique statistique pour les petits systèmes, par la comparaison avec les données expérimentales obtenues à l'aide de la spectroscopie de force et d'essais micromécaniques, fournissant ainsi des informations utiles sur les réponses induites par les forces ou les allongements appliqués. Ces analyses sont particulièrement importantes pour l'étude de tous les systèmes qui présentent deux (ou plus) états métastables, tels que les processus d'adhésion/déadhésion, les transformations de phase (pliage/dépliage et phénomènes pseudo-élastiques) et la propagation des fissures et des fractures dans les systèmes à l'échelle nano- et micro-métrique. À titre d'exemple, la température influence fortement les caractéristiques de transformation de phase des nanofils pseudo-élastiques utilisés comme actionneurs et capteurs en nanotechnologie, ou modifie les propriétés d'adhésion des cellules métastatiques dans les processus d'invasion du cancer. La réponse force-extension ou contrainte-déformation est l'une des principales caractéristiques utiles pour comprendre les effets des micro-instabilités et, pour l'obtenir analytiquement, il faut évaluer la fonction de partition du système, qui est l'outil essentiel de la mécanique statistique. Par conséquent, la forme complexe de l'énergie potentielle du problème étudié est approximée en utilisant la technique des variables de spin, ce qui permet d'obtenir une quantité discrète capable d'identifier les différents puits d'énergie potentielle. La première partie de cette thèse traite de l'état de l'art, des problèmes ouverts, des motivations et de la description des méthodologies adoptées. La partie suivante montre comment différents phénomènes physiques peuvent être étudiés par la même approche de modélisation.

Mots clés : micro-instabilités, transformations de phase, mécanique statistique, science des matériaux, fracture, propagation des fissures, attachement, détachement, biophysique, modèle d'ising

---